Two-Dimensional Flow Predictions in a Tube Bundle Using Orthogonal and Non-Orthogonal Grids

by

Lloyd Alan Penner

A thesis
presented to the University of Manitoba
in partial fulfilment of the
requirements for the degree of
Master of Science
in
Mechanical Engineering

Winnipeg, Manitoba, Canada 1996

THE UNIVERSITY OF MANITOBA

FACULTY OF GRADUATE STUDIES

COPYRIGHT PERMISSION

TWO-DIMENSIONAL FLOW PREDICTIONS IN A TUBE BUNDLE USING ORTHOGONAL AND NON-ORTOGONAL GRIDS

BY

LLOYD ALAN PENNER

A Thesis/Practicum submitted to the Faculty of Graduate Studies of the University of Manitoba in partial fulfillment of the requirements for the degree of

MASTER OF SCIENCE

Abstract

A computer procedure has been developed to model the two-dimensional isothermal flow in a cross-section of shell-and-tube heat exchangers with complex-shaped tube bundles, flow blockages, and shell of any arbitrary shape. The tube bundle region is modeled using the porous media concept and isotropic drag correlations. A grid generator has been developed to define the two-dimensional grids that model complex internal detail using a paneling method and transfinite interpolation. The purpose of this work was to compare the results of flow predictions for a simplified heat exchanger model using orthogonal and non-orthogonal grids.

The differential equations for conservation of mass and momentum in the x and y directions were discretized using a co-located variable storage scheme and a Finite Volume Method. The discrete equations for U and V velocities and pressure-correction were solved using a nine-diagonal iterative solver. The pressure-velocity coupling was handled using the PWIM and SIMPLEC algorithms. An energy conservation equation was also solved for selected test cases.

A series of tests were performed to validate the computer code. Then, the results of the orthogonal and non-orthogonal grids, were compared on a simple slug flow and a simplified heat exchanger that included a tube bundle tilted at 45^o. The results were compared in the form of streamlines, velocity profiles, and non-dimensional pressure drop in order to observe the trend toward grid independence as the grid resolution was increased.

The results of the slug flow test, showed that the orthogonal grid appears to give grid independent results with a coarse grid, while the non-orthogonal grid needed more refinement to produce the same results. The results for the rotated square tube bundle test showed that the non-orthogonal grid is more efficient in producing grid-independent overall measurements, as indicated by the non-dimensional pressure drop from inlet to outlet, but the orthogonal grid approach produced velocity profiles that were slightly closer to the grid independent solution for the finest grid density tested.

Acknowledgments

I would like to thank my supervisor Dr. S. J. Ormiston for his help and advice throughout the course of this study. Thanks to my fellow students, Lorenzo Auriti, Paul Bernatsky, Mike Marko, and Peregrin Maksimovich, who helped clean up some graphs, answered and asked questions.

This work was funded by the Natural Sciences and Engineering Research Council of Canada. Their support is gratefully acknowledged.

I would, also, like to thank my wife, Christine, for her patience and support during the years I spent in engineering education.

Contents

List of Tables

List of Figures

Nomenclature

A	area, $[m^2]$
b	source term in algebraic equations
C_p^*	non-dimensional pressure drop
Cp	specific heat, $[J/kg \cdot K]$
D	diffusion coefficient, $[m^2/s]$
DS	distance along $\hat{s}$ vector across the entire panel, [m]
D_V	tube volumetric equivalent (hydraulic) diameter,$[m]$
d	tube diameter, $[m]$
ds	distance along $\hat{s}$ vector for a single control volume, [m]
dt	distance along $\hat{t}$ vector for a single control volume, [m]
f	friction factor around tubes
f	interpolation coefficient
Gr	Grashof number
g	acceleration due to gravity, $[m/s^2]$
h	heat transfer coefficient, $[W/m^2 \cdot K]$
IB	first control volume on the west side of the domain
IE	last control volume on the east side of the domain
JB	first control volume on the south side of the domain
JE	last control volume on the north side of the domain

K	tube drag coefficient
k	thermal conductivity, $[W/m \cdot K]$
k	turbulence kinetic energy
M	mass of fluid, $[kg]$
$\dot{m}$	mass flow rate, $[kg/s]$
NX	number of nodes along the i index
NY	number of nodes along the j index
$\hat{n}$	$n_x\,\hat{\imath} + n_y\,\hat{\jmath}$ = normal unit vector
P	pressure, $[N/m^2]$
Pe	Peclet number
Pr	Prandtl number
p	tube pitch, $[m]$
Q	lagged part of linearized source term
q''	heat flux $[W/m^2]$
R	active nodal part of linearized source term
Ra	Rayleigh number
Re	Reynolds number
S	linearized source term
$\hat{s}$	$s_x\,\hat{\imath} + s_y\,\hat{\jmath}$ = west to east geometric grid unit vector
T	temperature, $[K]$
t	time, $[s]$
$\hat{t}$	$t_x\,\hat{\imath} + t_y\,\hat{\jmath}$ = south to north geometric grid unit vector
U	velocity in the Cartesian x direction, $[m/s]$
V	velocity in the Cartesian y direction, $[m/s]$
$\vec{V}$	$U\,\hat{\imath} + V\,\hat{\jmath}$ = velocity vector, $[m/s]$
$\forall$	volume, $[m^3]$
XPD	expansion factor

x	horizontal Cartesian direction, [m]
y	vertical Cartesian direction, [m]

Greek Letters

α	convective weighting coefficient for upwind differencing
β	volumetric thermal expansion coefficient, $[1/K]$
β	diffusive weighting coefficient for upwind differencing
γ	ratio of volume of porous media to total volume
Δ	measure of field change per step, compared to convergence criteria
ε	porosity, ratio of volume of fluid to total volume
ε_t	porosity of tube-filled control volumes
ϵ	eddy diffusivity, kinetic energy dissipation rate
κ	flow conductivity
λ	improved five-point lagging coefficient
μ	laminar (molecular) viscosity, $[N \cdot s/m^2]$
μ_t	turbulent (Eddy) viscosity, $[N \cdot s/m^2]$
μ_{eff}	effective viscosity, $[N \cdot s/m^2]$
ρ	density, $[kg/m^3]$
Φ	general variable (referring to U or V Velocity, T or P')

Subscripts

$bndry$	referring to boundary
d	referring to diameter
E, W, N, S	referring to nodal quantities to the east, west, north, and south of the present control volume
e, w, n, s	referring to face quantities to the east, west, north and south of the present control volume
eff	effective
f	referring to fluid
fs	referring to free stream
H	referring to high flow conditions
i	west to east control volume index
j	south to north control volume index
L	referring to low flow conditions
NB	referring to the neighboring nodal points of a standard control volume
nb	referring to the neighboring points of a shifted control volume centered at a face of a control volume.
NE, NW	referring to nodal quantities to the Northeast and Northwest of the present control volume
SE, SW	referring to nodal quantities to the Southeast and Southwest of the present control volume
ne, nw	referring to corner quantities to the northeast and northwest of the present control volume
se, sw	referring to corner quantities to the southeast and southwest of the present control volume
P	referring to the Present control volume

PE	referring to the East control volume as the Present control volume
Pe	referring to a shifted control volume centered at the east face of the Present control volume
pm	referring to porous media
$spec$	specified value
t	referring to tube filled region
x	referring to the Cartesian horizontal direction
y	referring to the Cartesian vertical direction

Superscripts

o	referring to value of variable from previous time step or previous iteration
u, v, c, t	referring to U or V momentum, continuity,and temperature equations
ϕ	referring to U or V momentum, T or P' equations
$\star$	referring to calculated value from the solver
$'$	referring to the correction value
$\tilde{}$	referring to a group of terms (ie. $\tilde{\Phi}$ refers to a group of Φ terms)
$\hat{}$	corrected for porosity
$\bar{}$	actual, corrected for porosity
$\cdot$	rate
$\oplus$	refers to modifications of continuity coefficients
$'''$	volumetric quantity

Acronyms

ADI	Alternating-Direction Implicit
CPU	Central Processing Unit
EDS	Exponential Differencing scheme
FEM	Finite Element Method
FVM	Finite Volume Method
ICE	Implicit Continuum-Fluid Eulerian
LGS	Line Gauss-Seidel
LGS2D	LGS two Dimensional solver
LR	Left to Right
PLR92D	Perić's nine-point Left to Right two Dimensional solver
PWIM	Pressure-Weighted Interpolation Method
SIMPLE	Semi-Implicit Method for Pressure-Linked Equations
SIMPLEC	SIMPLE-Consistent
TDMA	Tri-Diagonal matrix Algorithm
UDS	Upwind Differencing Scheme

Chapter 1

Introduction

1.1 Overview

Shell-and-tube heat exchangers are widely used in engineering applications and computer models that predict the shell-side flow and heat transfer have the potential to become important design tools. A detailed knowledge of the flow and the ability to predict the effect on the flow of changes to the tube bundle shape and the placement of sealing strips and baffles should help the designer to reduce tube vibration, to reduce pressure drop, and to improve the overall performance of the heat exchanger.

In practice, the shapes of the shell and the flow blockages will vary and the tube bundle boundary may be shaped irregularly. One approach to modeling is to develop a computer model using a simple, orthogonal grid system and then model the irregular shapes in some approximate way. A second approach is to develop a computer model that uses a non-orthogonal grid system that matches the irregular shapes. This work will compare these two modeling approaches.

This chapter provides a literature review in the background for the present work.

1.2 Background

In order to provide some background to the present work, some examples of the application of numerical methods to various heat exchanger designs is given in this section. This background is aimed at reviewing current methodology in order to put the present work in perspective with the state of the art.

There are three main aspects of heat exchanger modeling. The first aspect is the porous medium approximation to tube bundles. The porosity model of tube bundles along with a distributed resistance is commonly used instead of solving for the flow around every individual tube. The second aspect is the type of grid used to model the heat exchanger. Orthogonal Finite Volume Methods (FVM) are the standard, as described by Patankar [26]. The grid may be Cartesian, cylindrical or a general curvilinear orthogonal coordinate system. The FVM has been adapted for use on non-orthogonal grids as described, for example, by Karki and Patankar [17]. The use of co-located variables and Cartesian velocity components greatly reduced the complexity of the FVM on non-orthogonal grids, as described, for example, by Kobayashi [19] and Perić[30]. The third aspect is the turbulence effects for heat exchanger shell-side flows. The three common ways to model turbulence are a fixed effective viscosity, a mixing length model, and two-equation k–ϵ models. The fixed effective viscosity is used to keep the model for shell-side flow predictions simple, but yet retain the effects of turbulence.

1.2.1 Modeling of Tube Bundle Flow Application to Heat Exchanger Cross Flows

The model of the tube bundle used by most researchers is the porosity concept with a distributed resistance, which was first described by Patankar and Spalding [28]. Most computers are not powerful enough to practically model flow around individual tubes, so a global rep-

resentation of the tubes as a distributed flow blockage in a porous medium was developed. In a tube bundle the pitch, diameter of tubes, and layout information are used to assign a percentage of volume that is blocked, thus reducing the shell-side flow area. Correlations for tube drag are included in the source terms of the discretized equations as a means of modeling pressure drop and diffusion of momentum caused by the tubes.

The porosity-distributed resistance approach has become the most common method of treating tube bundle flows because of its simplicity. Rhodes and Carlucci [39] and Theodossiou et al. [42] reported simulations of a rectangular, isothermal model that compared well with velocity measurements. Al-Sanea et al. [1] simulated flow through the McAllister condenser using the PHOENICS code to model two-phase flow. Ormiston et al. [24, 25] also simulated the McAllister test problem. Zhang and Sousa [48] reported good agreement with experimental results on three condensers. Caremoli [4] simulated a fan-type condenser with a rectangular shell. Zhang [46] modeled a very large rectangular condenser with a complex tube bundle. Carlucci et al. [7] modeled a nuclear steam generator under isothermal conditions. Frisina et al. [10] simulated a moderator heat exchanger to resolve vibration problems. Kao and Cho [16] used a porosity approach in a three-dimensional model of a pressurized water reactor. Zhang and Sousa [49] simulated a disc-and-doughnut heat exchanger. Carlucci and Cheung [5] and Carver [8] used the porosity concept to model a CANDU nuclear reactor core. Lonsdale and Tierney [21] simulated an X-type cross-flow heat exchanger.

The following are examples of the different types of grid and numerical methods used to simulate shell-side flow. The first group of simulations used a Cartesian coordinate system to model rectangular-shell heat exchangers. Rhodes and Carlucci [39] and Theodossiou et al. [42] used the same experimental model but different methods to predict the flow. Rhodes and Carlucci used hybrid upwind/central differencing, the SIMPLE algorithm on a staggered grid and a TDMA solver while Theodossiou et al. used SIMPLEC algorithm and a Multi-grid solution technique. Al-Sanea et al. [1] simulated single-phase flow through a condenser with a rectangular tube bundle using the PHOENICS code. Ormiston et al. [24, 25]

used upwind differencing, the SIMPLEC algorithm on a staggered mesh, and an ADI solver.

Zhang and Sousa [48] simulated three different condenser configurations using the SIMPLEC algorithm on staggered grids. One of their examples had a tube bundle that was not aligned exactly with the grid so some aliasing of the tube bundle was necessary and they found good agreement with experimental results. Zhang [46] presented a numerical model of a large rectangular heat exchanger in which the tube bundle was complex. She simulated 16 profiles along the length of tubes, a quasi-three-dimensional procedure. Caremoli [4] used upwind differencing, the SIMPLE algorithm, staggered variables and a TDMA solver in a code called CALICO developed by Electricité de France. He simulated two-phase, two-dimensional flow in a power plant condenser with tube bundles that are in a fan arrangement. He found good agreement of pressure predictions compared with an actual working condenser.

The second group of simulations used a cylindrical coordinate system to model cylindrical shell heat exchangers. Carlucci et al. [7] used a hybrid upwind/central differencing scheme, the SIMPLE algorithm on a staggered mesh and a TDMA solver. Kao and Cho [16] used an Implicit Continuum-Fluid Eulerian (ICE) method on a three-dimensional system. Zhang and Sousa [49] simulate a disc-and-doughnut heat exchanger. Carlucci and Cheung [5] used hybrid upwind/central differencing, the SIMPLE algorithm on a staggered mesh and a TDMA solver. They found that the symmetry constraints prevent stabilizing influences from crossing the plane. Solving the full cylinder model gave a more stable flow pattern. They also used the time-marching approach to eliminate convergence problems.

Lonsdale and Tierney [21] reported using a three-dimensional unstructured mesh that matches all irregular shapes and the Finite Element Method (FEM) to solve the Navier-Stokes equations. This finite element approach is very powerful in modeling of the correct shape. Carlucci et al. [6] report a number of simulations in both Cartesian and cylindrical coordinates as part of ongoing work to validate modeling aspects such as turbulence mixing.

The following are examples of the different methods used to model turbulence in heat exchangers. Rhodes and Carlucci [39] and Theodossiou et al. [42] use a fixed viscosity which is estimated from a representative measured turbulence intensity from their model and an average mixing length. Theodossiou et al. concluded that resistance forces dominate the flow so complex turbulence modeling is unwarranted. Zhang [46] assumed turbulent viscosity to be 100 times dynamic viscosity and very little difference was found using different multiples because of the dominance of hydraulic resistance. Zhang and Sousa [48] used a turbulent viscosity uniformly set at twenty times the dynamic viscosity and reported only minor differences as the viscosity multiple increased four-fold and good agreement with experimental results. Ormiston et al. [24] set a constant turbulent viscosity of 1.0×10^{-3}. Carlucci et al. [7] set the effective viscosity equal to laminar viscosity so that the only effective momentum sinks were the resistance terms.

Al-Sanea et al. [1] compared fixed and variable properties and found that varying the turbulent viscosity produces more physically realistic results but also that reasonable simulations can be done with constant properties. For the tube-free region they used a fixed viscosity set by a mixing length model and the tube-filled region had a variable viscosity set by another mixing length model which included mass flow as a parameter.

Zhang and Sousa [49] use a modified k–ϵ model that deals with walls and baffles without the need for separate wall functions while Carlucci and Cheung [5] used a k–ϵ model and wall functions. Lonsdale and Tierney [21] used the k–ϵ model for the tube-free space only.

In the previous work, the simulations were mainly for orthogonal grid systems and only matched the shell shape and tube bundle in as much as they also had Cartesian or cylindrical shapes. Some of the simulations did not have pure cross flow but still used a porosity that was isotropic. Constant effective viscosity was commonly used in tube-filled regions to keep the model simple. Some turbulence models, however, showed an improvement in the accuracy of the simulation if the viscosity was not kept constant.

1.2.2 Numerical Method

Typically, in previous shell-side flow calculations in literature, the differential equations for momentum, continuity, and energy have been volume- and time-averaged in primitive variable form. A standard Finite Volume Method (FVM) is often used on a staggered grid. The tridiagonal matrix Algorithm (TDMA) based solver is commonly used in many orthogonal applications with the standard five point computational molecule because it does not demand much storage and is efficient for small matrices.

The pressure-velocity coupling is usually accomplished using a staggered grid and the SIMPLE algorithm by Patankar and Spalding [27]. Improvements have been made by Van Doormaal and Raithby [43] in the SIMPLEC algorithm which is more robust, efficient and is suitable for modeling heat exchanger shell-side flow.

Flow calculation methods on co-located, non-staggered grids have been developed recently and have several advantages over staggered grid methods. For non-orthogonal grids, however, a special scheme must be used to deal with the pressure-velocity coupling, as shown by Rhie and Chow [38]. Perić [33] compared the staggered and non-staggered grid approaches and found that the co-located method converges faster in some cases, and has advantages when using multi-grid and non-orthogonal grids.

1.3 The Present Work

In the present work, a shell-side flow solution scheme was developed that uses a FVM, co-located variable storage, and a non-orthogonal grid. The FVM, as described by Patankar [26], was used to discretize the U and V momentum, continuity and energy equations for incompressible, viscous, single phase flow. Cartesian velocity components are used.

The tube bundle is modeled as an isotropic porous medium. The porosity accounts for flow area reduction and depends on the tube pitch, diameter and arrangement. In the porous

region, tube drag correlations control the amount of cross-flow resistance and introduces drag in the source terms of the discrete momentum equations. To model turbulent flow, this work uses a constant effective viscosity and wall functions as described by Launder and Spalding [20], Brown and Raithby [2] and White [45].

The present work follows methods that are considered "state of the art" which are not yet in common use for heat exchanger shell-side flow calculations. Co-located variable storage was used specifically because of the purpose of comparing orthogonal and non-orthogonal grid systems. It would have been more difficult to implement solution techniques and boundary conditions on a non-orthogonal grid using a staggered grid approach. A grid generator was developed that creates non-orthogonal grids using a paneling method.

A segregated solution scheme based on the SIMPLEC algorithm developed by Van Doormaal and Raithby [43] is used along with the Pressure-Weighted Interpolation Method (PWIM) described by Rhie and Chow [38] and Miller and Schmidt [23]. The PWIM overcomes the pressure decoupling problems that arise on a non-staggered grid. A standard Alternating-Direction Implicit (ADI) method is used to solve the discretized equations when they are cast in five-point form. The use of severe non-orthogonal grids, however, required a nine-point formulation. In that case the nine-diagonal semi-implicit iterative solver presented by Perić [31], was used.

1.4 Scope

A simple method of modeling a complex tube bundle boundary in a heat exchanger shell-side flow simulation is to use an aliasing procedure on an orthogonal grid. A potentially more accurate method of modeling a tube bundle boundary would be to use a non-orthogonal, boundary-fitted grid. It has not been established that the second, newer, approach is an improvement on the first. To assess the two methods, characteristics such as stability, com-

putational time required, and sensitivity to grid refinement should be compared. The focus of this work is to compare simulations of heat exchanger shell-side flows using orthogonal and non-orthogonal grid systems. The main characteristic use will be sensitivity to grid refinement.

The simulations predict the two-dimensional, incompressible, shell-side flow in a cross-section of a simplified model of a heat exchanger. The tube bundle will be treated as a porous medium but each grid system will map the tube bundle region in a different way. An orthogonal grid will approximate non-aligned tube bundle boundary in a stepwise fashion (called "aliasing") and set the control volumes with a porosity that reflects the fact that only part of the control volume is filled with porous medium. A non-orthogonal grid will set a grid line directly on the tube bundle boundary and will match the defined tube bundle boundary. As a result, each control volume is either completely in, or outside, the tube bundle region. A comparison will be made between the results using orthogonal and non-orthogonal grids to observe the differences in the flow predictions and the characteristics of the solution as the grid is refined.

There are no suitable experiments that may be used to compare only the effects of how the tube bundle boundary is matched. Existing experiments are either for orthogonal and one-dimensional flow or are much too complex for clear comparison of the two grid systems. Therefore, the two grid systems can only be compared against each other in specially designed test problems.

Two test problems will be defined and used. The first simulates flow in and out of the center of a tube bundle with no walls or blockage effects. The second simulates more complex, more realistic heat exchanger shell-side flow.

The computer code developed for these comparisons will be validated on standard test problems in comparison with published results.

In the discussion of results, the issue of solution errors introduced by the interface between

the tube filled region and free fluid is addressed. These errors are important because of the complexity of the flow solution on the co-located non-orthogonal grid system and can have a significant effect on the behavior of the flow. The effort required to fully understand and resolve this issue is tremendous (a separate independent area of research) and is beyond the scope of this work.

1.5 Outline

The remainder of this thesis is arranged as follows: Chapter 2 presents the mathematical model based on Navier-Stokes equations in two dimensions. The theory behind the porosity model used is introduced. The simple turbulence model, wall functions, and the treatment of the boundary conditions are discussed.

Chapter 3 presents the method used to generate the grids in this work. The basic nomenclature of the grid system and a general paneling method of combining grids is described.

Chapter 4 presents the numerical model. The integration of the differential equations and the derivation of the algebraic equation set are presented. There is a detailed discussion of each of the terms in the equations and the velocity boundary conditions implementation is explained in detail. Special regions within the grid that represent the tube bundle and the blockages are also discussed.

Chapter 5 presents an explanation of the numerical solution method. The solvers that were used are discussed and the algorithm to treat the pressure-velocity coupling is given.

Chapter 6 presents test problems used to validate the computer code. Problems with known results, or published solutions, are solved using different grids to focus on and present the differences in the results. Each test is chosen to validate particular aspects of the code and the methods used.

Chapter 7 presents and discusses the two main test problems: the slug flow through a slanted tube bundle and the simple heat exchanger with a rotated square tube bundle.

Chapter 8 provides a summary of the main results in this work and presents conclusions.

Chapter 2

The Mathematical Model

2.1 Differential Equations

The equations governing fluid motion in this work are the Navier-Stokes equations. These equations are applicable for two-dimensional, incompressible, Newtonian, viscous flow and are presented in this section. The equations consist of one partial differential equation for conservation of mass, two partial differential equations for momentum conservation (one for each of the x and y Cartesian coordinate directions), and one partial differential equation for conservation of energy. These coupled, non-linear partial differential equations will be integrated over time and volume using a Finite Volume Method (FVM). The primitive variable form is retained and co-located (non-staggered) variable storage on a non-orthogonal grid is used. A unit depth in the z direction is assumed.

In Cartesian coordinates, the partial differential equation for conservation of mass is

$$\frac{\partial}{\partial t}(\varepsilon\rho) + \frac{\partial}{\partial x}(\varepsilon\rho U) + \frac{\partial}{\partial y}(\varepsilon\rho V) = 0 \tag{2.1}$$

This continuity equation controls the conservation of mass in time and space. The first term in Equation 2.1 is the transient term. The second and third terms balance the transport of

mass in the x–y plane carried by the U and V velocities. The porosity, ε, in each term is the ratio of fluid volume to total volume of a given volume of space. The porosity, ε, is included in every term as a result of the volume averaging [24] because it modifies the volume of fluid available in each control volume.

The governing equation for the U velocity (the Cartesian x-direction velocity) is found through the conservation of momentum in the x-direction. The x-direction conservation of momentum equation is

$$\frac{\partial}{\partial t}(\varepsilon\rho U) + \frac{\partial}{\partial x}(\varepsilon\rho UU) + \frac{\partial}{\partial y}(\varepsilon\rho VU) = -\varepsilon\frac{\partial P}{\partial x} - \varepsilon K^u \rho|\vec{V}|U + \frac{\partial}{\partial x}\left(\varepsilon\mu_{eff}\frac{\partial U}{\partial x}\right) + \frac{\partial}{\partial y}\left(\varepsilon\mu_{eff}\frac{\partial U}{\partial y}\right) - \varepsilon\rho g_x \quad (2.2)$$

The first term in Equation (2.2) is the transient term. The second and third terms are terms for the advection of momentum. The first term on the right side of the equation is the pressure gradient. The second term on the right side is the cross flow tube drag as proposed by Butterworth [3]. The third and fourth terms on the right side represent the diffusion of momentum. The last term in Equation (2.2) is the gravity body force term.

The governing equation for the V velocity (the Cartesian y-direction velocity) is found through the conservation of momentum in the y direction. The y-direction conservation of momentum equation is

$$\frac{\partial}{\partial t}(\varepsilon\rho V) + \frac{\partial}{\partial x}(\varepsilon\rho UV) + \frac{\partial}{\partial y}(\varepsilon\rho VV) = -\varepsilon\frac{\partial P}{\partial y} - \varepsilon K^v \rho|\vec{V}|V + \frac{\partial}{\partial x}\left(\varepsilon\mu_{eff}\frac{\partial V}{\partial x}\right) + \frac{\partial}{\partial y}\left(\varepsilon\mu_{eff}\frac{\partial V}{\partial y}\right) - \varepsilon\rho g_y \quad (2.3)$$

All the terms in Equation (2.3) are analogous to those in Equation (2.2).

The above equations are sufficient for an isothermal flow simulation. In selected cases, when validating the computer model, the governing equations were extended to include an equation for the temperature field.

The temperature field is governed by the conservation of energy equation. The partial differential equation for T is

$$\frac{\partial}{\partial t}(\varepsilon\rho T) + \frac{\partial}{\partial x}(\varepsilon\rho UT) + \frac{\partial}{\partial y}(\varepsilon\rho VT) = +\frac{\partial}{\partial x}\left(\varepsilon\frac{k}{Cp}\frac{\partial T}{\partial x}\right) + \frac{\partial}{\partial y}\left(\varepsilon\frac{k}{Cp}\frac{\partial T}{\partial y}\right) + \varepsilon\dot{S}_t''' \quad (2.4)$$

The first term in Equation (2.4) is the transient term. The second and third terms are the advection of energy terms. The first two terms on the right side of Equation (2.4) are energy transfer by conduction, and the last term is a volumetric energy source.

Equations (2.2), (2.3), and (2.4) are used for U, V, and T respectively. The only variable left is pressure, but the only equation not associated with a dependent variable is the continuity equation, (Equation (2.1)). The continuity equation only has velocities and only the momentum equations contain pressure terms, therefore continuity must serve to couple the pressure and velocity together. This is the basis of the pressure-velocity coupling algorithm used to solve the discrete equation set, as described later in Section 5.2.

Each of the above equations is integrated with respect to time and volume to produce a linear algebraic equation set that can be solved using numerical methods. The details of the discretization appear in Chapter 4.

2.2 Porosity

As previously mentioned, the porosity, ε, is the ratio of fluid volume to the total volume, $\forall_f/\forall_{total}$. It is used to describe the percentage of the flow not blocked by a solid. Porosity can vary between 1 in the tube-free region (fluid only) and the value for a control volume that is completely inside a tube bundle, ε_t. The portion, or percentage, of the control volume that is in the tube bundle is described by the porosity percentage, γ. For a specific control volume that is completely outside of a tube bundle $\gamma = 0$, but for a control volume completely inside a tube bundle $\gamma = 1$. For a control volume that straddles the tube bundle

boundary, γ is set at some intermediate value depending on where the defined boundary intersects the control volume faces. The following relation indicates in mathematical terms how the percentage and the porosity are linked:

$$\varepsilon = \frac{V_f}{V_P} = \gamma\, \varepsilon_t + (1 - \gamma) \tag{2.5}$$

The theoretical porosity value of a tube bundle, ε_t, is determined from the tube pitch, the diameter of the tubes, and the tube bundle layout.

The tube bundle layout is described in two general groups. The square tube bundle layout is described as rows of tubes with the distance between rows the same as between tubes. The triangular tube bundle is described as rows of tube offset in such a manner that for alternating rows, the tubes lie in between tubes in the neighboring rows. The distance between tubes along a row is the same as the distance diagonally to the tube in the next row, so that any three tubes produce an equilateral triangle. The porosity for a square tube bundle is

$$\varepsilon_t = 1 - \frac{\pi}{4}\left(\frac{d}{p}\right)^2 \tag{2.6}$$

and for a triangular tube bundle is

$$\varepsilon_t = 1 - \frac{\pi}{2\sqrt{3}}\left(\frac{d}{p}\right)^2 \tag{2.7}$$

In some applications distances between tubes and rows can vary but Equations (2.6) and (2.7) were derived for equal pitch in both directions.

It should be noted that when the pitch and diameter of the tubes are equal, flow across the tube bundle is completely blocked. In this case, a porosity of zero would be expected to be consistent with zero flow area, but the porosity give by Equations (2.6) and (2.7) would not be equal to zero. This inconsistency in the porosity calculation poses no problems since tubes in contact with each other is not an expected condition in a heat exchanger design. A separate mechanism is used to model flow blockages.

In the implementation of the computer model a volume variable represents the entire volume of a control volume. The porosity and the full volume are combined to indicate the volume of fluid in a control volume. The control volume face area is also reduced in the same manner. In the model a so-called free stream velocity may be calculated by multiplying the fluid velocity (found in calculations) by the porosity. In mathematical terms the relationships described above are given as:

$$\overline{\mathcal{V}_P} \equiv \mathcal{V}_f = \mathcal{E}_P \mathcal{V}_P \qquad \overline{A_e} = \mathcal{E}_e A_e \qquad \left|\vec{V}\right|_{fs} = \mathcal{E}_e \left|\vec{V}\right| \tag{2.8}$$

In the computer code all four control volume face areas (from grid generation) are multiplied by the porosity associated with that control volume. Conflicts arise, however, wherever porosity changes. At the interface between two control volumes of different porosities, the common face porosity is set equal to the lower of the two adjacent control volume porosities. The reason for choosing the lower porosity at a face is the prediction of physically realistic face velocities at the interface under the constraint of conservation of mass.

2.3 Turbulence Model

Turbulence effects are modeled using a constant effective viscosity. The effective viscosity, μ_{eff}, is defined as the sum of molecular and turbulent viscosities

$$\mu_{eff} = \mu + \mu_t \tag{2.9}$$

The turbulent viscosity can be many times larger than laminar viscosity and normally varies locally throughout the domain, depending on the flow.

In this work, the turbulence is modeled by the use of an effective viscosity that is a constant multiple of the molecular viscosity. The effective viscosity is set to a multiple of 25 to 100 times the laminar viscosity. The fixed viscosity eliminates the local changes in

turbulent diffusion of momentum. More detail on the fixed viscosity multiple is given in Section 4.6.

Wall functions are used at solid boundaries. The wall function method used in the present work is implemented as reported by Launder and Spalding [20] and following the example of Brown and Raithby [2] and White [45]. Wall functions replace the diffusion term with a shear stress in the control volume next to solid blockages and walls. The shear stress imposed at the wall is lower than without the wall functions because the effective viscosity is reduced. This change of wall shear stress effectively reduces the boundary layer to produce a profile that more closely matches the expected turbulent profile even though there are not enough control volumes near the boundary to model it accurately. More detail on the wall shear stress is given in Section 4.7.6.

2.4 Treatment of Boundary Conditions

There are two types of boundary condition used in the present work. First, the Dirichlet condition specifies the value of a variable at a boundary. Second, the Neumann condition specifies the value of the gradient of a variable at a boundary. Boundary conditions are described below in general, as they were applied for the velocity, pressure, and temperature. The details of the implementation of the discrete boundary conditions are discussed in Section 4.7

2.4.1 Nodal Velocity

The Dirichlet boundary condition, a desired value of velocity is specified on the boundary. In general terms, $\Phi_{bndry} = \Phi_{spec}$, where Φ is either U or V velocity and $_{bndry}$ refers to either the north, south, east or west boundary.

The Neumann boundary condition for velocity, is more difficult because of the non-orthogonal grid. The Neumann boundary condition may be for a gradient normal to the boundary, $\frac{\partial \Phi}{\partial n}$, or in a Cartesian direction (for example: $\frac{\partial \Phi}{\partial x}$). For a Cartesian vertical boundary these two gradients are equivalent. On a non-orthogonal grid, however, these two gradients may not be the same. The present work uses the boundary conditions in the Cartesian directions because the scope of the work is limited to the comparison between orthogonal and non-orthogonal grids with identical Cartesian external boundaries.

2.4.2 Pressure

There is no equation that solves for pressure directly, but pressure is found through the pressure-correction equation, which is the result of SIMPLEC and the PWIM, which are discussed in Chapter 5. Thus, the pressure is dependent on the face velocities and, by extension, the velocity boundary conditions. There is no direct pressure boundary condition specification in this work.

2.4.3 Face Velocity

The PWIM is used to calculate face velocities, whose boundary conditions are set the same way as nodal velocities (described in Section 2.4.1). Since all the boundaries have zero-width control volumes, the face and nodal points are coincident on the boundary. For a Dirichlet boundary condition, the face velocities on the boundary are set to equal the nodal velocities, $\Phi_{face} = \Phi_{nodal}$. For Neumann boundary conditions, $\frac{\partial \Phi}{\partial x}$ is applied to face velocities on a Cartesian vertical boundary, but the whole control volume width is used in the gradient calculation.

2.4.4 Blockages

The blockages are treated as solid wall and a Dirichlet boundary condition for velocity is set. The value of velocity is set to zero on the faces and everywhere inside a blockage. The momentum and continuity coefficients are adjusted to reflect both the zero velocities at the blockage faces and the removal of connections to pressure nodes inside the blockage.

2.4.5 Temperature

The Dirichlet boundary condition for temperature is exactly like the velocity Dirichlet condition. The desired value of temperature is specified for all the nodes that are on the boundary, mathematically represented as, $T_{bndry} = T_{spec}$.

The Neumann boundary condition for temperature is similar to that for velocity except that the heat flux is set rather than just the temperature gradient. Furthermore, the temperature gradient is taken normal to the boundary. The heat flux over the control volume face area is

$$q'' = \frac{q}{A} = -k \frac{\partial T}{\partial n} \tag{2.10}$$

Thus, setting the heat flux is analogous to setting the temperature gradient specified for the nodes on a boundary.

Chapter 3

Grid Generation

3.1 Introduction

In order to discretize the differential equations, the computational domain is subdivided into a set of control volumes (called a grid) that conforms to the domain boundaries and, as much as possible, to any of the interior boundaries. In this work, the grid is constrained to be structured. A non-orthogonal grid may be generated that is made up of quadrilateral control volumes that can be expanded or contracted across the domain. This general grid generation method is also used to produce Cartesian grids. The specific locations of all the coordinate points of the grid are controlled by transfinite interpolation as well as an expansion factor. A more complex domain can be mapped by assembling a number of grids together as panels.

3.2 Generation Method

The method of grid generation used in this work is very similar to the transfinite interpolation method as described by Knupp [18]. Once the four vertices of the grid are specified, the grid boundary can be defined as either a straight line, arc, or an arbitrary line defined by points.

An expansion factor can be applied along a straight or curved boundary. The interior grid is simply a double linear interpolation between opposite defined boundary points. The result is a clearly laid out set of coordinates that define nodes centered in control volumes. The distances, areas, and volumes are all calculated and stored as described in the next section. There is also a capability to combine these grids, using a paneling approach, to build up complex structured grids. The complex grid permits the modeling of interior structures such as tube bundles and blockages.

3.2.1 Grid Geometry

Figure 3.1 shows a sample grid consisting of nine control volumes. The grid does not have to be aligned with the Cartesian directions, it is shown this way to read the labels clearly. The control volumes are labeled in the compass-point notation. The reason for the "nine-point"

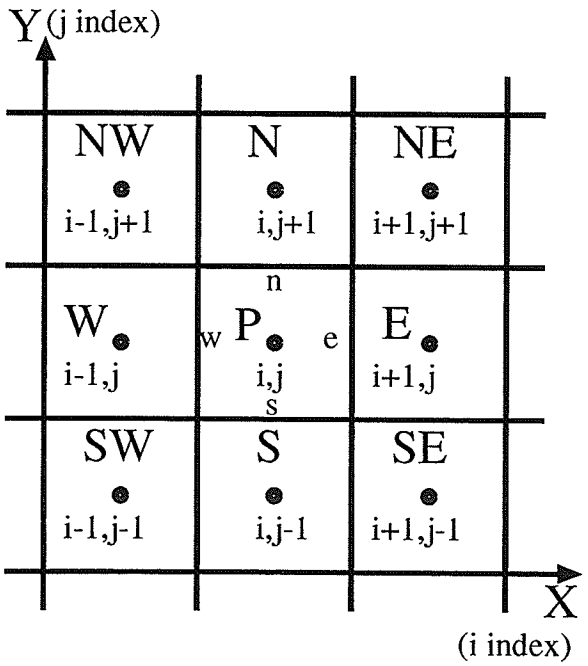

Figure 3.1: Indexing and Notation for Neighboring Control Volumes.

compass notation will be described later in connection with the solution of the algebraic equation in Chapter 4. The i and j indices reference each control volume in an organized fashion. The i index proceeds from IB ($i = 2$) for the first control volume on the west side of the domain to IE ($i = NX + 1$) for the last control volume on the east, where NX is the number of control volumes along the i index. The west to east direction of increasing i index is referred to as the $\hat{s}$ direction. The j index goes from the first control volume on the south, JB ($j = 2$), to the last control volume on the north, JE ($j = NY + 1$), where NY is the number of control volumes along the j index. The south to north direction of increasing j index is referred to as the $\hat{t}$ direction. Each control volume also has a north, south, west and east face as indicated by the lower case letters in the center (present) control volume labeled "P".

There are nodes in zero width control volumes on the boundaries of the domain to implement the boundary conditions. These nodes are referenced by $IB - 1$ on the west, $IE + 1$ on the east, $JB - 1$ on the south, and $JE + 1$ on the north and reside in zero-width control volumes referred to as fictitious control volumes[1].

Each control volume is made up of four quadrants, each referred to by geographical directions, northeast (NE), southeast (SE), northwest (NW), and southwest (SW). Figure 3.2 shows these quadrants with the node in the center.

The locations of point where x and y coordinate values are stored are labeled in Figure 3.3. The center node, "P", is referenced as "southwest" and the top right corner as "northeast". The south points are referenced as the north points of the control volume to the south, for example $(XNW_{(i,j-1)}, YNW_{(i,j-1)})$. The west points are referenced as the east points of the control volume to the west. The southwest corner is referenced as

[1]The boundary conditions are stored in the coefficients of the fictitious control volumes and are absorbed into the interior control volumes. Therefore, no computation ever occurs to calculate the nodal values of boundary control volumes. Their values are found from the boundary conditions after the interior nodes are known.

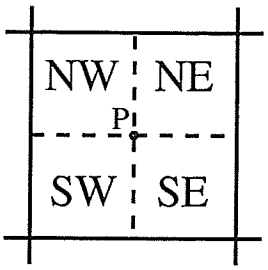

Figure 3.2: Quadrant Notation for a Control Volume.

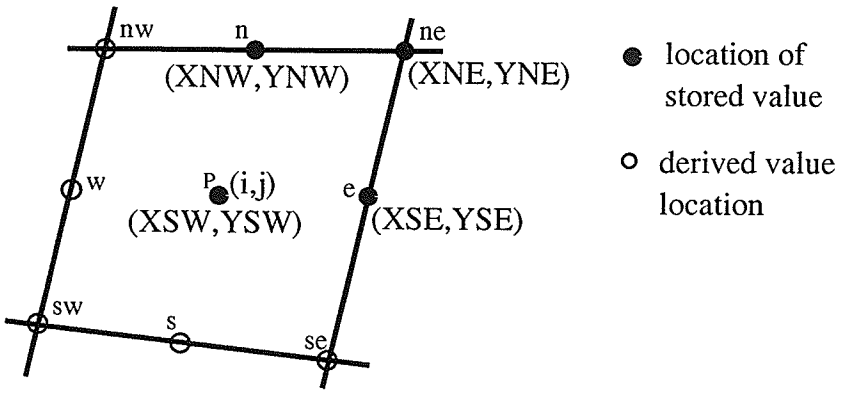

Figure 3.3: Coordinates of Control Volume Points.

$(XNE_{(i-1,j-1)}, YNE_{(i-1,j-1)})$.

The nomenclature for control volume distances, areas, and volumes are shown in Figure 3.4 on an orthogonal grid for simplicity. The distances are the length between points in the control volume. The areas are equal to the distance between points multiplied by a unit thickness of the control volume. When the grid is non-orthogonal the quadrants are split into two triangles each. The volume of each triangle is calculated and then the two are added together to get the correct volume for each quadrant.

The non-orthogonal grid needs some direction unit vectors and distances defined because the grid will not necessarily be aligned with the Cartesian coordinate directions. As shown in Figure 3.5, there are separate direction vectors for each face and the central node of the main control volume. The $\hat{s}$ vectors point from west to east and the $\hat{t}$ vectors point from

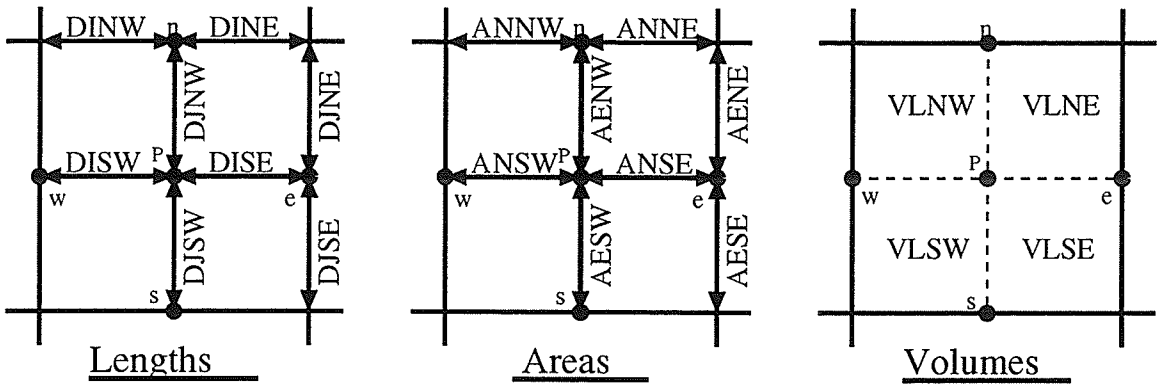

Figure 3.4: Lengths, Areas, and Volumes of a Control Volume.

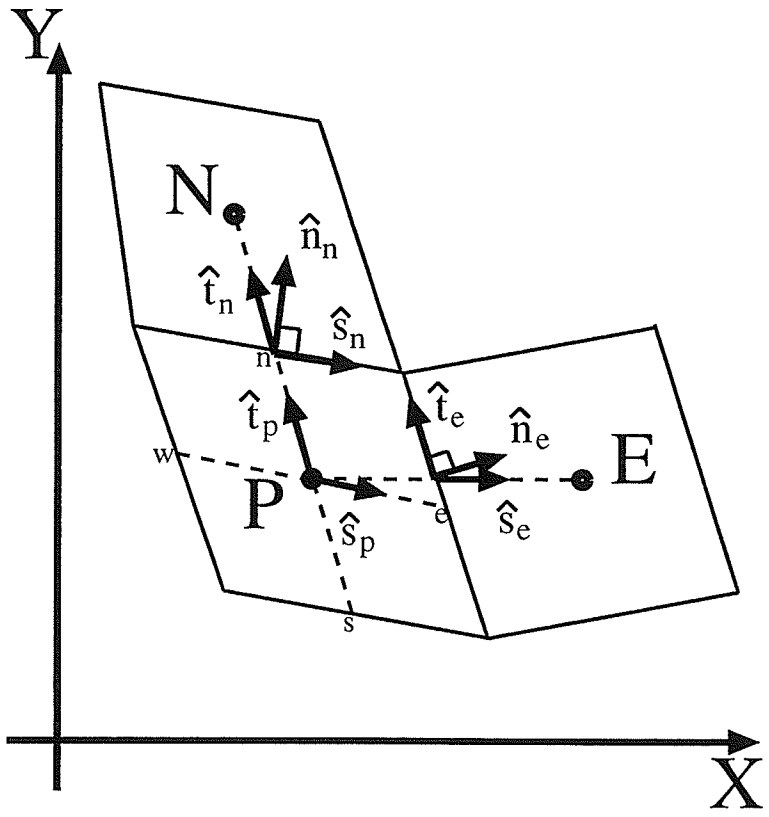

Figure 3.5: Grid Direction Vectors.

south to north. The vectors on the east face of the present node are labeled "e", and on the north face "n". The vectors would also occur on the west and south of the present node but would be referenced by $i-1$ and $j-1$ respectively.

Since the grid may be skewed, some variables are defined that describe the distance between locations. Figure 3.6 shows the location of these distance variables. The distance between a node and its neighbor to the east, along the $\hat{s}_e$ vector, is defined as:

$$(ds)_{e_{(i,j)}} = \sqrt{\left(XSW_{(i+1,j)} - XSW_{(i,j)}\right)^2 + \left(YSW_{(i+1,j)} - YSW_{(i,j)}\right)^2} \tag{3.1}$$

The distance between a node and its neighbor to the north, along the $\hat{t}_n$ vector, is defined as:

$$(dt)_{n_{(i,j)}} = \sqrt{\left(XSW_{(i,j+1)} - XSW_{(i,j)}\right)^2 + \left(YSW_{(i,j+1)} - YSW_{(i,j)}\right)^2} \tag{3.2}$$

The distances $(ds)_n$ and $(dt)_e$ are defined as

$$(ds)_{n_{(i,j)}} = DINW_{(i,j)} + DINE_{(i,j)} \tag{3.3}$$

and

$$(dt)_{e_{(i,j)}} = DJSE_{(i,j)} + DJNE_{(i,j)} \tag{3.4}$$

respectively, and are always equal to the sum of grid quadrant distance variables even if the grid is skewed. The distances (ds) and (dt) are also evaluated for the nodal location ($(ds)_p$ and $(dt)_p$), the west face ($(dt)_w$), and the south face ($(ds)_s$) in a similar fashion as Equations (3.3) and (3.4). Note that $(ds)_w$ and $(dt)_s$ are defined in a similar fashion to Equations (3.1)and (3.2) respectively, although they are not shown in Figure 3.6.

The north normal unit vector, $\hat{n}_n$, is defined outward normal to the north face of a control

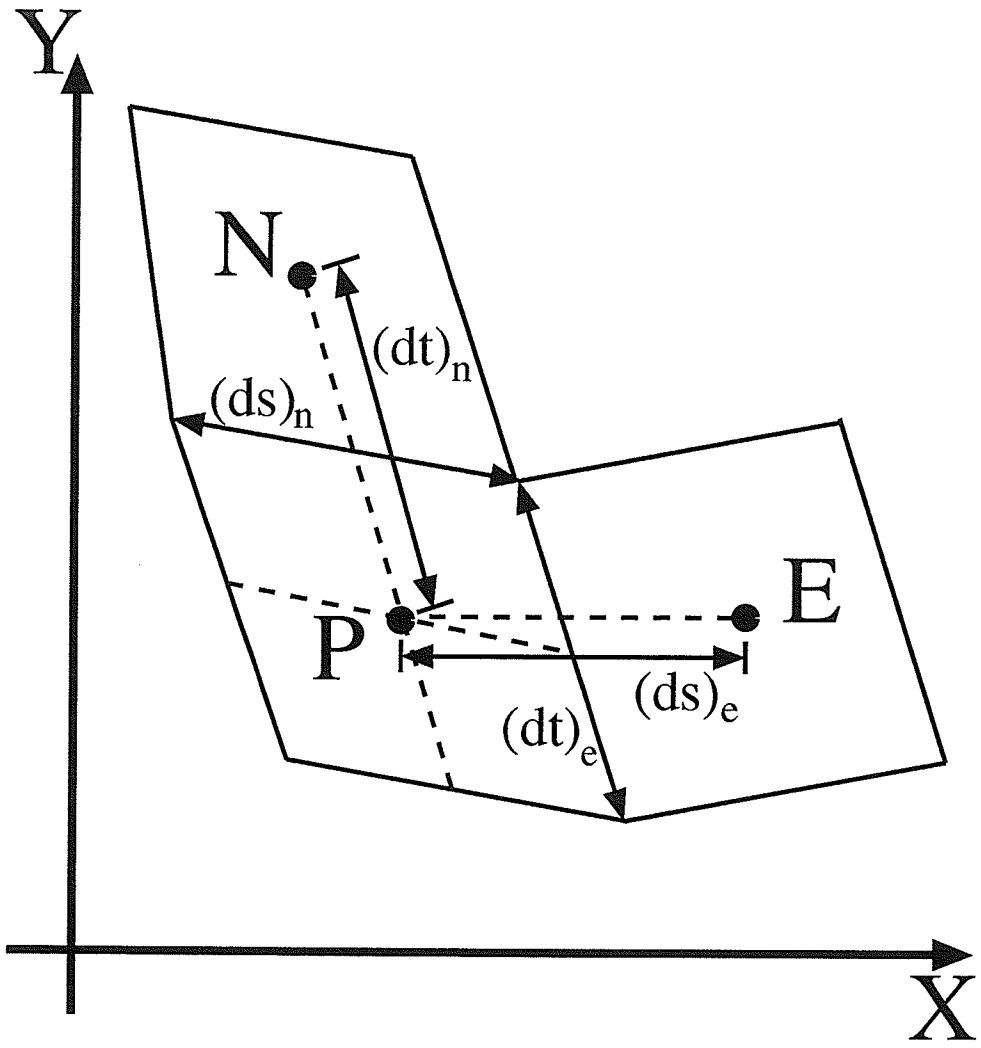

Figure 3.6: Location of Distance Variables.

volume as follows:

$$\hat{n}_{n(i,j)} = \frac{-\left(YNE_{(i,j)} - YNE_{(i-1,j)}\right)}{\sqrt{\left(XNE_{(i,j)} - XNE_{(i-1,j)}\right)^2 + \left(YNE_{(i,j)} - YNE_{(i-1,j)}\right)^2}}\,\hat{\imath} + \frac{\left(XNE_{(i,j)} - XNE_{(i-1,j)}\right)}{\sqrt{\left(XNE_{(i,j)} - XNE_{(i-1,j)}\right)^2 + \left(YNE_{(i,j)} - YNE_{(i-1,j)}\right)^2}}\,\hat{\jmath} \quad (3.5)$$

or in terms of arc lengths

$$\hat{n}_{n(i,j)} = \frac{-\left(YNE_{(i,j)} - YNE_{(i-1,j)}\right)}{(ds)_n}\,\hat{\imath} + \frac{\left(XNE_{(i,j)} - XNE_{(i-1,j)}\right)}{(ds)_n}\,\hat{\imath} \quad (3.6)$$

where the gradients are defined and evaluated at the north face and converted to normal unit vector notation

$$\hat{n}_{n(i,j)} = \left.\frac{\partial x}{\partial n}\right|_n \hat{\imath} + \left.\frac{\partial y}{\partial n}\right|_n \hat{\jmath} = n_{xn}\,\hat{\imath} + n_{yn}\,\hat{\jmath} \quad (3.7)$$

The east normal unit vector,$\hat{n}_e$, is defined outward normal to the east face of a control volume as follows:

$$\hat{n}_{e(i,j)} = \frac{\left(YNE_{(i,j)} - YNE_{(i,j-1)}\right)}{\sqrt{\left(XNE_{(i,j)} - XNE_{(i,j-1)}\right)^2 + \left(YNE_{(i,j)} - YNE_{(i,j-1)}\right)^2}}\,\hat{\imath} + \frac{-\left(XNE_{(i,j)} - XNE_{(i,j-1)}\right)}{\sqrt{\left(XNE_{(i,j)} - XNE_{(i,j-1)}\right)^2 + \left(YNE_{(i,j)} - YNE_{(i,j-1)}\right)^2}}\,\hat{\jmath} \quad (3.8)$$

or in terms of arc lengths

$$\hat{n}_{e(i,j)} = \frac{\left(YNE_{(i,j)} - YNE_{(i,j-1)}\right)}{(dt)_e}\,\hat{\imath} + \frac{-\left(XNE_{(i,j)} - XNE_{(i,j-1)}\right)}{(dt)_e}\,\hat{\imath} \quad (3.9)$$

where the gradients are defined and evaluated at the east face and converted to normal unit vector notation

$$\hat{n}_{e(i,j)} = \left.\frac{\partial x}{\partial n}\right|_e \hat{\imath} + \left.\frac{\partial y}{\partial n}\right|_e \hat{\jmath} = n_{xe}\,\hat{\imath} + n_{ye}\,\hat{\jmath} \quad (3.10)$$

The west to east geometric grid unit vector for the north face of a control volume, $\hat{s}_n$, is defined along the line between the northwest and northeast corners of a control volume as follows:

$$\hat{s}_{n(i,j)} = \frac{\left(XNE_{(i,j)} - XNE_{(i-1,j)}\right)}{\sqrt{\left(XNE_{(i,j)} - XNE_{(i-1,j)}\right)^2 + \left(YNE_{(i,j)} - YNE_{(i-1,j)}\right)^2}}\,\hat{\imath} + \frac{\left(YNE_{(i,j)} - YNE_{(i-1,j)}\right)}{\sqrt{\left(XNE_{(i,j)} - XNE_{(i-1,j)}\right)^2 + \left(YNE_{(i,j)} - YNE_{(i-1,j)}\right)^2}}\,\hat{\jmath} \quad (3.11)$$

or in terms of arc lengths

$$\hat{s}_{n(i,j)} = \frac{\left(XNE_{(i,j)} - XNE_{(i-1,j)}\right)}{(ds)_n}\,\hat{\imath} + \frac{\left(YNE_{(i,j)} - YNE_{(i-1,j)}\right)}{(ds)_n}\,\hat{\imath} \quad (3.12)$$

where the gradients are defined and evaluated at the north face and converted to a west to east geometric grid unit vector notation

$$\hat{s}_{n(i,j)} = \left.\frac{\partial x}{\partial s}\right|_n \hat{\imath} + \left.\frac{\partial y}{\partial s}\right|_n \hat{\jmath} = s_{xn}\,\hat{\imath} + s_{yn}\,\hat{\jmath} \quad (3.13)$$

The west to east geometric grid unit vector for the east face of a control volume, $\hat{s}_e$, is defined along the line between the present node and east node as follows:

$$\hat{s}_{e(i,j)} = \frac{\left(XSW_{(i+1,j)} - XSW_{(i,j)}\right)}{(ds)_{e_{(i,j)}}}\,\hat{\imath} + \frac{\left(YSW_{(i+1,j)} - YSW_{(i,j)}\right)}{(ds)_{e_{(i,j)}}}\,\hat{\jmath} \quad (3.14)$$

where the gradients are defined and evaluated at the east face and converted to a west to east geometric grid unit vector notation

$$\hat{s}_{e(i,j)} = \left.\frac{\partial x}{\partial s}\right|_e \hat{\imath} + \left.\frac{\partial y}{\partial s}\right|_e \hat{\jmath} = s_{xe}\,\hat{\imath} + s_{ye}\,\hat{\jmath} \quad (3.15)$$

The west to east geometric grid unit vector for the center of a control volume, $\hat{s}_p$, is defined along a line between the center of the west face and center of the east face as follows:

$$\hat{s}_{p(i,j)} = \frac{\left(XSE_{(i,j)} - XSE_{(i-1,j)}\right)}{\sqrt{\left(XSE_{(i,j)} - XSE_{(i-1,j)}\right)^2 + \left(YSE_{(i,j)} - YSE_{(i-1,j)}\right)^2}}\,\hat{\imath} + \frac{\left(YSE_{(i,j)} - YSE_{(i-1,j)}\right)}{\sqrt{\left(XSE_{(i,j)} - XSE_{(i-1,j)}\right)^2 + \left(YSE_{(i,j)} - YSE_{(i-1,j)}\right)^2}}\,\hat{\jmath} \quad (3.16)$$

or in terms of arc lengths

$$\hat{s}_{p(i,j)} = \frac{\left(XSE_{(i,j)} - XSE_{(i-1,j)}\right)}{(ds)_p}\,\hat{\imath} + \frac{\left(YSE_{(i,j)} - YSE_{(i-1,j)}\right)}{(ds)_p}\,\hat{\imath} \tag{3.17}$$

where the gradients are defined and evaluated at the center of a control volume and converted to a west to east geometric grid unit vector notation

$$\hat{s}_{p(i,j)} = \left.\frac{\partial x}{\partial s}\right|_p \hat{\imath} + \left.\frac{\partial y}{\partial s}\right|_p \hat{\jmath} = s_{xp}\,\hat{\imath} + s_{yp}\,\hat{\jmath} \tag{3.18}$$

The south to north geometric grid unit vector for the north face of a control volume, $\hat{t}_n$, is defined along the line between the present node and north node as follows:

$$\hat{t}_{n(i,j)} = \frac{\left(XSW_{(i,j+1)} - XSW_{(i,j)}\right)}{(dt)_{n_{(i,j)}}}\,\hat{\imath} + \frac{\left(YSW_{(i,j+1)} - YSW_{(i,j)}\right)}{(dt)_{n_{(i,j)}}}\,\hat{\jmath} \tag{3.19}$$

where the gradients are defined and evaluated at the north face and converted to a south to north geometric grid unit vector notation

$$\hat{t}_{n(i,j)} = \left.\frac{\partial x}{\partial t}\right|_n \hat{\imath} + \left.\frac{\partial y}{\partial t}\right|_n \hat{\jmath} = t_{xn}\,\hat{\imath} + t_{yn}\,\hat{\jmath} \tag{3.20}$$

The south to north geometric grid unit vector for the east face of a control volume, $\hat{t}_e$, is defined along the line between the southeast and northeast corners of a control volume as follows:

$$\hat{t}_{e(i,j)} = \frac{\left(XNE_{(i,j)} - XNE_{(i,j-1)}\right)}{\sqrt{\left(XNE_{(i,j)} - XNE_{(i,j-1)}\right)^2 + \left(YNE_{(i,j)} - YNE_{(i,j-1)}\right)^2}}\,\hat{\imath} + \frac{\left(YNE_{(i,j)} - YNE_{(i,j-1)}\right)}{\sqrt{\left(XNE_{(i,j)} - XNE_{(i,j-1)}\right)^2 + \left(YNE_{(i,j)} - YNE_{(i,j-1)}\right)^2}}\,\hat{\jmath} \tag{3.21}$$

or in terms of arc lengths

$$\hat{t}_{e(i,j)} = \frac{\left(XNE_{(i,j)} - XNE_{(i,j-1)}\right)}{(dt)_e}\,\hat{\imath} + \frac{\left(YNE_{(i,j)} - YNE_{(i,j-1)}\right)}{(dt)_e}\,\hat{\imath} \tag{3.22}$$

where the gradients are defined and evaluated at the east face and converted to a south to north geometric grid unit vector notation

$$\hat{t}_{e(i,j)} = \left.\frac{\partial x}{\partial t}\right|_e \hat{\imath} + \left.\frac{\partial y}{\partial t}\right|_e \hat{\jmath} = t_{xe}\,\hat{\imath} + t_{ye}\,\hat{\jmath} \tag{3.23}$$

The south to north geometric grid unit vector for the center of a control volume, $\hat{t}_p$, is defined along a line between the center of the south face and the center of the north face as follows:

$$\hat{t}_{p(i,j)} = \frac{\left(XNW_{(i,j)} - XNW_{(i,j-1)}\right)}{\sqrt{\left(XNW_{(i,j)} - XNW_{(i,j-1)}\right)^2 + \left(YNW_{(i,j)} - YNW_{(i,j-1)}\right)^2}}\,\hat{\imath} + \frac{\left(YNW_{(i,j)} - YNW_{(i,j-1)}\right)}{\sqrt{\left(XNW_{(i,j)} - XNW_{(i,j-1)}\right)^2 + \left(YNW_{(i,j)} - YNW_{(i,j-1)}\right)^2}}\,\hat{\jmath} \tag{3.24}$$

or in terms of arc lengths

$$\hat{t}_{p(i,j)} = \frac{\left(XNW_{(i,j)} - XNW_{(i,j-1)}\right)}{(dt)_p}\,\hat{\imath} + \frac{\left(YNW_{(i,j)} - YNW_{(i,j-1)}\right)}{(dt)_p}\,\hat{\imath} \tag{3.25}$$

where the gradients are defined and evaluated at the center of a control volume and converted to a south to north geometric grid unit vector notation

$$\hat{t}_{p(i,j)} = \left.\frac{\partial x}{\partial t}\right|_p \hat{\imath} + \left.\frac{\partial y}{\partial t}\right|_p \hat{\jmath} = t_{xp}\,\hat{\imath} + t_{yp}\,\hat{\jmath} \tag{3.26}$$

3.2.2 Grid Expansion Factor

The control volumes need not be uniformly spaced between vertices of the grid. An expansion factor is defined such that the neighboring control volume along a grid boundary is a given percentage larger (expanded) or smaller (contracted) than the present control volume. This geometric expansion is carried out on all four boundaries separately. As an example, the equation

$$(ds)_{n_{(i+1,JB-1)}} = (ds)_{n_{(i,JB-1)}}\,XPD_s \tag{3.27}$$

shows that the expansion factor for the south boundary of a grid, XPD_s, multiplies the present control volume south-face length to find the length of the adjacent control volume south face . The result of this expansion is that the overall arc length of the south boundary of the grid, $(DS)_s$, is

$$\begin{aligned}(DS)_s &= \sum_{i=1,NX} (ds)_{n_{(i+1,JB-1)}} \\ &= (ds)_{n_{(IB,JB-1)}} + (ds)_{n_{(IB+1,JB-1)}} + (ds)_{n_{(IB+2,JB-1)}} + \cdots + (ds)_{n_{(IE,JB-1)}} \\ &= (ds)_{n_{(IB,JB-1)}} XPD_s^0 + (ds)_{n_{(IB,JB-1)}} XPD_s^1 + (ds)_{n_{(IB,JB-1)}} XPD_s^2 + \cdots \\ &+ (ds)_{n_{(IB,JB-1)}} XPD_s^{NX-1}\end{aligned} \tag{3.28}$$

where the last (IE) control volume on the south-face length is equal to the length of the first (IB) times the expansion factor to the $NX-1$ power. The exponent on the expansion factor is one less than the number of control volumes across the domain. If that particular grid boundary is an arc, the expansion factor would be applied to the increment of angle. The problem of creating large aspect ratios in control volumes must be considered when choosing the expansion factor.

The expansion factor is applied to each panel separately, so different panels can have control volumes that expand or contract at different rates and the way of controlling the change in control volume size between panels becomes somewhat complicated. From a previous panel the last control volume width is known. To achieve a smooth transition between panels, the ratio of the width of the last control volume in the first panel to the first control volume in the next panel is specified. In addition, overall width and the number of control volumes are known, but the expansion factor is not known. A Newton-Raphson root search is used to solve an algebraic equation for the sum of the expansion factor geometric progression for the present panel.

The panel method is a very powerful development tool to produce grids that match the shape of a complicated solution domain. The next section gives more detail on how paneling is used.

3.3 Paneling

The panel method is used to build up complex grids that match shell shape, baffle locations, and tube bundle region boundaries. Individual sections of the grid are defined to match certain locations and then combined to completely map the whole domain. The panel method provides the flexibility to refine the control volume size in specific regions of greater interest. Even though the grid is still structured, the freedom of grid manipulation that the panels provide gives some of the advantages of unstructured Finite Element Method grids.

With the paneling approach both the boundary and internal structures can be modeled more accurately than if a purely orthogonal grid was used. Orthogonal curvilinear grids generated by the solution of partial differential or algebraic equations can match exterior boundaries but they would also require a paneling approach to match complex interior shapes. Orthogonal Cartesian grids would just apply an aliasing procedure to model a non-orthogonal boundary. Although the more detailed non-orthogonal grids are time-consuming to develop, there is also more control over internal boundary locations. The greater control makes it easier and less time-consuming to apply the correct porosity for tube bundles and block out control volumes for baffles and sealing strips.

The paneling approach is simply the process of generating a grid and then adding another grid to one side as shown in Figure 3.7. Figure 3.7(a) shows two grids put together as follows: Panel "A", the 5×5 Cartesian grid, was defined first. Panel "B" was generated by matching the grid points on the right (east) side of panel "A", adding an arc for the bottom, prescribing 5 more control volumes in the i direction, and defining two more vertices (lower right and upper right corners of grid "B"). Once this grid is assembled it acts as if it had been generated all at once. There is no gap or indication that they were generated separately. The two-panel grid now behaves as a single 10×5 grid.

The two-panel grid is now considered to be a single grid (now called panel "AB"), and another panel may be added to any side of it. Another panel with 10 control volumes in

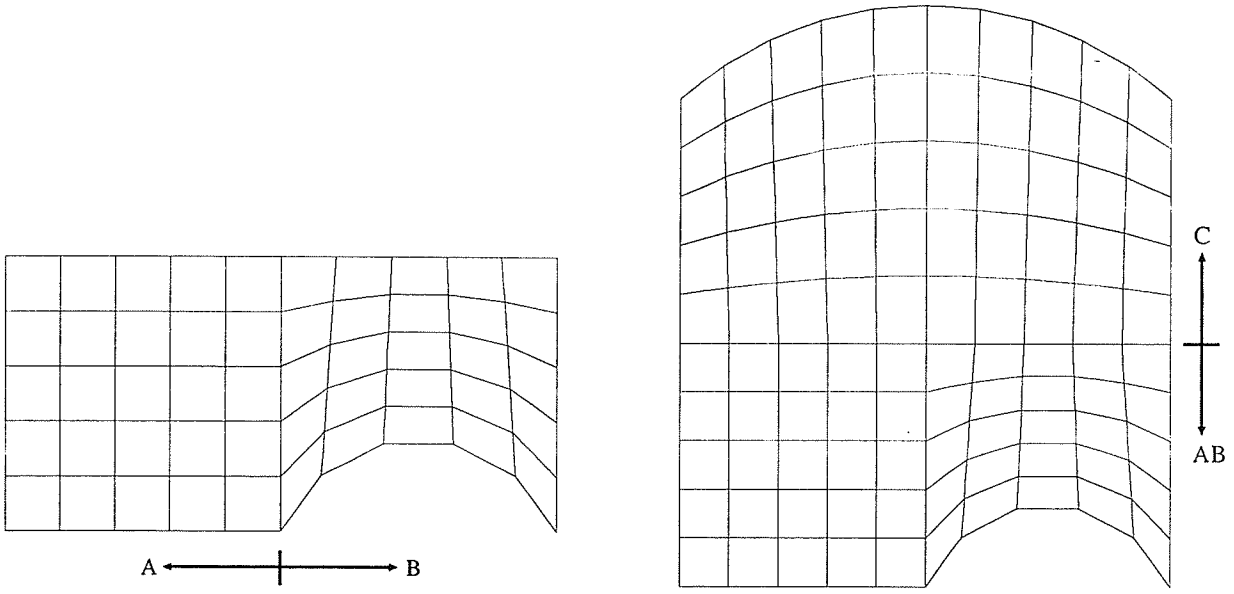

(a) Two Panels

(b) Three Panels

Figure 3.7: Example of the Paneling Method.

the i direction can be added to the top of the first grid, as shown in Figure 3.7(b). The three-panel grid was generated by adding 5 more control volumes in the j direction, two more vertices (upper left and upper right corners), and an arc over the entire top boundary of panel "C".

The normal grid has zero width control volumes around the boundary, but the paneling method has to strip off those control volumes along the side on which another panel is added. When a very complicated grid is to be defined, and all the vertices of the panels are known, the series of grids can be processed in a "batch mode" by the grid generation software developed for this thesis. The overall grid is assembled one panel at a time, each previous panel being used as the "pre-existing" grid to which the next panel is to be attached. For example, the non-orthogonal grids in Section 7.2 were made of 35 panels, 7 in the i direction and 5 in the j direction. Each panel is described in a data file using vertices, boundary

definitions, and expansion factors. All the appropriate data describing the internal detail of the final grid are included in the data file.

The paneling features of the powerful grid generation procedure described here enable a user to produce a grid with the capability to model a wide variety of shapes. The transfinite interpolation itself is very simple, but when combined into panels, is able to generate grids to fit complex domains. Examples of the some capabilities of the grid generator can be seen in Chapters 6 and 7.

Chapter 4

The Numerical Model

4.1 Introduction

This chapter will discuss the discretization of the differential equations: conservation of mass, U and V momentum, and energy. The tube drag, effective viscosity, wall functions, boundary conditions and distorted transient formulations are also discussed. The modifications made to the discretized equations, for the special regions defined within the grid, are also discussed.

Figure 4.1 represents a control volume over which the governing equations are integrated. There are two velocity components at the faces of a control volume that are used in mass conservation and found using the PWIM. Discrete values of nodal velocity, pressure and temperature are located in the center of the control volume. After the discretization process, the nodal value in this central control volume is related to the nodal values in th eight control volumes around it as shown in Figure 3.1.

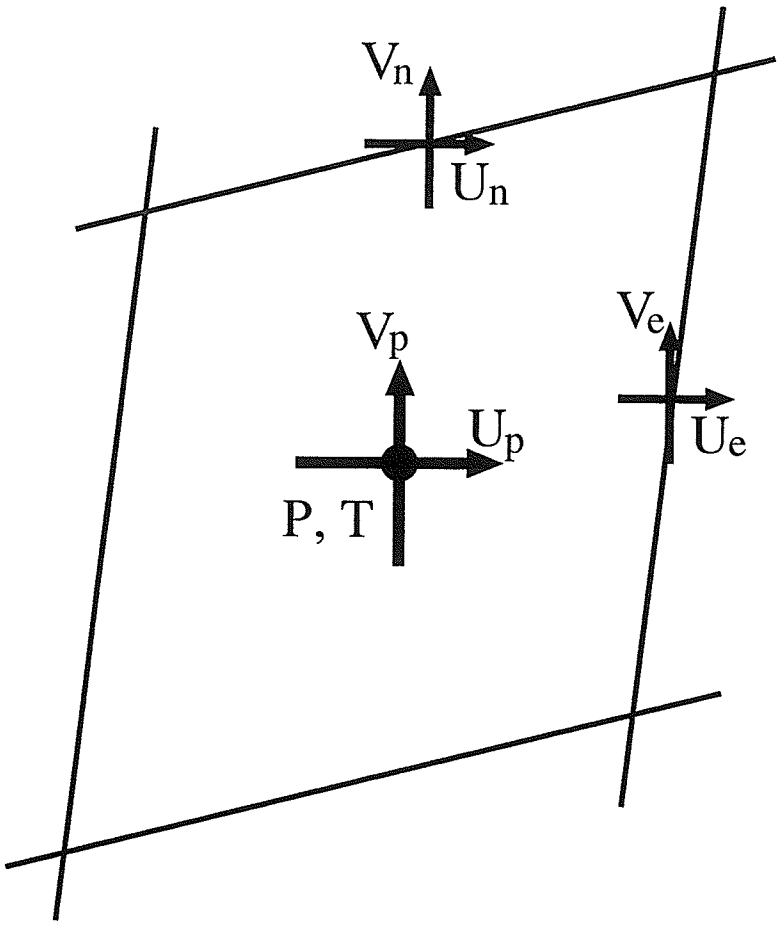

Figure 4.1: Co-located Variable Storage.

4.2 Algebraic Equation for Mass Conservation

The continuity partial differential equation (Equation (2.1)) is the governing equation for mass conservation. The mass conservation is of prime importance for a conservative finite volume approach to fluid flow and therefore overall conservation of mass must be maintained at all times. Equation (2.1) is integrated with respect to time and volume and each term is

labeled for closer examination below

$$\underbrace{\int_{\forall}\int_{t}\left[\frac{\partial}{\partial t}(\varepsilon\rho)\right]d\forall\,dt}_{I}+\underbrace{\int_{\forall}\int_{t}\left[\frac{\partial}{\partial x}(\varepsilon\rho U)\right]d\forall\,dt}_{II}+\underbrace{\int_{\forall}\int_{t}\left[\frac{\partial}{\partial y}(\varepsilon\rho V)\right]d\forall\,dt}_{III} \quad = \quad 0 \quad (4.1)$$

The first term in Equation (4.1) is the transient term

$$\int_{\forall}\int_{t}\left[\frac{\partial}{\partial t}(\varepsilon\rho)\right]d\forall\,dt=\varepsilon_P\forall_P(\rho-\rho^o)_p=M_P-M_P^o \quad (4.2)$$

that represents the change in mass in the control volume over time. The transient solution may be approached for small time steps, but in the present work only the final steady state solution is required, so this transient term is used as a relaxation factor[1]. The second term in Equation (4.1) is the x-direction mass flow term

$$\int_{\forall}\int_{t}\left[\frac{\partial}{\partial x}(\varepsilon\rho U)\right]d\forall\,dt\approx\Delta t\int_{A}\int_{w}^{e}\left[\frac{\partial}{\partial x}(\varepsilon\rho\vec{V}\cdot\hat{n})\right]dA\,dx$$

$$=\Delta t\left[(\varepsilon_eA_e)\rho(U_en_{xe}+V_en_{ye})-(\varepsilon_wA_w)\rho(U_wn_{xw}+V_wn_{yw})\right] \quad (4.3)$$

The mass flows at the faces are calculated from both U and V velocity components at the face. The third term in Equation (4.1) is the y-direction mass flow term

$$\int_{\forall}\int_{t}\left[\frac{\partial}{\partial y}(\varepsilon\rho V)\right]d\forall\,dt=\Delta t\int_{A}\int_{s}^{n}\left[\frac{\partial}{\partial y}(\varepsilon\rho\vec{V}\cdot\hat{n})\right]dA\,dy$$

$$=\Delta t\left[(\varepsilon_nA_n)\rho(U_nn_{xn}+V_nn_{yn})-(\varepsilon_sA_s)\rho(U_sn_{xs}+V_sn_{ys})\right] \quad (4.4)$$

Combining equations (4.2), (4.3), and (4.4) and dividing by Δt, produces:

$$\left[\rho(\varepsilon_eA_e)n_{xe}\,U_e+\rho(\varepsilon_eA_e)n_{ye}\,V_e\right]-\left[\rho(\varepsilon_wA_w)n_{xw}\,U_w+\rho(\varepsilon_wA_w)n_{yw}\,V_w\right]$$

$$+\left[\rho(\varepsilon_nA_n)n_{xn}\,U_n+\rho(\varepsilon_nA_n)n_{yn}\,V_n\right]-\left[\rho(\varepsilon_sA_s)n_{xs}\,U_s+\rho(\varepsilon_sA_s)n_{ys}\,V_s\right]$$

$$+\frac{M_P-M_P^o}{\Delta t}=0 \quad (4.5)$$

[1]Relaxation using this term is discussed in Section 4.8

An algebraic continuity equation in now defined from Equation (4.5) as:

$$\left(A^c_{u_e}U_e + A^c_{v_e}V_e\right) + \left(A^c_{u_w}U_w + A^c_{v_w}V_w\right) + \left(A^c_{u_n}U_n + A^c_{v_n}V_n\right) + \left(A^c_{u_s}U_s + A^c_{v_s}V_s\right) + b^c_P = 0 \quad (4.6)$$

where

$$\left.\begin{array}{llll} A^c_{u_e} = -\rho(\mathcal{E}_e A_e)n_{xe} & & A^c_{v_e} = -\rho(\mathcal{E}_e A_e)n_{ye} \\ A^c_{u_w} = \rho(\mathcal{E}_w A_w)n_{xw} & & A^c_{v_w} = \rho(\mathcal{E}_w A_w)n_{yw} \\ A^c_{u_n} = -\rho(\mathcal{E}_n A_n)n_{xn} & & A^c_{v_n} = -\rho(\mathcal{E}_n A_n)n_{yn} \\ A^c_{u_s} = \rho(\mathcal{E}_s A_s)n_{xs} & & A^c_{v_s} = \rho(\mathcal{E}_s A_s)n_{ys} \\ & & b^c_P = -\frac{(M_P - M^o_P)}{\Delta t} \end{array}\right\} \quad (4.7)$$

Note that the sign of the coefficients in Equation (4.7) has been chosen so that mass entering the control volumes has a positive sign. Note also that the normal vector components n_x and n_y from Section 3.2.1 are also used at each control volume face. The mass flows across control volume faces are defined as:

$$\left.\begin{array}{llll} \dot{m}_e = -A^c_{u_e}U_e - A^c_{v_e}V_e & & \dot{m}_w = A^c_{u_w}U_w + A^c_{v_w}V_w \\ \dot{m}_n = -A^c_{u_n}U_n - A^c_{v_n}V_n & & \dot{m}_s = A^c_{u_s}U_s + A^c_{v_s}V_s \end{array}\right\} \quad (4.8)$$

Another way of viewing the continuity equation is in terms of mass flows

$$-\dot{m}_e + \dot{m}_w - \dot{m}_n + \dot{m}_s - \frac{(M_P - M^o_P)}{\Delta t} = 0 \quad (4.9)$$

Equation (4.9) emphasizes the conservative approach by its focus on mass flows. Tight solution of the continuity equation is needed to ensure conservation of mass. Note that the transient term becomes equal to zero when steady state is reached.

4.3 Algebraic Equation of Conservation of U Momentum

4.3.1 Integration

The U momentum partial differential equation Equation (2.2) is used to find U velocity. The U momentum equation is integrated with respect to time and volume

$$\underbrace{\int_{\forall}\int_{t}\left[\frac{\partial}{\partial t}\left(\varepsilon\rho U\right)\right]d\forall\,dt}_{I}+\underbrace{\int_{\forall}\int_{t}\left[\frac{\partial}{\partial x}\left(\varepsilon\rho UU\right)+\frac{\partial}{\partial y}\left(\varepsilon\rho VU\right)\right]d\forall\,dt}_{II}=-\underbrace{\int_{\forall}\int_{t}\left[\varepsilon\frac{\partial P}{\partial x}\right]d\forall\,dt}_{III}$$
$$-\underbrace{\int_{\forall}\int_{t}\left[\varepsilon K^{u}\rho\left|\vec{V}\right|U\right]d\forall\,dt}_{IV}+\underbrace{\int_{\forall}\int_{t}\left[\frac{\partial}{\partial x}\left(\varepsilon\mu_{eff}\frac{\partial U}{\partial x}\right)+\frac{\partial}{\partial y}\left(\varepsilon\mu_{eff}\frac{\partial U}{\partial y}\right)\right]d\forall\,dt}_{V}$$
$$+\underbrace{\int_{\forall}\int_{t}\left[\varepsilon g_{x}\beta\rho\left(T-T_{\infty}\right)\right]d\forall dt}_{VI} \quad (4.10)$$

The first term in Equation (4.10) is the transient term

$$\int_{\forall}\int_{t}\left[\frac{\partial}{\partial t}(\varepsilon\rho U)\right]d\forall\,dt=\varepsilon_{P}\forall_{P}(\rho U-\rho^{o}U^{o})_{p}=M_{P}U_{P}-M_{P}^{o}U_{P}^{o} \quad (4.11)$$

The first part of the second term in Equation (4.10) is advection of U momentum in the x direction. First integrate with respect to time then in the x direction and finally over the face area

$$\int_{\forall}\int_{t}\left[\frac{\partial}{\partial x}\left(\varepsilon\rho UU\right)\right]dx\,dA\,dt\approx\Delta t\int_{A}\int_{w}^{e}\left[\frac{\partial}{\partial x}\left(\varepsilon\rho\vec{V}\cdot\hat{n}\,U\right)\right]dx\,dA$$

$$=\Delta t\left[\left(\varepsilon_{e}A_{e}\right)\rho\left(U_{e}n_{xe}+V_{e}n_{ye}\right)U_{e}-\left(\varepsilon_{w}A_{w}\right)\rho\left(U_{w}n_{xw}+V_{w}n_{yw}\right)U_{w}\right]=\Delta t\left(\dot{m}_{e}U_{e}-\dot{m}_{w}U_{w}\right) \quad (4.12)$$

Similarly,

$$\int_{\forall}\int_{t}\left[\frac{\partial}{\partial y}(\varepsilon\rho VU)\right]dy\,dA\,dt \approx \Delta t\int_{A}\int_{s}^{n}\left[\frac{\partial}{\partial y}(\varepsilon\rho\vec{V}\cdot\hat{n}\,U)\right]dy\,dA$$

$$= \Delta t\left[(\varepsilon_n A_n)\rho(U_n n_{xn} + V_n n_{yn})U_n - (\varepsilon_s A_s)\rho(U_s n_{xs} + V_s n_{ys})U_s\right] = \Delta t\left(\dot{m}_n U_n - \dot{m}_s U_s\right) \tag{4.13}$$

The third term in Equation (4.10) is the pressure gradient term

$$-\int_{\forall}\int_{t}\left[\varepsilon\frac{\partial P}{\partial x}\right]d\forall\,dt = -\Delta t\;\varepsilon_P\;\forall_P\;\left.\frac{\partial P}{\partial x}\right|_P = -\Delta t\;\overline{\forall_P}\;\left.\frac{\partial P}{\partial x}\right|_P \tag{4.14}$$

The approximation of the pressure gradient in the x direction is made complex by the non-orthogonal grid and the co-located variable storage. The details of the pressure gradient approximation are given in terms of the gradient of pressure corrections as discussed in Section 5.2.5.

The fourth term in Equation (4.10) is the resistance to flow through a tube bundle

$$-\int_{\forall}\int_{t}\left[\varepsilon K^u\rho\left|\vec{V}\right|U\right]d\forall\,dt = -\Delta t\;\varepsilon_P\;\forall_P\;K^u\rho\left|\vec{V}\right|U_P = -\Delta t\;\overline{\forall_P}\;K^u\rho\left|\vec{V}\right|U_P \tag{4.15}$$

where the tube drag coefficient K is discussed in more detail in Section 4.5.1

The first part of the fifth term in Equation (4.10) is the diffusion of U momentum in the x direction. First integrate with respect to time then in the x direction to separate out the east and west velocity gradients. Finally, integrate over the face to obtain

$$\int_{\forall}\int_{t}\left[\frac{\partial}{\partial x}\left(\varepsilon\mu_{eff}\frac{\partial U}{\partial x}\right)\right]d\forall\,dt \approx \Delta t\int_{A}\int_{w}^{e}\left[\frac{\partial}{\partial x}\left(\varepsilon\mu_{eff}\frac{\partial U}{\partial x}\cdot\hat{n}\right)\right]dx\,dA$$

$$= \Delta t\int_{A}\left[\varepsilon_e\mu_{eff}\left.\frac{\partial U}{\partial x}\right|_e\cdot\hat{n}_e - \varepsilon_w\mu_{eff}\left.\frac{\partial U}{\partial x}\right|_w\cdot\hat{n}_w\right]dA$$

$$= \Delta t\left[\varepsilon_e A_e\mu_{eff}\left.\frac{\partial U}{\partial n}\right|_e - \varepsilon_w A_w\mu_{eff}\left.\frac{\partial U}{\partial n}\right|_w\right]$$

$$= \Delta t\left[\frac{\varepsilon_e A_e\mu_{eff}}{\hat{n}_e\cdot\hat{s}_e}\left(\left.\frac{\partial U}{\partial s}\right|_e - \left.\frac{\partial U}{\partial t}\right|_e\hat{t}_e\cdot\hat{s}_e\right) - \frac{\varepsilon_w A_w\mu_{eff}}{\hat{n}_w\cdot\hat{s}_w}\left(\left.\frac{\partial U}{\partial s}\right|_w - \left.\frac{\partial U}{\partial t}\right|_w\hat{t}_w\cdot\hat{s}_w\right)\right] \tag{4.16}$$

where the velocity gradients are dotted with the normal to the control volume faces to reflect the physics of diffusion across a defined boundary.

The second part of the fifth term in Equation (4.10) is the diffusion of U momentum in the y direction. Integrate in the same manner as Equation (4.16)

$$\begin{aligned}\int_{\forall}\int_{t}\left[\frac{\partial}{\partial y}\left(\varepsilon\mu_{eff}\frac{\partial U}{\partial y}\right)\right]d\forall\,dt &\approx \Delta t\int_{A}\int_{s}^{n}\left[\frac{\partial}{\partial y}\left(\varepsilon\mu_{eff}\frac{\partial U}{\partial y}\cdot\hat{n}\right)\right]dx\,dA\\ &= \Delta t\int_{A}\left[\varepsilon_n\mu_{eff}\left.\frac{\partial U}{\partial y}\right|_n\cdot\hat{n}_n-\varepsilon_s\mu_{eff}\left.\frac{\partial U}{\partial y}\right|_s\cdot\hat{n}_s\right]dA\\ &= \Delta t\left[\varepsilon_n A_n\mu_{eff}\left.\frac{\partial U}{\partial n}\right|_n-\varepsilon_s A_s\mu_{eff}\left.\frac{\partial U}{\partial n}\right|_s\right]\\ = \Delta t\left[\frac{\varepsilon_n A_n\mu_{eff}}{\hat{n}_n\cdot\hat{t}_n}\left(\left.\frac{\partial U}{\partial t}\right|_n-\left.\frac{\partial U}{\partial s}\right|_n\hat{t}_n\cdot\hat{s}_n\right)\right.&\left.-\frac{\varepsilon_s A_s\mu_{eff}}{\hat{n}_s\cdot\hat{t}_s}\left(\left.\frac{\partial U}{\partial t}\right|_s-\left.\frac{\partial U}{\partial s}\right|_s\hat{t}_s\cdot\hat{s}_s\right)\right]\end{aligned}\quad(4.17)$$

The normal velocity derivative is split into two forms. The primary derivative reflects the rate of change along the primary coordinate direction. For example, $\left.\frac{\partial U}{\partial t}\right|_n$ in Equation (4.17) reflects diffusion of momentum in the south to north direction across the control volume north face. The secondary derivative, $\left.\frac{\partial U}{\partial s}\right|_n\hat{t}_n\cdot\hat{s}_n$, (cross-derivative term), reflects diffusion of momentum in the west to east direction along the control volume north face. The dot product is always less than 1 so the secondary derivative is less than the primary derivative as long as the two gradients are relatively the same magnitude. When the grid is Cartesian, the dot product is equal to zero and the formulation returns to that which is derived for orthogonal grids only. In this case the normal vector and the Cartesian direction are co-linear.

In the last term, the buoyancy force term, the Boussinesq approximation is used as described by Incropera and Dewitt [14]. This approach assumes that only density variation in the buoyancy force term is significant. In addition, the pressure is separated into dynamic and hydrostatic components.

The final result obtained when integrating with respect to time and volume produces

$$\int_{\forall}\int_{t}\left[\varepsilon\, g_x\, \beta\, \rho\,(T-T_\infty)\right] d\forall\, dt = \Delta t\, \varepsilon_P\, \forall_P\, g_x\, \beta\, \rho\,(T_P-T_\infty) = \Delta t\, \overline{\forall_P}\, g_x\, \beta\, \rho\,(T_P-T_\infty) \tag{4.18}$$

where the coefficient of thermal expansion, β, is

$$\beta = -\frac{1}{\rho}\frac{\partial \rho}{\partial T} \approx -\frac{1}{\rho}\left(\frac{\rho_\infty - \rho}{T_\infty - T}\right) \tag{4.19}$$

Combining Equations (4.11) through (4.17) and (4.18) and dividing by Δt produces:

$$\begin{aligned}
&\frac{1}{\Delta t}\left(M_P U_P - M_P^o U_P^o\right) + \dot{m}_e U_e - \dot{m}_w U_w + \dot{m}_n U_n - \dot{m}_s U_s = \\
&\qquad -\overline{\forall_P}\left.\frac{\partial P}{\partial x}\right|_P - \overline{\forall_P}\, K^u \rho \left|\vec{V}\right| U_P + \overline{\forall_P}\, g_x\, \beta\, \rho\,(T_P - T_\infty) \\
&\qquad + \frac{\varepsilon_e A_e \mu_{eff}}{\hat{n}_e \cdot \hat{s}_e}\frac{(U_E - U_P)}{(ds)_e} - \frac{\varepsilon_e A_e \mu_{eff}}{\hat{n}_e \cdot \hat{s}_e}\frac{(U_{ne} - U_{se})}{(dt)_e}\hat{t}_e \cdot \hat{s}_e \\
&\qquad - \frac{\varepsilon_w A_w \mu_{eff}}{\hat{n}_w \cdot \hat{s}_w}\frac{(U_P - U_W)}{(ds)_w} + \frac{\varepsilon_w A_w \mu_{eff}}{\hat{n}_w \cdot \hat{s}_w}\frac{(U_{nw} - U_{sw})}{(dt)_w}\hat{t}_w \cdot \hat{s}_w \\
&\qquad + \frac{\varepsilon_n A_n \mu_{eff}}{\hat{n}_n \cdot \hat{t}_n}\frac{(U_N - U_P)}{(dt)_n} - \frac{\varepsilon_n A_n \mu_{eff}}{\hat{n}_n \cdot \hat{t}_n}\frac{(U_{ne} - U_{nw})}{(ds)_n}\hat{t}_n \cdot \hat{s}_n \\
&\qquad - \frac{\varepsilon_s A_s \mu_{eff}}{\hat{n}_s \cdot \hat{t}_s}\frac{(U_P - U_S)}{(dt)_s} + \frac{\varepsilon_s A_s \mu_{eff}}{\hat{n}_s \cdot \hat{t}_s}\frac{(U_{se} - U_{sw})}{(ds)_s}\hat{t}_s \cdot \hat{s}_s
\end{aligned} \tag{4.20}$$

The velocity gradients have been approximated by central differences. For example,

$$\left.\frac{\partial U}{\partial s}\right|_e \approx \beta_e \frac{U_E - U_P}{(ds)_e} \tag{4.21}$$

where β_e is a diffusion weighting coefficient (not the same as β in Equation (4.19)). The calculation of the diffusion weighting coefficients β_e, β_w, β_n, and β_s is discussed shortly, with the details of the face velocity approximations.

A diffusion coefficient, D, is defined for each face as follows:

$$\left.\begin{array}{lll} D_e = \dfrac{\mathcal{E}_e A_e (\mu_{eff})_e}{(ds)_e} & & D_n = \dfrac{\mathcal{E}_n A_n (\mu_{eff})_n}{(dt)_n} \\ D_w = \dfrac{\mathcal{E}_w A_w (\mu_{eff})_w}{(ds)_w} & & D_s = \dfrac{\mathcal{E}_s A_s (\mu_{eff})_s}{(dt)_s} \end{array}\right\} \quad (4.22)$$

In all control volumes the diffusion coefficient is set using that harmonic mean of the nodal viscosity value as follows (at the east face for example):

$$(\mu_{eff})_e = \frac{\mu_{eff_{(i,j)}} * \mu_{eff_{(i+1,j)}}}{f_e * \mu_{eff_{(i,j)}} + (1 - f_e) * \mu_{eff_{(i+1,j)}}} \quad (4.23)$$

where the interpolation factor f_e is defined as

$$f_e = \frac{DISW_{(i+1,j)}}{DISE_{(i,j)} + DISW_{(i+1,j)}} \quad (4.24)$$

using grid distances.

Approximations for the face velocities are also required. The face velocities, in terms of convective weights, α, at each face, are

$$\left.\begin{array}{lll} U_e &=& (0.5 + \alpha_e)\, U_P + (0.5 - \alpha_e)\, U_E \\ U_w &=& (0.5 + \alpha_w)\, U_W + (0.5 - \alpha_w)\, U_P \\ U_n &=& (0.5 + \alpha_n)\, U_P + (0.5 - \alpha_n)\, U_N \\ U_s &=& (0.5 + \alpha_s)\, U_S + (0.5 - \alpha_s)\, U_P \end{array}\right\} \quad (4.25)$$

The standard upwind differencing scheme uses the upwind nodal velocity as the local face velocity, ($\alpha = \pm 0.5$). The Exponential Differencing Scheme (EDS), described by Patankar [26], defines the Peclet number (local Reynolds number in the case of velocity). For example, for the east face of a control volume

$$Pe_e = Re_L = \frac{\rho U L}{\mu} = \frac{\rho U_e (ds)_e}{\mu_{eff}} = \frac{\dot{m}_e}{D_e} \quad (4.26)$$

and for the north face of a control volume

$$Pe_n = Re_L = \frac{\rho V L}{\mu} = \frac{\rho V_n (dt)_n}{\mu_{eff}} = \frac{\dot{m}_n}{D_n} \tag{4.27}$$

Raithby et al. [35, 37] approximated the EDS exponential calculations from Patankar [26], which consumes a great deal of computational time, using the following formulae:

$$\alpha_e = \text{sign}\,(\dot{m}_e)\,\frac{0.5\,(Pe_e^2)}{5 + (Pe_e^2)} \qquad \alpha_n = \text{sign}\,(\dot{m}_n)\,\frac{0.5\,(Pe_n^2)}{5 + (Pe_n^2)} \tag{4.28}$$

and

$$\beta_e = \frac{1 + 0.005\,(Pe_e^2)}{1 + 0.05\,(Pe_e^2)} \qquad \beta_n = \frac{1 + 0.005\,(Pe_n^2)}{1 + 0.05\,(Pe_n^2)} \tag{4.29}$$

These weightings are more robust than the EDS function because no range checking is required. The weights for the west and south faces are the same as the weights for the east and north faces of the control volumes to the west and south. Using Equation (4.25) for the face velocities in Equation (4.20) produces

$$\begin{aligned}
&\frac{(M_P U_P - M_P^o U_P^o)}{\Delta t} \\
&+ \dot{m}_e\left[(0.5 + \alpha_e)\,U_P + (0.5 - \alpha_e)\,U_E\right] - \dot{m}_w\left[(0.5 + \alpha_w)\,U_W + (0.5 - \alpha_w)\,U_P\right] \\
&+ \dot{m}_n\left[(0.5 + \alpha_n)\,U_P + (0.5 - \alpha_n)\,U_N\right] - \dot{m}_s\left[(0.5 + \alpha_s)\,U_S + (0.5 - \alpha_s)\,U_P\right] = \\
&\quad - \overline{\forall_P}\,\frac{\partial P}{\partial x}\bigg|_P - \overline{\forall_P}\,K^u \rho \left|\vec{V}\right| U_P + \overline{\forall_P}\,g_x\,\beta\,\rho\,(T_P - T_\infty) \\
&\quad + D_e\beta_e\frac{(U_E - U_P)}{\hat{n}_e \cdot \hat{s}_e} - D_e\beta_e\frac{(ds)_e}{(dt)_e}\,\frac{(U_{ne} - U_{se})}{\hat{n}_e \cdot \hat{s}_e}\hat{t}_e \cdot \hat{s}_e \\
&\quad - D_w\beta_w\frac{(U_P - U_W)}{\hat{n}_w \cdot \hat{s}_w} + D_w\beta_w\frac{(ds)_w}{(dt)_w}\,\frac{(U_{nw} - U_{sw})}{\hat{n}_w \cdot \hat{s}_w}\hat{t}_w \cdot \hat{s}_w \\
&\quad + D_n\beta_n\frac{(U_N - U_P)}{\hat{n}_n \cdot \hat{t}_n} - D_n\beta_n\frac{(dt)_n}{(ds)_n}\,\frac{(U_{ne} - U_{nw})}{\hat{n}_n \cdot \hat{t}_n}\hat{t}_n \cdot \hat{s}_n \\
&\quad - D_s\beta_s\frac{(U_P - U_S)}{\hat{n}_s \cdot \hat{t}_s} + D_s\beta_s\frac{(dt)_s}{(ds)_s}\,\frac{(U_{se} - U_{sw})}{\hat{n}_s \cdot \hat{t}_s}\hat{t}_s \cdot \hat{s}_s
\end{aligned} \tag{4.30}$$

The flow resistance term in Equation (4.30) is linearized, as Patankar [26] suggested, as follows:

$$S_P^u = Q_P^u + R_P^u U_P \tag{4.31}$$

For this work the resistance term is put completely in the active nodal coefficient , R_P^u, and the buoyancy term is put completely in the lagged source term, Q_P^u. The final result for Q_P^u and R_P^u is

$$Q_P^u = + \overline{\forall_P}\, g_x \beta \rho (T_P - T_\infty) \qquad R_P^u = -\overline{\forall_P}\, K^u \rho \left|\vec{V}\right| \tag{4.32}$$

The final algebraic equation for U velocity will be obtained once an approximation for U_{ne}, U_{nw}, U_{se} and U_{sw} is made. Two methods of approximating these velocities were used. One leads to a five-point computational molecule, which is presented in Appendix B, and the other leads to a nine-point molecule, which is presented below.

4.3.2 Nine-Point Equation

The nine-point solution method is used to improve convergence behavior for non-orthogonal grids. The corner velocities, northeast, northwest, southeast and southwest are approximated as suggested by Perić [32] as follows:

$$U_{ne} = \frac{1}{4}(U_N + U_{NE} + U_P + U_E) \tag{4.33}$$

To solve Equation (4.30) using a nine-point solver, it is necessary to collect terms into nine coefficients and produce a nine-point algebraic equation in the form

$$A_P^u U_P = A_E^u U_E + A_W^u U_W + A_N^u U_N + A_S^u U_S + A_{NE}^u U_{NE} + A_{SW}^u U_{SW}$$

$$+ A_{NW}^u U_{NW} + A_{SE}^u U_{SE} + b^u = \sum A_{NB}^u U_{NB} + b^u \tag{4.34}$$

where

$$A_E^u = \frac{D_e\beta_e}{\hat{n}_e \cdot \hat{s}_e} - 0.5\ \dot{m}_e + |\alpha_e|\,|\dot{m}_e| - \frac{1}{4}D_n\beta_n\frac{(dt)_n}{(ds)_n}\frac{\hat{t}_n \cdot \hat{s}_n}{\hat{n}_n \cdot \hat{t}_n} + \frac{1}{4}D_s\beta_s\frac{(dt)_s}{(ds)_s}\frac{\hat{t}_s \cdot \hat{s}_s}{\hat{n}_s \cdot \hat{t}_s} \tag{4.35}$$

$$A_W^u = \frac{D_w\beta_w}{\hat{n}_w \cdot \hat{s}_w} + 0.5\ \dot{m}_w + |\alpha_W|\,|\dot{m}_w| + \frac{1}{4}D_n\beta_n\frac{(dt)_n}{(ds)_n}\frac{\hat{t}_n \cdot \hat{s}_n}{\hat{n}_n \cdot \hat{t}_n} - \frac{1}{4}D_s\beta_s\frac{(dt)_s}{(ds)_s}\frac{\hat{t}_s \cdot \hat{s}_s}{\hat{n}_s \cdot \hat{t}_s} \tag{4.36}$$

$$A_N^u = \frac{D_n\beta_n}{\hat{n}_n \cdot \hat{t}_n} - 0.5\ \dot{m}_n + |\alpha_n|\,|\dot{m}_n| - \frac{1}{4}D_e\beta_e\frac{(ds)_e}{(dt)_e}\frac{\hat{t}_e \cdot \hat{s}_e}{\hat{n}_e \cdot \hat{s}_e} + \frac{1}{4}D_w\beta_w\frac{(ds)_w}{(dt)_w}\frac{\hat{t}_w \cdot \hat{s}_w}{\hat{n}_w \cdot \hat{s}_w} \tag{4.37}$$

$$A_S^u = \frac{D_s\beta_s}{\hat{n}_s \cdot \hat{t}_s} + 0.5\ \dot{m}_s + |\alpha_s|\,|\dot{m}_s| + \frac{1}{4}D_e\beta_e\frac{(ds)_e}{(dt)_e}\frac{\hat{t}_e \cdot \hat{s}_e}{\hat{n}_e \cdot \hat{s}_e} - \frac{1}{4}D_w\beta_w\frac{(ds)_w}{(dt)_w}\frac{\hat{t}_w \cdot \hat{s}_w}{\hat{n}_w \cdot \hat{s}_w} \tag{4.38}$$

$$A_{NE}^u = -\frac{1}{4}\left(D_e\beta_e\frac{(ds)_e}{(dt)_e}\frac{\hat{t}_e \cdot \hat{s}_e}{\hat{n}_e \cdot \hat{s}_e} + D_n\beta_n\frac{(dt)_n}{(ds)_n}\frac{\hat{t}_n \cdot \hat{s}_n}{\hat{n}_n \cdot \hat{t}_n}\right) \tag{4.39}$$

$$A_{NW}^u = \frac{1}{4}\left(D_w\beta_w\frac{(ds)_w}{(dt)_w}\frac{\hat{t}_w \cdot \hat{s}_w}{\hat{n}_w \cdot \hat{s}_w} + D_n\beta_n\frac{(dt)_n}{(ds)_n}\frac{\hat{t}_n \cdot \hat{s}_n}{\hat{n}_n \cdot \hat{t}_n}\right) \tag{4.40}$$

$$A_{SE}^u = \frac{1}{4}\left(D_e\beta_e\frac{(ds)_e}{(dt)_e}\frac{\hat{t}_e \cdot \hat{s}_e}{\hat{n}_e \cdot \hat{s}_e} + D_s\beta_s\frac{(dt)_s}{(ds)_s}\frac{\hat{t}_s \cdot \hat{s}_s}{\hat{n}_s \cdot \hat{t}_s}\right) \tag{4.41}$$

$$A_{SW}^u = -\frac{1}{4}\left(D_w\beta_w\frac{(ds)_w}{(dt)_w}\frac{\hat{t}_w \cdot \hat{s}_w}{\hat{n}_w \cdot \hat{s}_w} + D_s\beta_s\frac{(dt)_s}{(ds)_s}\frac{\hat{t}_s \cdot \hat{s}_s}{\hat{n}_s \cdot \hat{t}_s}\right) \tag{4.42}$$

$$b^u = \left(\frac{M_P^o}{\Delta t}\right)U_P^o - \overline{V_P}\left.\frac{\partial P}{\partial x}\right|_P + Q_P^u \tag{4.43}$$

The diagonal coefficient, A_P^u, is

$$A_P^u = \frac{D_e\beta_e}{\hat{n}_e \cdot \hat{s}_e} + 0.5\ \dot{m}_e + |\alpha_e|\,|\dot{m}_e| + \frac{D_w\beta_w}{\hat{n}_w \cdot \hat{s}_w} - 0.5\ \dot{m}_w + |\alpha_W|\,|\dot{m}_w| + \frac{D_n\beta_n}{\hat{n}_n \cdot \hat{t}_n} + 0.5\ \dot{m}_n + |\alpha_n|\,|\dot{m}_n| + \frac{D_s\beta_s}{\hat{n}_s \cdot \hat{t}_s} - 0.5\ \dot{m}_s + |\alpha_s|\,|\dot{m}_s| + \frac{M_P}{\Delta t} - R_P^u \quad (4.44)$$

Defining $A_P^{u^*}$ as

$$A_P^{u^*} = \frac{D_e\beta_e}{\hat{n}_e \cdot \hat{s}_e} - 0.5\ \dot{m}_e + |\alpha_e|\,|\dot{m}_e| + \frac{D_w\beta_w}{\hat{n}_w \cdot \hat{s}_w} + 0.5\ \dot{m}_w + |\alpha_W|\,|\dot{m}_w| + \frac{D_n\beta_n}{\hat{n}_n \cdot \hat{t}_n} - 0.5\ \dot{m}_n + |\alpha_n|\,|\dot{m}_n| + \frac{D_s\beta_s}{\hat{n}_s \cdot \hat{t}_s} + 0.5\ \dot{m}_s + |\alpha_s|\,|\dot{m}_s| \quad (4.45)$$

and using continuity, Equation (4.9), to reduce Equation (4.44) to simpler form produces:

$$A_P^u = A_P^{u^*} - R_P^u + \frac{M_P^o}{\Delta t} \quad (4.46)$$

The A_P^u coefficient is not equal to the sum of neighbors because of the the cross-derivative terms in the eight neighboring coefficients.

4.4 Algebraic Equation of Conservation of V Momentum

Each term in V momentum is analogous to U momentum. Integrate Equation (2.3) with respect to time and volume

$$\underbrace{\int_{\forall}\int_{t}\left[\frac{\partial}{\partial t}(\varepsilon\rho V)\right]d\forall dt}_{I}+\underbrace{\int_{\forall}\int_{t}\left[\frac{\partial}{\partial x}(\varepsilon\rho UV)+\frac{\partial}{\partial y}(\varepsilon\rho VV)\right]d\forall dt}_{II}=-\underbrace{\int_{\forall}\int_{t}\left[\varepsilon\frac{\partial P}{\partial y}\right]d\forall dt}_{III}$$
$$-\underbrace{\int_{\forall}\int_{t}\left[\varepsilon K^{v}\rho\left|\vec{V}\right|V\right]d\forall dt}_{IV}+\underbrace{\int_{\forall}\int_{t}\left[\frac{\partial}{\partial x}\left(\varepsilon\mu_{eff}\frac{\partial V}{\partial x}\right)+\frac{\partial}{\partial y}\left(\varepsilon\mu_{eff}\frac{\partial V}{\partial y}\right)\right]d\forall dt}_{V}$$
$$+\underbrace{\int_{\forall}\int_{t}\left[\varepsilon g_{y}\beta\,\rho\,(T-T_{\infty})\right]d\forall dt}_{VI} \quad (4.47)$$

to produce a nine-point algebraic equation

$$A_P^v V_P = A_E^v V_E + A_W^v V_W + A_N^v V_N + A_S^v V_S + A_{NE}^v V_{NE} + A_{SW}^v V_{SW}$$
$$+ A_{NW}^v V_{NW} + A_{SE}^v V_{SE} + b^v = \sum A_{NB}^v V_{NB} + b^v \quad (4.48)$$

where

$$A_E^v = \frac{D_e\beta_e}{\hat{n}_e\cdot\hat{s}_e} - 0.5\,\dot{m}_e + |\alpha_e|\,|\dot{m}_e| - \frac{1}{4}D_n\beta_n\frac{(dt)_n}{(ds)_n}\frac{\hat{t}_n\cdot\hat{s}_n}{\hat{n}_n\cdot\hat{t}_n} + \frac{1}{4}D_s\beta_s\frac{(dt)_s}{(ds)_s}\frac{\hat{t}_s\cdot\hat{s}_s}{\hat{n}_s\cdot\hat{t}_s} \quad (4.49)$$

$$A_W^v = \frac{D_w\beta_w}{\hat{n}_w\cdot\hat{s}_w} + 0.5\,\dot{m}_w + |\alpha_W|\,|\dot{m}_w| + \frac{1}{4}D_n\beta_n\frac{(dt)_n}{(ds)_n}\frac{\hat{t}_n\cdot\hat{s}_n}{\hat{n}_n\cdot\hat{t}_n} - \frac{1}{4}D_s\beta_s\frac{(dt)_s}{(ds)_s}\frac{\hat{t}_s\cdot\hat{s}_s}{\hat{n}_s\cdot\hat{t}_s} \quad (4.50)$$

$$A_N^v = \frac{D_n\beta_n}{\hat{n}_n\cdot\hat{t}_n} - 0.5\,\dot{m}_n + |\alpha_n|\,|\dot{m}_n| - \frac{1}{4}D_e\beta_e\frac{(ds)_e}{(dt)_e}\frac{\hat{t}_e\cdot\hat{s}_e}{\hat{n}_e\cdot\hat{s}_e} + \frac{1}{4}D_w\beta_w\frac{(ds)_w}{(dt)_w}\frac{\hat{t}_w\cdot\hat{s}_w}{\hat{n}_w\cdot\hat{s}_w} \quad (4.51)$$

$$A_S^v = \frac{D_s\beta_s}{\hat{n}_s \cdot \hat{t}_s} + 0.5\,\dot{m}_s + |\alpha_s|\,|\dot{m}_s| + \frac{1}{4}D_e\beta_e\frac{(ds)_e}{(dt)_e}\frac{\hat{t}_e \cdot \hat{s}_e}{\hat{n}_e \cdot \hat{s}_e} - \frac{1}{4}D_w\beta_w\frac{(ds)_w}{(dt)_w}\frac{\hat{t}_w \cdot \hat{s}_w}{\hat{n}_w \cdot \hat{s}_w} \tag{4.52}$$

$$A_{NE}^v = -\frac{1}{4}\left(D_e\beta_e\frac{(ds)_e}{(dt)_e}\frac{\hat{t}_e \cdot \hat{s}_e}{\hat{n}_e \cdot \hat{s}_e} + D_n\beta_n\frac{(dt)_n}{(ds)_n}\frac{\hat{t}_n \cdot \hat{s}_n}{\hat{n}_n \cdot \hat{t}_n}\right) \tag{4.53}$$

$$A_{NW}^v = \frac{1}{4}\left(D_w\beta_w\frac{(ds)_w}{(dt)_w}\frac{\hat{t}_w \cdot \hat{s}_w}{\hat{n}_w \cdot \hat{s}_w} + D_n\beta_n\frac{(dt)_n}{(ds)_n}\frac{\hat{t}_n \cdot \hat{s}_n}{\hat{n}_n \cdot \hat{t}_n}\right) \tag{4.54}$$

$$A_{SE}^v = \frac{1}{4}\left(D_e\beta_e\frac{(ds)_e}{(dt)_e}\frac{\hat{t}_e \cdot \hat{s}_e}{\hat{n}_e \cdot \hat{s}_e} + D_s\beta_s\frac{(dt)_s}{(ds)_s}\frac{\hat{t}_s \cdot \hat{s}_s}{\hat{n}_s \cdot \hat{t}_s}\right) \tag{4.55}$$

$$A_{SW}^v = -\frac{1}{4}\left(D_w\beta_w\frac{(ds)_w}{(dt)_w}\frac{\hat{t}_w \cdot \hat{s}_w}{\hat{n}_w \cdot \hat{s}_w} + D_s\beta_s\frac{(dt)_s}{(ds)_s}\frac{\hat{t}_s \cdot \hat{s}_s}{\hat{n}_s \cdot \hat{t}_s}\right) \tag{4.56}$$

$$b^v = \left(\frac{M_P^o}{\Delta t}\right)V_P^o - \overline{\forall_P}\left.\frac{\partial P}{\partial x}\right|_P + Q_P^v \tag{4.57}$$

The diagonal coefficient, A_P^v, is

$$\begin{aligned} A_P^v = {} & \frac{D_e\beta_e}{\hat{n}_e \cdot \hat{s}_e} + 0.5\,\dot{m}_e + |\alpha_e|\,|\dot{m}_e| + \frac{D_w\beta_w}{\hat{n}_w \cdot \hat{s}_w} - 0.5\,\dot{m}_w + |\alpha_W|\,|\dot{m}_w| \\ & + \frac{D_n\beta_n}{\hat{n}_n \cdot \hat{t}_n} + 0.5\,\dot{m}_n + |\alpha_n|\,|\dot{m}_n| + \frac{D_s\beta_s}{\hat{n}_s \cdot \hat{t}_s} - 0.5\,\dot{m}_s + |\alpha_s|\,|\dot{m}_s| + \frac{M_P}{\Delta t} - R_P^v \end{aligned} \tag{4.58}$$

or, in short form,

$$A_P^v = A_P^{v^*} + \frac{M_P^o}{\Delta t} - R_P^v \tag{4.59}$$

where $A_P^{v^*}$ is defined analogously to $A_P^{u^*}$.

4.5 Algebraic Equation for Temperature

The integration of the conservation of energy equation (Equation (2.4)) is analogous to the integration for the momentum equations. Integrating with respect to time and volume as follows:

$$\underbrace{\int_{\forall}\int_{t}\left[\frac{\partial}{\partial t}(\varepsilon\rho T)\right]d\forall\,dt}_{I}+\underbrace{\int_{\forall}\int_{t}\left[\frac{\partial}{\partial x}(\varepsilon\rho UT)+\frac{\partial}{\partial y}(\varepsilon\rho VT)\right]d\forall\,dt}_{II}=$$

$$+\underbrace{\int_{\forall}\int_{t}\left[\frac{\partial}{\partial x}\left(\varepsilon\frac{k}{Cp}\frac{\partial T}{\partial x}\right)+\frac{\partial}{\partial y}\left(\varepsilon\frac{k}{Cp}\frac{\partial T}{\partial y}\right)\right]d\forall\,dt}_{III}+\underbrace{\int_{\forall}\int_{t}\left[\varepsilon\dot{S}_{t}'''\right]d\forall\,dt}_{IV} \quad (4.60)$$

produces

$$\frac{1}{\Delta t}\left(M_P T_P - M_P^o T_P^o\right)+\dot{m}_e T_e-\dot{m}_w T_w+\dot{m}_n T_n-\dot{m}_s T_s=$$

$$+\frac{\varepsilon_e A_e}{\hat{n}_e\cdot\hat{s}_e}\frac{k}{Cp}\frac{(T_E-T_P)}{(ds)_e}-\frac{\varepsilon_e A_e}{\hat{n}_e\cdot\hat{s}_e}\frac{k}{Cp}\frac{(T_{ne}-T_{se})}{(dt)_e}\hat{t}_e\cdot\hat{s}_e$$

$$-\frac{\varepsilon_w A_w}{\hat{n}_w\cdot\hat{s}_w}\frac{k}{Cp}\frac{(T_P-T_W)}{(ds)_w}+\frac{\varepsilon_w A_w}{\hat{n}_w\cdot\hat{s}_w}\frac{k}{Cp}\frac{(T_{nw}-T_{sw})}{(dt)_w}\hat{t}_w\cdot\hat{s}_w$$

$$+\frac{\varepsilon_n A_n}{\hat{n}_n\cdot\hat{t}_n}\frac{k}{Cp}\frac{(T_N-T_P)}{(dt)_n}-\frac{\varepsilon_n A_n}{\hat{n}_n\cdot\hat{t}_n}\frac{k}{Cp}\frac{(T_{ne}-T_{nw})}{(ds)_n}\hat{t}_n\cdot\hat{s}_n$$

$$-\frac{\varepsilon_s A_s}{\hat{n}_s\cdot\hat{t}_s}\frac{k}{Cp}\frac{(T_P-T_S)}{(dt)_s}+\frac{\varepsilon_s A_s}{\hat{n}_s\cdot\hat{t}_s}\frac{k}{Cp}\frac{(T_{se}-T_{sw})}{(ds)_s}\hat{t}_s\cdot\hat{s}_s+\dot{S}_P^t \quad (4.61)$$

Defining

$$\left.\begin{aligned} D_e^t &= \frac{\varepsilon_e A_e}{(ds)_e}\frac{k}{Cp} & D_n^t &= \frac{\varepsilon_n A_n}{(dt)_n}\frac{k}{Cp}\\ D_w^t &= \frac{\varepsilon_w A_w}{(ds)_w}\frac{k}{Cp} & D_s^t &= \frac{\varepsilon_s A_s}{(dt)_s}\frac{k}{Cp}\end{aligned}\right\} \quad (4.62)$$

and using the same approximations for face values and derivatives (with α and β weighting factors), Equation (4.61) becomes

$$\frac{(M_P T_P - M_P^o T_P^o)}{\Delta t}$$

$$+ \dot{m}_e \left[(0.5 + \alpha_e) T_P + (0.5 - \alpha_e) T_E\right] - \dot{m}_w \left[(0.5 + \alpha_w) T_W + (0.5 - \alpha_w) T_P\right]$$

$$+ \dot{m}_n \left[(0.5 + \alpha_n) T_P + (0.5 - \alpha_n) T_N\right] - \dot{m}_s \left[(0.5 + \alpha_s) T_S + (0.5 - \alpha_s) T_P\right] =$$

$$+ D_e^t \beta_e \frac{(T_E - T_P)}{\hat{n}_e \cdot \hat{s}_e} - D_e^t \beta_e \frac{(ds)_e}{(dt)_e} \frac{(T_{ne} - T_{se})}{\hat{n}_e \cdot \hat{s}_e} \hat{t}_e \cdot \hat{s}_e$$

$$- D_w^t \beta_w \frac{(T_P - T_W)}{\hat{n}_w \cdot \hat{s}_w} + D_w^t \beta_w \frac{(ds)_w}{(dt)_w} \frac{(T_{nw} - T_{sw})}{\hat{n}_w \cdot \hat{s}_w} \hat{t}_w \cdot \hat{s}_w$$

$$+ D_n^t \beta_n \frac{(T_N - T_P)}{\hat{n}_n \cdot \hat{t}_n} - D_n^t \beta_n \frac{(dt)_n}{(ds)_n} \frac{(T_{ne} - T_{nw})}{\hat{n}_n \cdot \hat{t}_n} \hat{t}_n \cdot \hat{s}_n$$

$$- D_s^t \beta_s \frac{(T_P - T_S)}{\hat{n}_s \cdot \hat{t}_s} + D_s^t \beta_s \frac{(dt)_s}{(ds)_s} \frac{(T_{se} - T_{sw})}{\hat{n}_s \cdot \hat{t}_s} \hat{t}_s \cdot \hat{s}_s + \dot{S}_P^t \quad (4.63)$$

The source term, although unused in the present work, can be linearized in the same way as for momentum:

$$\dot{S}_P^t = Q_P^t + R_P^t T_P \quad (4.64)$$

To solve Equation (4.63) using a nine-point solver, collect the terms into the form

$$A_P^t T_P = A_E^t T_E + A_W^t T_W + A_N^t T_N + A_S^t T_S + A_{NE}^t T_{NE} + A_{SW}^t T_{SW}$$

$$+ A_{NW}^t T_{NW} + A_{SE}^t T_{SE} + b^t = \sum A_{NB}^t T_{NB} + b^t \quad (4.65)$$

where

$$A_E^t = \frac{D_e^t \beta_e}{\hat{n}_e \cdot \hat{s}_e} - 0.5\, \dot{m}_e + |\alpha_e|\, |\dot{m}_e| - \frac{1}{4} D_n^t \beta_n \frac{(dt)_n}{(ds)_n} \frac{\hat{t}_n \cdot \hat{s}_n}{\hat{n}_n \cdot \hat{t}_n} + \frac{1}{4} D_s^t \beta_s \frac{(dt)_s}{(ds)_s} \frac{\hat{t}_s \cdot \hat{s}_s}{\hat{n}_s \cdot \hat{t}_s} \quad (4.66)$$

$$A_W^t = \frac{D_w^t \beta_w}{\hat{n}_w \cdot \hat{s}_w} + 0.5\ \dot{m}_w + |\alpha_W|\,|\dot{m}_w| + \frac{1}{4} D_n^t \beta_n \frac{(dt)_n}{(ds)_n} \frac{\hat{t}_n \cdot \hat{s}_n}{\hat{n}_n \cdot \hat{t}_n} - \frac{1}{4} D_s^t \beta_s \frac{(dt)_s}{(ds)_s} \frac{\hat{t}_s \cdot \hat{s}_s}{\hat{n}_s \cdot \hat{t}_s} \tag{4.67}$$

$$A_N^t = \frac{D_n^t \beta_n}{\hat{n}_n \cdot \hat{t}_n} - 0.5\ \dot{m}_n + |\alpha_n|\,|\dot{m}_n| - \frac{1}{4} D_e^t \beta_e \frac{(ds)_e}{(dt)_e} \frac{\hat{t}_e \cdot \hat{s}_e}{\hat{n}_e \cdot \hat{s}_e} + \frac{1}{4} D_w^t \beta_w \frac{(ds)_w}{(dt)_w} \frac{\hat{t}_w \cdot \hat{s}_w}{\hat{n}_w \cdot \hat{s}_w} \tag{4.68}$$

$$A_S^t = \frac{D_s^t \beta_s}{\hat{n}_s \cdot \hat{t}_s} + 0.5\ \dot{m}_s + |\alpha_s|\,|\dot{m}_s| + \frac{1}{4} D_e^t \beta_e \frac{(ds)_e}{(dt)_e} \frac{\hat{t}_e \cdot \hat{s}_e}{\hat{n}_e \cdot \hat{s}_e} - \frac{1}{4} D_w^t \beta_w \frac{(ds)_w}{(dt)_w} \frac{\hat{t}_w \cdot \hat{s}_w}{\hat{n}_w \cdot \hat{s}_w} \tag{4.69}$$

$$A_{NE}^t = -\frac{1}{4} \left(D_e^t \beta_e \frac{(ds)_e}{(dt)_e} \frac{\hat{t}_e \cdot \hat{s}_e}{\hat{n}_e \cdot \hat{s}_e} + D_n^t \beta_n \frac{(dt)_n}{(ds)_n} \frac{\hat{t}_n \cdot \hat{s}_n}{\hat{n}_n \cdot \hat{t}_n} \right) \tag{4.70}$$

$$A_{NW}^t = \frac{1}{4} \left(D_w^t \beta_w \frac{(ds)_w}{(dt)_w} \frac{\hat{t}_w \cdot \hat{s}_w}{\hat{n}_w \cdot \hat{s}_w} + D_n^t \beta_n \frac{(dt)_n}{(ds)_n} \frac{\hat{t}_n \cdot \hat{s}_n}{\hat{n}_n \cdot \hat{t}_n} \right) \tag{4.71}$$

$$A_{SE}^t = \frac{1}{4} \left(D_e^t \beta_e \frac{(ds)_e}{(dt)_e} \frac{\hat{t}_e \cdot \hat{s}_e}{\hat{n}_e \cdot \hat{s}_e} + D_s^t \beta_s \frac{(dt)_s}{(ds)_s} \frac{\hat{t}_s \cdot \hat{s}_s}{\hat{n}_s \cdot \hat{t}_s} \right) \tag{4.72}$$

$$A_{SW}^t = -\frac{1}{4} \left(D_w^t \beta_w \frac{(ds)_w}{(dt)_w} \frac{\hat{t}_w \cdot \hat{s}_w}{\hat{n}_w \cdot \hat{s}_w} + D_s^t \beta_s \frac{(dt)_s}{(ds)_s} \frac{\hat{t}_s \cdot \hat{s}_s}{\hat{n}_s \cdot \hat{t}_s} \right) \tag{4.73}$$

$$b^t = \left(\frac{M_P^o}{\Delta t} \right) T_P^o + Q_P^t \tag{4.74}$$

and

$$A_P^t = \frac{D_e^t \beta_e}{\hat{n}_e \cdot \hat{s}_e} + 0.5\ \dot{m}_e + |\alpha_e|\,|\dot{m}_e| + \frac{D_w^t \beta_w}{\hat{n}_w \cdot \hat{s}_w} - 0.5\ \dot{m}_w + |\alpha_W|\,|\dot{m}_w| + \frac{D_n^t \beta_n}{\hat{n}_n \cdot \hat{t}_n} + 0.5\ \dot{m}_n + |\alpha_n|\,|\dot{m}_n| + \frac{D_s^t \beta_s}{\hat{n}_s \cdot \hat{t}_s} - 0.5\ \dot{m}_s + |\alpha_s|\,|\dot{m}_s| + \frac{M_P}{\Delta t} - R_P^t \tag{4.75}$$

or, in short form,

$$A_P^t = A_P^{t^*} - R_P^t + \frac{M_P^o}{\Delta t} \tag{4.76}$$

4.5.1 The Tube Bundle Flow Resistance Term

The tube bundle introduces a resistance to flow that is modeled by a source term in the U and V equations. The coefficient K in both U and V momentum resistance source terms is the tube-bundle loss coefficient for cross flow as derived by Carlucci et al. [7]

$$K^{\phi} = 2\left(\frac{f}{d}\right)(\mathcal{E})^2\left[\frac{1-\mathcal{E}}{1-\mathcal{E}_t}\right] \tag{4.77}$$

where ϕ is U and V velocity and f is a friction factor that is defined for various tube arrangements and flow parameters. In Equation (4.77), the term in square brackets is equal to the ratio of porous region volume to total volume of the control volume. Using the definition for $\mathcal{E}$ in Equation (2.5),

$$\left[\frac{1-\mathcal{E}}{1-\mathcal{E}_t}\right] = \frac{1-[\gamma\mathcal{E}_t+(1-\gamma)]}{1-\mathcal{E}_t} = \frac{\gamma-\gamma\mathcal{E}_t}{1-\mathcal{E}_t} = \gamma\left[\frac{1-\mathcal{E}_t}{1-\mathcal{E}_t}\right] = \gamma \tag{4.78}$$

To find pressure drop in a tube bundle, Butterworth [3] used Darcy's law:

$$U_{fs} = -\frac{\kappa}{\mu}\frac{\partial p}{\partial x} \tag{4.79}$$

where the free stream velocity, U_{fs}, depends on pressure drop and flow conductivity and inversely on viscosity. The pressure gradient is found from a friction factor

$$\frac{\partial p}{\partial x} = -\frac{4f}{d}\frac{\rho U_{fs}^2}{2} \tag{4.80}$$

Substituting Equation (4.80) into Equation (4.79), rearranging to get the friction factor around the tubes, and defining the free stream Reynolds number based on tube diameter yields

$$f = \frac{U_{fs}\,\mu d}{2\kappa\,\rho U_{fs}^2} = \frac{d^2}{2\kappa}\,\frac{\mu}{\rho U_{fs}\,d} = \frac{d^2}{2\kappa}\,\underbrace{\frac{\mu}{\rho\,\mathcal{E}\left|\vec{V}\right|d}}_{1/Re_d} = \frac{d^2}{2\,\kappa\,Re_d} \tag{4.81}$$

Butterworth [3] defines the flow conductivity, κ, using a number of different pitch to diameter ratios, for both low and high flow conditions for both square and triangular tube bundles. Low flow is in the range $1 \leq Re_d < 10$. High flow is in the range $Re_d > 120$. For flows in between, $10 < Re_d < 120$, one can interpolate between the low and high schemes, as will be described later. Butterworth shows that for square tube bundles under low flow conditions it is reasonable to use the following definition for κ, which corresponds to $p/d = 1.5$.

$$\kappa_L = 4.23 \times 10^{-3} \ \frac{d\, D_V^3}{p^2} \tag{4.82}$$

For triangular tube bundles the following is suggested as a good compromise between the different pitch to diameter ratios.

$$\kappa_L = 6.8 \times 10^{-3} \ \frac{d\, D_V^3}{p^2} \tag{4.83}$$

For square tube bundles under high flow conditions, κ is defined as:

$$\kappa_H = \frac{8.19\,(p-d)^3}{D_V} Re_d^{-0.912} \tag{4.84}$$

For triangular tube bundles , under high flow conditions κ is defined as:

$$\kappa_H = \frac{1.11\,(p-d)^3}{D_V} Re_d^{-0.733} \tag{4.85}$$

The hydraulic tube diameter for a square tube bundle is

$$D_V = \frac{4p^2 - \pi d^2}{\pi d} \tag{4.86}$$

and triangular tube bundles is

$$D_V = \frac{2\sqrt{3}\, p^2 - \pi d^2}{\pi d} \tag{4.87}$$

Substituting Equation (4.82) into Equation (4.81), it follows that the low flow friction factor for square tube bundles is:

$$f_L = 118 \ \frac{d\, p^2}{D_V^3} Re_d^{-1} \tag{4.88}$$

Substituting Equation (4.83) into Equation (4.81), the low flow friction factor for triangular tube bundles is:

$$f_L = 73.5 \ \frac{d\, p^2}{D_V^3} Re_d^{-1} \tag{4.89}$$

Substituting Equation (4.84) into Equation (4.81), the high flow friction factor for square tube bundles is:

$$f_H = 0.061 \ \frac{d^2\, D_V}{(p-d)^3} Re_d^{-0.088} \tag{4.90}$$

Substituting Equation (4.85) into Equation (4.81), the high flow friction factor for triangular tube bundles is:

$$f_H = 0.45 \ \frac{d^2\, D_V}{(p-d)^3} Re_d^{-0.267} \tag{4.91}$$

For flow that is moderate, $10 < Re_d < 120$, the friction factor is interpolated by

$$f = \sqrt{f_L^2 + f_H^2} \tag{4.92}$$

The friction factor is then used in Equation (4.77) to calculate K.

4.6 Turbulence model

4.6.1 Background

A simple turbulence model consisting of a constant effective viscosity that is set to be a specific multiple of molecular viscosity is used in this work. More accurate turbulence models are available, but adding variable viscosity would complicate the calculations and is outside the scope of this work. The focus, again, is to determine the differences between the orthogonal and non-orthogonal grids, and keeping the turbulence model simple helps make

that comparison clearer. The constant viscosity turbulence model has been used by other researchers in simulating shell-side flows. A brief discussion of that work is given below to indicate the range of values used in previous work.

Al-Sanea et al. [1] use correlations which, in their studies of condensers, produce turbulent viscosities, μ_t, in the range of 170 to 680 times the laminar viscosity, μ.

Zhang [46] and Zhang et al. [50] indicate that turbulent viscosity should be kept at a range of 10 to 100 times laminar viscosity. Typical values used were about 20 times the value of laminar viscosity and only slight differences were observed when the multiple was changed from 10 to 100. They based their estimate of viscosity multiple on previous work done by Zhang and Sousa [47, 49] which used k–ϵ turbulence models. They found that effective kinematic viscosity gradients are relatively small in a tube bundle.

Rhodes and Carlucci [39] found good agreement between measured and predicted velocities in a tube-filled isothermal heat exchanger using the porous media concept and a constant turbulent viscosity which was estimated from the measured turbulence intensity. The resulting effective viscosity they used is approximately 100 to 400 times the laminar viscosity.

Theodossiou et al. [42] used a fixed viscosity which was estimated using a mixing length model and a representative measured turbulence intensity. Theodossiou et al. justified their model by the argument that resistance forces dominate the flow, so complex turbulence modeling is unwarranted.

Carlucci et al. [7] set the effective viscosity equal to laminar viscosity so that the only effective momentum sinks were the resistance terms. They were developing a two-dimensional isothermal model of heat-exchangers and wanted quick, robust convergence behavior.

Lonsdale and Tierney [21] used a k–ϵ turbulence model for the tube-free space only and constant viscosity in the tube bundle.

4.6.2 Present Work

The above review of previous literature indicates that for a variety of heat exchanger flow models the effective viscosity has been in the range of approximately 10 to 700 times the molecular viscosity. This work uses viscosity multiples of 25, 50 and 100 to show the consequences of changing the effective viscosity on the results for both orthogonal and non-orthogonal grids.

4.7 General Treatment of the Discrete Boundary Conditions

Discrete analogues to the boundary conditions for the partial differential equations are required. Two boundary conditions each in x and y for each of U and V and T. The boundary conditions on pressure are derived from the velocity boundary conditions. A pressure reference level is specified.

4.7.1 Nomenclature for the Boundary Conditions

For the discussion of boundary conditions Φ represents U or V velocities or temperature, T. There are two types of boundary conditions implemented in the computer code. The first is Dirichlet, where a prescribed value of velocity or temperature is imposed on the boundary, $\Phi_P = \Gamma^{\phi}_{bc}$. The second type of boundary condition is Neumann, where the velocity gradient is prescribed ($\frac{\partial \Phi}{\partial x} = \Gamma^{\phi}_{bc}$, where $\Phi = U$ or V), or the heat flux is specified using $k\frac{\partial T}{\partial x} = \Gamma^{t}_{bc}$.

In the following discussion, the west boundary is used to demonstrate how boundary conditions are applied. The boundary conditions are introduced by considering the nine-point equation for the zero width boundary control volume at $(IB-1, j)$ as in Figure 4.2(a). The

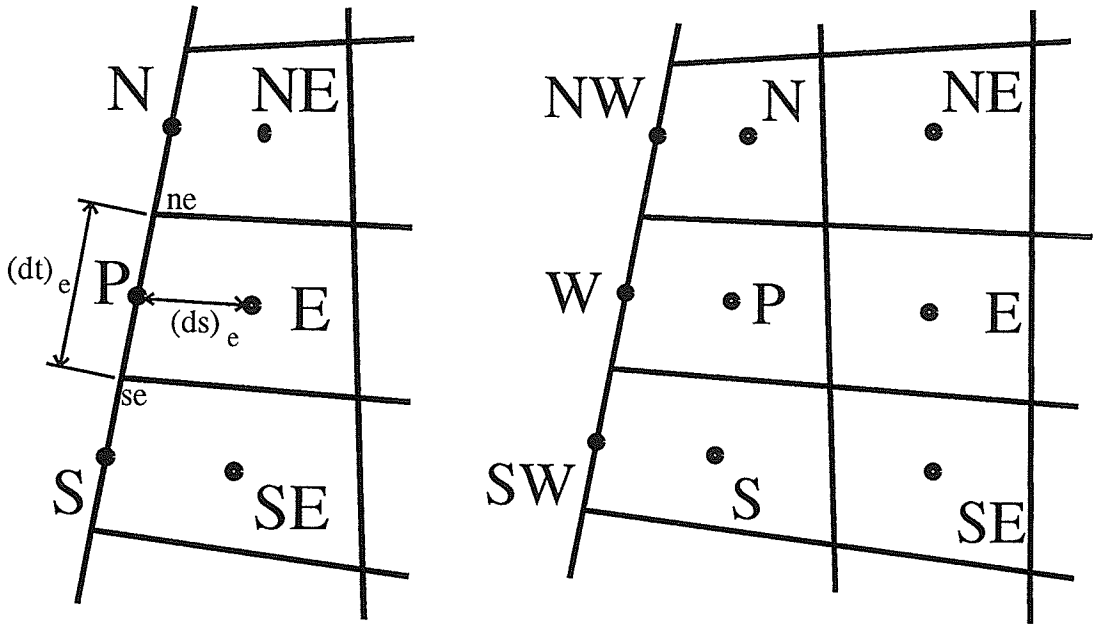

(a) ($i = IB - 1$). (b) ($i = IB$).

Figure 4.2: West Boundary Computational Molecule.

boundary condition connects the boundary node, P, with the next interior node, E. Therefore, only A_P^ϕ, A_E^ϕ and b^ϕ coefficients are used in the algebraic equations for the boundary node. The result of reducing Equation (4.34) for the fictitious boundary node, $(IB-1, j)$, is as follows:

$$A^\phi_{P(IB-1,j)}\Phi_{P(IB-1,j)} = A^\phi_{E(IB-1,j)}\Phi_{E(IB-1,j)} + b^\phi_{(IB-1,j)} \tag{4.93}$$

Note that $\Phi_{E(IB-1,j)}$ is the first interior node near the boundary.

4.7.2 Dirichlet

The west Dirichlet boundary condition is implemented by setting $A^\phi_{P(IB-1,j)} = 1$, $A^\phi_{E(IB-1,j)} = 0$, $b^\phi_{(IB-1,j)} = \Gamma^\phi_{bc}$, and all other neighboring coefficients are set to zero. This ensures that the boundary velocity will be the prescribed value, $\Phi_{P(IB-1,j)} = \Gamma^\phi_{bc}$.

4.7.3 Neumann

Because of the non-orthogonal grid, the Neumann boundary condition is slightly more complicated to implement than the Dirichlet boundary condition. On a non-orthogonal grid $\frac{\partial \Phi}{\partial x}$ must be defined in terms of the gradient along the unit vector directions, $\hat{s}$ and $\hat{t}$. The change in Φ in the west to east direction, $\hat{s}$, can be expanded out in a chain rule as follows:

$$\frac{\partial \Phi}{\partial s} = \frac{\partial \Phi}{\partial x}\frac{\partial x}{\partial s} + \frac{\partial \Phi}{\partial y}\frac{\partial y}{\partial s} \tag{4.94}$$

Likewise, the change in Φ in the south to north direction, $\hat{t}$, can be expanded out in a chain rule as follows:

$$\frac{\partial \Phi}{\partial t} = \frac{\partial \Phi}{\partial x}\frac{\partial x}{\partial t} + \frac{\partial \Phi}{\partial y}\frac{\partial y}{\partial t} \tag{4.95}$$

Using Cramer's rule, the change in Φ in the Cartesian x direction is defined as follows:

$$\frac{\partial \Phi}{\partial x} = \frac{\begin{vmatrix} \frac{\partial \Phi}{\partial s} & \frac{\partial y}{\partial s} \\ \frac{\partial \Phi}{\partial t} & \frac{\partial y}{\partial t} \end{vmatrix}}{\begin{vmatrix} \frac{\partial x}{\partial s} & \frac{\partial y}{\partial s} \\ \frac{\partial x}{\partial t} & \frac{\partial y}{\partial t} \end{vmatrix}} = \frac{\frac{\partial \Phi}{\partial s}\frac{\partial y}{\partial t} - \frac{\partial \Phi}{\partial t}\frac{\partial y}{\partial s}}{\frac{\partial x}{\partial s}\frac{\partial y}{\partial t} - \frac{\partial y}{\partial s}\frac{\partial x}{\partial t}} \tag{4.96}$$

Equation (4.96) is rewritten for the east face of a control volume as follows:

$$\left.\frac{\partial \Phi}{\partial x}\right|_e = \frac{\left.\frac{\partial \Phi}{\partial s}\right|_e \left.\frac{\partial y}{\partial t}\right|_e - \left.\frac{\partial \Phi}{\partial t}\right|_e \left.\frac{\partial y}{\partial s}\right|_e}{\left.\frac{\partial x}{\partial s}\right|_e \left.\frac{\partial y}{\partial t}\right|_e - \left.\frac{\partial y}{\partial s}\right|_e \left.\frac{\partial x}{\partial t}\right|_e} = \frac{\left.\frac{\partial \Phi}{\partial s}\right|_e t_{ye} - \left.\frac{\partial \Phi}{\partial t}\right|_e s_{ye}}{s_{xe}t_{ye} - t_{xe}s_{ye}} \tag{4.97}$$

Equation (4.96) can also be written for the north face as:

$$\left.\frac{\partial \Phi}{\partial x}\right|_n = \frac{\left.\frac{\partial \Phi}{\partial s}\right|_n \left.\frac{\partial y}{\partial t}\right|_n - \left.\frac{\partial \Phi}{\partial t}\right|_n \left.\frac{\partial y}{\partial s}\right|_n}{\left.\frac{\partial x}{\partial s}\right|_n \left.\frac{\partial y}{\partial t}\right|_n - \left.\frac{\partial y}{\partial s}\right|_n \left.\frac{\partial x}{\partial t}\right|_n} = \frac{\left.\frac{\partial \Phi}{\partial s}\right|_n t_{yn} - \left.\frac{\partial \Phi}{\partial t}\right|_n s_{yn}}{s_{xn}t_{yn} - t_{xn}s_{yn}} \tag{4.98}$$

Only Equation (4.97) is used for Neumann boundary conditions on the east and west face of a control volume.

For the north and south boundaries, the change in Φ in the Cartesian y direction is defined as follows:

$$\frac{\partial \Phi}{\partial y} = \frac{\begin{vmatrix} \frac{\partial x}{\partial s} & \frac{\partial \Phi}{\partial s} \\ \frac{\partial x}{\partial t} & \frac{\partial \Phi}{\partial t} \end{vmatrix}}{\begin{vmatrix} \frac{\partial x}{\partial s} & \frac{\partial y}{\partial s} \\ \frac{\partial x}{\partial t} & \frac{\partial y}{\partial t} \end{vmatrix}} = \frac{\frac{\partial \Phi}{\partial t}\frac{\partial x}{\partial s} - \frac{\partial \Phi}{\partial s}\frac{\partial x}{\partial t}}{\frac{\partial x}{\partial s}\frac{\partial y}{\partial t} - \frac{\partial y}{\partial s}\frac{\partial x}{\partial t}} \tag{4.99}$$

Equation (4.99) is rewritten for the north face of a control volume as:

$$\left.\frac{\partial \Phi}{\partial y}\right|_n == \frac{\left.\frac{\partial \Phi}{\partial t}\right|_n \left.\frac{\partial x}{\partial s}\right|_n - \left.\frac{\partial \Phi}{\partial s}\right|_n \left.\frac{\partial x}{\partial t}\right|_n}{\left.\frac{\partial x}{\partial s}\right|_n \left.\frac{\partial y}{\partial t}\right|_n - \left.\frac{\partial y}{\partial s}\right|_n \left.\frac{\partial x}{\partial t}\right|_n} = \frac{\left.\frac{\partial \Phi}{\partial t}\right|_n s_{xn} - \left.\frac{\partial \Phi}{\partial s}\right|_n t_{xn}}{s_{xn}t_{yn} - t_{xn}s_{yn}} \tag{4.100}$$

Equation (4.99) can also be written for the east face as:

$$\left.\frac{\partial \Phi}{\partial y}\right|_e == \frac{\left.\frac{\partial \Phi}{\partial t}\right|_e \left.\frac{\partial x}{\partial s}\right|_e - \left.\frac{\partial \Phi}{\partial s}\right|_e \left.\frac{\partial x}{\partial t}\right|_e}{\left.\frac{\partial x}{\partial s}\right|_e \left.\frac{\partial y}{\partial t}\right|_e - \left.\frac{\partial y}{\partial s}\right|_e \left.\frac{\partial x}{\partial t}\right|_e} = \frac{\left.\frac{\partial \Phi}{\partial t}\right|_e s_{xe} - \left.\frac{\partial \Phi}{\partial s}\right|_e t_{xe}}{s_{xe}t_{ye} - t_{xe}s_{ye}} \tag{4.101}$$

Only Equation (4.100) is used for Neumann boundary conditions on the north and south face of a control volume.

To implement the Neumann boundary condition on the west boundary, $\frac{\partial \Phi}{\partial x}$ must be set at the west boundary equal to a desired value, Γ^{ϕ}_{bc}. Equation (4.97), is applied to the east face of the west boundary control volume, (at $i = IB-1$), and the derivatives are approximated to obtain:

$$\left.\frac{\partial \Phi}{\partial x}\right|_{e_{(IB-1,j)}} = \Gamma^{\phi}_{bc} = \frac{\frac{\Phi_E - \Phi_P}{(ds)_e}t_{ye} - \frac{\Phi_{ne} - \Phi_{se}}{(dt)_e}s_{ye}}{s_{xe}t_{ye} - t_{xe}s_{ye}} \tag{4.102}$$

Rearrange into the form of the boundary algebraic equation, Equation (4.93), as follows:

$$\Phi_P = \Phi_E - (\Phi_{ne} - \Phi_{se}) \frac{(ds)_e}{(dt)_e} \frac{s_{ye}}{t_{ye}} - \Gamma^{\phi}_{bc}(ds)_e \frac{s_{xe}t_{ye} - t_{xe}s_{ye}}{t_{ye}} \tag{4.103}$$

The coefficients of the fictitious control volume are then set as follows:

$$\left.\begin{aligned} A^{\phi}_{P_{(IB-1,j)}} &= 1 \qquad A^{\phi}_{E_{(IB-1,j)}} = 1 \\ b^{\phi}_{(IB-1,j)} &= -(\Phi_{ne} - \Phi_{se}) \frac{(ds)_e}{(dt)_e} \frac{s_{ye}}{t_{ye}} - \Gamma^{\phi}_{bc}(ds)_e \frac{s_{xe}t_{ye} - t_{xe}s_{ye}}{t_{ye}} \end{aligned}\right\} \tag{4.104}$$

and all other neighbor coefficients are set to zero. The control volume corner velocities (Φ_{ne} and Φ_{se}) are set to using linear interpolation between the nearest nodal values that are also on the boundary. If the control volume in question is in a corner of the domain, for example (IB,JB), and the two boundaries have Neumann conditions, then $\Phi_{se} = \Phi_{(IB,JB)}$ If one of the boundaries is a Dirichlet condition then $\Phi_{se} = \Gamma^{\phi}_{bc}$ is set.

4.7.4 Absorbing the Boundary Conditions

The first interior node adjacent to the west boundary needs information from nodes that are on the boundary as illustrated in Figure 4.2(b). The following is Equation (4.34) rewritten for the first interior node adjacent to the west boundary, ($\Phi_{P_{(IB,j)}}$ in Figure 4.2(b)):

$$\begin{aligned} A^{\phi}_{P_{(IB,j)}}\Phi_{P_{(IB,j)}} &= A^{\phi}_{E_{(IB,j)}}\Phi_{E_{(IB,j)}} + A^{\phi}_{W_{(IB,j)}}\Phi_{W_{(IB,j)}} + A^{\phi}_{N_{(IB,j)}}\Phi_{N_{(IB,j)}} + A^{\phi}_{S_{(IB,j)}}\Phi_{S_{(IB,j)}} \\ &+ A^{\phi}_{NE_{(IB,j)}}\Phi_{NE_{(IB,j)}} + A^{\phi}_{SW_{(IB,j)}}\Phi_{SW_{(IB,j)}} + A^{\phi}_{NW_{(IB,j)}}\Phi_{NW_{(IB,j)}} + A^{\phi}_{SE_{(IB,j)}}\Phi_{SE_{(IB,j)}} + b^{\phi}_{(IB,j)} \end{aligned} \tag{4.105}$$

This equation includes nodal values that are on the boundary, namely Φ_W, Φ_{NW}, and Φ_{SW}, which are controlled by the boundary conditions. To eliminate the boundary nodes from the computational domain they must be expressed in terms of interior nodes. The following is an the algebraic boundary condition equation, for the node at $\Phi_{W(IB)}$, (which is just Equation (4.93) applied at $\Phi_{W(IB,j)}$):

$$A^{\phi}_{P_{(IB-1,j)}}\Phi_{W_{(IB,j)}} = A^{\phi}_{E_{(IB-1,j)}}\Phi_{P_{(IB,j)}} + b^{\phi}_{(IB-1,j)} \tag{4.106}$$

Similarly, the equations for Φ_{NW} and Φ_{SW} are

$$A^{\phi}_{P_{(IB-1,j+1)}}\Phi_{NW_{(IB,j)}} = A^{\phi}_{E_{(IB-1,j+1)}}\Phi_{N_{(IB,j)}} + b^{\phi}_{(IB-1,j+1)} \tag{4.107}$$

and

$$A^{\phi}_{P_{(IB-1,j-1)}}\Phi_{SW_{(IB,j)}} = A^{\phi}_{E_{(IB-1,j-1)}}\Phi_{S_{(IB,j)}} + b^{\phi}_{(IB-1,j-1)} \tag{4.108}$$

respectively. Equations (4.106) through (4.108) are substituted into Equation (4.105) to eliminate the boundary nodes. This substitution yields

$$\begin{aligned} A^{\phi}_{P_{(IB,j)}}\Phi_{P_{(IB,j)}} = {} & A^{\phi}_{E_{(IB,j)}}\Phi_{E_{(IB,j)}} + A^{\phi}_{N_{(IB,j)}}\Phi_{N_{(IB,j)}} + A^{\phi}_{S_{(IB,j)}}\Phi_{S_{(IB,j)}} \\ & + A^{\phi}_{NE_{(IB,j)}}\Phi_{NE_{(IB,j)}} + A^{\phi}_{SE_{(IB,j)}}\Phi_{SE_{(IB,j)}} \\ & + A^{\phi}_{W_{(IB,j)}}\left[\frac{A^{\phi}_{E_{(IB-1,j)}}}{A^{\phi}_{P_{(IB-1,j)}}}\Phi_{P_{(IB,j)}} + \frac{b^{\phi}_{(IB-1)}}{A^{\phi}_{P_{(IB-1)}}}\right] \\ & + A^{\phi}_{SW_{(IB,j)}}\left[\frac{A^{\phi}_{E_{(IB-1,j-1)}}}{A^{\phi}_{P_{(IB-1,j-1)}}}\Phi_{S_{(IB,j)}} + \frac{b^{\phi}_{(IB-1,j-1)}}{A^{\phi}_{P_{(IB-1,j-1)}}}\right] \\ & + A^{\phi}_{NW_{(IB,j)}}\left[\frac{A^{\phi}_{E_{(IB-1,j+1)}}}{A^{\phi}_{P_{(IB-1,j+1)}}}\Phi_{N_{(IB,j)}} + \frac{b^{\phi}_{(IB-1,j+1)}}{A^{\phi}_{P_{(IB-1,j+1)}}}\right] + b^{\phi}_{(IB,j)} \end{aligned} \tag{4.109}$$

Rearranging and collecting coefficients in Equation (4.109) produces

$$\begin{aligned} & \left(A^{\phi}_{P_{(IB,j)}} - A^{\phi}_{W_{(IB,j)}}\frac{A^{\phi}_{E_{(IB-1,j)}}}{A^{\phi}_{P_{(IB-1,j)}}}\right)\Phi_{P_{(IB,j)}} = \\ & \qquad A^{\phi}_{E_{(IB,j)}}\Phi_{E_{(IB,j)}} + \left(A^{\phi}_{N_{(IB,j)}} + A^{\phi}_{NW_{(IB,j)}}\frac{A^{\phi}_{E_{(IB-1,j+1)}}}{A^{\phi}_{P_{(IB-1,j+1)}}}\right)\Phi_{N_{(IB,j)}} \\ & + \left(A^{\phi}_{S_{(IB,j)}} + A^{\phi}_{SW_{(IB,j)}}\frac{A^{\phi}_{E_{(IB-1,j-1)}}}{A^{\phi}_{P_{(IB-1,j-1)}}}\right)\Phi_{S_{(IB,j)}} + A^{\phi}_{NE_{(IB,j)}}\Phi_{NE_{(IB,j)}} + A^{\phi}_{SE_{(IB,j)}}\Phi_{SE_{(IB,j)}} \\ & + \left(b^{\phi}_{(IB,j)} + A^{\phi}_{W_{(IB,j)}}\frac{b^{\phi}_{(IB-1,j)}}{A^{\phi}_{P_{(IB-1,j)}}} + A^{\phi}_{SW_{(IB,j)}}\frac{b^{\phi}_{(IB-1,j-1)}}{A^{\phi}_{P_{(IB-1,j-1)}}} + A^{\phi}_{NW_{(IB,j)}}\frac{b^{\phi}_{(IB-1,j+1)}}{A^{\phi}_{P_{(IB-1,j+1)}}}\right) \end{aligned} \tag{4.110}$$

Equation (4.110) is the basis for boundary condition absorption. To absorb (implicitly account for) the boundary conditions, the coefficients of the equation for $\Phi_{P_{(IB,j)}}$ are modified

as follows:

$$\left.\begin{aligned}
A^{\phi}_{P(IB,j)} &= A^{\phi}_{P(IB,j)} - A^{\phi}_{W(IB,j)} \frac{A^{\phi}_{E(IB-1,j)}}{A^{\phi}_{P(IB-1,j)}} \\
A^{\phi}_{N(IB,j)} &= A^{\phi}_{N(IB,j)} + A^{\phi}_{NW(IB,j)} \frac{A^{\phi}_{E(IB-1,j+1)}}{A^{\phi}_{P(IB-1,j+1)}} \\
A^{\phi}_{S(IB,j)} &= A^{\phi}_{S(IB,j)} + A^{\phi}_{SW(IB,j)} \frac{A^{\phi}_{E(IB-1,j-1)}}{A^{\phi}_{P(IB-1,j-1)}} \\
b^{\phi}_{(IB,j)} &= b^{\phi}_{(IB,j)} + A^{\phi}_{W(IB,j)} \frac{b^{\phi}_{(IB-1,j)}}{A^{\phi}_{P(IB-1,j)}} \\
&\quad + A^{\phi}_{SW(IB,j)} \frac{b^{\phi}_{(IB-1,j-1)}}{A^{\phi}_{P(IB-1,j-1)}} + A^{\phi}_{NW(IB,j)} \frac{b^{\phi}_{(IB-1,j+1)}}{A^{\phi}_{P(IB-1,j+1)}}
\end{aligned}\right\} \quad (4.111)$$

The boundary conditions are held in the fictitious coefficients and no boundary velocities appear in the computational domain. Therefore, the west, northwest, and southwest coefficients of the nine-point equation, at (IB, j), are equal to zero.

If the control volume in question is in a corner of the domain, for example (IB,JB), then the south and southeast coefficients also have to be set to zero after the south boundary conditions are set in a manner analogous to the description above.

4.7.5 Face Velocity Boundary Conditions

The face velocity boundary conditions are based on the continuity equation, and are used to derive the pressure correction equation boundary conditions (discussed later). As with the other boundary conditions, the west boundary is used as an example and east, south, and north boundaries are analogous.

First, the continuity equation for the control volume adjacent to the west boundary, (IB)

as in Figure 4.2(b), is written as follows:

$$\left(A^c_{u_e(IB-1)}U_e + A^c_{v_e(IB-1)}V_e\right) + \left(A^c_{u_w(IB-1)}U_w + A^c_{v_w(IB-1)}V_w\right) + \left(A^c_{u_n(IB-1)}U_n + A^c_{v_n(IB-1)}V_n\right) + \left(A^c_{u_s(IB-1)}U_s + A^c_{v_s(IB-1)}V_s\right) + b^c_P = 0 \quad (4.112)$$

where, for simplicity, all coefficients are assumed to be for the j control volume. The U and V velocity boundary conditions are specified separately so it is assumed that the U and V velocities do not affect each other at the boundary. Therefore, Equation (4.112) is solved for U_w to obtain:

$$U_w = \frac{-1}{A^c_{u_w(IB-1)}}\left\{\left(A^c_{u_e(IB-1)}U_e + A^c_{v_e(IB-1)}V_e\right) + A^c_{v_w(IB-1)}V_w + \left(A^c_{u_n(IB-1)}U_n + A^c_{v_n(IB-1)}V_n\right) + \left(A^c_{u_s(IB-1)}U_s + A^c_{v_s(IB-1)}V_s\right) + b^c_P\right\} \quad (4.113)$$

and separately for V_w:

$$V_w = \frac{-1}{A^c_{v_w(IB-1)}}\left\{\left(A^c_{u_e(IB-1)}U_e + A^c_{v_e(IB-1)}V_e\right) + A^c_{u_w(IB-1)}U_w + \left(A^c_{u_n(IB-1)}U_n + A^c_{v_n(IB-1)}V_n\right) + \left(A^c_{u_s(IB-1)}U_s + A^c_{v_s(IB-1)}V_s\right) + b^c_P\right\} \quad (4.114)$$

The coefficient, $A^c_{u_w(IB-1)}$, in the denominator of Equation (4.113) is not needed so it is replaced by -1 and moved to act as source term as follows:

$$U_w = \left(A^c_{u_e(IB-1)}U_e + A^c_{v_e(IB-1)}V_e\right) + A^c_{v_w(IB-1)}V_w \left(+A^c_{u_n(IB-1)}U_n + A^c_{v_n(IB-1)}V_n\right)\left(+A^c_{u_s(IB-1)}U_s + A^c_{v_s(IB-1)}V_s\right) + A^c_{u_w(IB-1)} \quad (4.115)$$

The V_w equation is rearranged in a similar way to obtain:

$$V_w = \left(A^c_{u_e(IB-1)}U_e + A^c_{v_e(IB-1)}V_e\right) + A^c_{u_w(IB-1)}U_w \left(+A^c_{u_n(IB-1)}U_n + A^c_{v_n(IB-1)}V_n\right)\left(+A^c_{u_s(IB-1)}U_s + A^c_{v_s(IB-1)}V_s\right) + A^c_{v_w(IB-1)} \quad (4.116)$$

Since the U and V velocity boundary conditions are set independently, and the north and south face velocities are not used to set the west boundary conditions, Equation (4.115) and

(4.116) can be simplified to:

$$U_w = A^c_{u_e(IB-1)} U_e + A^c_{u_w(IB-1)} \tag{4.117}$$

and

$$V_w = A^c_{v_e(IB-1)} V_e + A^c_{v_w(IB-1)} \tag{4.118}$$

respectively.

The Dirichlet west face boundary condition is implemented by setting $A^c_{u_w(IB-1)} = \Gamma^u_{bc}$ for the U velocity and $A^c_{v_w(IB-1)} = \Gamma^v_{bc}$ for the V velocity. All the rest of the continuity coefficients are then set to zero.

The Neumann west face boundary condition is implemented in a way similar to that for the nodal boundary conditions by applying the gradient, $\frac{\partial \Phi}{\partial x} = \Gamma^\phi_{bc}$ at the west boundary across the first control volume, from west face to east face, instead of between nodes.

$$\left.\frac{\partial \Phi}{\partial x}\right|_{(IB,j)} = \Gamma^\phi_{bc} = \frac{\frac{\Phi_e - \Phi_w}{(ds)_p} t_{yw} - \frac{\Phi_{nw} - \Phi_{sw}}{(dt)_w} s_{yp}}{s_{xp} t_{yw} - t_{xw} s_{yp}} \tag{4.119}$$

Rearranging Equation (4.119) in the form of Equation (4.117) and Equation (4.118) produces:

$$\Phi_w = \Phi_e - (\Phi_{nw} - \Phi_{sw}) \frac{(ds)_p}{(dt)_w} \frac{s_{yp}}{t_{yw}} - \Gamma^\phi_{bc} (ds)_p \frac{s_{xp} t_{yw} - t_{xw} s_{yp}}{t_{yw}} \tag{4.120}$$

which leads to the following specification for the continuity coefficients on the boundary:

$$\left.\begin{array}{lll} A^c_{u_e(IB-1)} = 1 & & A^c_{v_e(IB-1)} = 0 \\ A^c_{u_n(IB-1)} = 0 & & A^c_{v_n(IB-1)} = 0 \\ A^c_{u_s(IB-1)} = 0 & & A^c_{v_s(IB-1)} = 0 \\ A^c_{v_w(IB-1)} = 0 & & \\ A^c_{u_w(IB-1)} = -(U_{nw} - U_{sw}) \frac{(ds)_p}{(dt)_w} \frac{s_{yp}}{t_{yw}} - \Gamma^u_{bc} (ds)_p \frac{s_{xp} t_{yw} - t_{xw} s_{yp}}{t_{yw}} & & \end{array}\right\} \tag{4.121}$$

and

$$\left.\begin{aligned}
A^c_{u_e(IB-1)} &= 0 \qquad & A^c_{v_e(IB-1)} &= 1 \\
A^c_{u_n(IB-1)} &= 0 \qquad & A^c_{v_n(IB-1)} &= 0 \\
A^c_{u_s(IB-1)} &= 0 \qquad & A^c_{v_s(IB-1)} &= 0 \\
A^c_{u_w(IB-1)} &= 0 \\
A^c_{v_w(IB-1)} &= -\left(V_{nw}-V_{sw}\right)\frac{(ds)_p}{(dt)_w}\frac{s_{yp}}{t_{yw}} - \Gamma^v_{bc}(ds)_p\frac{s_{xp}t_{yw}-t_{xw}s_{yp}}{t_{yw}}
\end{aligned}\right\} \quad (4.122)$$

To absorb these boundary conditions into the regular computational domain, Equation (4.117) and (4.118) are substituted into the continuity equation, Equation (4.6), as follows:

$$\begin{aligned}
&\left(A^c_{u_e(IB)}U_e + A^c_{v_e(IB)}V_e\right) \\
&\quad + A^c_{u_w(IB)}\left(A^c_{u_e(IB-1)}U_e + A^c_{u_w(IB-1)}\right) + A^c_{v_w(IB)}\left(A^c_{v_e(IB-1)}V_e + A^c_{v_w(IB-1)}\right) \\
&\qquad + \left(A^c_{u_n(IB)}U_n + A^c_{v_n(IB)}V_n\right) + \left(A^c_{u_s(IB)}U_s + A^c_{v_s(IB)}V_s\right) + b^c_P = 0
\end{aligned} \quad (4.123)$$

Collecting terms yields:

$$\begin{aligned}
&\left(A^c_{u_e(IB)} + A^c_{u_w(IB)}A^c_{u_e(IB-1)}\right)U_e + \left(A^c_{v_e(IB)} + A^c_{v_w(IB)}A^c_{v_e(IB-1)}\right)V_e \\
&\qquad + A^c_{u_w(IB)}A^c_{u_w(IB-1)} + A^c_{v_w(IB)}A^c_{v_w(IB-1)} \\
&\quad + \left(A^c_{u_n(IB)}U_n + A^c_{v_n(IB)}V_n\right) + \left(A^c_{u_s(IB)}U_s + A^c_{v_s(IB)}V_s\right) + b^c_{P(IB)} = 0
\end{aligned} \quad (4.124)$$

The east U and V continuity coefficients are then modified for the west boundary and the

source term has additional terms as follows:

$$\left.\begin{aligned}
\left(A^c_{u_e(IB)}\right)^{\oplus} &= A^c_{u_e(IB)} + A^c_{u_w(IB)}A^c_{u_e(IB-1)} \\
\left(A^c_{v_e(IB)}\right)^{\oplus} &= A^c_{v_e(IB)} + A^c_{v_w(IB)}A^c_{v_e(IB-1)} \\
\left(b^c_{P(IB)}\right)^{\oplus} &= b^c_{P(IB)} + A^c_{u_w(IB)}A^c_{u_w(IB-1)} + A^c_{v_w(IB)}A^c_{v_w(IB-1)}
\end{aligned}\right\} \tag{4.125}$$

where the superscript "$\oplus$" refers to modifications to the continuity coefficients in Equation (4.6).

4.7.6 Wall Function

As a simple means of modeling turbulent flow, a constant effective viscosity has been used as discussed in Section 4.6. A simple wall function method is used to obtain the correct shear stress at a wall (including blockages) without the need for a refined grid near the wall. The wall function is used only on Cartesian horizontal and vertical walls in this work.

Figure 4.3 shows the nomenclature used in the derivation of the wall function equations that follow below. Following the example of Brown and Raithby [2], and White [45], the perpendicular distance of the first node from the wall is indicated by y, and the non-dimensional distance is given by:

$$y^+ = \frac{\rho u_\tau y}{\mu} \tag{4.126}$$

where u_τ is the wall-friction velocity. The non-dimensional velocity, u^+ is:

$$u^+ = \frac{u}{u_\tau} \tag{4.127}$$

Following the definition of wall shear stress:

$$u_\tau = \sqrt{\frac{\tau_w}{\rho}} \tag{4.128}$$

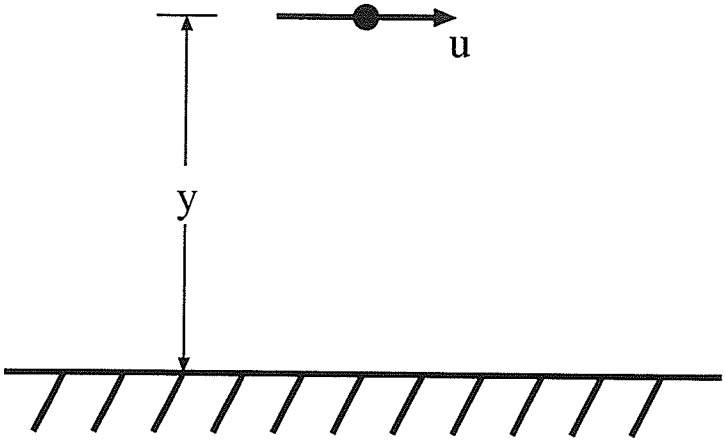

Figure 4.3: Nomenclature for Wall Function Definition.

Substituting Equation (4.126) into Equation (4.128) produces:

$$\tau_w = \frac{1}{\rho}\left(\frac{\mu y^+}{y}\right)^2 \tag{4.129}$$

A local Reynolds number is defined using the nearest nodal velocity parallel to the wall and the distance from the wall as follows:

$$Re = \frac{\rho u y}{\mu} = \frac{\rho\left(u^+ u_\tau\right)\left(\frac{y^+\mu}{\rho u_\tau}\right)}{\mu} = u^+ y^+ \tag{4.130}$$

Very near the wall, in the inner layer, $y^+ < 11.63$, the viscous shear dominates and the velocity profile should be linear so:

$$u^+ = y^+ \tag{4.131}$$

Farther from the wall, $y^+ > 11.63$, the velocity profile is better described by the logarithmic overlap layer and is given by:

$$u^+ = \frac{1}{\kappa}\ln\left(y^+\right) + B \tag{4.132}$$

Where $\kappa = 0.40$ and $B = 5.5$. Equations (4.131) and (4.132) are equal when $y^+ = 11.63$.

The logarithmic overlap equation is quite accurate within the range of $35 \leq y^+ \leq 350$. The local Reynolds number when $y^+ = 11.63$ would be:

$$Re = u^+ y^+ = 11.63 * 11.63 = 135 \tag{4.133}$$

The following method is applied to find the wall shear stress. First, calculate the local Reynolds number using the first part of Equation (4.130). Second, calculate y^+ using $y^+ = \sqrt{Re}$. If $Re \leq 135$ then that value for y^+ is correct and no iteration is necessary. If, however, $Re > 135$ then a Newton-Raphson root search is used to solve Equation (4.132) for y^+. Third, apply Equation (4.129) to get the wall shear stress. Care must be taken to ensure the sign of the shear stress is opposite the sign of the nodal velocity nearest the wall.

4.8 E-Factor

Since this work is focused only on the steady-state solution to the governing equations, the true transient terms in the equations are, strictly speaking, not needed. They are retained, however, to provide needed relaxation in the solution of the coupled non-linear set of equations.

Van Doormaal and Raithby [43] and Raithby and Schneider [36] replaced the transient term with a distorted transient term and define a so-called E-factor, E. To use the distorted transient part of the original transient term is redefined as:

$$\frac{M_P^o}{\Delta t} = \frac{A_P^{u^*} - R_P^u}{E^u} \tag{4.134}$$

Substituting Equation (4.134) into Equation (4.46) and Equation (4.43) produces the following new definition of the A_P^ϕ and b^ϕ coefficients:

$$A_P^u = \left(A_P^{u^*} - R_P^u\right)\left(\frac{A_P^{u^*} - R_P^u}{E^u}\right) \tag{4.135}$$

and

$$b^u = \left(\frac{A_P^{u^*} - R_P^u}{E^u}\right) U_P^o - \overline{V_P} \left.\frac{\partial P}{\partial x}\right|_P + Q_P^u \tag{4.136}$$

respectively. A similar definition is used for the V and T equations.

The E-factor formulation allows taking a different Δt in each control volume (if the control volumes have different sizes). In the computer code implementation of the coefficient calculations, both the E-factor and true transient formulations are available and are selected through the specification of E and Δt values.

4.9 Special Regions Within the Grid

There are two special regions defined within a grid. The first is a tube bundle region where a porosity is specified to account for the volume occupied by the tubes. The second is a flow blockage which simulates baffles and sealing strips in a heat exchanger.

4.9.1 Tube Bundles

There are two different ways to simulate a tube bundle region. The first way is to approximate the boundary in some stepwise fashion, referred to as "aliasing". Figure 4.4 shows a diagram of two possible aliasing situations. The shaded squares indicate control volumes at least partially filled with tubes and the blank squares indicate tube-free control volumes. If the tube bundle boundary crosses the Cartesian control volumes exactly along line "A" in Figure 4.4, then half of the volume in control volumes marked "1", "3" and "5" is outside the tube bundle and half of it is inside. In this case $\gamma = 0.5$ in those three control volumes. In control volumes marked "2" and "4", $\gamma = 1$. The porosity, ε, in these control volumes is set using γ and Equation (2.5).

If the tube bundle boundary crosses the Cartesian control volumes exactly along line "B" in Figure 4.4, then 87.5% of each of the control volumes marked "1", "3" and "5" is outside the tube bundle and 12.5% is inside. Therefore, $\gamma = 0.125$ for those control volumes. Line "B" also goes through control volumes "2" and "4" which have $\gamma = 0.875$. See Section 2.2 for more details of the porosity calculation.

The second way to match the tube bundle region boundary is to use a non-orthogonal grid

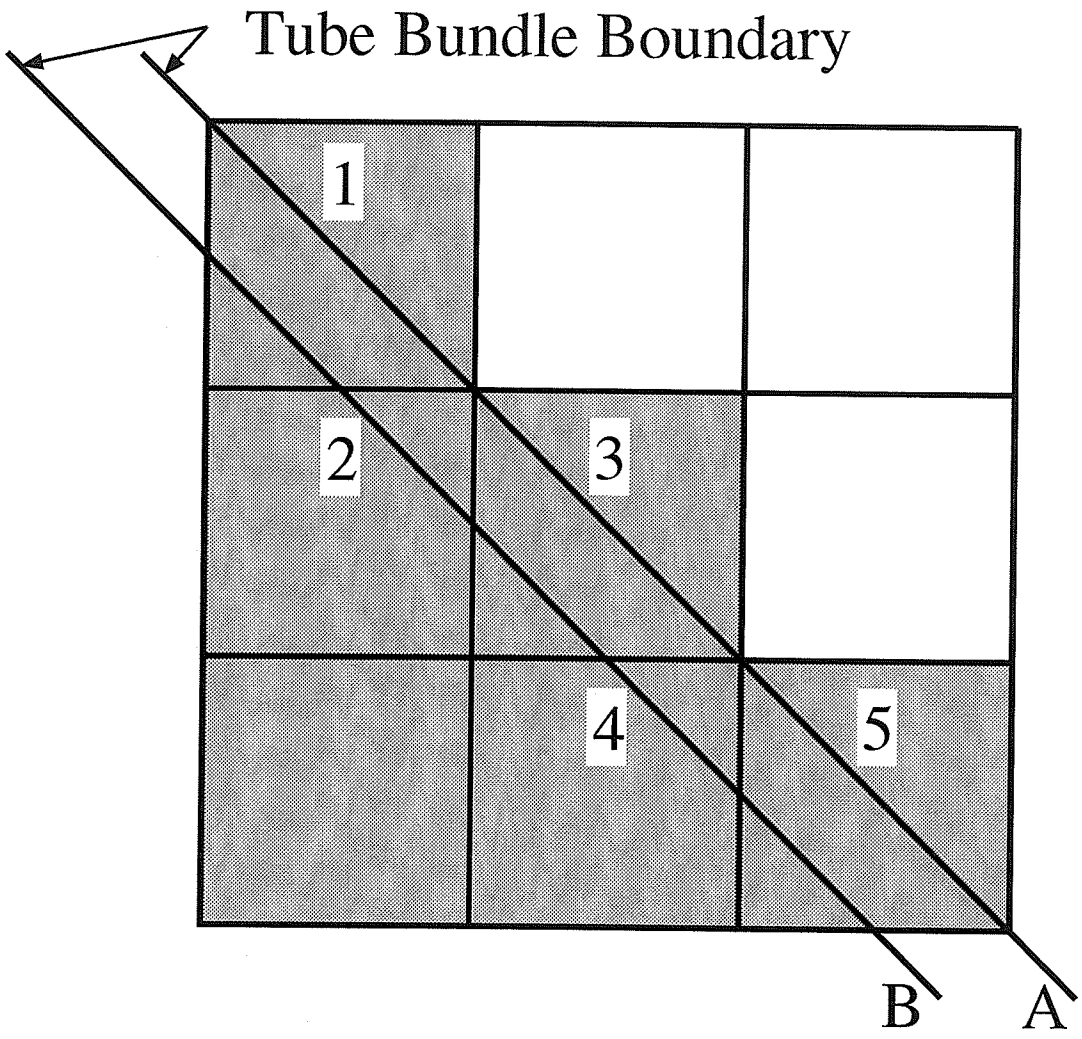

Figure 4.4: Diagram of Aliasing Procedure.

so that a control volume face lies exactly on the defined boundary. This method minimizes the aliasing required and smaller tube bundle detail can be simulated. More time and effort is involved in developing the complex grid, but less time is needed to assign porosities to individual control volumes depending on where they lie with respect to the defined tube bundle boundary.

4.9.2 Flow Blockages

The concept of flow blockages used in this study is one that uses the grid itself to represent the geometry of the actual blockage. To obtain the correct behavior, coefficients in or next to a blockage control volume, are adjusted in four ways. First, to satisfy the continuity equation, the face velocities on the blockage boundaries are set to zero so that no flow can enter or leave a blockage. Second, to prevent the momentum equation from allowing convection across a blockage, the convection coefficients defined in Equation (5.44) are set to zero as follows. The east face coefficients in the control volume just to the west of the blockage are set to zero just like an ordinary east boundary. The north face coefficients in the control volume just to the south of the blockage are set analogously. Thirdly, all convection coefficients are set to zero inside a blockage so that no convection can take place within a blocked region.

To illustrate, if the blockage goes from $i = IA$ to IZ and from $j = JA$ to JZ, then each convection coefficient should be set as follows:

$$\left.\begin{array}{lll} C_{Ue_{(IA-1\Rightarrow IZ,\ JA\Rightarrow JZ)}} = 0 & & C_{Ve_{(IA-1\Rightarrow IZ,\ JA\Rightarrow JZ)}} = 0 \\ C_{Un_{(IA\Rightarrow IZ,\ JA-1\Rightarrow JZ)}} = 0 & & C_{Vn_{(IA\Rightarrow IZ,\ JA-1\Rightarrow JZ)}} = 0 \\ C_{U_{(IA\Rightarrow IZ,\ JA\Rightarrow JZ)}} = 0 & & C_{V_{(IA\Rightarrow IZ,\ JA\Rightarrow JZ)}} = 0 \end{array}\right\} \quad (4.137)$$

Finally, the approximation of gradient terms in the momentum equations must be corrected to account for the zero velocity at the face of the blockage. This correction was done

through the diffusion coefficient by setting the viscosity very high to indicate a solid. Regular boundaries have zero-width control volumes whereas control volumes around blockages are not zero-width.

The diffusion coefficient, as defined in Equation (4.22), has the inter-nodal distance in the denominator and viscosity in the numerator. Therefore, when using a uniform grid beside a zero-width control volume, for example, the diffusion coefficient would be set to double its normal value because the distance between the node in the boundary and the nearest interior node is half the regular distance. This doubling in the diffusion coefficient indicates the presence of a solid wall. However, around a blockage there are no zero-width control volumes, so one must either go around each blockage and change the inter-nodal distance variables used in the diffusion coefficient to make them like a zero-width boundary, or use the inherent characteristic of the harmonic mean to set the diffusion coefficient as normal, only with a very high viscosity in the blocked control volumes. Continuing with the example of a uniform grid, the harmonic mean of the artificially large blockage "viscosity" and the fluid viscosity produce double the viscosity of the fluid control volume so the diffusion coefficient would be doubled just like a boundary control volume. Since the harmonic mean is used already to set the diffusion coefficient the additional work of adjusting the inter-nodal distances is eliminated.

The procedure above sets the diffusion coefficient to the same value beside a blockage and at a regular wall boundary. This result ensures that the momentum equations "see" zero velocity at a solid wall in either case.

The tube bundles and blockages are easily handled by defining their location in control volumes and modifying the coefficients.

Chapter 5

The Numerical Solution Procedure

Finite Volume methods described by Patankar [26] are widely used for fluid flow problems. The solution procedure for primitive variables on a staggered grid is well established. The resulting five-point scheme is an efficient and robust solution method. For non-orthogonal grids, however, the cross-derivative terms become important so a nine-point computational molecule is needed. In addition, a co-located variable arrangement has many advantages when using non-orthogonal grids. All the variables, U, V, P, and T, are at one node and the grid has the flexibility to match boundaries and internal structures. Multi-grid acceleration is also easier to use for co-located storage compared to staggered grid storage. The details of the solution of the coupled set of algebraic equations is given in this chapter. Special algorithms that deal with coupling between the pressure and velocity fields are discussed.

5.1 Solvers for the Linearized Equation

5.1.1 Five-Point Solver

The five-point algebraic equation can be solved using an Alternating-Direction Implicit method (ADI) first described by Peaceman and Rachford [29] (also called Line Gauss-Seidel (LGS)). The five-point solver was used in this work for orthogonal problems only.

5.1.2 Nine-Point Solver

An iterative solver developed by Perić [31] (LR version) was implemented in this work to solve nine-point algebraic equations. The nine-point method has a larger computational molecule and larger storage requirements than the five-point method, but it is more stable when solving problems on non-orthogonal grids with large aspect ratio changes and skewing.

5.2 Pressure-Velocity Coupling

5.2.1 Introduction

A commonly-used method for accounting for the pressure-velocity coupling is the Semi-Implicit Method for Pressure-Linked Equation (SIMPLE) algorithm by Patankar and Spalding [27], often on a staggered grid. Van Doormaal and Raithby [43] developed the SIMPLE-Consistent (SIMPLEC) algorithm which is more robust and efficient. The principle of the SIMPLE or SIMPLEC algorithm is that guessed velocities are solved using momentum conservation and then pressure-correction equation (based on continuity) is used to correct the velocities in order to conserve mass.

Co-located, non-staggered, grids are becoming more commonly used, and have advantages for non-orthogonal grids but a special scheme must be used to avoid the decoupling of

the pressure fields [26], (the so-called checkerboard pressure effect). Perić [33] compared the staggered and non-staggered grid approaches and found that the co-located method converges faster in some cases, and has advantages when using non-orthogonal grids. In this work pressure-velocity coupling is accomplished for co-located variable storage using an algorithm referred to as the Pressure Weighted Interpolation Method (PWIM) [22].

5.2.2 Pressure Weighted Interpolation Method

Miller and Schmidt [23] modified a momentum interpolation scheme first described by Rhie and Chow [38] to remove dependence on relaxation factors. The PWIM is also known as the momentum interpolation method described by Seok et al. [40] because the momentum equations are interpolated to find a face velocity. The cell face velocities are also Cartesian and are stored for both the east and north face of every control volume. The cell face velocities must conserve mass through the continuity equation and nodal velocities must conserve momentum. Therefore, it is possible that the face and nodal velocities can converge to different values. Seok et al. [40], Majumdar [22], and Miller and Schmidt [23], found that physically unrealistic solutions may occur in regions of rapidly changing pressure gradients. In this work, rapidly changing pressure gradients were found near the interface between the tube bundle and free-fluid regions. The effects that are seen in the flow, because of the PWIM, are discussed later in Section 6.3.2. This work has implemented the PWIM as described by Miller and Schmidt [23], Stubley [41] and Raithby [34].

Contrary to a staggered grid, the co-located approach stores velocities and pressures at the same location. Special approximations for face velocities and pressure gradients are needed. On the staggered grid, face velocities come from EDS between nodes, but using the co-located grid they come from averaging the local algebraic momentum equations. On a staggered grid, the pressure gradient is just the difference between nodal pressures, while on a co-located grid, three pressure gradients are used as described in detail below.

The derivation begins by writing the complete nodal, five-point or nine-point, equation (for the nine-point equation the $\widetilde{b^u} = 0$) for the present control volume, as follows:

$$A_P^u U_P = \sum_P A_{NB}^u U_{NB} + \left(\frac{M_P^o}{\Delta t}\right) U_P^o - \overline{\forall_P} \left.\frac{\partial P}{\partial x}\right|_P + Q_P^u + \widetilde{b_P^u} \tag{5.1}$$

and for the east control volume:

$$A_{PE}^u U_E = \sum_E A_{NB}^u U_{NB} + \left(\frac{M_E^o}{\Delta t}\right) U_E^o - \overline{\forall_E} \left.\frac{\partial P}{\partial x}\right|_E + Q_E^u + \widetilde{b_E^u} \tag{5.2}$$

Now, consider a control volume centered at the east face of a control volume:

$$A_{Pe}^u U_e = \sum_e A_{nb}^u U_{nb} + \left(\frac{M_e^o}{\Delta t}\right) U_e^o - \overline{\forall_e} \left.\frac{\partial P}{\partial x}\right|_e + Q_e^u + \widetilde{b_e^u} \tag{5.3}$$

Dividing Equation (5.1) by A_P^u produces:

$$U_P = \frac{\sum_P A_{NB}^u U_{NB} + Q_P^u}{A_P^u} + \left(\frac{M_P^o}{\Delta t}\right) \frac{U_P^o}{A_P^u} - \frac{\overline{\forall_P}}{A_P^u} \left.\frac{\partial P}{\partial x}\right|_P + \frac{\widetilde{b_P^u}}{A_P^u} \tag{5.4}$$

Dividing Equation (5.2) by A_{PE}^u produces:

$$U_E = \frac{\sum_E A_{NB}^u U_{NB} + Q_E^u}{A_{PE}^u} + \left(\frac{M_E^o}{\Delta t}\right) \frac{U_E^o}{A_{PE}^u} - \frac{\overline{\forall_E}}{A_{PE}^u} \left.\frac{\partial P}{\partial x}\right|_E + \frac{\widetilde{b_E^u}}{A_{PE}^u} \tag{5.5}$$

Dividing Equation (5.3) by A_{Pe}^u produces:

$$U_e = \underbrace{\frac{\sum_e A_{nb}^u U_{nb} + Q_e^u}{A_{Pe}^u}}_{\widetilde{U_e}} + \left(\frac{M_e^o}{\Delta t}\right) \frac{U_e^o}{A_{Pe}^u} - \frac{\overline{\forall_e}}{A_{Pe}^u} \left.\frac{\partial P}{\partial x}\right|_e + \frac{\widetilde{b_e^u}}{A_{Pe}^u} \tag{5.6}$$

The $\widetilde{U_e}$ portion of Equation (5.6) is assumed to be a linear interpolation of similar portions of Equation (5.4) and Equation (5.5) as follows:

$$\widetilde{U_e} = f_e \widetilde{U_P} + (1 - f_e) \widetilde{U_E} \tag{5.7}$$

where

$$f_e = \frac{(ds)_e^+}{(ds)_e} \tag{5.8}$$

$$\widetilde{U_P} = U_P - \left(\frac{M_P^o}{\Delta t}\right)\frac{U_P^o}{A_P^u} + \frac{\overline{\forall_P}}{A_P^u}\left.\frac{\partial P}{\partial x}\right|_P - \frac{\widetilde{b_P^u}}{A_P^u} \tag{5.9}$$

$$\widetilde{U_E} = U_E - \left(\frac{M_E^o}{\Delta t}\right)\frac{U_E^o}{A_{PE}^u} + \frac{\overline{\forall_E}}{A_{PE}^u}\left.\frac{\partial P}{\partial x}\right|_E - \frac{\widetilde{b_E^u}}{A_{PE}^u} \tag{5.10}$$

For distorted transient, the E-factor definition (Equation (4.134)) is substituted in place of the transient term. For example, $\widetilde{U_P}$, is then:

$$\widetilde{U_P} = U_P - \left(\frac{A_P^{u^*} - R_P^u}{E^u}\right)\frac{U_P^o}{A_P^u} + \frac{\overline{\forall_P}}{A_P^u}\left.\frac{\partial P}{\partial x}\right|_P - \frac{\widetilde{b_P^u}}{A_P^u} \tag{5.11}$$

Since the definition of A_P^u is similar to the term in parentheses in Equation (5.11), the combination of the terms can be simplified and the following term reduces to:

$$\left(\frac{A_P^{u^*} - R_P^u}{E^u}\right)\frac{1}{A_P^u} = \left(\frac{A_P^{u^*} - R_P^u}{E^u}\right)\frac{1}{(A_P^{u^*} - R_P^u)\left(1 + \frac{1}{E^u}\right)}$$
$$= \frac{\left(A_P^{u^*} - R_P^u\right)}{(A_P^{u^*} - R_P^u)}\frac{\frac{1}{E^u}}{\left(1 + \frac{1}{E^u}\right)} = \frac{1}{E^u + 1} \tag{5.12}$$

The result (Equation (5.12)) is that when using the distorted transient method, the transient part of the equation is the same for the center node , east node, or east face equations for U.

To aid in the derivation of the true transient form of the equation, a simplifying assumption is made. The transient term is now assumed to tend toward the same value whether it is for the center or east control volume, as follows:

$$\left.\begin{aligned}\left(\frac{M_P^o}{\Delta t}\right)\frac{1}{A_P^u} &\rightarrow \left(\frac{M_e^o}{\Delta t}\right)\frac{1}{A_{Pe}^u} \\ \left(\frac{M_E^o}{\Delta t}\right)\frac{1}{A_{PE}^u} &\rightarrow \left(\frac{M_e^o}{\Delta t}\right)\frac{1}{A_{Pe}^u}\end{aligned}\right\} \tag{5.13}$$

In general, since $\widetilde{U_e}$ is the linear interpolation of center and east values (given by Equation (5.7)):

$$\left(\frac{M_e^o}{\Delta t}\right)\frac{1}{A_{Pe}^u} = f_e\left(\frac{M_P^o}{\Delta t}\right)\frac{1}{A_P^u} + (1.0 - f_e)\left(\frac{M_E^o}{\Delta t}\right)\frac{1}{A_{PE}^u} \tag{5.14}$$

Substituting Equations (5.9) and (5.10) into Equation (5.7) produces:

$$\begin{aligned}\widetilde{U_e} = {} & f_e\, U_P + (1.0 - f_e)\, U_E - f_e\left(\frac{M_P^o}{\Delta t}\right)\frac{U_P^o}{A_P^u} - (1.0 - f_e)\left(\frac{M_E^o}{\Delta t}\right)\frac{U_E^o}{A_{PE}^u} \\ & + f_e\,\frac{\overline{\nabla_P}}{A_P^u}\left.\frac{\partial P}{\partial x}\right|_P + (1.0 - f_e)\,\frac{\overline{\nabla_E}}{A_{PE}^u}\left.\frac{\partial P}{\partial x}\right|_E - f_e\,\frac{\widetilde{b_P^u}}{A_P^u} - (1.0 - f_e)\,\frac{\widetilde{b_E^u}}{A_{PE}^u}\end{aligned} \tag{5.15}$$

Now, apply the simplifying assumptions given in Equations (5.13) and (5.14) to Equation (5.15) to obtain:

$$\begin{aligned}\widetilde{U_e} = {} & f_e\, U_P + (1.0 - f_e)\, U_E + \left(\frac{M_e^o}{\Delta t}\right)\frac{1}{A_{Pe}^u}\left[- f_e\, U_P^o - (1.0 - f_e)\, U_E^o\right] \\ & + f_e\,\frac{\overline{\nabla_P}}{A_P^u}\left.\frac{\partial P}{\partial x}\right|_P + (1.0 - f_e)\,\frac{\overline{\nabla_E}}{A_{PE}^u}\left.\frac{\partial P}{\partial x}\right|_E - f_e\,\frac{\widetilde{b_P^u}}{A_P^u} - (1.0 - f_e)\,\frac{\widetilde{b_E^u}}{A_{PE}^u}\end{aligned} \tag{5.16}$$

Substituting Equation (5.16) into Equation (5.6) produces:

$$\begin{aligned}U_e = {} & f_e\, U_P + (1.0 - f_e)\, U_E + \left(\frac{M_e^o}{\Delta t}\right)\frac{1}{A_{Pe}^u}\left[U_e^o - f_e\, U_P^o - (1.0 - f_e)\, U_E^o\right] \\ & - \frac{\overline{\nabla_e}}{A_{Pe}^u}\left.\frac{\partial P}{\partial x}\right|_e + f_e\,\frac{\overline{\nabla_P}}{A_P^u}\left.\frac{\partial P}{\partial x}\right|_P + (1.0 - f_e)\,\frac{\overline{\nabla_E}}{A_{PE}^u}\left.\frac{\partial P}{\partial x}\right|_E \\ & + \frac{\widetilde{b_e^u}}{A_{Pe}^u} - f_e\,\frac{\widetilde{b_P^u}}{A_P^u} - (1.0 - f_e)\,\frac{\widetilde{b_E^u}}{A_{PE}^u}\end{aligned} \tag{5.17}$$

By analogy the V velocity at the east face is:

$$\begin{aligned}V_e = {} & f_e\, V_P + (1.0 - f_e)\, V_E + \left(\frac{M_e^o}{\Delta t}\right)\frac{1}{A_{Pe}^v}\left[V_e^o - f_e\, V_P^o - (1.0 - f_e)\, V_E^o\right] \\ & - \frac{\overline{\nabla_e}}{A_{Pe}^v}\left.\frac{\partial P}{\partial y}\right|_e + f_e\,\frac{\overline{\nabla_P}}{A_P^v}\left.\frac{\partial P}{\partial y}\right|_P + (1.0 - f_e)\,\frac{\overline{\nabla_E}}{A_{PE}^v}\left.\frac{\partial P}{\partial y}\right|_E \\ & + \frac{\widetilde{b_e^v}}{A_{Pe}^v} - f_e\,\frac{\widetilde{b_P^v}}{A_P^v} - (1.0 - f_e)\,\frac{\widetilde{b_E^v}}{A_{PE}^v}\end{aligned} \tag{5.18}$$

the U velocity at the north face is:

$$U_n = f_n\, U_P + (1.0 - f_n)\, U_N + \left(\frac{M_n^o}{\Delta t}\right) \frac{1}{A_{Pn}^u} \left[U_n^o - f_n\, U_P^o - (1.0 - f_n)\, U_N^o\right] - \frac{\overline{\nabla}_n}{A_{Pn}^u} \left.\frac{\partial P}{\partial x}\right|_n + f_n \frac{\overline{\nabla}_P}{A_P^u} \left.\frac{\partial P}{\partial x}\right|_P + (1.0 - f_n) \frac{\overline{\nabla}_N}{A_{PN}^u} \left.\frac{\partial P}{\partial x}\right|_N + \frac{\widetilde{b_n^u}}{A_{Pn}^u} - f_n \frac{\widetilde{b_P^u}}{A_P^u} - (1.0 - f_n) \frac{\widetilde{b_N^u}}{A_{PN}^u} \quad (5.19)$$

and the V velocity at the north face is:

$$V_n = f_n\, V_P + (1.0 - f_n)\, V_N + \left(\frac{M_n^o}{\Delta t}\right) \frac{1}{A_{Pn}^v} \left[V_n^o - f_n\, V_P^o - (1.0 - f_n)\, V_N^o\right] - \frac{\overline{\nabla}_n}{A_{Pn}^v} \left.\frac{\partial P}{\partial y}\right|_n + f_n \frac{\overline{\nabla}_P}{A_P^v} \left.\frac{\partial P}{\partial y}\right|_P + (1.0 - f_n) \frac{\overline{\nabla}_N}{A_{PN}^v} \left.\frac{\partial P}{\partial y}\right|_N + \frac{\widetilde{b_n^v}}{A_{Pn}^v} - f_n \frac{\widetilde{b_P^v}}{A_P^v} - (1.0 - f_n) \frac{\widetilde{b_N^u}}{A_{PN}^v} \quad (5.20)$$

5.2.3 Velocity Corrections

The solution to the momentum equations will not necessarily produce a mass-conserving velocity field (until convergence) because the U and V momentum equations do not enforce continuity. A correction to the velocity solution that is governed by the continuity equation is needed. A "starred" value of velocity indicates the guessed value for the solution for the momentum equations, and the "prime" value indicates the correction added to produce a mass conserving field as follows:

$$U = U^\star + U' \quad (5.21)$$

The correction value is then:

$$U' = U - U^\star \quad (5.22)$$

To derive the velocity correction equation, Equation (5.4) is divided by A_P^u. The desired U velocity for the P control volume is then:

$$U_P = \frac{\sum_P A_{NB}^u U_{NB} + Q_P^u}{A_P^u} + \left(\frac{M_P^o}{\Delta t}\right)\frac{U_P^o}{A_P^u} - \frac{\overline{\forall_P}}{A_P^u}\left.\frac{\partial P}{\partial x}\right|_P + \frac{\widetilde{b^u}}{A_P^u} \tag{5.23}$$

By analogy the guessed U velocity for the the P control volume is:

$$U_P^\star = \frac{\sum_P A_{NB}^u U_{NB}^\star + Q_P^u}{A_P^u} + \left(\frac{M_P^o}{\Delta t}\right)\frac{U_P^o}{A_P^u} - \frac{\overline{\forall_P}}{A_P^u}\left.\frac{\partial P^\star}{\partial x}\right|_P + \frac{\widetilde{b^{u^\star}}}{A_P^u} \tag{5.24}$$

Subtracting the guessed velocity equation from the desired velocity produces the velocity correction:

$$U_P' = \frac{\sum_P A_{NB}^u U_{NB}'}{A_P^u} - \frac{\overline{\forall_P}}{A_P^u}\left.\frac{\partial P'}{\partial x}\right|_P + \frac{\widetilde{b^{u'}}}{A_P^u} \tag{5.25}$$

The cross derivative terms are lumped in the source term, $\widetilde{b^u}$, for the five-point equation, or integrated into the active nodal coefficients so that $\widetilde{b^u} = 0$, for the nine-point equation. Those terms do not contribute much to the mass imbalance and when the grid is orthogonal, all cross derivatives are zero. Neglecting the $\widetilde{b^u}$ contribution to the correction (an approximation only for the five-point equation) produces the simplified nodal velocity correction equation:

$$U_P' = \frac{\sum_P A_{NB}^u U_{NB}'}{A_P^u} - \frac{\overline{\forall_P}}{A_P^u}\left.\frac{\partial P'}{\partial x}\right|_P \tag{5.26}$$

By analogy the east face U velocity, Equation (5.17), is corrected by the following:

$$U_e' = f_e\, U_P' + (1.0 - f_e)\, U_E' - \frac{\overline{\forall_e}}{A_{Pe}^u}\left.\frac{\partial P'}{\partial x}\right|_e + f_e\,\frac{\overline{\forall_P}}{A_P^u}\left.\frac{\partial P'}{\partial x}\right|_P + (1.0 - f_e)\,\frac{\overline{\forall_E}}{A_{PE}^u}\left.\frac{\partial P'}{\partial x}\right|_E \tag{5.27}$$

Now, substituting the simplified velocity correction equations into Equation (5.27) produces:

$$\begin{aligned} U_e' = f_e & \left[\frac{\sum_P A_{NB}^u U_{NB}'}{A_P^u} - \frac{\overline{\forall_P}}{A_P^u}\left.\frac{\partial P'}{\partial x}\right|_P\right] + (1.0 - f_e)\left[\frac{\sum_E A_{NB}^u U_{NB}'}{A_{PE}^u} - \frac{\overline{\forall_E}}{A_{PE}^u}\left.\frac{\partial P'}{\partial x}\right|_E\right] \\ & - \frac{\overline{\forall_e}}{A_{Pe}^u}\left.\frac{\partial P'}{\partial x}\right|_e + f_e\,\frac{\overline{\forall_P}}{A_P^u}\left.\frac{\partial P'}{\partial x}\right|_P + (1.0 - f_e)\,\frac{\overline{\forall_E}}{A_{PE}^u}\left.\frac{\partial P'}{\partial x}\right|_E \end{aligned} \tag{5.28}$$

Finally, using:

$$\frac{\sum_e A^u_{nb} U'_{nb}}{A^u_{Pe}} = f_e \left[\frac{\sum_P A^u_{NB} U'_{NB}}{A^u_P} \right] + (1.0 - f_e) \left[\frac{\sum_E A^u_{NB} U'_{NB}}{A^u_{PE}} \right] \tag{5.29}$$

and canceling the repeated pressure gradient terms produces:

$$U'_e = \frac{\sum_e A^u_{nb} U'_{nb}}{A^u_{Pe}} - \frac{\overline{\forall_e}}{A^u_{Pe}} \left. \frac{\partial P'}{\partial x} \right|_e \tag{5.30}$$

By analogy the V velocity correction is:

$$V'_P = \frac{\sum_P A^v_{NB} V'_{NB}}{A^v_P} - \frac{\overline{\forall_P}}{A^v_P} \left. \frac{\partial P'}{\partial y} \right|_P \tag{5.31}$$

and the east face V velocity correction is:

$$V'_e = \frac{\sum_e A^v_{nb} V'_{nb}}{A^v_{Pe}} - \frac{\overline{\forall_e}}{A^v_{Pe}} \left. \frac{\partial P'}{\partial y} \right|_e \tag{5.32}$$

The north face U and V velocities are corrected in a manner analogous to Equations (5.30) and (5.32).

5.2.4 SIMPLEC

Starting with the U nodal velocity correction, Equation (5.26) in the form:

$$A^u_P U'_P = \sum_P A^u_{NB} U'_{NB} - \overline{\forall_P} \left. \frac{\partial P'}{\partial x} \right|_P \tag{5.33}$$

The term $\sum_P A^u_{NB} U'_P$ is subtracted from both sides of Equation (5.33)

$$\left(A^u_P - \sum_P A^u_{NB} \right) U'_P = \sum_P A^u_{NB} \left(U'_{NB} - U'_P \right) - \overline{\forall_P} \left. \frac{\partial P'}{\partial x} \right|_P \tag{5.34}$$

The SIMPLEC assumption is to neglect the first term on the right side of Equation (5.34). This assumption leads to:

$$U'_P = - \frac{\overline{\forall_P}}{\left(A^u_P - \sum_P A^u_{NB} \right)} \left. \frac{\partial P'}{\partial x} \right|_P \tag{5.35}$$

By analogy to Equation (5.35) the V velocity correction is:

$$V'_P = - \frac{\overline{\forall_P}}{\left(A^v_P - \sum_P A^v_{NB}\right)} \left.\frac{\partial P'}{\partial y}\right|_P \tag{5.36}$$

The east face U velocity correction follows from Equation (5.30):

$$U'_e = - \frac{\overline{\forall_e}}{\left(A^u_{Pe} - \sum_e A^u_{nb}\right)} \left.\frac{\partial P'}{\partial x}\right|_e \tag{5.37}$$

The east face V velocity correction follows from Equation (5.32):

$$V'_e = - \frac{\overline{\forall_e}}{\left(A^v_{Pe} - \sum_e A^v_{nb}\right)} \left.\frac{\partial P'}{\partial y}\right|_e \tag{5.38}$$

The north face U and V velocities are corrected in a manner analogous to the east face U and V velocity corrections given by Equations (5.37) and (5.38). The approximate equations for the face velocity corrections just derived are now used in the continuity equation to derive the pressure correction equation.

5.2.5 Formulation of the P′ Equation

As mentioned earlier, there are three equations, (continuity, U momentum, and V momentum), and three unknowns, (U velocity, V velocity, and pressure). Pressure only appears in the U and V momentum equations which are already used to find U and V velocity. Therefore, we must use continuity (Equation (4.6)) to find the pressure. The pressure field is determined by first guessing a pressure field, then correcting it in a manner analogous to Equation (5.21). The first step in deriving the pressure correction (P') equation is to substitute Equation (5.21) (and the analogous equation for V) into the continuity equation:

$$\begin{aligned}&\left[A^c_{u_e}(U^\star_e + U'_e) + A^c_{v_e}(V^\star_e + V'_e)\right] + \left[A^c_{u_w}(U^\star_w + U'_w) + A^c_{v_w}(V^\star_w + V'_w)\right] \\ &\quad + \left[A^c_{u_n}(U^\star_n + U'_n) + A^c_{v_n}(V^\star_n + V'_n)\right] + \left[A^c_{u_s}(U^\star_s + U'_s) + A^c_{v_s}(V^\star_s + V'_s)\right] + b^c_P = 0\end{aligned} \tag{5.39}$$

Gathering the terms produces:

$$-\left[(A^c_{u_e}U'_e + A^c_{v_e}V'_e) + (A^c_{u_w}U'_w + A^c_{v_w}V'_w) + (A^c_{u_n}U'_n + A^c_{v_n}V'_n) + (A^c_{u_s}U'_s + A^c_{v_s}V'_s)\right]$$
$$= (A^c_{u_e}U^\star_e + A^c_{v_e}V^\star_e) + (A^c_{u_w}U^\star_w + A^c_{v_w}V^\star_w)$$
$$+ (A^c_{u_n}U^\star_n + A^c_{v_n}V^\star_n) + (A^c_{u_s}U^\star_s + A^c_{v_s}V^\star_s) + b^c_P = \Delta m \quad (5.40)$$

Substituting the face velocity correction equations (Equations (5.37) and (5.38) and the analogous equations for U' and V' for the other faces) produces:

$$\Delta m = -\left[A^c_{u_e}\left\{\frac{-\overline{\forall_e}}{\left(A^u_{Pe} - \sum_e A^u_{nb}\right)}\left.\frac{\partial P'}{\partial x}\right|_e\right\} + A^c_{v_e}\left\{\frac{-\overline{\forall_e}}{\left(A^v_{Pe} - \sum_e A^v_{nb}\right)}\left.\frac{\partial P'}{\partial y}\right|_e\right\}\right.$$
$$+ A^c_{u_w}\left\{\frac{-\overline{\forall_w}}{\left(A^u_{Pw} - \sum_w A^u_{nb}\right)}\left.\frac{\partial P'}{\partial x}\right|_w\right\} + A^c_{v_w}\left\{\frac{-\overline{\forall_w}}{\left(A^v_{Pw} - \sum_w A^v_{nb}\right)}\left.\frac{\partial P'}{\partial y}\right|_w\right\}$$
$$+ A^c_{u_n}\left\{\frac{-\overline{\forall_n}}{\left(A^u_{Pn} - \sum_n A^u_{nb}\right)}\left.\frac{\partial P'}{\partial x}\right|_n\right\} + A^c_{v_n}\left\{\frac{-\overline{\forall_n}}{\left(A^v_{Pn} - \sum_n A^v_{nb}\right)}\left.\frac{\partial P'}{\partial y}\right|_n\right\}$$
$$\left. + A^c_{u_s}\left\{\frac{-\overline{\forall_s}}{\left(A^u_{Ps} - \sum_s A^u_{nb}\right)}\left.\frac{\partial P'}{\partial x}\right|_s\right\} + A^c_{v_s}\left\{\frac{-\overline{\forall_s}}{\left(A^v_{Ps} - \sum_s A^v_{nb}\right)}\left.\frac{\partial P'}{\partial y}\right|_s\right\}\right] \quad (5.41)$$

Now substitute the pressure gradient approximations, that are analogous to Equations (4.97), (4.98), (4.100), and (4.101), into Equation (5.41) to get:

$$\begin{aligned}
\Delta m = -\Bigg[& A^c_{u_e}\left\{\frac{-\overline{V_e}}{\left(A^u_{Pe}-\sum_e A^u_{nb}\right)}\,\frac{\left.\frac{\partial P'}{\partial s}\right|_e t_{ye}-\left.\frac{\partial P'}{\partial t}\right|_e s_{ye}}{s_{xe}t_{ye}-t_{xe}s_{ye}}\right\} \\
& + A^c_{v_e}\left\{\frac{-\overline{V_e}}{\left(A^v_{Pe}-\sum_e A^v_{nb}\right)}\,\frac{\left.\frac{\partial P'}{\partial t}\right|_e s_{xe}-\left.\frac{\partial P'}{\partial s}\right|_e t_{xe}}{s_{xe}t_{ye}-t_{xe}s_{ye}}\right\} \\
& + A^c_{u_w}\left\{\frac{-\overline{V_w}}{\left(A^u_{Pw}-\sum_w A^u_{nb}\right)}\,\frac{\left.\frac{\partial P'}{\partial s}\right|_w t_{yw}-\left.\frac{\partial P'}{\partial t}\right|_w s_{yw}}{s_{xw}t_{yw}-t_{xw}s_{yw}}\right\} \\
& + A^c_{v_w}\left\{\frac{-\overline{V_w}}{\left(A^v_{Pw}-\sum_w A^v_{nb}\right)}\,\frac{\left.\frac{\partial P'}{\partial t}\right|_w s_{xw}-\left.\frac{\partial P'}{\partial s}\right|_w t_{xw}}{s_{xw}t_{yw}-t_{xw}s_{yw}}\right\} \\
& + A^c_{u_n}\left\{\frac{-\overline{V_n}}{\left(A^u_{Pn}-\sum_n A^u_{nb}\right)}\,\frac{\left.\frac{\partial P'}{\partial s}\right|_n t_{yn}-\left.\frac{\partial P'}{\partial t}\right|_n s_{yn}}{s_{xn}t_{yn}-t_{xn}s_{yn}}\right\} \\
& + A^c_{v_n}\left\{\frac{-\overline{V_n}}{\left(A^v_{Pn}-\sum_n A^v_{nb}\right)}\,\frac{\left.\frac{\partial P'}{\partial t}\right|_n s_{xn}-\left.\frac{\partial P'}{\partial s}\right|_n t_{xn}}{s_{xn}t_{yn}-t_{xn}s_{yn}}\right\} \\
& + A^c_{u_s}\left\{\frac{-\overline{V_s}}{\left(A^u_{Ps}-\sum_s A^u_{nb}\right)}\,\frac{\left.\frac{\partial P'}{\partial s}\right|_s t_{ys}-\left.\frac{\partial P'}{\partial t}\right|_s s_{ys}}{s_{xs}t_{ys}-t_{xs}s_{ys}}\right\} \\
& + A^c_{v_s}\left\{\frac{-\overline{V_s}}{\left(A^v_{Ps}-\sum_s A^v_{nb}\right)}\,\frac{\left.\frac{\partial P'}{\partial t}\right|_s s_{xs}-\left.\frac{\partial P'}{\partial s}\right|_s t_{xs}}{s_{xs}t_{ys}-t_{xs}s_{ys}}\right\}\Bigg] \qquad (5.42)
\end{aligned}$$

Evaluating the pressure gradients in terms of nodal and corner P' values produces:

$$\Delta m = -\Bigg[A^c_{u_e} \left\{ \frac{-\overline{V_e}}{\left(A^u_{Pe} - \sum_e A^u_{nb}\right)} \frac{\frac{P'_E - P'_P}{(ds)_e} t_{ye} - \frac{P'_{ne} - P'_{se}}{(dt)_e} s_{ye}}{s_{xe}t_{ye} - t_{xe}s_{ye}} \right\}$$
$$+ A^c_{v_e} \left\{ \frac{-\overline{V_e}}{\left(A^v_{Pe} - \sum_e A^v_{nb}\right)} \frac{\frac{P'_{ne} - P'_{se}}{(dt)_e} s_{xe} - \frac{P'_E - P'_P}{(ds)_e} t_{xe}}{s_{xe}t_{ye} - t_{xe}s_{ye}} \right\}$$
$$+ A^c_{u_w} \left\{ \frac{-\overline{V_w}}{\left(A^u_{Pw} - \sum_w A^u_{nb}\right)} \frac{\frac{P'_P - P'_W}{(ds)_w} t_{yw} - \frac{P'_{nw} - P'_{sw}}{(dt)_w} s_{yw}}{s_{xw}t_{yw} - t_{xw}s_{yw}} \right\}$$
$$+ A^c_{v_w} \left\{ \frac{-\overline{V_w}}{\left(A^v_{Pw} - \sum_w A^v_{nb}\right)} \frac{\frac{P'_{nw} - P'_{sw}}{(dt)_w} s_{xw} - \frac{P'_P - P'_W}{(ds)_w} t_{xw}}{s_{xw}t_{yw} - t_{xw}s_{yw}} \right\}$$
$$+ A^c_{u_n} \left\{ \frac{-\overline{V_n}}{\left(A^u_{Pn} - \sum_n A^u_{nb}\right)} \frac{\frac{P'_{ne} - P'_{nw}}{(ds)_n} t_{yn} - \frac{P'_N - P'_P}{(dt)_n} s_{yn}}{s_{xn}t_{yn} - t_{xn}s_{yn}} \right\}$$
$$+ A^c_{v_n} \left\{ \frac{-\overline{V_n}}{\left(A^v_{Pn} - \sum_n A^v_{nb}\right)} \frac{\frac{P'_N - P'_P}{(dt)_n} s_{xn} - \frac{P'_{ne} - P'_{nw}}{(ds)_n} t_{xn}}{s_{xn}t_{yn} - t_{xn}s_{yn}} \right\}$$
$$+ A^c_{u_s} \left\{ \frac{-\overline{V_s}}{\left(A^u_{Ps} - \sum_s A^u_{nb}\right)} \frac{\frac{P'_{se} - P'_{sw}}{(ds)_s} t_{ys} - \frac{P'_P - P'_S}{(dt)_s} s_{ys}}{s_{xs}t_{ys} - t_{xs}s_{ys}} \right\}$$
$$+ A^c_{v_s} \left\{ \frac{-\overline{V_s}}{\left(A^v_{Ps} - \sum_s A^v_{nb}\right)} \frac{\frac{P'_P - P'_S}{(dt)_s} s_{xs} - \frac{P'_{se} - P'_{sw}}{(ds)_s} t_{xs}}{s_{xs}t_{ys} - t_{xs}s_{ys}} \right\} \Bigg] \quad (5.43)$$

In order to simplify, collect some of the terms in Equation (5.43) by defining the coefficients

$$\left.\begin{aligned} C_{Ue} &= \frac{\overline{V_e}}{(ds)_e} & C_{Ve} &= \frac{\overline{V_e}}{(dt)_e} \\ C_{Un} &= \frac{\overline{V_n}}{(ds)_n} & C_{Vn} &= \frac{\overline{V_n}}{(dt)_n} \\ C_{Up} &= \frac{\overline{V_p}}{(ds)_p} & C_{Vp} &= \frac{\overline{V_p}}{(dt)_p} \end{aligned}\right\} \tag{5.44}$$

In Equation (5.43) there are also geometry terms that are repeated at each face. Simplify by referring to each term as one of the following with an appropriate face subscript:

$$\left.\begin{aligned} h_{t_y} &= \frac{t_y}{s_x t_y - t_x s_y} & h_{s_y} &= \frac{s_y}{s_x t_y - t_x s_y} \\ h_{s_x} &= \frac{s_s}{s_x t_y - t_x s_y} & h_{t_x} &= \frac{t_x}{s_x t_y - t_x s_y} \end{aligned}\right\} \tag{5.45}$$

Another repeated term in Equation (5.43) is the momentum coefficients in the denominator. Combining the simplifications of Equations (5.44) and (5.45) with these momentum

coefficients produces:

$$
\left.
\begin{aligned}
C_{Ue}Uh &= \frac{-\overline{V_e}\, t_{ye}}{\left(A^u_{Pe} - \sum_e A^u_{nb}\right)(ds)_e\,(s_{xe}t_{ye} - t_{xe}s_{ye})} = \frac{-C_{Ue}\, h_{t_{ye}}}{A^u_{Pe} - \sum_e A^u_{nb}} \\
C_{Ve}Uh &= \frac{-\overline{V_e}\, s_{ye}}{\left(A^u_{Pe} - \sum_e A^u_{nb}\right)(dt)_e\,(s_{xe}t_{ye} - t_{xe}s_{ye})} = \frac{-C_{Ve}\, h_{s_{ye}}}{A^u_{Pe} - \sum_e A^u_{nb}} \\
C_{Ve}Vh &= \frac{-\overline{V_e}\, s_{xe}}{\left(A^v_{Pe} - \sum_e A^v_{nb}\right)(dt)_e\,(s_{xe}t_{ye} - t_{xe}s_{ye})} = \frac{-C_{Ve}\, h_{s_{xe}}}{A^v_{Pe} - \sum_e A^v_{nb}} \\
C_{Ue}Vh &= \frac{-\overline{V_e}\, t_{xe}}{\left(A^v_{Pe} - \sum_e A^v_{nb}\right)(ds)_e\,(s_{xe}t_{ye} - t_{xe}s_{ye})} = \frac{-C_{Ue}\, h_{t_{xe}}}{A^v_{Pe} - \sum_e A^v_{nb}} \\
C_{Un}Uh &= \frac{-\overline{V_n}\, t_{yn}}{\left(A^u_{Pn} - \sum_n A^u_{nb}\right)(ds)_n\,(s_{xn}t_{yn} - t_{xn}s_{yn})} = \frac{-C_{Un}\, h_{t_{yn}}}{A^u_{Pn} - \sum_n A^u_{nb}} \\
C_{Vn}Uh &= \frac{-\overline{V_n}\, s_{yn}}{\left(A^u_{Pn} - \sum_n A^u_{nb}\right)(dt)_n\,(s_{xn}t_{yn} - t_{xn}s_{yn})} = \frac{C_{Vn}\, h_{s_{yn}}}{A^u_{Pn} - \sum_n A^u_{nb}} \\
C_{Vn}Vh &= \frac{-\overline{V_n}\, s_{xn}}{\left(A^v_{Pn} - \sum_n A^v_{nb}\right)(dt)_n\,(s_{xn}t_{yn} - t_{xn}s_{yn})} = \frac{-C_{Vn}\, h_{s_{xn}}}{A^u_{Pn} - \sum_n A^u_{nb}} \\
C_{Un}Vh &= \frac{-\overline{V_n}\, t_{xn}}{\left(A^v_{Pn} - \sum_n A^v_{nb}\right)(ds)_n\,(s_{xn}t_{yn} - t_{xn}s_{yn})} = \frac{-C_{Un}\, h_{t_{xn}}}{A^v_{Pn} - \sum_n A^v_{nb}}
\end{aligned}
\right\} \quad (5.46)
$$

Rewriting Equation (5.43) including the simplifications of Equation (5.46) produces:

$$\begin{aligned}\Delta m = -\Big[& A^c_{u_e}\left\{C_{Ue}Uh\ (P'_E - P'_P) - C_{Ve}Uh\ (P'_{ne} - P'_{se})\right\} \\ & + A^c_{v_e}\left\{C_{Ve}Vh\ (P'_{ne} - P'_{se}) - C_{Ue}Vh\ (P'_E - P'_P)\right\} \\ & + A^c_{u_w}\left\{C_{Uw}Uh\ (P'_P - P'_W) - C_{Vw}Uh\ (P'_{nw} - P'_{sw})\right\} \\ & + A^c_{v_w}\left\{C_{Vw}Vh\ (P'_{nw} - P'_{sw}) - C_{Uw}Vh\ (P'_P - P'_W)\right\} \\ & + A^c_{u_n}\left\{C_{Un}Uh\ (P'_{ne} - P'_{nw}) - C_{Vn}Uh\ (P'_N - P'_P)\right\} \\ & + A^c_{v_n}\left\{C_{Vn}Vh\ (P'_N - P'_P) - C_{Un}Vh\ (P'_{ne} - P'_{nw})\right\} \\ & + A^c_{u_s}\left\{C_{Us}Uh\ (P'_{se} - P'_{sw}) - C_{Vs}Uh\ (P'_P - P'_S)\right\} \\ & + A^c_{v_s}\left\{C_{Vs}Vh\ (P'_P - P'_S) - C_{Us}Vh\ (P'_{se} - P'_{sw})\right\}\Big] \end{aligned} \quad (5.47)$$

In Equation (5.47) there are pressure correction values at the corners of a control volume. An approximation for these corners in terms of the closest nodal pressure corrections is required. The simplest approximation is the average of the surrounding pressure corrections, in a form similar to Equation (4.33) as follows:

$$P'_{ne} = \frac{1}{4}\left(P'_P + P'_E + P'_N + P'_{NE}\right) \quad (5.48)$$

This approximation is reasonable for a uniform grid but it becomes poor when the grid becomes strongly skewed or has a large aspect ratio. Control volumes with large aspect ratios have the central node too far away from the corners to be a good representation of the value of the pressure correction field at that location. This may result in convergence behavior problems.

Substituting Equation (5.48) and similar approximations for the other three corners into

Equation (5.47) to remove reference to corner pressure corrections produces:

$$\begin{aligned}
\Delta m = -\Big[& A^c_{u_e}\Big\{C_{Ue}Uh\ (P'_E - P'_P) \\
& \quad -C_{Ve}Uh\ \frac{1}{4}\Big((P'_P + P'_E + P'_N + P'_{NE}) - (P'_P + P'_E + P'_S + P'_{SE})\Big)\Big\} \\
& + A^c_{v_e}\Big\{C_{Ve}Vh\ \frac{1}{4}\Big((P'_P + P'_E + P'_N + P'_{NE}) - (P'_P + P'_E + P'_S + P'_{SE})\Big) - C_{Ue}Vh\ (P'_E - P'_P)\Big\} \\
& + A^c_{u_w}\Big\{C_{Uw}Uh\ (P'_P - P'_W) - C_{Vw}Uh\ \frac{1}{4}\Big((P'_P + P'_W + P'_N + P'_{NW}) - (P'_P + P'_W + P'_S + P'_{SW})\Big)\Big\} \\
& + A^c_{v_w}\Big\{C_{Vw}Vh\ \frac{1}{4}\Big((P'_P + P'_W + P'_N + P'_{NW}) - (P'_P + P'_W + P'_S + P'_{SW})\Big) - C_{Uw}Vh\ (P'_P - P'_W)\Big\} \\
& + A^c_{u_n}\Big\{C_{Un}Uh\ \frac{1}{4}\Big((P'_P + P'_E + P'_N + P'_{NE}) - (P'_P + P'_W + P'_N + P'_{NW})\Big) - C_{Vn}Uh\ (P'_N - P'_P)\Big\} \\
& + A^c_{v_n}\Big\{C_{Vn}Vh\ (P'_N - P'_P) - C_{Un}Vh\ \frac{1}{4}\Big((P'_P + P'_E + P'_N + P'_{NE}) - (P'_P + P'_W + P'_N + P'_{NW})\Big)\Big\} \\
& + A^c_{u_s}\Big\{C_{Us}Uh\ \frac{1}{4}\Big((P'_P + P'_E + P'_S + P'_{SE}) - (P'_P + P'_W + P'_S + P'_{SW})\Big) - C_{Vs}Uh\ (P'_P - P'_S)\Big\} \\
& \quad + A^c_{v_s}\Big\{C_{Vs}Vh\ (P'_P - P'_S) \\
& \quad -C_{Us}Vh\ \frac{1}{4}\Big((P'_P + P'_E + P'_S + P'_{SE}) - (P'_P + P'_W + P'_S + P'_{SW})\Big)\Big\}\Big] \qquad (5.49)
\end{aligned}$$

Simplification of Equation (5.49) yields:

$$\begin{aligned}
\Delta m = -\Big[& A^c_{u_e}\Big\{C_{Ue}Uh\ (P'_E - P'_P) - C_{Ve}Uh\ \frac{1}{4}\Big((P'_N + P'_{NE}) - (P'_S + P'_{SE})\Big)\Big\} \\
& + A^c_{v_e}\Big\{C_{Ve}Vh\ \frac{1}{4}\Big((P'_N + P'_{NE}) - (P'_S + P'_{SE})\Big) - C_{Ue}Vh\ (P'_E - P'_P)\Big\} \\
& + A^c_{u_w}\Big\{C_{Uw}Uh\ (P'_P - P'_W) - C_{Vw}Uh\ \frac{1}{4}\Big((P'_N + P'_{NW}) - (P'_S + P'_{SW})\Big)\Big\} \\
& + A^c_{v_w}\Big\{C_{Vw}Vh\ \frac{1}{4}\Big((P'_N + P'_{NW}) - (P'_S + P'_{SW})\Big) - C_{Uw}Vh\ (P'_P - P'_W)\Big\} \\
& + A^c_{u_n}\Big\{C_{Un}Uh\ \frac{1}{4}\Big((P'_E + P'_{NE}) - (P'_W + P'_{NW})\Big) - C_{Vn}Uh\ (P'_N - P'_P)\Big\} \\
& + A^c_{v_n}\Big\{C_{Vn}Vh\ (P'_N - P'_P) - C_{Un}Vh\ \frac{1}{4}\Big((P'_E + P'_{NE}) - (P'_W + P'_{NW})\Big)\Big\} \\
& + A^c_{u_s}\Big\{C_{Us}Uh\ \frac{1}{4}\Big((P'_E + P'_{SE}) - (P'_W + P'_{SW})\Big) - C_{Vs}Uh\ (P'_P - P'_S)\Big\} \\
& + A^c_{v_s}\Big\{C_{Vs}Vh\ (P'_P - P'_S) - C_{Us}Vh\ \frac{1}{4}\Big((P'_E + P'_{SE}) - (P'_W + P'_{SW})\Big)\Big\}\Big] \qquad (5.50)
\end{aligned}$$

Equation (5.50) can be written in either nine-point of five-point form. The five-point form of the algebraic equation appears in Appendix B. To solve Equation (5.50) using a nine-point solver, it is necessary to collect terms into nine coefficients and produce a nine-point algebraic equation as follows:

$$A_P^{p'}P'_P = A_E^{p'}P'_E + A_W^{p'}P'_W + A_N^{p'}P'_N + A_S^{p'}P'_S + A_{NE}^{p'}P'_{NE} + A_{SW}^{p'}P'_{SW} + A_{NW}^{p'}P'_{NW} + A_{SE}^{p'}P'_{SE} + b^{p'} = \sum A_{NB}^{p'}P'_{NB} + b^{p'} \quad (5.51)$$

Where

$$A_S^{p'} = A_{u_s}^c C_{Vs} Uh - A_{v_s}^c C_{Vs} Vh + \frac{1}{4}\left(A_{u_e}^c C_{Ve} Uh - A_{v_e}^c C_{Ve} Vh + A_{u_w}^c C_{Vw} Uh - A_{v_w}^c C_{Vw} Vh\right) \quad (5.52)$$

$$A_N^{p'} = -A_{u_n}^c C_{Vn} Uh + A_{v_n}^c C_{Vn} Vh + \frac{1}{4}\left(-A_{u_e}^c C_{Ve} Uh + A_{v_e}^c C_{Ve} Vh - A_{u_w}^c C_{Vw} Uh + A_{v_w}^c C_{Vw} Vh\right) \quad (5.53)$$

$$A_E^{p'} = A_{u_e}^c C_{Ue} Uh - A_{v_e}^c C_{Ue} Vh + \frac{1}{4}\left(A_{u_n}^c C_{Un} Uh - A_{v_n}^c C_{Un} Vh + A_{u_s}^c C_{Us} Uh - A_{v_s}^c C_{Us} Vh\right) \quad (5.54)$$

$$A_W^{p'} = -A_{u_w}^c C_{Uw} Uh + A_{v_w}^c C_{Uw} Vh + \frac{1}{4}\left(-A_{u_n}^c C_{Un} Uh + A_{v_n}^c C_{Un} Vh - A_{u_s}^c C_{Us} Uh + A_{v_s}^c C_{Us} Vh\right) \quad (5.55)$$

$$A_{SW}^{p'} = \frac{1}{4}\left(A_{u_w}^c C_{Vw} Uh - A_{v_w}^c C_{Vw} Vh - A_{u_s}^c C_{Us} Uh + A_{v_s}^c C_{Us} Vh\right) \quad (5.56)$$

$$A_{SE}^{p'} = \frac{1}{4}\left(A_{u_e}^c C_{Ve} Uh - A_{v_e}^c C_{Ve} Vh + A_{u_s}^c C_{Us} Uh - A_{v_s}^c C_{Us} Vh\right) \quad (5.57)$$

$$A_{NW}^{p'} = \frac{1}{4}\left(-A_{u_w}^c C_{Vw} Uh + A_{v_w}^c C_{Vw} Vh - A_{u_n}^c C_{Un} Uh + A_{v_n}^c C_{Un} Vh\right) \quad (5.58)$$

$$A_{NE}^{p'} = \frac{1}{4}\left(-A_{u_e}^c C_{Ve} Uh + A_{v_e}^c C_{Ve} Vh + A_{u_n}^c C_{Un} Uh - A_{v_n}^c C_{Un} Vh\right) \tag{5.59}$$

$$\begin{aligned} A_P^{p'} = {} & A_{u_e}^c C_{Ue} Uh - A_{v_e}^c C_{Ue} Vh - A_{u_w}^c C_{Uw} Uh + A_{v_w}^c C_{Uw} Vh \\ & + A_{u_s}^c C_{Vs} Uh - A_{v_s}^c C_{Vs} Vh - A_{u_n}^c C_{Vn} Uh + A_{v_n}^c C_{Vn} Vh \end{aligned} \tag{5.60}$$

$$\begin{aligned} b^{p'} = {} & (A_{u_e}^c U_e^\star + A_{v_e}^c V_e^\star) + (A_{u_w}^c U_w^\star + A_{v_w}^c V_w^\star) + (A_{u_n}^c U_n^\star + A_{v_n}^c V_n^\star) \\ & + (A_{u_s}^c U_s^\star + A_{v_s}^c V_s^\star) + b_P^c = -\dot{m}_e + \dot{m}_w - \dot{m}_n + \dot{m}_s + b_P^c \end{aligned} \tag{5.61}$$

5.2.6 Boundary Conditions for P′

The pressure correction boundary conditions are based on the face velocity boundary conditions given in Equation (4.124). The same steps as for formulating the pressure correction equations in Section 5.2.5 are used except that Equation (4.124) is the starting point instead of Equation (4.6). The procedure begins by substituting Equation (5.21) (and the analogous equation for V) into Equation (4.124) and gathering terms to produce:

$$\begin{aligned} & -\left[\left(A_{u_e}^c\right)^{\oplus} U_e' + \left(A_{v_e}^c\right)^{\oplus} V_e' + \left(A_{u_n}^c U_n' + A_{v_n}^c V_n'\right) + \left(A_{u_s}^c U_s' + A_{v_s}^c V_s'\right)\right] = \\ & \qquad \left(A_{u_e}^c\right)^{\oplus} U_e^\star + \left(A_{v_e}^c\right)^{\oplus} V_e^\star + \left(A_{u_n}^c U_n^\star + A_{v_n}^c V_n^\star\right) \\ & \qquad + \left(A_{u_s}^c U_s^\star + A_{v_s}^c V_s^\star\right) + \left(b_P^c\right)^{\oplus} = \Delta m \end{aligned} \tag{5.62}$$

and results in an equation similar to Equation (5.47) but with no west continuity coefficients:

$$\begin{aligned} \Delta m = -\Big[& \left(A_{u_e}^c\right)^{\oplus} \{C_{Ue} Uh\ (P_E' - P_P') - C_{Ve} Uh\ (P_{ne}' - P_{se}')\} \\ & + \left(A_{v_e}^c\right)^{\oplus} \{C_{Ve} Vh\ (P_{ne}' - P_{se}') - C_{Ue} Vh\ (P_E' - P_P')\} \\ & + A_{u_n}^c \{C_{Un} Uh\ (P_{ne}' - P_{nw}') - C_{Vn} Uh\ (P_N' - P_P')\} \\ & + A_{v_n}^c \{C_{Vn} Vh\ (P_N' - P_P') - C_{Un} Vh\ (P_{ne}' - P_{nw}')\} \\ & + A_{u_s}^c \{C_{Us} Uh\ (P_{se}' - P_{sw}') - C_{Vs} Uh\ (P_P' - P_S')\} \\ & + A_{v_s}^c \{C_{Vs} Vh\ (P_P' - P_S') - C_{Us} Vh\ (P_{se}' - P_{sw}')\}\Big] \end{aligned} \tag{5.63}$$

The northeast and southeast corner pressure corrections are approximated as the average of the four nearest nodal values, as in Equation (5.48). On the west boundary, the pressure at the northwest corner of a control volume will be between the west nodal pressure and the northwest nodal pressure. Therefore, the pressure correction for this northwest corner can be approximated by a linear interpolation along the boundary as follows:

$$P'_{nw} = f_n \, P'_W + (1 - f_n) \, P'_{NW} \tag{5.64}$$

where

$$f_n = \frac{DJSW_{(IB-1,j+1)}}{(dt)_{n(IB-1,j)}} \tag{5.65}$$

similarly for the southwest corner

$$P'_{sw} = f_s \, P'_{SW} + (1 - f_s) \, P'_W \tag{5.66}$$

where

$$f_s = \frac{DJSW_{(IB-1,j)}}{(dt)_{n(IB-1,j-1)}} \tag{5.67}$$

Substituting the interpolations and the corner approximation (Equation (5.48)) into Equation (5.63) produces:

$$\begin{aligned}
&- \Big[\left(A^c_{u_e}\right)^{\oplus} \Big\{ C_{Ue} U h \, (P'_E - P'_P) - C_{Ve} U h \, \frac{1}{4} \Big((P'_N + P'_{NE}) - (P'_S + P'_{SE}) \Big) \Big\} \\
&\quad + \left(A^c_{v_e}\right)^{\oplus} \Big\{ C_{Ve} V h \, \frac{1}{4} \Big((P'_N + P'_{NE}) - (P'_S + P'_{SE}) \Big) - C_{Ue} V h \, (P'_E - P'_P) \Big\} \\
&\quad + A^c_{u_n} \Big\{ C_{Un} U h \, \Big(\frac{1}{4} (P'_N + P'_P + P'_E + P'_{NE}) - (f_n P'_W + (1 - f_n) \, P'_{NW}) \Big) \\
&\qquad - C_{Vn} U h \, (P'_N - P'_P) \Big\} + A^c_{v_n} \Big\{ C_{Vn} V h \, (P'_N - P'_P) \\
&\qquad - C_{Un} V h \, \Big(\frac{1}{4} (P'_N + P'_P + P'_E + P'_{NE}) - (f_n P'_W + (1 - f_n) \, P'_{NW}) \Big) \Big\} \\
&\quad + A^c_{u_s} \Big\{ C_{Us} U h \, \Big(\frac{1}{4} (P'_S + P'_P + P'_E + P'_{SE}) - (f_s P'_{SW} + (1 - f_s) \, P'_W) \Big) \\
&\qquad - C_{Vs} U h \, (P'_P - P'_S) \Big\} + A^c_{v_s} \Big\{ C_{Vs} V h \, (P'_P - P'_S) \\
&\quad - C_{Us} V h \, \Big(\frac{1}{4} (P'_S + P'_P + P'_E + P'_{SE}) - (f_s P'_{SW} + (1.0 - f_s) \, P'_W) \Big) \Big\} \Big] = \Delta m
\end{aligned} \tag{5.68}$$

The boundary pressure corrections still need to be removed from Equation (5.63). The pressure correction boundary condition is not set directly, but is set indirectly based on velocity boundary conditions. Since the pressure correction field will reduce to zero upon convergence, a simple approximation like linear extrapolation is considered sufficient. The linear extrapolation for the west boundary is:

$$P'_{W_{(IB,j)}} = \left(1 + \frac{DISW_{(IB,j)}}{DISE_{(IB,j)} + DISW_{(IB+1,j)}}\right) P'_{P_{(IB,j)}} + \left(\frac{-DISW_{(IB,j)}}{DISE_{(IB,j)} + DISW_{(IB+1,j)}}\right) P'_{E_{(IB,j)}} = A^{p'}_{P(IB-1,j)}\, P'_{P_{(IB,j)}} + A^{p'}_{E(IB-1,j)}\, P'_{E_{(IB,j)}} \quad (5.69)$$

As Equation(5.69) shows, the geometric terms are stored in the fictitious pressure correction coefficients, which are used in setting the fictitious pressure correction after the solution of the interior field. Analogous extrapolations are made for the northwest and southwest pressure corrections on the west boundary. Similar extrapolations are made for all boundary values on the east, south and north faces.

Substituting Equation (5.69) for the west, and analogous equations for the northwest,

and southwest pressure corrections in Equation (5.68) produces:

$$
\begin{aligned}
&-\Big[\left(A^c_{u_e}\right)^{\oplus}\Big\{C_{Ue}Uh\ (P'_E-P'_P)-C_{Ve}Uh\ \frac{1}{4}\Big((P'_N+P'_{NE})-(P'_S+P'_{SE})\Big)\Big\}\\
&\quad+\left(A^c_{v_e}\right)^{\oplus}\Big\{C_{Ve}Vh\ \frac{1}{4}\Big((P'_N+P'_{NE})-(P'_S+P'_{SE})\Big)-C_{Ue}Vh\ (P'_E-P'_P)\Big\}\\
&\quad+A^c_{u_n}\Big\{C_{Un}Uh\ \Big(\frac{1}{4}(P'_N+P'_P+P'_E+P'_{NE})\\
&-f_n\left(A^{p'}_{P(IB-1,j)}P'_P+A^{p'}_{E(IB-1,j)}P'_E\right)-(1-f_n)\left(A^{p'}_{P(IB-1,j+1)}P'_N+A^{p'}_{E(IB-1,j+1)}P'_{NE}\right)\Big)\\
&-C_{Vn}Uh\ (P'_N-P'_P)\Big\}+A^c_{v_n}\Big\{C_{Vn}Vh\ (P'_N-P'_P)-C_{Un}Vh\ \Big(\frac{1}{4}(P'_N+P'_P+P'_E+P'_{NE})\\
&-f_n\left(A^{p'}_{P(IB-1,j)}P'_P+A^{p'}_{E(IB-1,j)}P'_E\right)-(1-f_n)\left(A^{p'}_{P(IB-1,j+1)}P'_N+A^{p'}_{E(IB-1,j+1)}P'_{NE}\right)\Big)\Big\}\\
&\quad+A^c_{u_s}\Big\{C_{Us}Uh\ \Big(\frac{1}{4}(P'_S+P'_P+P'_E+P'_{SE})\\
&-f_s\left(A^{p'}_{P(IB-1,j-1)}P'_S+A^{p'}_{E(IB-1,j-1)}P'_{SE}\right)-(1-f_s)\left(A^{p'}_{P(IB-1,j)}P'_P+A^{p'}_{E(IB-1,j)}P'_E\right)\Big)\\
&-C_{Vs}Uh\ (P'_P-P'_S)\Big\}+A^c_{v_s}\Big\{C_{Vs}Vh\ (P'_P-P'_S)-C_{Us}Vh\ \Big(\frac{1}{4}(P'_S+P'_P+P'_E+P'_{SE})\\
&\quad-f_s\left(A^{p'}_{P(IB-1,j-1)}P'_S+A^{p'}_{E(IB-1,j-1)}P'_{SE}\right)\\
&\quad-(1-f_s)\left(A^{p'}_{P(IB-1,j)}P'_P+A^{p'}_{E(IB-1,j)}P'_E\right)\Big)\Big\}\Big]=\Delta m
\end{aligned}
\tag{5.70}
$$

Equation (5.70) can be written in either nine-point or five-point form. The five-point form appears in Appendix B. After application of the boundary conditions, the modified coefficients for the nine-point P' equation are:

$$
\begin{aligned}
A^{p'}_S=&A^c_{u_s}\left(C_{Vs}Uh+C_{Us}Uh\left(\frac{1}{4}-f_s\,A^{p'}_{P(IB-1,j-1)}\right)\right)\\
&-A^c_{v_s}\left(C_{Vs}Vh+C_{Us}Vh\left(\frac{1}{4}-f_s\,A^{p'}_{P(IB-1,j-1)}\right)\right)\\
&+\frac{1}{4}\left(\left(A^c_{u_e}\right)^{\oplus}C_{Ve}Uh-\left(A^c_{v_e}\right)^{\oplus}C_{Ve}Vh\right)
\end{aligned}
\tag{5.71}
$$

$$
\begin{aligned}
A^{p'}_N=&-A^c_{u_n}\left(C_{Vn}Uh-C_{Un}Uh\left(\frac{1}{4}-(1-f_n)\,A^{p'}_{P(IB-1,j+1)}\right)\right)\\
&+A^c_{v_n}\left(C_{Vn}Vh-C_{Un}Vh\left(\frac{1}{4}-(1-f_n)\,A^{p'}_{P(IB-1,j+1)}\right)\right)\\
&+\frac{1}{4}\left(-\left(A^c_{u_e}\right)^{\oplus}C_{Ve}Uh+\left(A^c_{v_e}\right)^{\oplus}C_{Ve}Vh\right)
\end{aligned}
\tag{5.72}
$$

$$A_E^{p'} = \left(A_{u_e}^c\right)^{\oplus} C_{Ue}Uh - \left(A_{v_e}^c\right)^{\oplus} C_{Ue}Vh + \left(A_{u_n}^c C_{Un}Uh - A_{v_n}^c C_{Un}Vh\right)\left(\frac{1}{4} - f_n\, A_{E(IB-1,j)}^{p'}\right) + \left(A_{u_s}^c C_{Us}Uh - A_{v_s}^c C_{Us}Vh\right)\left(\frac{1}{4} - (1-f_s)\, A_{E(IB-1,j)}^{p'}\right) \quad (5.73)$$

$$A_{SE}^{p'} = \frac{1}{4}\left(\left(A_{u_e}^c\right)^{\oplus} C_{Ve}Uh - \left(A_{v_e}^c\right)^{\oplus} C_{Ve}Vh\right) + \left(A_{u_s}^c C_{Us}Uh - A_{v_s}^c C_{Us}Vh\right)\left(\frac{1}{4} - f_s\, A_{E(IB-1,j-1)}^{p'}\right) \quad (5.74)$$

$$A_{NE}^{p'} = \frac{1}{4}\left(-\left(A_{u_e}^c\right)^{\oplus} C_{Ve}Uh + \left(A_{v_e}^c\right)^{\oplus} C_{Ve}Vh\right) + \left(A_{u_n}^c C_{Un}Uh - A_{v_n}^c C_{Un}Vh\right)\left(\frac{1}{4} + (1-f_n)\, A_{E(IB-1,j+1)}^{p'}\right) \quad (5.75)$$

$$\begin{aligned} A_P^{p'} = {} & \left(A_{u_e}^c\right)^{\oplus} C_{Ue}Uh - \left(A_{v_e}^c\right)^{\oplus} C_{Ue}Vh \\ & + A_{u_s}^c\left(C_{Vs}Uh - C_{Us}Uh\left(\frac{1}{4} - (1-f_s)\, A_{P(IB-1,j)}^{p'}\right)\right) \\ & - A_{v_s}^c\left(C_{Vs}Vh - C_{Us}Vh\left(\frac{1}{4} - (1-f_s)\, A_{P(IB-1,j)}^{p'}\right)\right) \\ & - A_{u_n}^c\left(C_{Vn}Uh + C_{Un}Uh\left(\frac{1}{4} - f_n\, A_{P(IB-1,j)}^{p'}\right)\right) \\ & + A_{v_n}^c\left(C_{Vn}Vh + C_{Un}Vh\left(\frac{1}{4} - f_n\, A_{P(IB-1,j)}^{p'}\right)\right) \end{aligned} \quad (5.76)$$

$$\begin{aligned} b^{p'} = {} & \left(A_{u_e}^c\right)^{\oplus} U_e^{\star} + \left(A_{v_e}^c\right)^{\oplus} V_e^{\star} + \left(A_{u_n}^c U_n^{\star} + A_{v_n}^c V_n^{\star}\right) + \left(A_{u_s}^c U_s^{\star} + A_{v_s}^c V_s^{\star}\right) + (b_P^c)^{\oplus} \\ & = -\dot{m}_e + \dot{m}_w - \dot{m}_n + \dot{m}_s + b_P^c \end{aligned} \quad (5.77)$$

The west, northwest, and southwest boundary pressure corrections have now been eliminated from the computational domain so these coefficients can be set to zero as follows:

$$\left.\begin{aligned} A_W^{p'} &= 0 \\ A_{NW}^{p'} &= 0 \\ A_{SW}^{p'} &= 0 \end{aligned}\right\} \quad (5.78)$$

There is a south boundary as well as a west boundary at the southwest corner. So the south and southeast pressure corrections need to be extrapolated as well and their coefficients can be set to zero as follows:

$$\left.\begin{aligned} A^{p'}_{S(IB,JB)} &= 0 \\ A^{p'}_{SE(IB,JB)} &= 0 \end{aligned}\right\} \tag{5.79}$$

An analogous procedure is used for the other corners of the computational domain.

5.3 Solution Algorithm

The solution procedure is, briefly:

1. Read in all input data and grid information.
2. Calculate the continuity coefficients.
3. Calculate the coefficients of the two momentum equations.
4. Set boundary conditions, including blockages.
5. Add the pressure gradient term to the momentum source terms.
6. Add the buoyancy force to U and V momentum source terms.
7. Solve momentum equations for the guessed velocities, U^* and V^*.
8. Use the PWIM to calculate the guessed face velocities.
9. Calculate the pressure correction source term.
10. Solve for the pressure correction field.

11. Correct the face and nodal velocities using the new pressure correction field.

12. Correct the pressure field using the new pressure correction field.

13. Calculate the coefficients for temperature equation.

14. Solve for the temperature field.

15. Repeat from step 5 through 14 until the steady-state convergence criteria are met.

Further details of the solution algorithm are given in Appendix A.

5.4 Convergence Criteria

5.4.1 Linear Equation Convergence

The linear equations convergence criterion limits the number of solver iterations for each algebraic equation based on a residual reduction. The residual is defined (similar to the method use by Perić [31]) as the sum of absolute values of all residuals normalized by the number of control volumes as follows:

$$R^{\phi} = \frac{\sum\limits_{all(i,j)} \left| \left(\sum\limits_{P} A^{\phi}_{NB} \Phi_{NB} + b^{\phi} - A^{\phi}_{P} \Phi_{P} \right) \right|}{NX * NY} \tag{5.80}$$

where Φ is one of (U, V, P', or T). The solver ceases iterating when the residual from the n^{th} iteration is less than a specified fraction, R^{ϕ}_{spec}, of the residual from the first iteration. In mathematical terms, when

$$\frac{R^{\phi}_{n}}{R^{\phi}_{1}} < R^{\phi}_{spec} \tag{5.81}$$

The typical values of R^{ϕ}_{spec} for each variable were: $R^{U}_{spec} = 5.0 \times 10^{-3}$, $R^{V}_{spec} = 5.0 \times 10^{-3}$, $R^{P}_{spec} = 1.0 \times 10^{-7}$, and $R^{T}_{spec} = 1.0 \times 10^{-5}$. Note that these convergence criteria are quite tight.

Van Doormaal and Raithby [43] use a root mean squared residual and claim a reduction factor of 0.25 to 0.05 as optimal. The tight convergence criterion on the linear equation solvers used in this work does not affect the converged solution, and maintains strong conservation at each time step.

5.4.2 Steady State Convergence

A steady-state convergence criterion, Δ^{ϕ}_{spec}, is set separately for each solution variable, Φ being one of (U, V, P, or T). At each time step, at each control volume, the ϕ value is compared with its value at the previous time step and normalized by the range of values of that variable to calculate:

$$\Delta^{\phi} = max(\Delta^{\phi}_{all(i,j)}) = \frac{|\Phi_{(i,j)} - \Phi^{o}_{(i,j)}|}{(max(\Phi_{all(i,j)}) - min(\Phi_{all(i,j)}))} \tag{5.82}$$

The largest value of $\Delta^{\phi}_{(i,j)}$ is used as the measure of convergence for that variable field and that step. Steady-state convergence is declared when

$$\Delta^{\phi} < \Delta^{\phi}_{spec} \tag{5.83}$$

for the U, V, P, and T fields.

The typical values of Δ^{ϕ}_{spec} for each variable were: $\Delta^{U}_{spec} = 1.0\times10^{-5}$, $\Delta^{V}_{spec} = 1.0\times10^{-5}$, $\Delta^{P}_{spec} = 1.0\times10^{-7}$, and $\Delta^{T}_{spec} = 1.0\times10^{-7}$. Van Doormaal et al. [44] use a convergence criterion of $\Delta^{\phi}_{spec} = 5\times10^{-5}$. The small steady-state convergence criteria were used in this work to ensure tightly converged solutions.

The typical amount of CPU time used on a Sun Microsystems Sparc 5 for the 120×80 problem in Section 7.2 was 10 hours.

Chapter 6

Validity Checks and Test Problems

6.1 Introduction

This chapter presents the results of tests designed to verify the accuracy and validity of the results produced by the computer code written for this work. The results of the present work are compared with the results given in the literature. The focus is on problems that require a non-orthogonal grid in order to validate the non-orthogonal aspects of the solution method. Simple tests were performed using orthogonal (Cartesian) grids and the results compared well to the literature.

This chapter contains two sections. The first section presents two test problems each of which use a single non-orthogonal grid. The first test problem checks the flow only and the second test problem checks heat transfer and buoyancy forces. The second section presents comparisons between orthogonal and non-orthogonal grids on parallel plate and lid-driven cavity flows. It also presents the results of solution of a so-called slug flow through a tube bundle by using two orthogonal grids.

6.2 Single Grid Flow Tests

This section compares individual grid results with simple published results of two standard test problems. The first test is the so called tilted lid-driven cavity. The cavity represents a recirculating flow in a grid where the cross-derivative terms are very important. The second test is natural convection in a hexagonal annulus and is used to validate the heat transfer and buoyancy forces as well as the composite non-orthogonal grid. These problems test the code results for complex non-orthogonal boundaries on a single grid. In both problems the flow is laminar.

6.2.1 Tilted Lid-Driven Cavity

The lid-driven, or shear-driven cavity tilted at 45^o uses a very simple grid. This test is chosen to exercise the non-orthogonal grid at a fairly steep angle and with a recirculating type of flow that ensures strong flow for both velocity components. The results will be compared with those published by Perić [32] on the same grid density (80×80). Perić uses an upwind differencing scheme, (UDS), that gives similar accuracy to the exponential upwinding scheme, (EDS), especially in high flow regions. The accuracy of the results depends strongly on the upwind scheme, so the two methods are expected to compare well.

The tilted cavity is created from a standard uniform square grid but with the top shifted to the right so the sides make a 45^o angle with the vertical. The bottom left corner is at $(0, 0)$ and the top right corner is at $(2, 1)$, in Cartesian coordinates. The cavity width and height are therefore $L = 1$ $[m]$. The lid velocity, U_{lid} is chosen to be 1 $[m/s]$, and the fluid viscosity is 1.846×10^{-5} $[N \cdot s/m^2]$. The fluid density is chosen so that the Reynolds number, based on lid velocity and cavity width is

$$Re = \frac{\rho\, U_{lid}\, L}{\mu} = 100 \tag{6.1}$$

The sides and bottom are solid, zero slip walls. Results will be presented from calculations

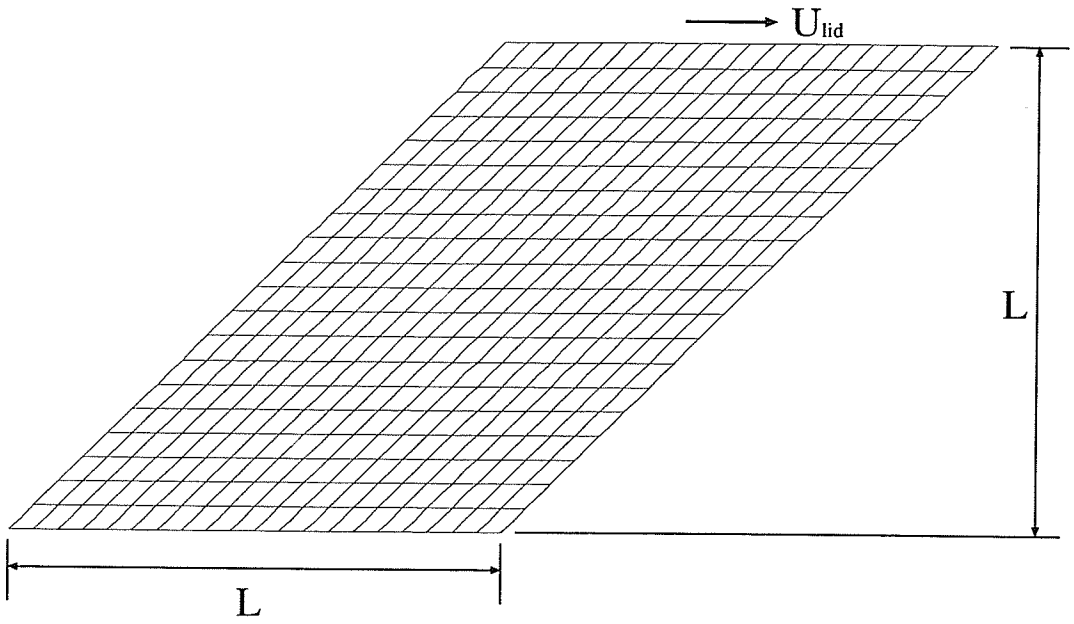

Figure 6.1: Tilted Lid-Driven Cavity, 20×20 Grid.

on a grid similar to that shown in Figure 6.1, but with an 80×80 grid density.

The streamlines, shown in Figure 6.2, compare well with the streamlines given by Perić. There are a few more streamlines shown in Figure 6.2 to more completely illustrate the flow. The stream-function values are given in Table 6.1. The following are the approximate locations of the main features of the streamlines. The center of the primary vortex, rotating clockwise, is at $(1.40, 0.84)$. The center of the secondary vortex, rotating counter-clockwise, is at $(0.67, 0.26)$. The first zero streamline crosses the domain from the left wall at $(0.61, 0.61)$ to the right wall at $(1.18, 0.18)$. The second zero streamline is in the bottom left corner from $(0.21, 0.21)$ to $(0.30, 0)$. The third zero streamline is in the bottom left corner from $(0.08, 0.08)$ to $(0.1, 0)$. There is a weak rotational flow between each of these smaller zero streamlines as well, they just do not show up with the stream function levels chosen. The flow is weak in the lower left corner and the the streamlines are not well resolved in that location at this grid density.

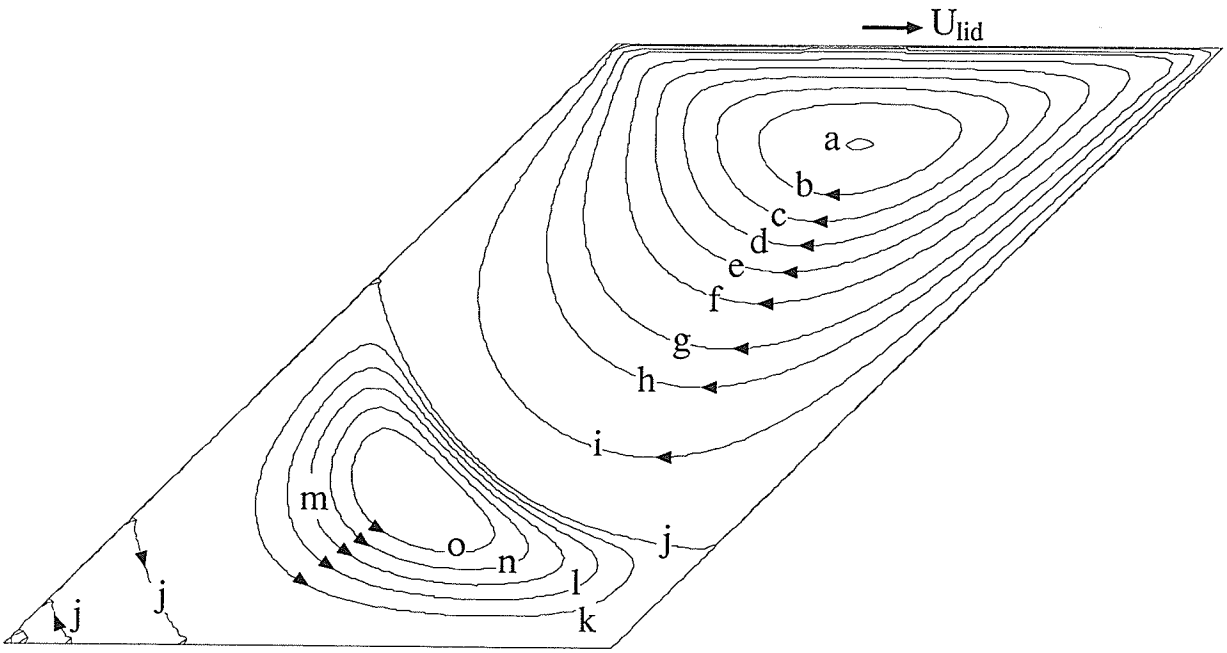

Figure 6.2: Tilted Lid-Driven Cavity, Streamlines: 80×80 grid.

a	−0.07	f	−0.02	k	0.000026
b	−0.06	g	−0.01	l	0.000052
c	−0.05	h	−0.005	m	0.000077
d	−0.04	i	−0.001	n	0.000103
e	−0.03	j	0.0	o	0.000129

Table 6.1: Stream Function Levels for Figure 6.2.

A plot of U velocity profiles at three locations is shown in Figure 6.3. The present results compare very well to Perić's results. The $x = 1.0$ profile is actually from the bottom right vertex to the top left vertex of the domain. It shows small deviations from zero in the U component of velocity, except near the top. At $y = 1.0$, the very top of the domain, this velocity profile shows a velocity of 0.5 $[m/s]$. This lower velocity is an artifact that only occurs in corners where the two different Dirichlet boundary conditions are averaged. The $x = 1.25$ profile goes from $y = 0.25$, at the slanted wall, to the lid, passing just to the left of the main vortex center. The $x = 1.5$ profile, however, passes to the right of the main

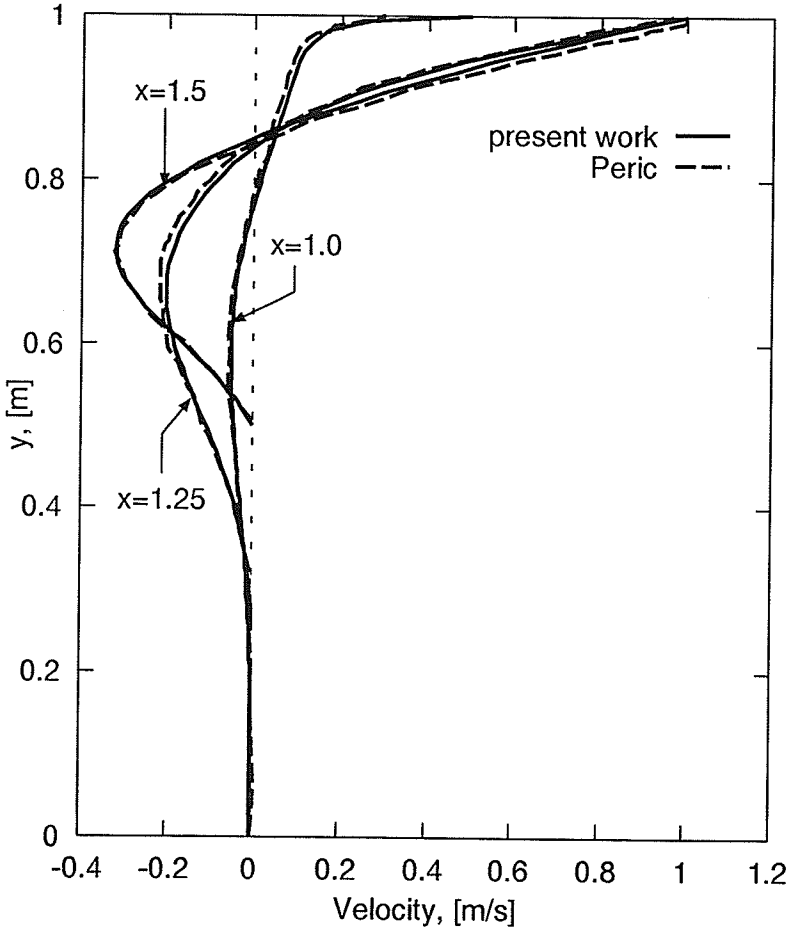

Figure 6.3: Tilted Lid-Driven Cavity, U velocity profiles.

vortex center where the velocity is higher. The three profiles have a slight offset from Perić's results. The percentage difference of peak negative velocities along the $x = 1.5$ line is 0.3%, while along the $x = 1.25$ line the peak velocity difference is 6.5%.

A comparison of V velocity profiles in Figure 6.4 shows that the present study is very close to Perić's results. The V velocity profile is given at three y locations, and all three profiles match almost exactly except for a few locations. At those locations, error in digitizing Perićś curves from literature may be the cause of the deviations. Note that the V profiles are much closer to Perić's results than are the U profiles. The curve for $y = 0.4$ is just below the

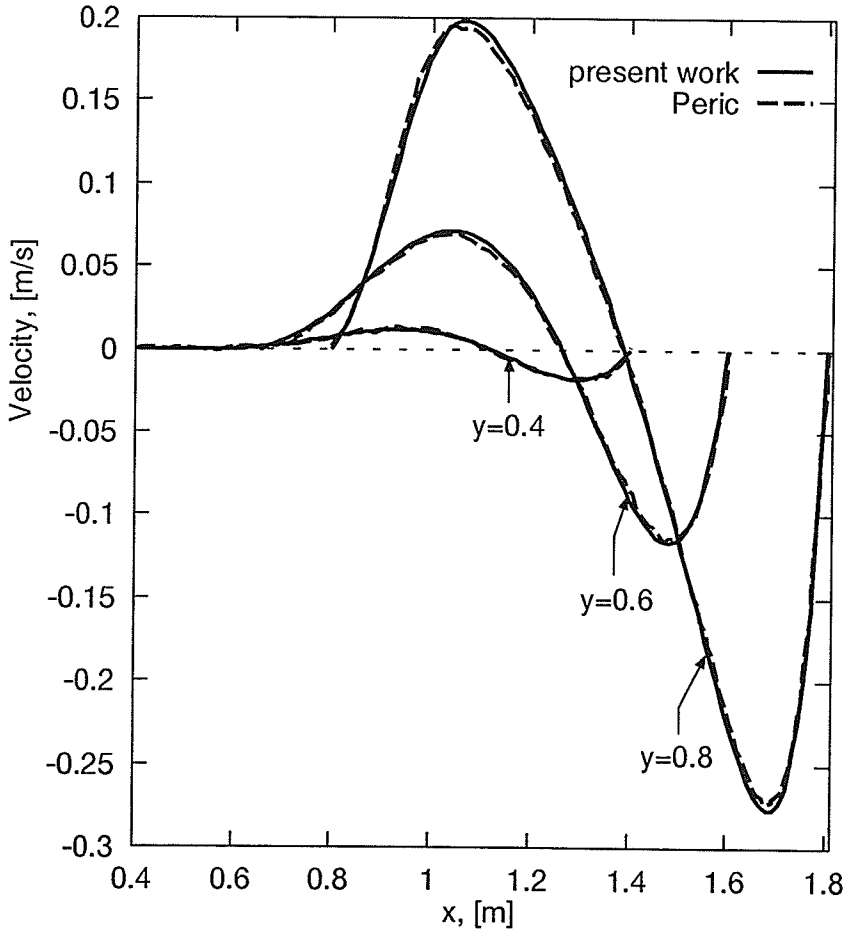

Figure 6.4: Tilted Lid-Driven Cavity, V velocity profiles.

horizontal center of the domain, beginning at $x = 0.4$ and ending at $x = 1.4$. There is very little flow in the lower part of the domain so this curve does not deviate very much from zero. The curve for $y = 0.6$ begins at $x = 0.6$, ends at $x = 1.6$ and shows a larger velocity. Near the top of the domain, at $y = 0.8$, the velocity is much larger. This location is just below the center of the primary vortex and the cross over from positive to negative velocities is just to the left of $x = 1.4$. These results are consistent with the streamline pattern shown in Figure 6.2.

This test has shown that the present work compares well with previous published results for this problem.

6.2.2 Natural Convection in a Hexagonal Annulus

Another test problem that exercises the flow solution on a non-orthogonal grid is the so-called hexagonal annulus. This study will be compared with published results of Glakpe and Asfaw [12], who used it as a model of a spent-fuel storage container, and with Raithby et al. [35] who also used this application as a test problem. The annulus has been studied using many diameter ratios but this work compares results for only one diameter ratio, as described below.

Half of the hexagonal annulus is shown in Figure 6.5 along with dimensions and boundary conditions. The annulus in this test has a diameter ratio $\frac{\Delta}{R} = 0.5$. That is the inside radius, $r = 0.5$, to the center of a flat surface, and the outside radius, $R = 1.0$. The distance between the inner flat surface and the outer cylinder is called the gap, $\Delta = 0.5$. The inner hexagonal cylinder is isothermal at, $T_2 = 1$ while the outer circular cylinder is at a lower temperature, $T_1 = 0$. The Rayleigh number based on the gap width is defined as:

$$Ra_\Delta = \frac{g\beta(T_2 - T_1)\Delta^3\rho^2\, Cp}{\mu\, k} \tag{6.2}$$

The working fluid is air at 300 $[K]$ ($Pr = 0.707$), the properties of which are found

in Incropera and Dewitt [14]. Using the ideal gas assumption, the coefficient of thermal expansion was taken as $\beta = \frac{1}{T}$, where $T = 300\,[K]$. The density was adjusted to produce a Rayleigh number of $Ra = 9.2 \times 10^4$ for this comparison. The inner hexagonal cylinder and the outer circular cylinder are zero slip walls. There is also a symmetry plane that intersects the annulus at both top and bottom as shown in Figure 6.5

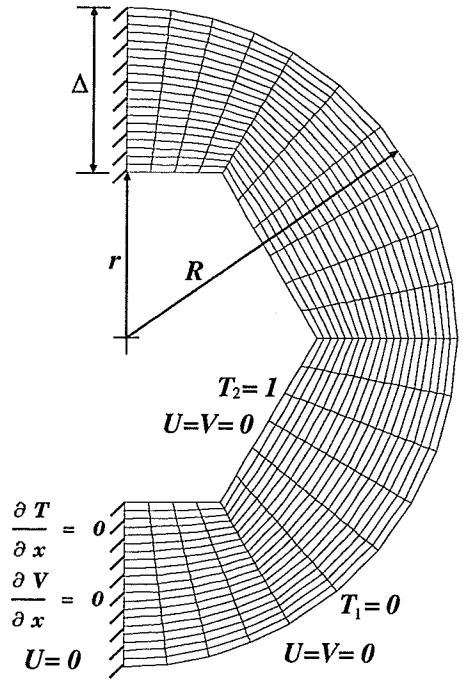

Figure 6.5: Hexagonal Annulus, 20×20 Grid.

The grid was generated using the paneling method in Cartesian coordinates instead of radial coordinates and transformation equations used by Glakpe and Asfaw [12]. They used a staggered grid, representing convective terms by upwind differencing, and a variant of the SIMPLE algorithm.

Raithby et al. [35] used an orthogonal curvilinear 40×40 grid that conforms to the boundaries. They also used a "stress-flux formulation" of the equations, a staggered grid, and the SIMPLEC solution method for pressure-velocity coupling.

Figure 6.5 shows a 20×20 grid of the solution domain. Each panel in the domain begins and ends at a vertex of the inner hexagon with control volumes uniformly-spaced in each panel so the present grid is slightly different from the grid used in the cited references. In other words, the present grid is a single non-orthogonal composite made up of four non-orthogonal pieces. The arc was generated by using straight line segments and the interior was mapped using transfinite interpolation as described in Section 3.2.

A 40×40 was chosen to match the grid used in Raithby et al. [35]. The results for that grid are shown in the form of streamlines in Figure 6.6(a) and isotherms in Figure 6.6(b). These results are qualitatively the same as the two published results. The values of the streamlines in Figure 6.6(a) are listed in Table 6.2.

In Figure 6.6 the streamlines show that there is a vortex that separates at the uppermost vertex of the hexagon. The fluid in the bottom corner is virtually stagnant because of the stratified temperature layers. The cooler air at the bottom does not rise and mix in the main vortex.

A quantitative comparison is given by use of the graphs of k_{eff}/k (as defined in [35]) versus Raleigh number in both Glakpe and Asfaw [12] and Raithby et al. [35]. The present simulation finds a $k_{eff}/k = 3.265$ for $Ra = 9.2 \times 10^4$ while the published results both give a value of 3.3. This represents an error of approximately 1%, which is excellent agreement and well within the accuracy of reading the value from the graph in the literature.

The results of this natural convection flow calculation compare very well with previously published results and therefore show that the present code accurately predicts the correct flow patterns for this problem.

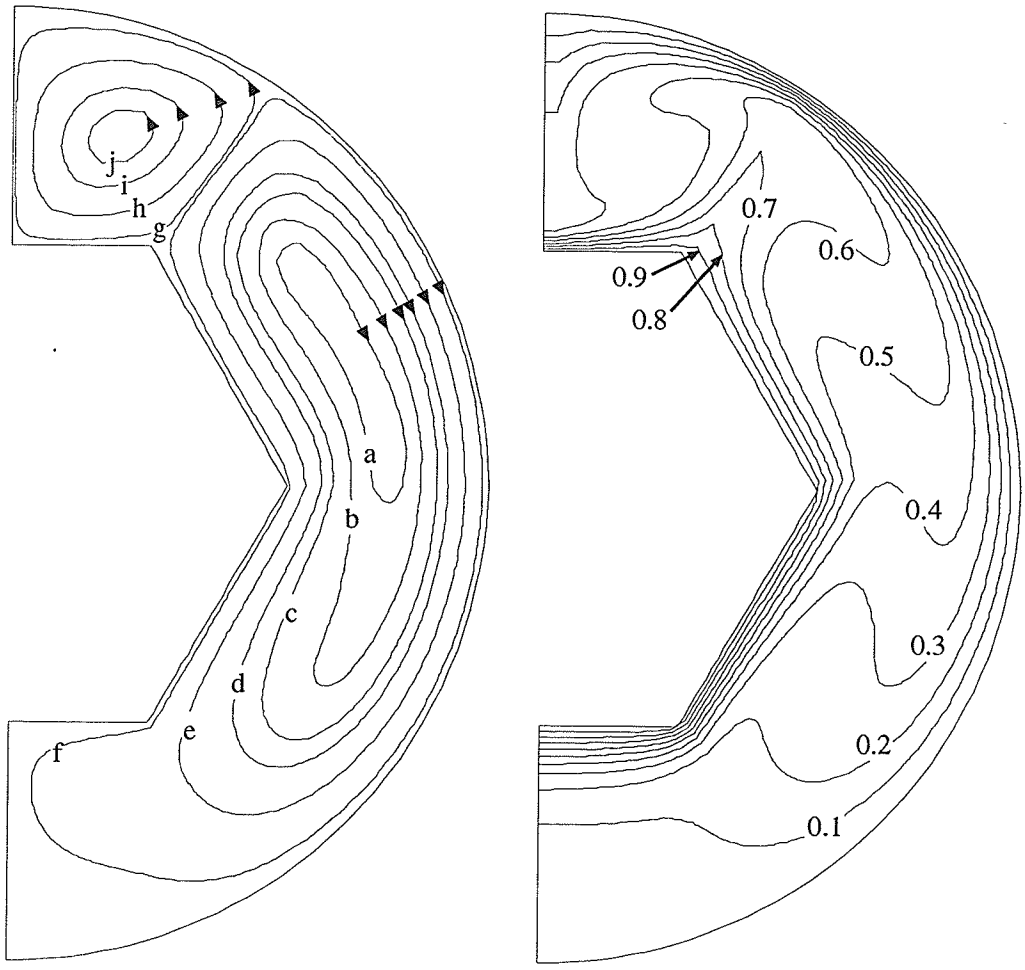

(a) Streamlines. (b) Isotherms.

Figure 6.6: Hexagonal Annulus Results.

a	-6.5×10^{-3}	f	-2.0×10^{-4}
b	-6.0×10^{-3}	g	2.0×10^{-4}
c	-5.0×10^{-3}	h	2.0×10^{-3}
d	-4.0×10^{-3}	i	4.0×10^{-3}
e	-2.0×10^{-3}	j	5.0×10^{-3}

Table 6.2: Stream Function Levels for Figure 6.6(a).

6.3 Multiple Grid Flow Tests

This section deals with flow tests on different grids. The first test is a model of the square lid-driven cavity to compare the results from an orthogonal grid and non-orthogonal grid. The second test serves as an illustration of the edge effect of the tube bundle and a comparison is made between coarse and fine control volumes at the tube bundle boundary. The third test extends modeling capability by tilting a grid region (which will represent a tube bundle in another test). This simulation will compare results on an orthogonal and two non-orthogonal grids. The flow is laminar in tests one and three. In test two effective viscosity is used.

6.3.1 Square Lid Driven Cavity

The purpose of this test is to compare the results using orthogonal and non-orthogonal grids to published results for the standard lid-driven cavity.

The orthogonal grid with uniformly-spaced control volumes, shown in Figure 6.7, represents a simple 1 $[m]$ by 1 $[m]$ square cavity with solid walls on both sides and bottom. The top lid is moving to the right with a velocity of $U_{lid} = 1\ [m/s]$. For this test a Reynolds number based on lid velocity and cavity height, $Re_L = 400$ was chosen by adjusting the density. The fluid viscosity is $1.846 \times 10^{-5}\ [N \cdot s/m^2]$.

The non-orthogonal grid shown in Figure 6.8 uses the same outside dimensions as the orthogonal grid, but the interior control volumes are skewed to exercise the non-orthogonal terms in the equations. There is a boarder region of orthogonal control volumes having a width of 0.1 [m]. The central region is skewed using an expansion factor in order to obtain the greatest degree of skewing possible without making the control volumes near the corners too large or too small. The expansion factors used on the top and bottom of the center region were 0.87 and 1.13, respectively.

This test problem was solved on two grid resolutions, 20×20 and 80×80, both of which

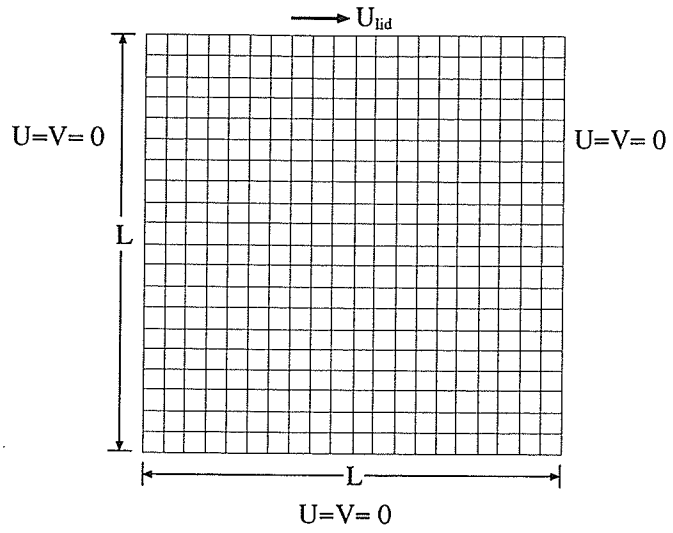

Figure 6.7: Square Orthogonal 20×20 Grid.

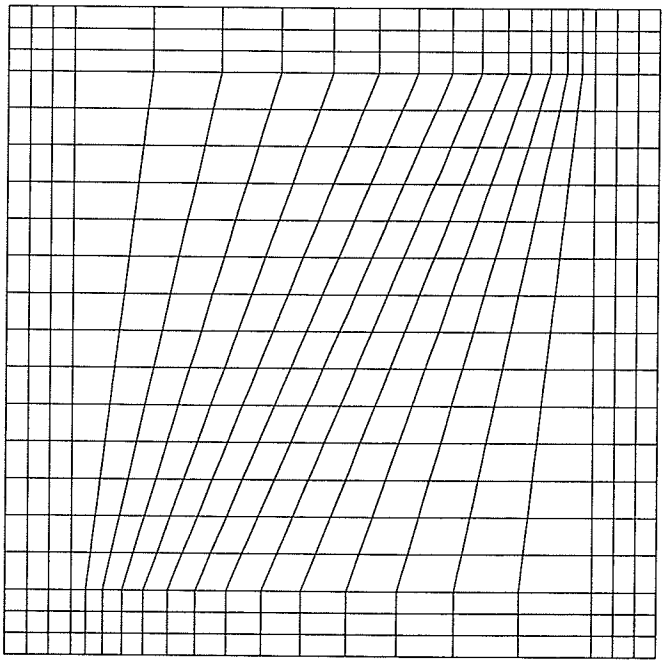

Figure 6.8: Square Non-Orthogonal 20×20 Grid.

had uniform grid spacing. The non-orthogonal 80×80 grid is shown in Figure 6.9. It should be noted that the 80×80 grid has a slightly different angle in the center compared to the 20×20 non-orthogonal grid. This is caused by the different expansion factor from that for the coarse grid and is simply because of the number of control volumes over which the expansion must be spread. For this grid, the expansion factors used on the top and bottom of the center region were 0.96 and 1.04, respectively.

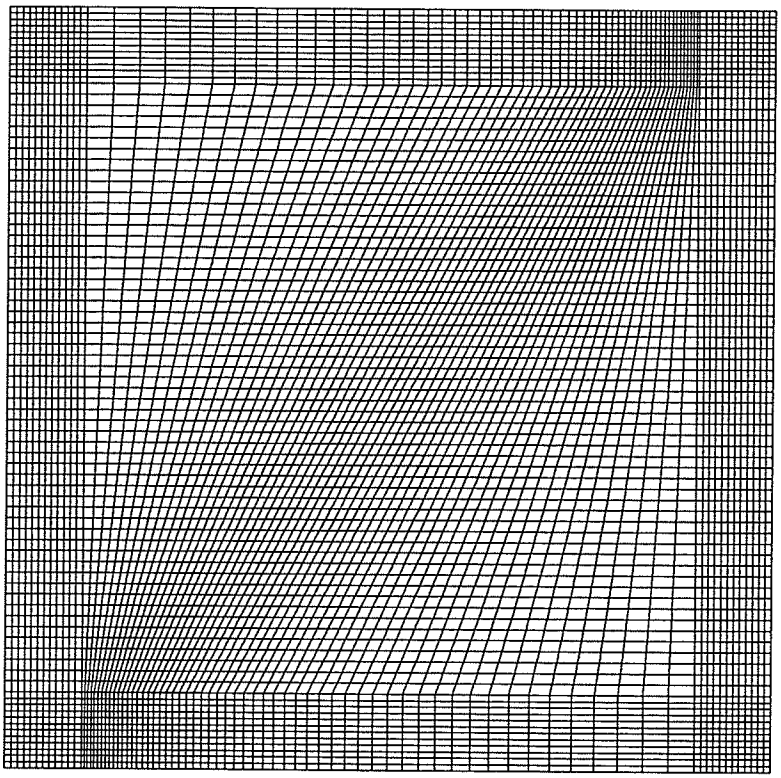

Figure 6.9: Square Non-Orthogonal 80×80 Grid.

The present work compares results of the lid-driven square cavity with Jessee and Fiveland [15], Ghia et al. [11], and Miller and Schmidt [23]. Jessee and Fiveland use a non-staggered grid and a similar pressure-velocity coupling method as the present work. They used the lid-driven cavity to compare differencing schemes. Ghia et al. use a stream function-vorticity method and a multi-grid procedure to produce a detailed benchmark for the lid-

driven cavity problem. Miller and Schmidt have tested their co-located FVM, PWIM and QUICK differencing on the lid driven cavity.

Jessee and Fiveland [15] and Miller and Schmidt [23] both indicated that upwind (UDS) is less accurate than higher order schemes. In the present work, EDS becomes nearly equal to UDS in high flow regions so it is expected that the present code will under-predict the velocities in areas of rapidly changing flow in the manner indicated in Figure 5(b) in [15].

The first method of comparison is the streamlines for the different orthogonal and non-orthogonal grids. The values of stream function shown in Figure 6.10 are listed in Table 6.3. The first test was with the orthogonal 20×20 grid as shown in Figure 6.10. The results indicate that the 20×20 grid is too coarse to accurately predict the flow. The main vortex minimum stream function value is 0.0835 $[m^3/s]$ which deviates by almost 27% from the minimum reported by Ghia et al.

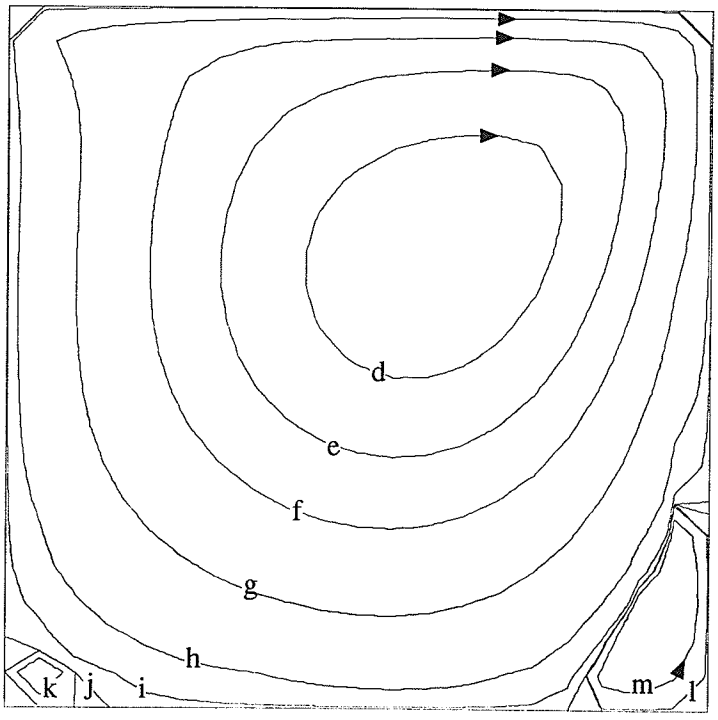

Figure 6.10: Square Lid-Driven Cavity Streamlines: Orthogonal 20×20 Grid.

At a resolution of 80×80, the streamlines shown in Figure 6.11 are qualitatively similar to those of Ghia et al. [11], with all the vortex centers in the correct locations. The location of the main vortex center is at (0.56,61). The location of the bottom right secondary vortex is at (0.89,0.13). The location of the bottom left secondary vortex is at (0.05,0.05). Ghia et al. resolve two additional vortices in the bottom corners with a 129×129 grid. The 80×80 grid used in this work does not resolve those details. The minimum stream function value for the main vortex is 0.1107 $[m^3/s]$ which deviates by only 2.8%.

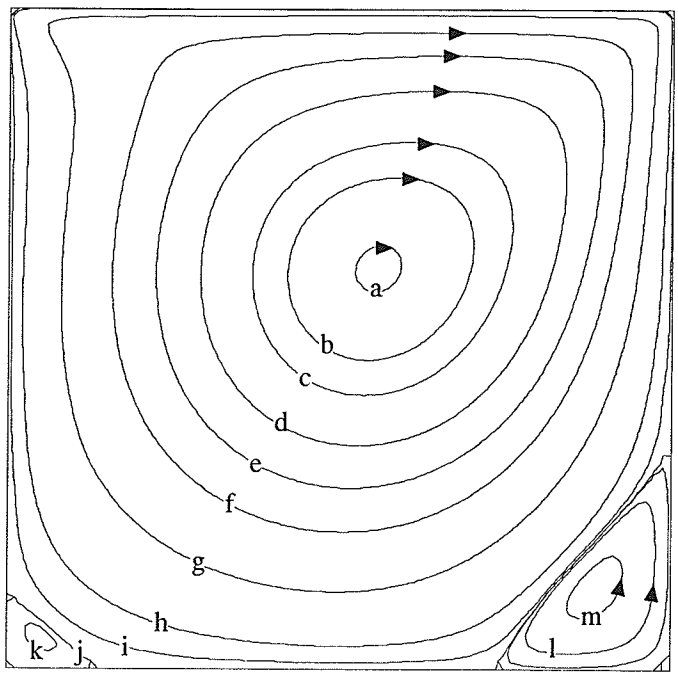

Figure 6.11: Square Lid-Driven Cavity Streamlines: Orthogonal 80×80 Grid.

In the process of generating the non-orthogonal grid, certain areas of the grid become more refined while others become more coarse. The non-orthogonal 20×20 grid results, shown in Figure 6.12, are slightly better than the coarse orthogonal grid because of some local grid refinement near the walls. The minimum stream function value for the main vortex is 0.0863 $[m^3/s]$ which deviates by 24%, so, overall, there is only a small improvement over the uniform orthogonal grid.

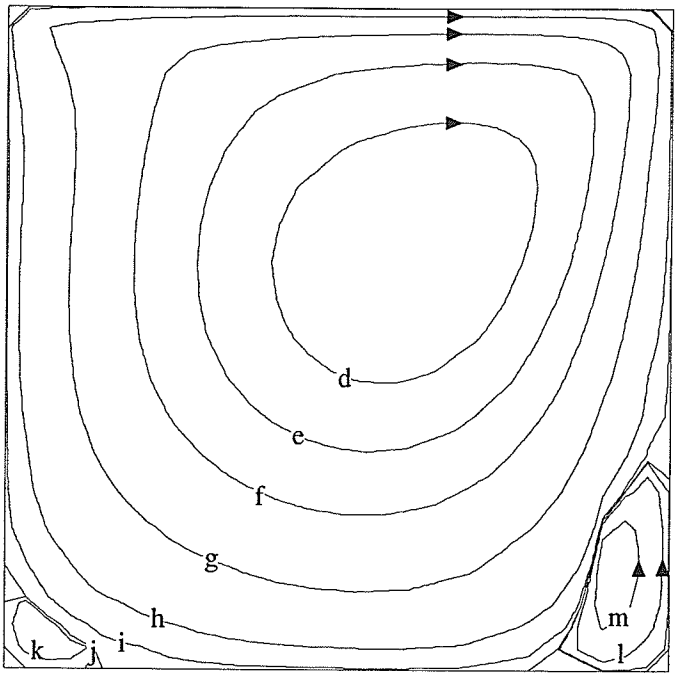

Figure 6.12: Square Lid-Driven Cavity Streamlines: Non-Orthogonal 20×20 Grid.

The non-orthogonal 80×80 grid results shown in Figure 6.13, also compare well with the results of Ghia et al.[11]. The vortex centers are at the same locations as in the orthogonal 80×80 grid so the different grid shape did not greatly affect the flow prediction. The minimum stream function value for the main vortex is $0.1107\,[m^3/s]$ which deviates by only 2.8%. This, again, was almost exactly the same as the orthogonal grid. The difference between the minimum stream function values of the orthogonal and non-orthogonal grid was only 0.03%.

A second method of comparison is by using the velocity profiles. Both Jessee and Fiveland [15] and Miller and Schmidt [23] have presented results that appear to be in agreement with Ghia et al. The present work has slightly lower peak velocities than Ghia et al [11]. For example, in Figure 6.14, the Ghia et al. data point at $y = 0.2813$ has a U velocity of $-0.32726\,[m/s]$, but the orthogonal grid result is $-0.3127\,[m/s]$, and the non-orthogonal grid result is $-0.3125\,[m/s]$, which are deviations of 4.4% and 4.5% respectively. There is only a

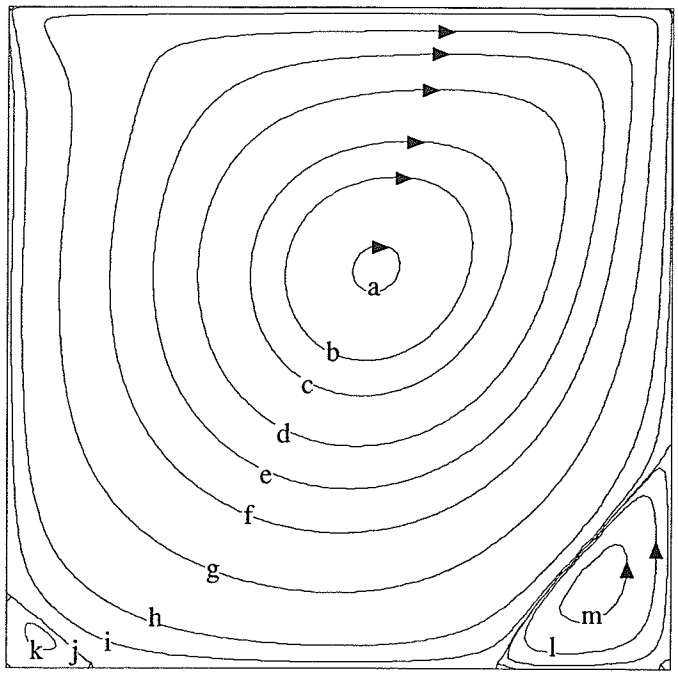

Figure 6.13: Square Lid-Driven Cavity Streamlines: Non-Orthogonal 80×80 Grid.

a	−0.11	f	−0.03	k	0.00001
b	−0.1	g	−0.01	l	0.0001
c	−0.09	h	−0.001	m	0.0005
d	−0.07	i	−0.0001		
e	−0.05	j	0.0		

Table 6.3: Stream Function Levels for Figures 6.10 through 6.13.

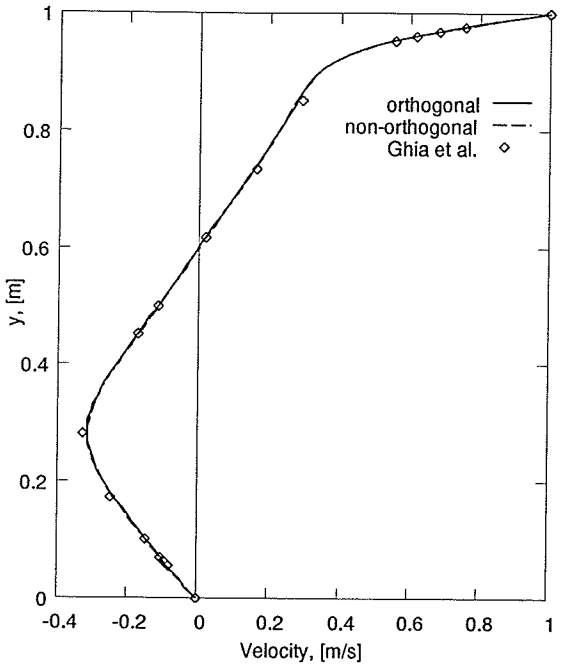

Figure 6.14: Square Lid-Driven Cavity U Velocity Profile along Vertical Centerline.

0.06% difference between the orthogonal and non-orthogonal peak U velocity.

The V velocity profile at the horizontal centerline is plotted in Figure 6.15. Ghia et al. report a V velocity of $-0.44993\,[m/s]$ at $x = 0.8594$. The results from the present work are velocity values of $-0.4374\,[m/s]$ for the orthogonal grid and $-0.4393\,[m/s]$ for the non-orthogonal grid, which are deviations of 2.8% and 2.4% respectively. There is a 0.4% difference between the orthogonal and non-orthogonal peak V velocity.

Considering that results of Ghia et al. were on a 129×129 grid and the present work only used an 80×80 grid, the results are quite satisfactory. Even though the present work uses different methods than either of the cited results, the solution was well within expected error and can be explained by the low-order, exponential upwinding scheme used in the present work. There is also no significant difference in the results produced by the orthogonal and non-orthogonal grids.

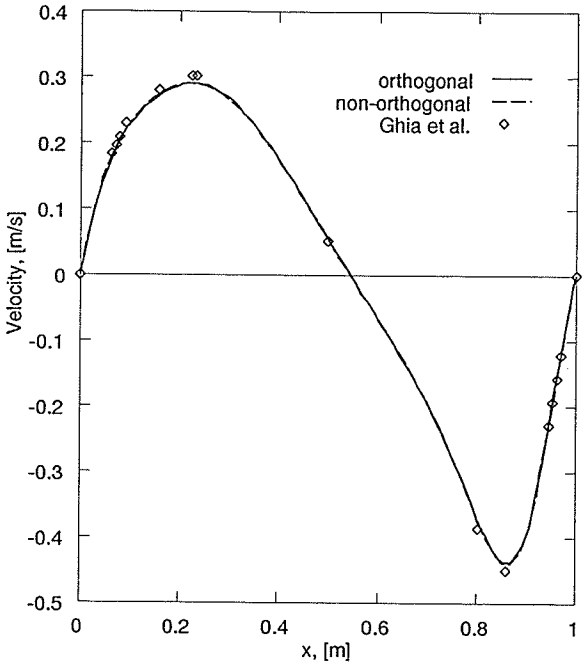

Figure 6.15: Square Lid-Driven Cavity V Velocity Profile along Horizontal Centerline.

6.3.2 Slug flow Through Tube Bundle

Flow between two parallel zero-shear boundaries is referred to in this work as a slug flow. In this demonstration, a fluid enters the left with a uniform inlet velocity of 1 $[m/s]$ between zero-shear boundaries, top and bottom, and has a fully-developed exit at the right. The fully-developed boundary condition is $\frac{\partial U}{\partial x} = 0$ and $V = 0$. The flow is expected to maintain the uniform profile and also to eventually recover it if disturbed. The fluid molecular viscosity is 2.082×10^{-5} $[N \cdot s/m^2]$ and the density is 0.995 $[kg/m^3]$.

This section is a demonstration of the pressure and velocity fluctuations at the edges of a tube bundle region. The test grids, as shown in Figure 6.16, provide different grid resolutions near the tube bundle boundary (the shaded area). Each grid is made of four panels of widths 0.2, 0.1, 0.1 and 0.2 $[m]$, with a height of 0.1 $[m]$. The two central panels define the tube bundle area. In Figure 6.16(a) each panel has expanding or contracting control

volumes so that the control volumes are concentrated at the edges of the tube bundle. The expansion factors of the four panels are 0.7, 1.15, 0.85, 1.3, respectively. In Figure 6.16(b) the control volumes remain uniform in each panel so no refinement occurs near the tube bundle boundaries.

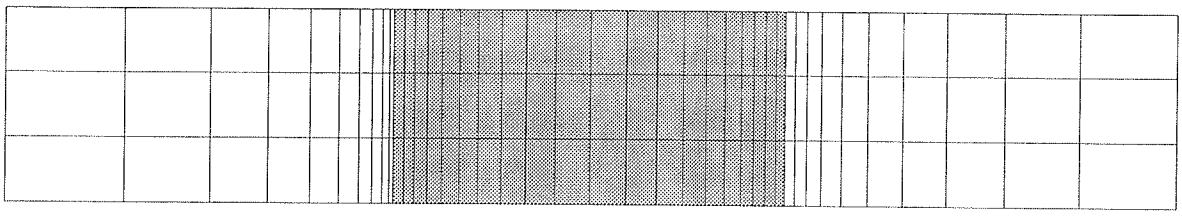

(a) Fine Grid.

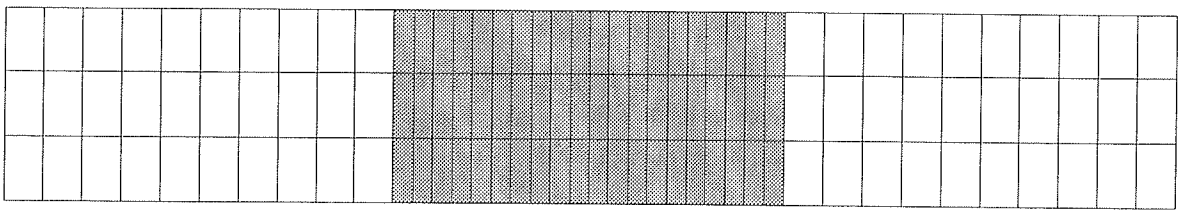

(b) Coarse Grid.

Figure 6.16: 40×3 Grids for Slug Flow with Porosity.

Figure 6.17 shows the velocity profiles along the horizontal centerline. The vertical lines indicate the leading and trailing edges of the tube bundle. The velocity increases inside the tube bundle because of the reduced flow area. The porosity is equal to 0.742 so the velocity is $1.0/0.742 = 1.348\,[m/s]$. The solid line represents a viscosity multiple of 25 and the dashed line a viscosity multiple of 100 on the refined grid. There appears to be very little difference in the velocity profile with respect to viscosity multiple. The dotted line in Figure 6.17 represents the velocity profile for $\mu * 100$, but on the coarse grid. The curve is much smoother than with the fine grid. The velocity details are not resolved on the coarse grid, the peaks are smaller and further away from the tube bundle.

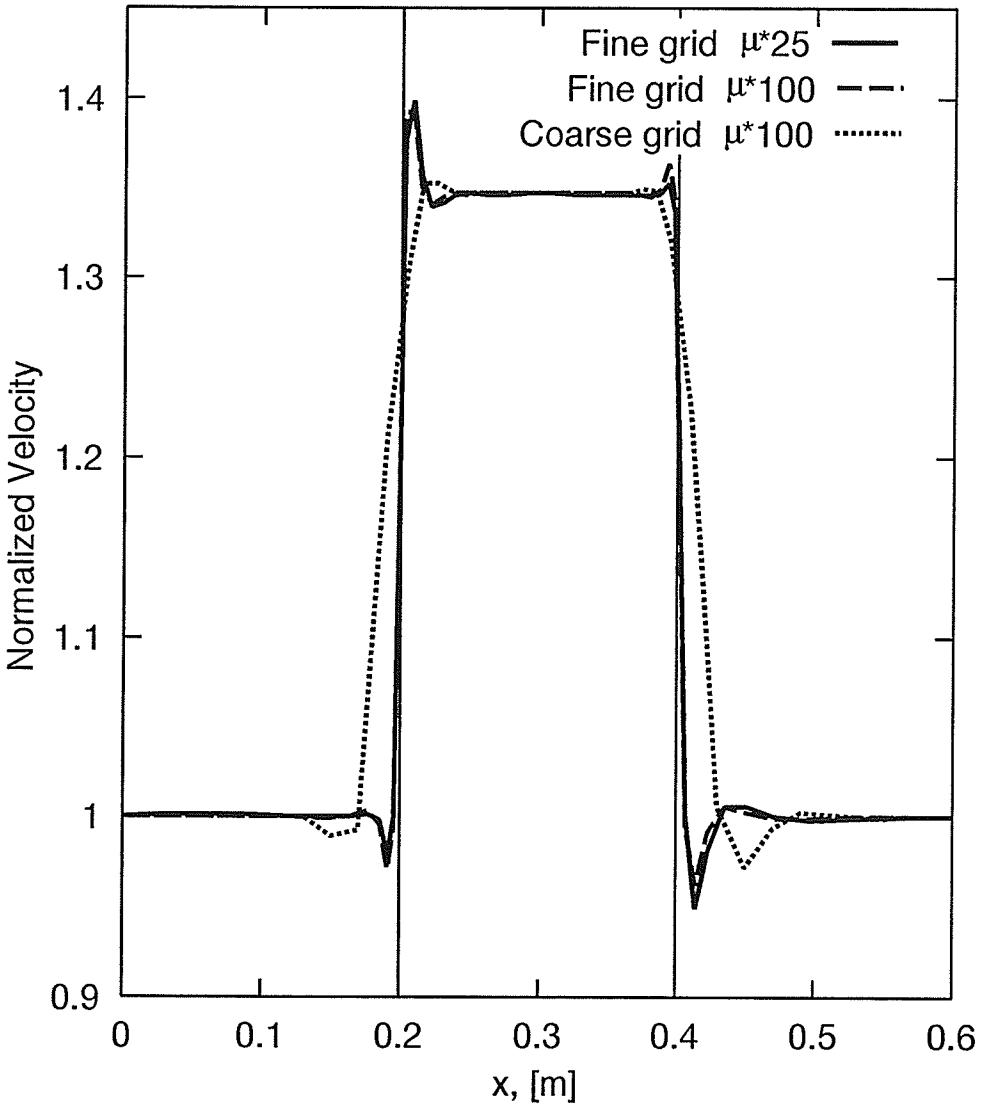

Figure 6.17: Slug Flow Velocity Profile.

Pressure profiles along the horizontal centerline are shown in Figure 6.18. The pressure profile for $\mu * 25$, the solid line, shows a small peak at both the leading and trailing edges of the tube bundle. As the viscosity multiple increases to $\mu * 100$, the dashed line, the pressure spike increase in size. This shows that the increase in viscosity multiple increases the severity of the edge effect. The coarser grid pressure profile at $\mu * 100$, the dotted line, has smoother transitions at the tube bundle edges than does the fine grid. The effect of the transition is spread over a larger area when using a coarse grid because only the first few control volumes are affected. If the control volumes are small all the change has to happen in a very short space thus creating larger pressure spikes. These pressure fluctuations cause problems in the PWIM which produce unrealistic face velocities as noted by Miller and Schmidt [23].

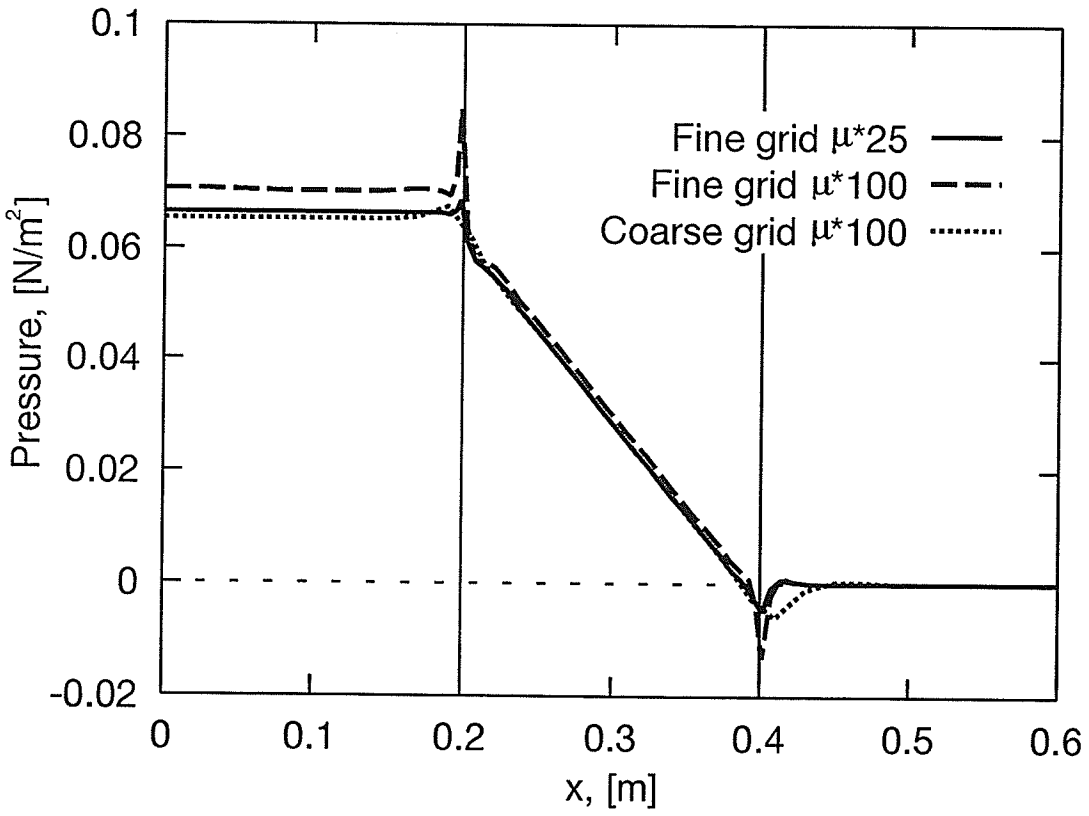

Figure 6.18: Slug Flow Pressure Drop.

The effective viscosity value has a significant effect on the overall pressure drop. The non-dimensional pressure drop, $\frac{\Delta p}{\frac{1}{2}\rho V_{in}^2}$, is 6.2% higher for the viscosity multiple of 100 than the multiple of 25 on the fine grid. The coarse grid pressure drop is for the fine grid even though the viscosity multiple is 100. Frisina et al.[9] refer to false pressure drop at tube bundle boundaries, or anywhere porosity changes, as being associated with upwind differencing. They indicate that central differencing should be used in the tube bundle to correct this problem. There also appears to be an effect caused by a change in the grid density and the turbulence level.

The pressure drop correlation used by Butterworth [3] gives a pressure gradient of $\frac{\partial P}{\partial x} = -0.3234\,[N/m^3]$ for the conditions used in this test problem. To compare with the theoretical value, the pressure gradient in the tube bundle was estimated by subtracting the pressure at $x = 0.25$ from the pressure at $x = 0.35$ and dividing by the distance between the two chosen nodal pressures. This method avoids including the edge effects in the pressure drop measurement. The measured pressure drop inside the tube bundle is $\frac{\partial P}{\partial x} = -0.3235\,[N/m^3]$ for the coarse grid and $\frac{\partial P}{\partial x} = -0.3237\,[N/m^3]$ for the fine grid. This close comparison of the pressure gradient shows that the computer code is reproducing virtually the same results as the correlation.

The overall pressure drop can be estimated by taking the pressure drop of the tube bundle interior and extrapolating over the entire tube bundle width, $0.2\,[m]$. The result is a pressure drop of $\frac{\Delta P}{0.2} = -0.0647\,[N/m^3]$ for the correlation. To compare the present with this value the pressure at the entrance was subtracted from the exit pressure, and divided by the tube bundle width. The fine grid pressure drop for $\mu * 25$ was $\frac{\Delta P}{0.2} = -0.0662\,[N/m^3]$, which is 2.3% too high, and, for $\mu * 100$, was $\frac{\Delta P}{0.2} = -0.0703\,[N/m^3]$, which is 8.6% too high. The coarse grid at $\mu * 100$ had a pressure drop of $\frac{\partial P}{\partial x} = -0.0653\,[N/m^3]$, which is 0.9% too high. These measurements quantify the amount of false pressure drop for each grid and viscosity multiple.

This section has demonstrated that refining the grid at a tube bundle boundary causes velocity and pressure fluctuations when combined with increased viscosity. The pressure drop in the interior of the tube bundle, avoiding edge effects, compares well with the pressure drop correlation given by Butterworth [3].

This test problem is presented to briefly introduce the fluctuations in velocity and pressure that occur when simulating flow in and out of a porous region. These phenomena are presented because they occur in problems in Chapter 7. The resolution of these issues is beyond the scope of this work.

6.3.3 Parallel Plates

The purpose of the parallel plate flow test is to show the effect the grid has on the solution and to compare the results to theoretical values. For flow between parallel plates, a long narrow solution domain was defined representing half the distance between plates. The aspect ratio of the domain is 10 : 1 with the half width $h = 1$. The geometry is shown in Figure 6.19. The first section, from the entrance to $x = 4.5h$, contains either an orthogonal or a non-orthogonal grid. The rest of the domain, up to $x = 10h$ was the same for all grids. That region has expanding orthogonal control volumes, with a factor of 1.02, in order to allow the fluid enough length to become fully-developed. The dashed lines indicate the

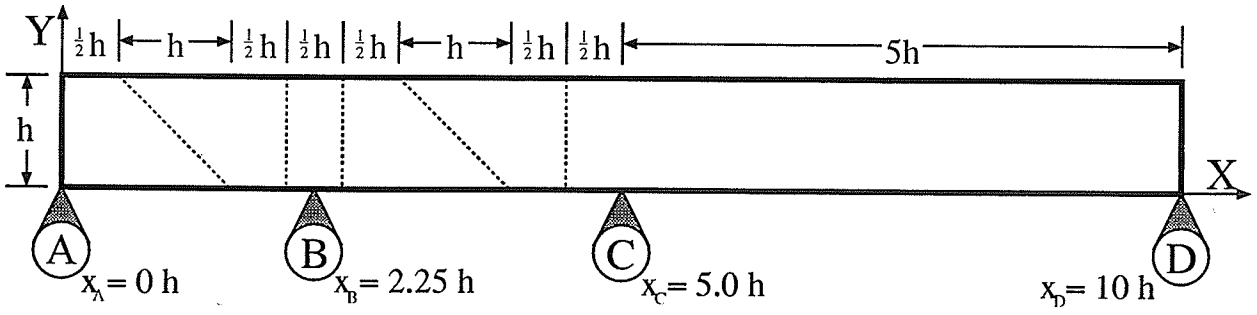

Figure 6.19: Parallel Plate Test Problem Domain Dimensions.

edges of panels for the non-orthogonal grids.

Three grids were used to produce results for this problem. The first was the orthogonal grid shown in Figure 6.20(a). The first 45 control volumes are uniformly spaced up to $x = 4.5h$ and then 25 more are expanded up to $x = 10h$. The second is a non-orthogonal grid shown in Figure 6.20(b). This grid has three panels of uniformly-spaced control volumes: 10 control volumes from the entrance to the first diagonal dashed line in Figure 6.19, 25 control volumes up to the second diagonal dashed line, and another 10 up to the dashed line at $x = 4.5h$. The third grid is also non-orthogonal (Figure 6.20(c)) but with an orthogonal section around marker "B", in the middle of the skewed area of the second grid. This grid has five panels of uniformly-spaced control volumes: 10 control volumes from the entrance to the first diagonal dashed line, 10 control volumes up to the first vertical dashed line, 5 control volumes up to the second vertical dashed line, 10 control volumes up to the second diagonal dashed line, and another 10 up to the dashed line at $x = 4.5h$.

The boundary conditions for this problem are a solid wall on the bottom, symmetry on the top, a uniform inlet on the left, and fully developed conditions on the right. The inlet velocity is 7.7685×10^{-4} $[m/s]$. The working fluid viscosity is 2.082×10^{-5} $[N \cdot s/m^2]$ and the density is 0.995 $[kg/m^3]$. The Reynolds number based on channel width, $2h$, is $Re = 74.25$, so the flow should be fully developed at about $x = 7.4h$ and the fully-developed boundary condition is acceptable.

Figure 6.21 shows normalized U velocity profiles at three different x locations on the three different grids. The first profile is at $x = 2.25h$ (marker "B" in Figure 6.19). The second profile is at $x = 5.0h$ (marker "C") and the third profile is at the end of the grid, at $x = 10.0h$ (marker "D").

It is clear in Figure 6.21 that the U velocity becomes fully developed towards $x = 10h$. The profiles for $x = 5.0h$ and $x = 10h$ are very similar, indicating that the flow is almost fully developed at $x = 5.0h$. In addition, the three different grids produce the same velocity

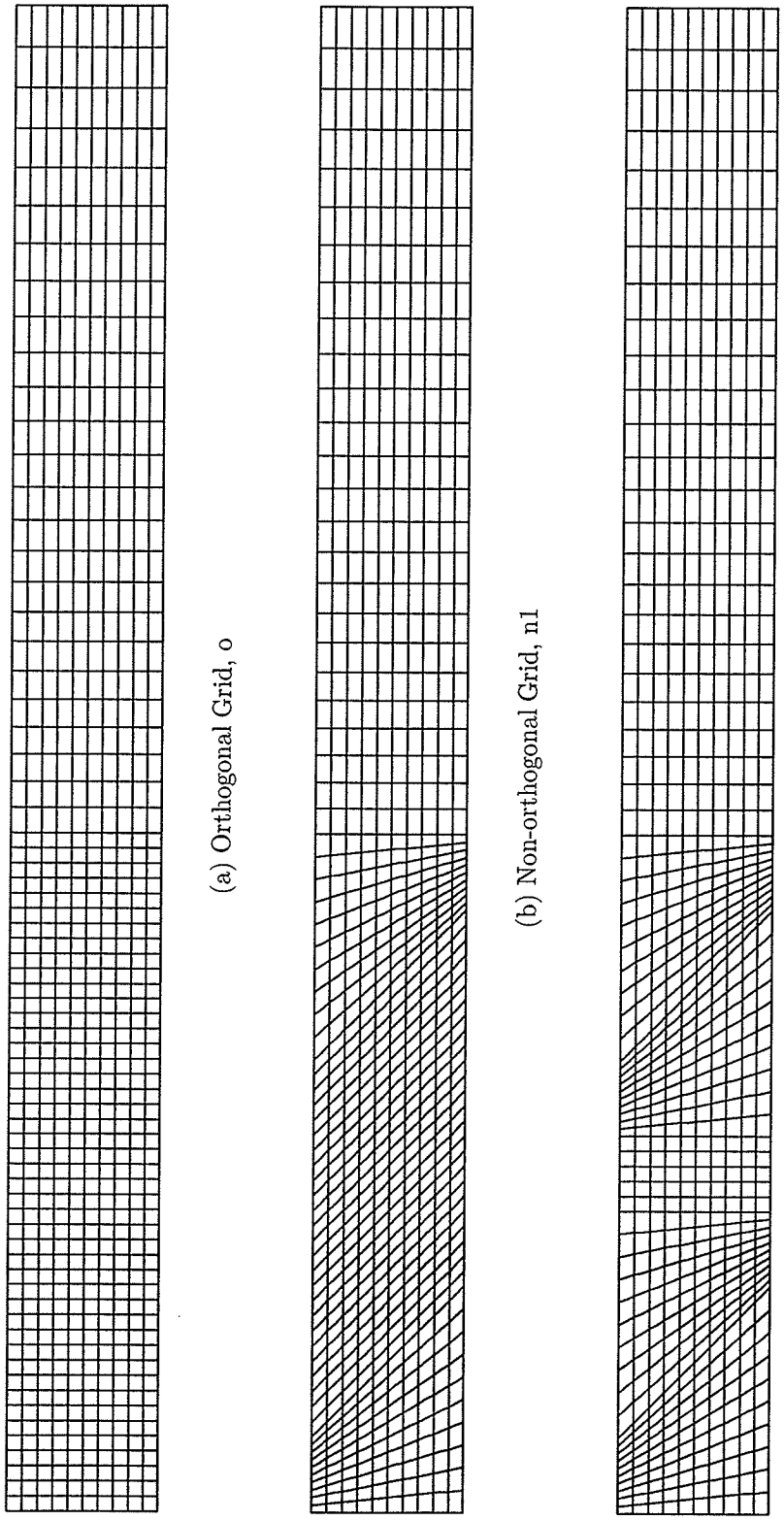

(a) Orthogonal Grid, o

(b) Non-orthogonal Grid, n1

(c) Non-orthogonal Grid, n2

Figure 6.20: Parallel Plate Problem, 70×10 Grids.

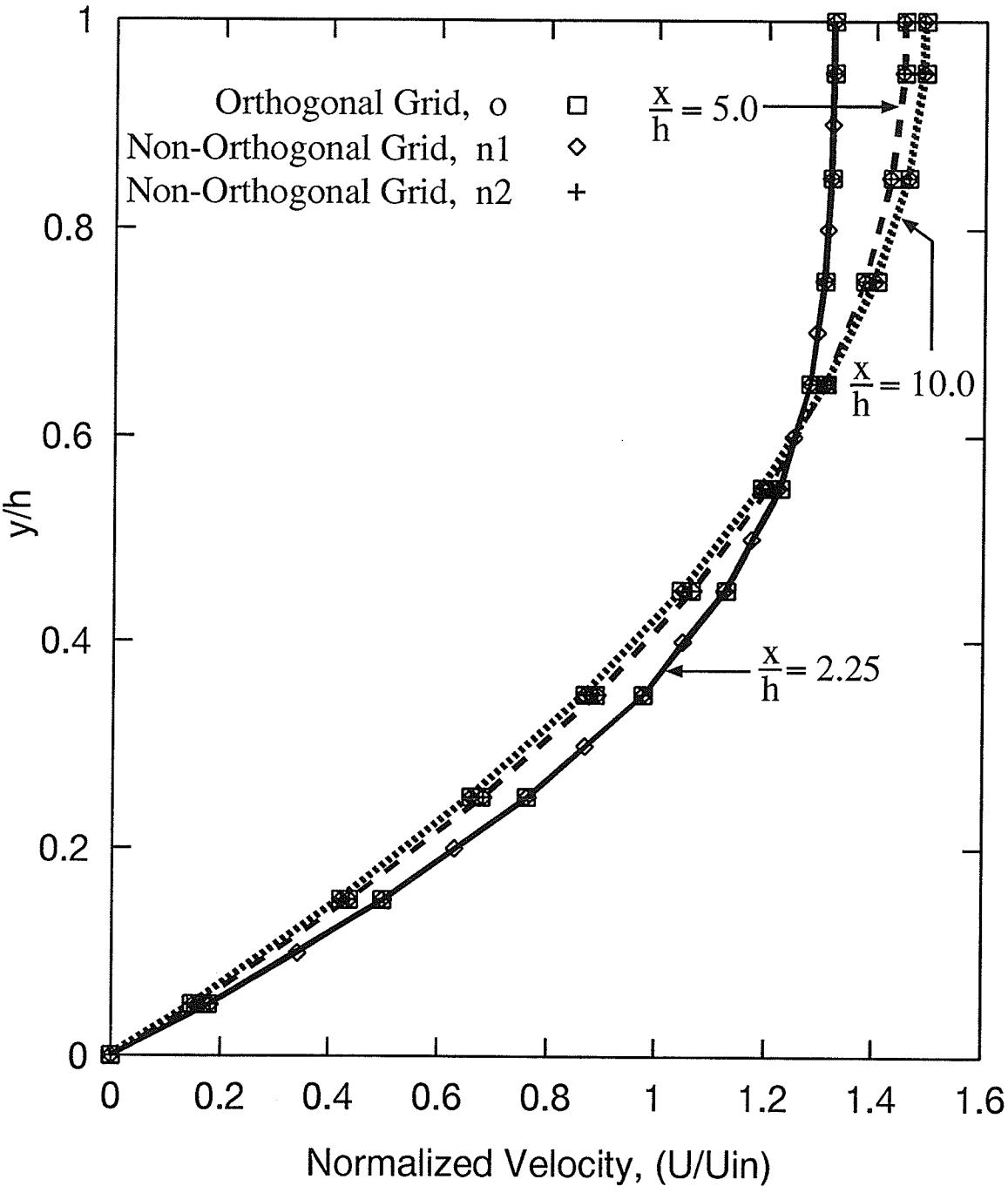

Figure 6.21: Parallel Plates U Velocity Profiles.

profiles at each of the three locations. At this resolution, 10 control volumes in half the cross stream width, there is no significant difference between the orthogonal and the two non-orthogonal grid solutions. Maximum normalized U velocity is 1.4879 $[m/s]$ which is 0.8% error from the expected theoretical value of 1.5 $[m/s]$.

Chapter 7

Results and Discussion

7.1 Introduction

This chapter presents the results for two advanced test problems. The test problems each contain a tube bundle region that is not aligned with a Cartesian grid. This permits comparing the results for aliasing the tube bundle boundaries, on a Cartesian grid, versus matching of the boundaries, with a non-orthogonal grid.

The first test problem presented here builds on the parallel plate problem in Section 6.3.3 by adding a tube bundle in the slanted part of the grid. Tube bundle effects were first demonstrated in the slug flow through an orthogonal tube bundle in Section 6.3.2. The first test problem focuses on the effects of the porous region and the non-orthogonal grid together by analyzing slug flow through a tube bundle slanted at 45 degrees. The 45^o slant is designed to cause the greatest aliasing error in the orthogonal grid.

The second test, a simple model of a heat exchanger, combines non-orthogonal porous region boundaries with blockages, sealing strips and a rectangular shell. The blockages, sealing strips, and shell are kept Cartesian so the orthogonal grid lines match the general shape. Only the tube bundle sides and the tip of one blockage are at a 45^o angle to maximize

aliasing and utilize the advantages of the non-orthogonal grid. Therefore, the only aliasing is of the tube bundle and blockage. In heat exchangers the flow is often turbulent so a simple constant viscosity turbulence model is used along with wall functions. The same effective viscosity is used for both grid systems.

7.1.1 Slug flow through a Tube Bundle.

Slug flow is a simple test with a known solution which was introduced in Section 6.3.2 with an orthogonal tube bundle perpendicular to the direction of flow. A uniform inlet velocity profile should remain uniform, unless some disturbance exists, and should return to uniform profile given sufficient distance. This test problem does not contain any solid wall boundaries or internal blockages so that the focus is only on the aliasing issue on the boundaries of a the slanted tube bundle.

The test grids are the same as for the parallel plate test and the dimensions are shown in Figure 6.19. The inlet flow velocity is $U_{in} = 1.4647 \times 10^{-2}$ $[m/s]$ entering the left boundary (at marker "A" in Figure 6.19). The outflow at the right (marker "D") was fully developed. Both top and bottom are zero-shear boundaries. The fluid density is 0.995 $[kg/m^3]$ and the molecular viscosity is 2.082×10^{-5} $[N \cdot s/m^2]$.

Figure 7.1 shows the grids used in this test with an addition of a tube bundle. The tube bundle region, shown as the shaded area, is defined by the 45^o diagonal line from $0.5h$ to $1.5h$ on the left, and the 45^o diagonal line from $3h$ to $4h$ on the right. The stepwise aliasing of the tube bundle boundary can be seen in Figure 7.1(a). The grid shown in Figure 7.1(b) is the first of two non-orthogonal grids that were used. The grid lines are skewed so that they match the tube bundle boundary along the control volume faces. The grid shown in Figure 7.1(c) is a second non-orthogonal grid. It was created with an orthogonal section, of width $0.5h$, embedded in the center of tube bundle region (at marker "B" in Figure 6.19) to compare the velocity profiles in that region.

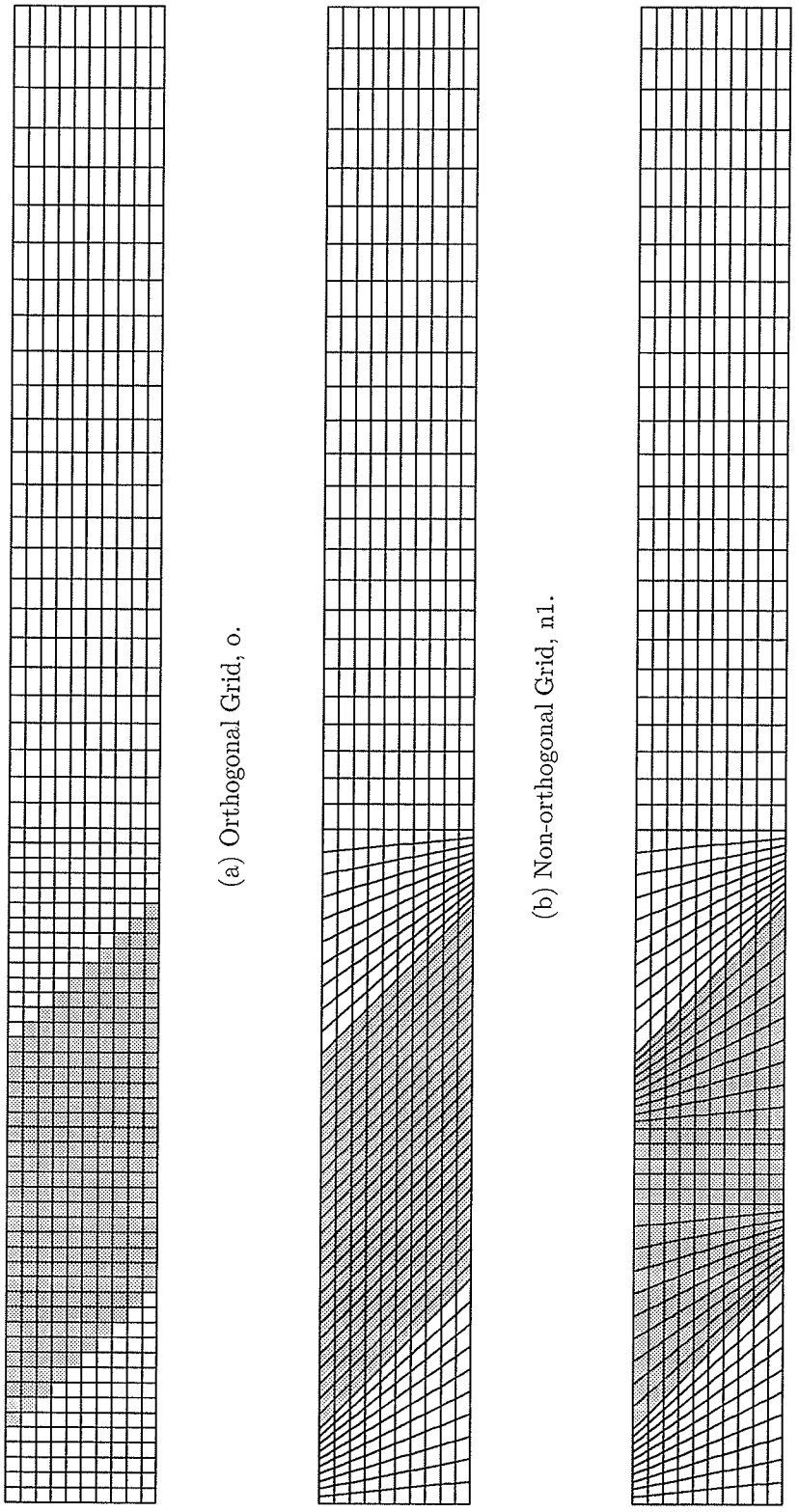

(a) Orthogonal Grid, o.

(b) Non-orthogonal Grid, n1.

(c) Non-orthogonal Grid, n2.

Figure 7.1: Slug Flow with 45° Tilted Tube Bundle, 70×10 Grids.

Three grid resolutions were used: 70×10, 140×20, and 210×30 to determine how grid density affects the solution. The grids were chosen by defining a coarse grid and multiplying the number of nodes in each direction by 2 and 3 to define the finer grids. For this work, a particular solution is said to be grid independent if the change in a representative measurement of the solution falls below a given criterion as the grid is refined by the steps indicated above. The non-dimensional pressure drop was chosen as an overall measurement and the velocity ranges at cross-section "C" were used as a local measurement of the solution.

There are also three viscosity multiples: the effective viscosity is set to 25, 50 and 100 times the molecular viscosity. These viscosity multiples are used to verify the trends toward grid independence for different models of turbulence effects. The $\mu * 25$ and $\mu * 100$ results are presented here while the $\mu * 50$ results are found in Appendix C.1.

Streamline Plots

Figures 7.2 through 7.7 show plots of the streamlines for slug flow with a slanted tube bundle. The stream function levels are chosen to illustrate the general flow patterns. The streamlines are evenly spaced except for at the top and bottom boundaries. In those areas more streamlines are shown to resolve flow details. A zero stream function level is used to mark the edge of a recirculation zone if one exists.

The first set of results for a 70×10 grid and a viscosity multiple of $\mu * 25$ are shown in Figure 7.2. The streamlines show that, at this grid density, there can be a large difference in the flow solution depending on which type of grid is used. The streamlines, in all three cases, are similar through the tube bundle but differ at the trailing edge. There exists a recirculation zone after the trailing edge of the tube bundle because flow is diverted upward to exit the tube bundle in the shortest possible path. The orthogonal grid solution, with the same properties, shows a much smaller recirculation zone than solutions on the non-orthogonal grids. This difference is caused by the edge effects at the 45^o diagonal in the

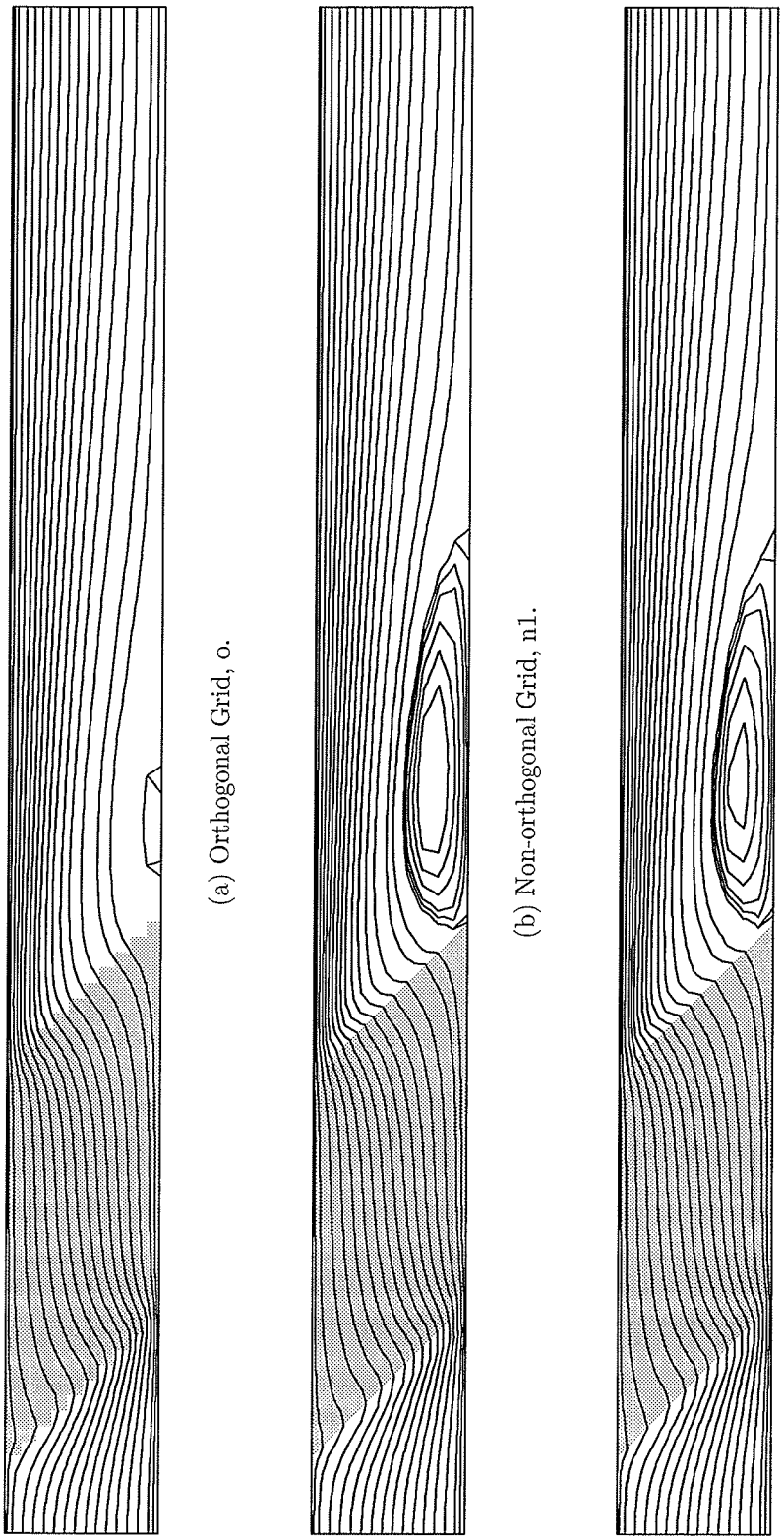

(a) Orthogonal Grid, o.

(b) Non-orthogonal Grid, n1.

(c) Non-orthogonal Grid, n2.

Figure 7.2: Slug Flow Streamlines: 70×10 Grid, $\mu * 25$.

non-orthogonal grid. A discontinuity of the streamlines at the trailing edge can be seen in Figures 7.2(b) and 7.2(c). The extra diversion of flow upward causes a larger recirculation zone (flow separation) that takes longer to close. There will be more discussion of the porous region edge effects and the PWIM shortly.

The outlet is forced to be fully-developed by the outlet boundary conditions. Figure 7.2 indicates that the streamlines are not evenly spaced like at the inlet, but are compressed towards the top of the domain. Later the velocity profiles will show more clearly that the flow does not return completely to a uniform profile at the exit for the $\mu * 25$ viscosity multiple.

The second set of results, shown in Figure 7.3, has the same conditions as in Figure 7.2, but double the grid density, 140×20. Smaller recirculation zones and smoother streamlines are seen in Figure 7.3 as compared to Figure 7.2. The discontinuity at the trailing edge of the tube bundle is still there, but it is smaller than the coarser grid. The orthogonal grid shows almost no change from the coarser grid, while the results on the two non-orthogonal grids show a dramatically reduced recirculation zone.

The third set of streamlines, shown in Figure 7.4, has the same conditions as in Figure 7.2, but triple the grid density, 210×30. These results have smaller recirculation zones than either Figure 7.2 or Figure 7.3. Note that while the orthogonal grid streamlines have not changed very much from the 70×10 grid results, the two non-orthogonal grid results have changed markedly to become much closer to the orthogonal grid.

The fourth set of streamlines are for the 70×10 grid, but with $\mu * 100$, are shown in Figure 7.5. The streamlines appear very similar for each grid. The discontinuity at the trailing edge of the tube bundle is still visible although not as pronounced as with the lower viscosity multiples and there is no recirculation zone.

The fifth set of streamlines, shown in Figure 7.6, has the same effective viscosity as in Figure 7.5, but are the results for the 140×20 Grid. These results have no recirculation zone and all three grids produce qualitatively the same results. Very little change can be seen

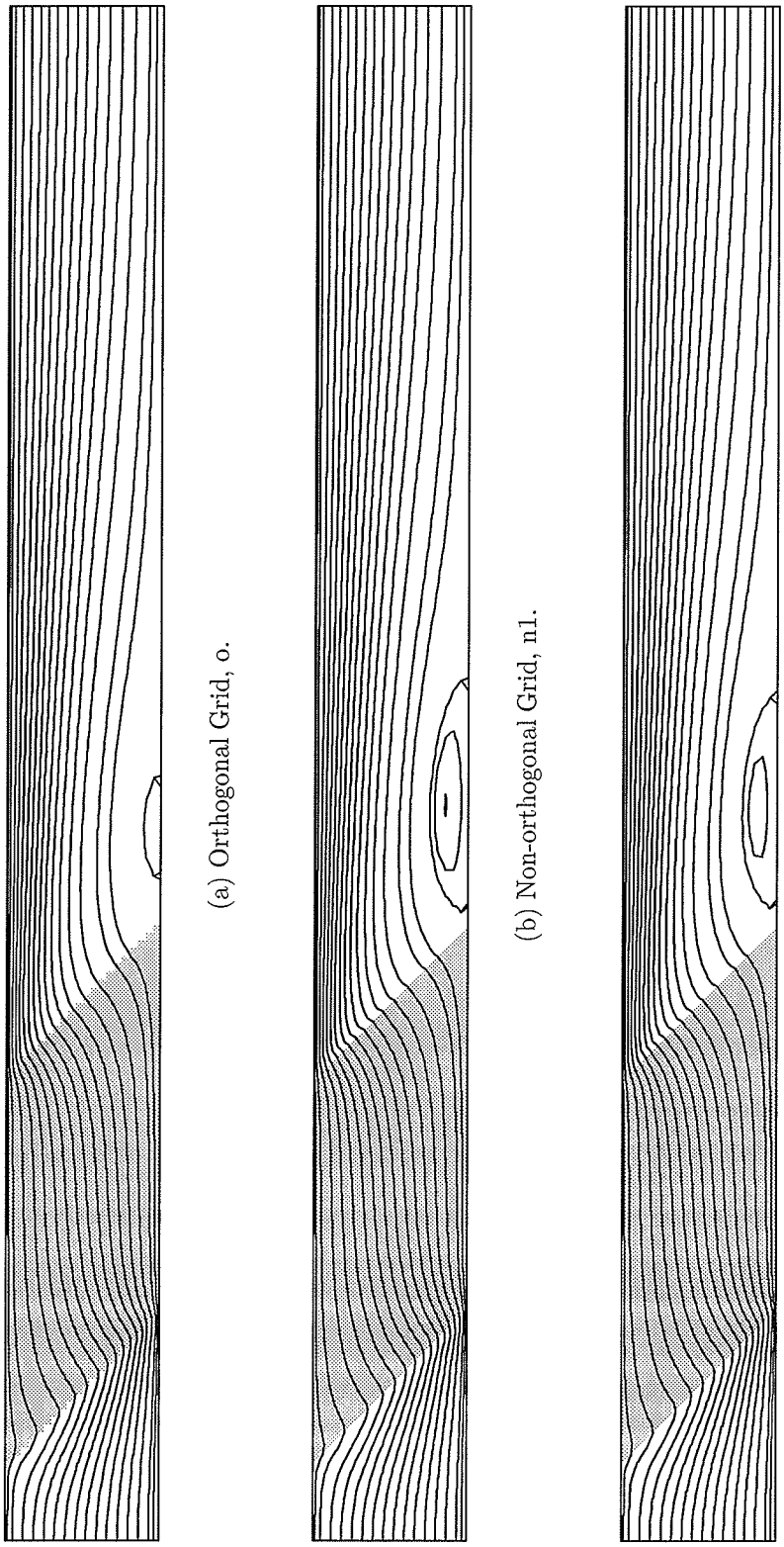

(a) Orthogonal Grid, o.

(b) Non-orthogonal Grid, n1.

(c) Non-orthogonal Grid, n2.

Figure 7.3: Slug Flow Streamlines: 140×20 Grid, $\mu * 25$.

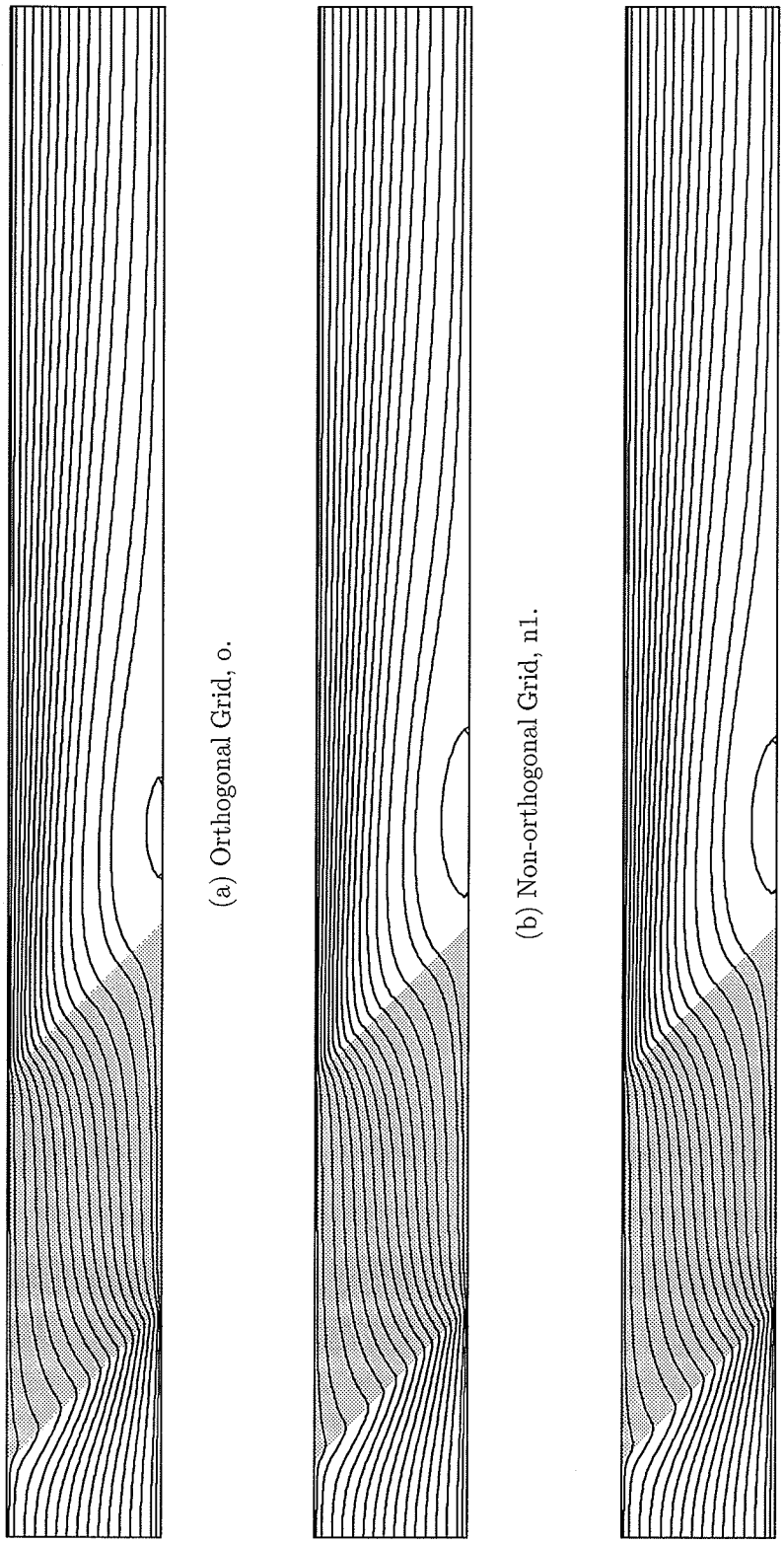

(a) Orthogonal Grid, o.

(b) Non-orthogonal Grid, n1.

(c) Non-orthogonal Grid, n2.

Figure 7.4: Slug Flow Streamlines: 210×30 Grid, $\mu * 25$.

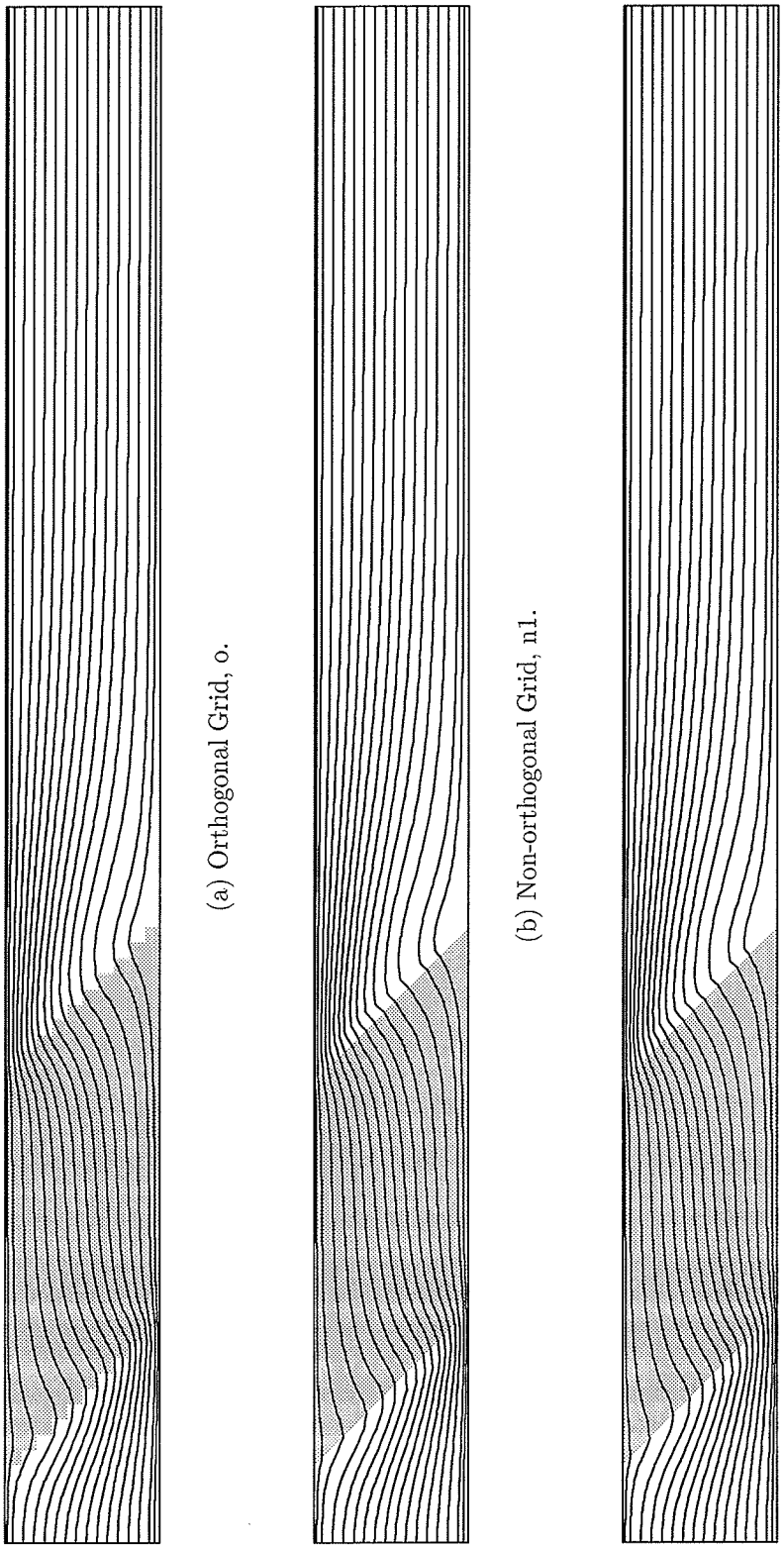

(a) Orthogonal Grid, o.

(b) Non-orthogonal Grid, n1.

(c) Non-orthogonal Grid, n2.

Figure 7.5: Slug Flow Streamlines: 70×10 Grid, $\mu * 100$.

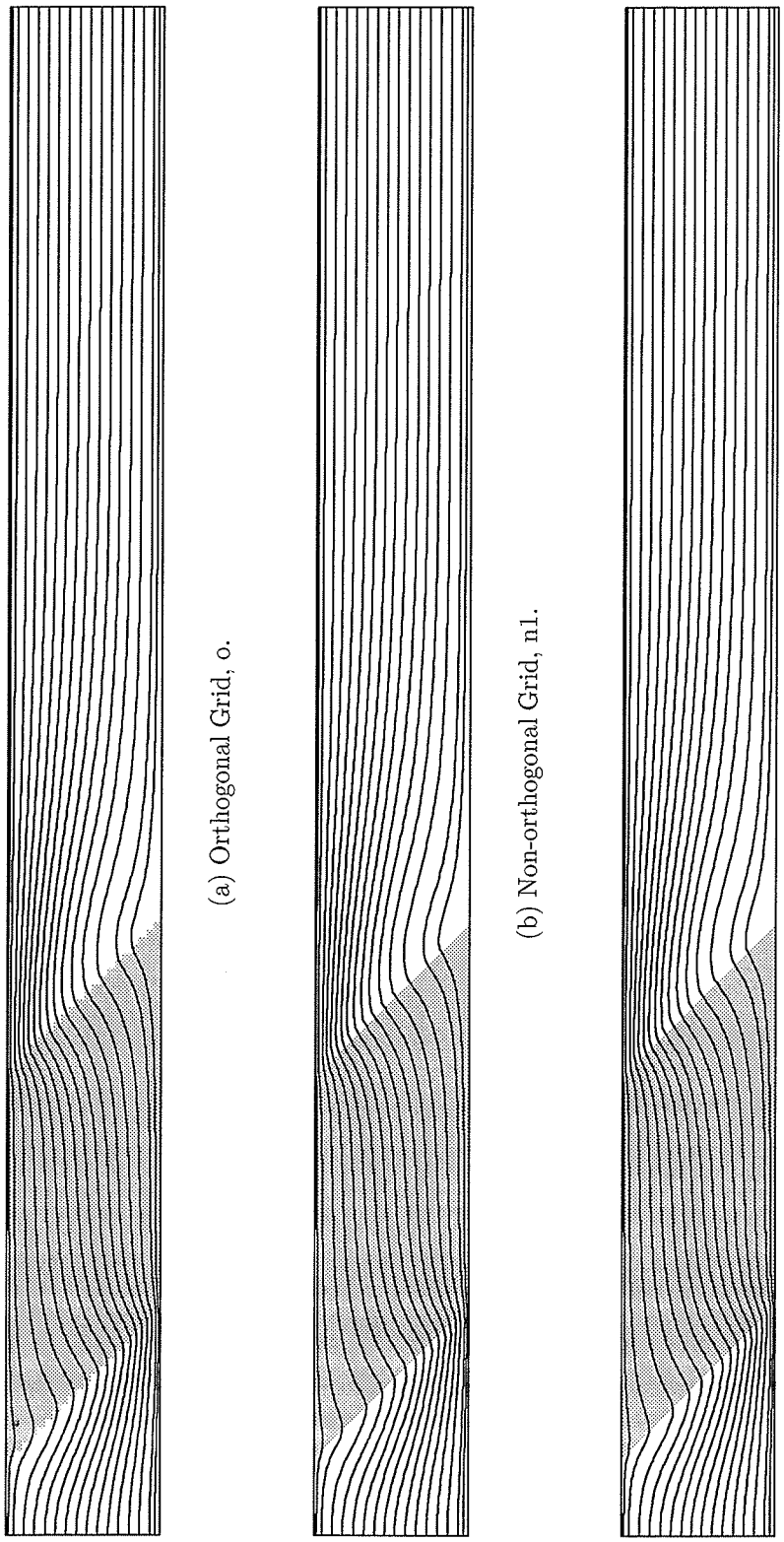

(a) Orthogonal Grid, o.

(b) Non-orthogonal Grid, n1.

(c) Non-orthogonal Grid, n2.

Figure 7.6: Slug Flow Streamlines: 140×20 Grid, $\mu * 100$.

from the coarser grid results for the same viscosity multiple (Figure 7.5).

The sixth set of streamlines, shown in Figure 7.7, has the same effective viscosity as in Figure 7.5, but are the results for the 210×30 Grid. These results have no recirculation zone and are very similar to their counter parts for the lower grid density (140×20).

Velocity Profile Plots

The velocity profiles, Figures 7.8 through 7.13, show the U component of velocity normalized by the inlet velocity. The y axis is the vertical distance across the domain normalized by the grid height. The three profiles are taken at $x = 2.25h$, $x = 5h$, and $x = 10h$. These positions are indicated in Figure 6.19 by the markers "B", "C", and "D", respectively. For each profile location there are three grids indicated as "o", "n1", and "n2" for the orthogonal, non-orthogonal, and composite non-orthogonal grids, respectively, as shown in Figure 7.1.

Figure 7.8 shows the profiles for the coarsest (70×10) grid and the lowest viscosity multiple, $\mu * 25$. The cross-section velocity profile, at marker "B", appears like a normal slug flow. Even though the flow has been diverted towards the bottom of the domain by the tube bundle entrance, the flow has come back to normal by the middle of the tube bundle. The increased velocity is because of the reduced flow area from the porosity approximation to the tube bundle, $1/\mathcal{E} = 1.35$.

The cross-section at marker "C", is just after the tube bundle and therefore shows the recirculation zone for the non-orthogonal grids. Figure 7.8 shows that the non-orthogonal grids have a higher velocity than the orthogonal solution near the top of the domain and a larger negative velocity at the bottom. The U velocity profile at marker "C" on the orthogonal grid at the bottom boundary is very close to zero and at about $2.36\,[m/s]$ at the top boundary. The second non-orthogonal grid, "n2", has a velocity range of $-0.19\,[m/s]$ at the bottom to $2.74\,[m/s]$ at the top. This represents a 24% larger range of velocities than the orthogonal grid results. In all cases the "n2" grid had a slightly smaller range than the

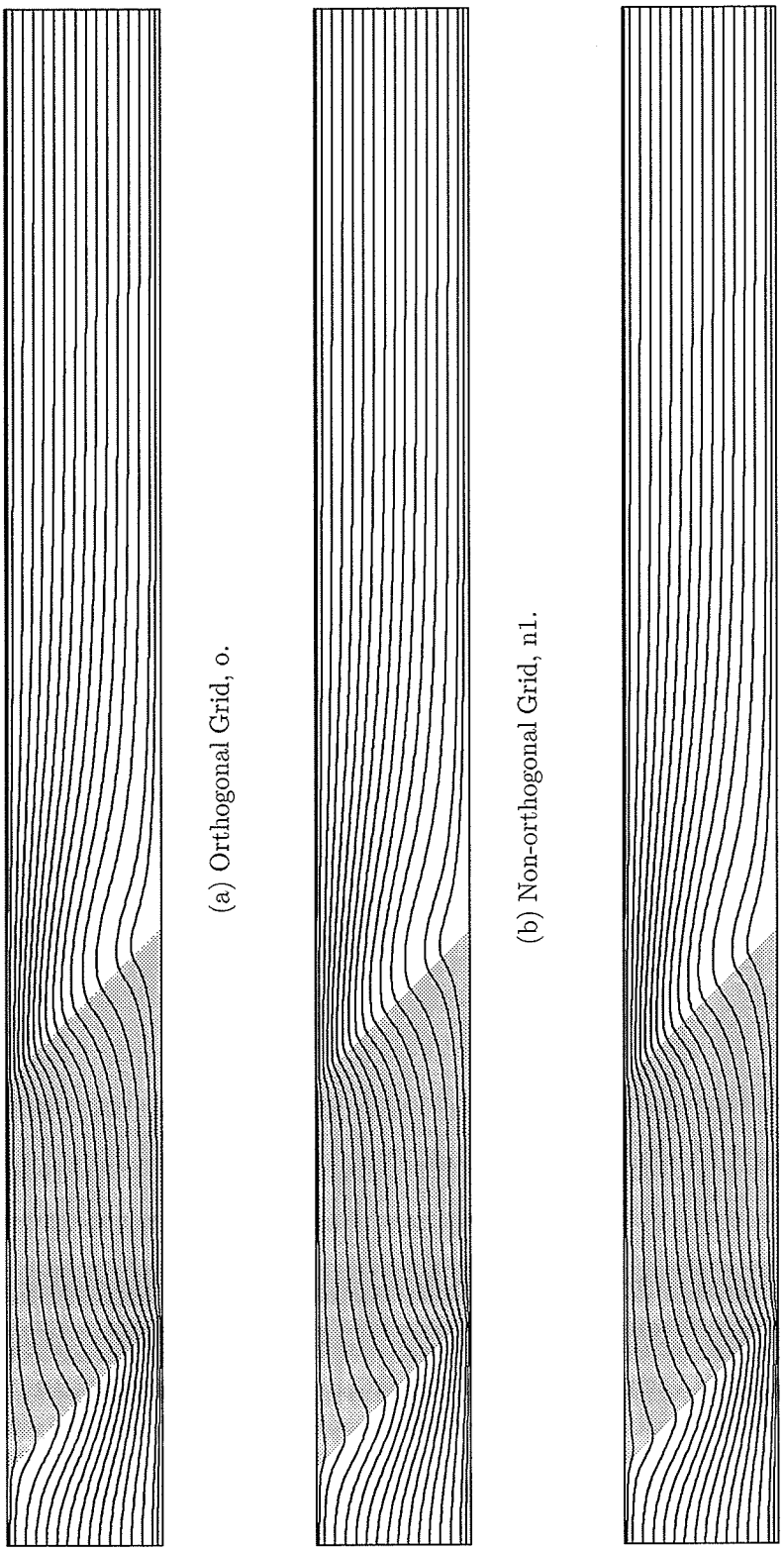

(a) Orthogonal Grid, o.

(b) Non-orthogonal Grid, n1.

(c) Non-orthogonal Grid, n2.

Figure 7.7: Slug Flow Streamlines: 210×30 Grid, $\mu * 100$.

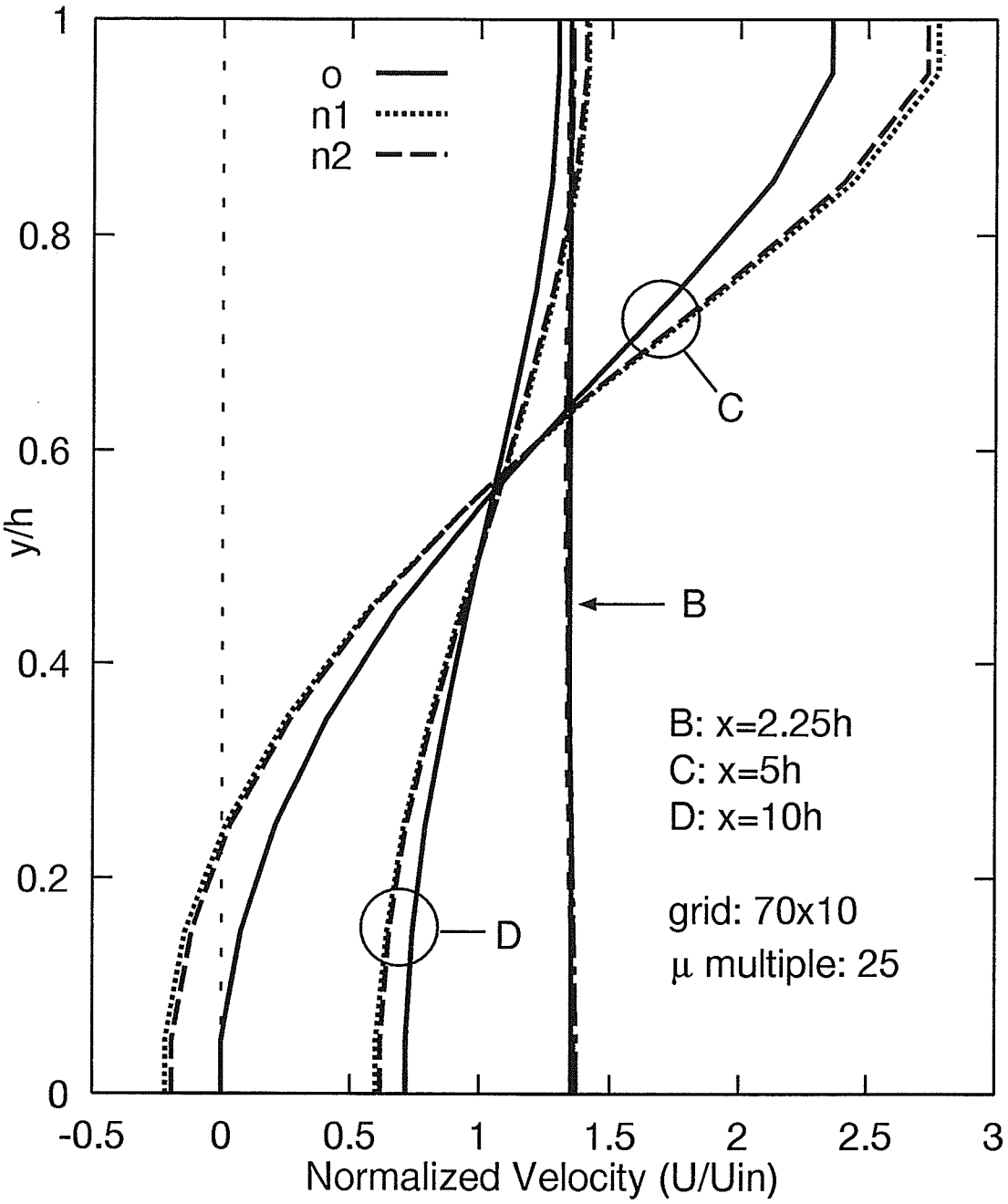

Figure 7.8: Slug Flow Normalized U Velocity Profiles: 70×10 Grid, $\mu * 25$.

"n1" grid. The only difference between the "n1" and "n2" grid is that the "n2" grid has the small orthogonal section in the middle of the tube bundle, at $y = 2.25h$. Therefore, only the "n2" grid profiles are presented here in comparison with the orthogonal grid results.

The cross-section velocity profiles at marker "D", at the end of the domain, show that the flow has not recovered the expected uniform profile. The velocity profile on the orthogonal grid varies from about 0.71 $[m/s]$ at the bottom to about 1.30 $[m/s]$ at the top which is a range of 0.59 $[m/s]$.

Figure 7.9 shows the profiles for the middle grid density, 140×20, and the same effective viscosity as in Figure 7.8. The velocity profile at "C" on the orthogonal grid now ranges from very close to zero at the bottom to 2.33 $[m/s]$ at the top. This represents a 1.3% decrease in range from the lowest grid resolution of Figure 7.8. This shows that the doubling of grid resolution had a very small effect on the orthogonal grid.

The second non-orthogonal grid, "n2", has a velocity ranging from -0.05 $[m/s]$ at the bottom to 2.44 $[m/s]$ at the top. This represents a 6.9% larger range of velocities than the orthogonal grid results, and a 15% decrease in range of velocities from the coarser non-orthogonal grid. This shows that the doubling of the non-orthogonal grid resolution had a large effect, bringing its results much closer to that of the orthogonal grid.

The velocity profile at "D" has not recovered the expected uniform profile, its range is very similar to the coarser grid. The velocity profile for the orthogonal grid varies from about 0.73 $[m/s]$ at the bottom to about 1.28 $[m/s]$ at the top which is a range of 0.55 $[m/s]$. In each cross-section the velocity profiles for the non-orthogonal grid have come closer to the orthogonal grid results with the increase in grid resolution.

Figure 7.10 shows the profiles for the fine grid, 210×30, and the same effective viscosity as in Figure 7.8. The velocity profile at "C" on the orthogonal grid now ranges from very close to zero at the bottom to 2.32 $[m/s]$ at the top. This represents a 0.4% decrease in range from the middle grid resolution of Figure 7.9.

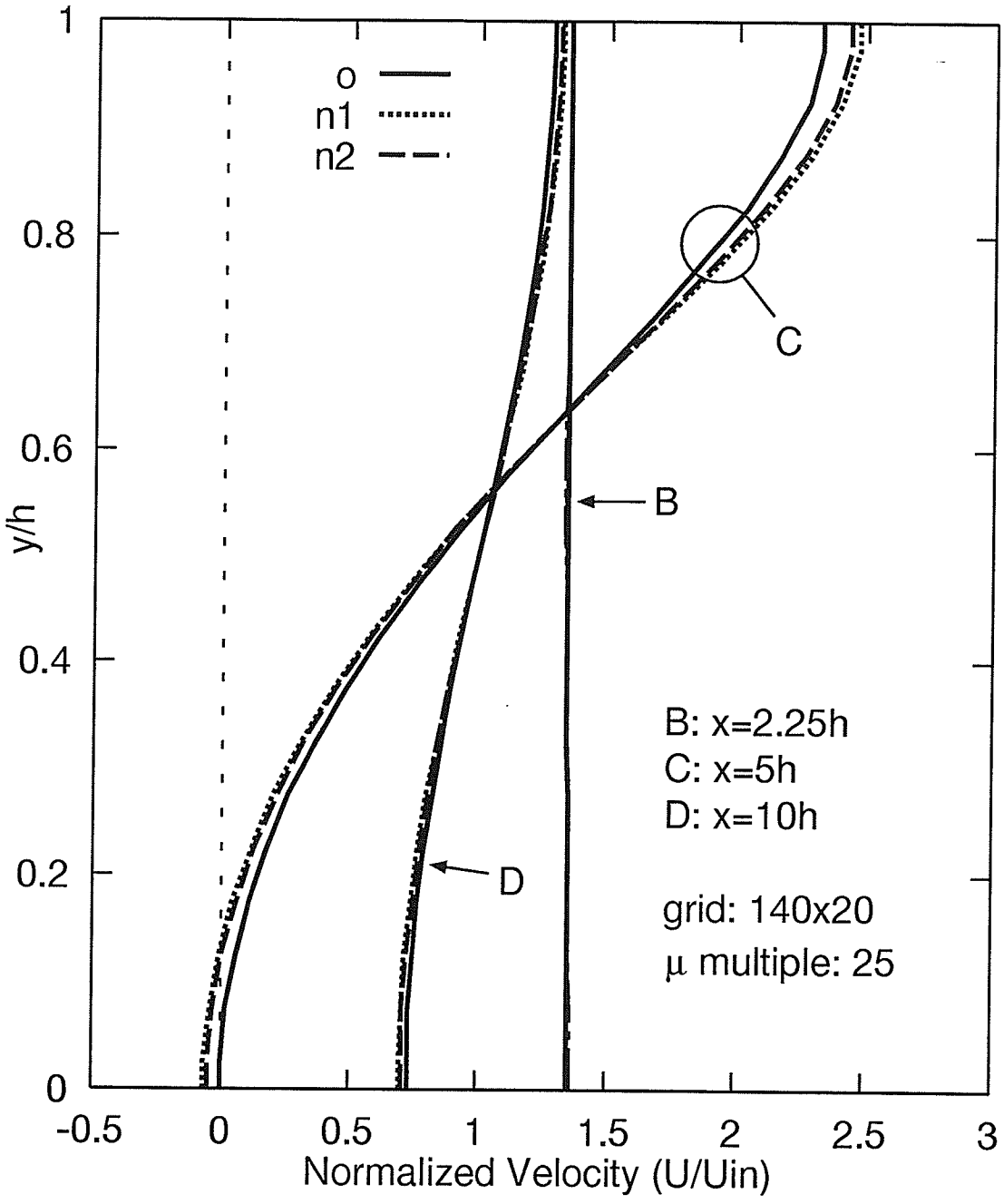

Figure 7.9: Slug Flow Normalized U Velocity Profiles: 140×20 Grid, $\mu * 25$.

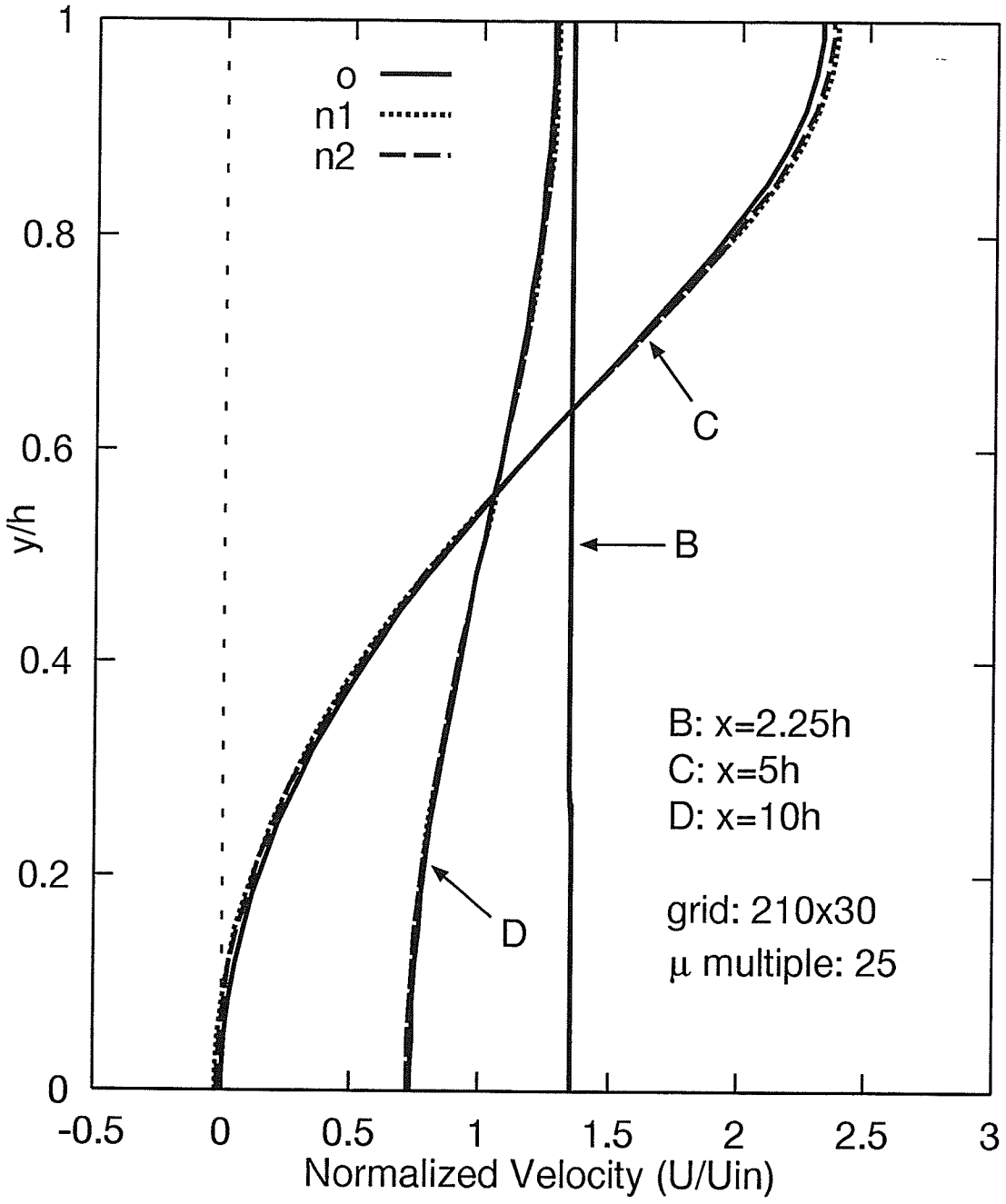

Figure 7.10: Slug Flow Normalized U Velocity Profiles: 210×30 Grid, $\mu * 25$.

The second non-orthogonal grid, "n2", has a velocity ranging from $-0.02\,[m/s]$ at the bottom to $2.36\,[m/s]$ at the top. This represents a 2.6% larger range of velocities than the orthogonal grid results, and a 4.4% decrease in range of velocities from the 140×20 non-orthogonal grid. These results show that, while the non-orthogonal results are much closer to that of the orthogonal grid, the non-orthogonal grid results may still not meet the grid independence criterion for this viscosity multiple, even when using triple the resolution, 210×30.

The velocity profile at "D" cross-section has not recovered the expected uniform profile, but its range is very similar to the coarsest grid. The orthogonal grid profile varies from about $0.73\,[m/s]$ at the bottom to about $1.27\,[m/s]$ at the top.

In order to confirm the trends that were indicated for $\mu * 25$ as the grid resolution was increased, a second set of results for the viscosity multiple $\mu * 100$ is discussed next.

Figure 7.11 shows the profiles for the coarsest (70×10) grid and the third viscosity multiple, $\mu*100$. The velocity profile at the marker "B" appears uniform, but the velocity profile at "C" now ranges from $0.64\,[m/s]$ at the bottom to $1.37\,[m/s]$ at the top. The results on the second non-orthogonal grid, "n2" show a velocity range of $0.62\,[m/s]$ at the bottom to $1.39\,[m/s]$ at the top. This represents a 5.5% larger range of velocities than the orthogonal grid results. In addition, the velocity profile at "D" has become closer to uniform than the results of the lower viscosity multiple. In each cross-section velocity profiles using the non-orthogonal grid have come very close to velocity profiles using the orthogonal grid with the increase in viscosity multiple to $\mu * 100$.

Figure 7.12 shows the profiles for the 140×20 grid and the same viscosity multiple as Figure 7.11. The velocity profile at "C" on the orthogonal grid now ranges from $0.65\,[m/s]$ at the bottom to $1.36\,[m/s]$ at the top. This represents a 2.7% decrease in range from the lower grid resolution. The second non-orthogonal grid, 'n2', has a velocity ranging from $0.65\,[m/s]$ at the bottom to $1.36\,[m/s]$ at the top. This result matches the range of velocities

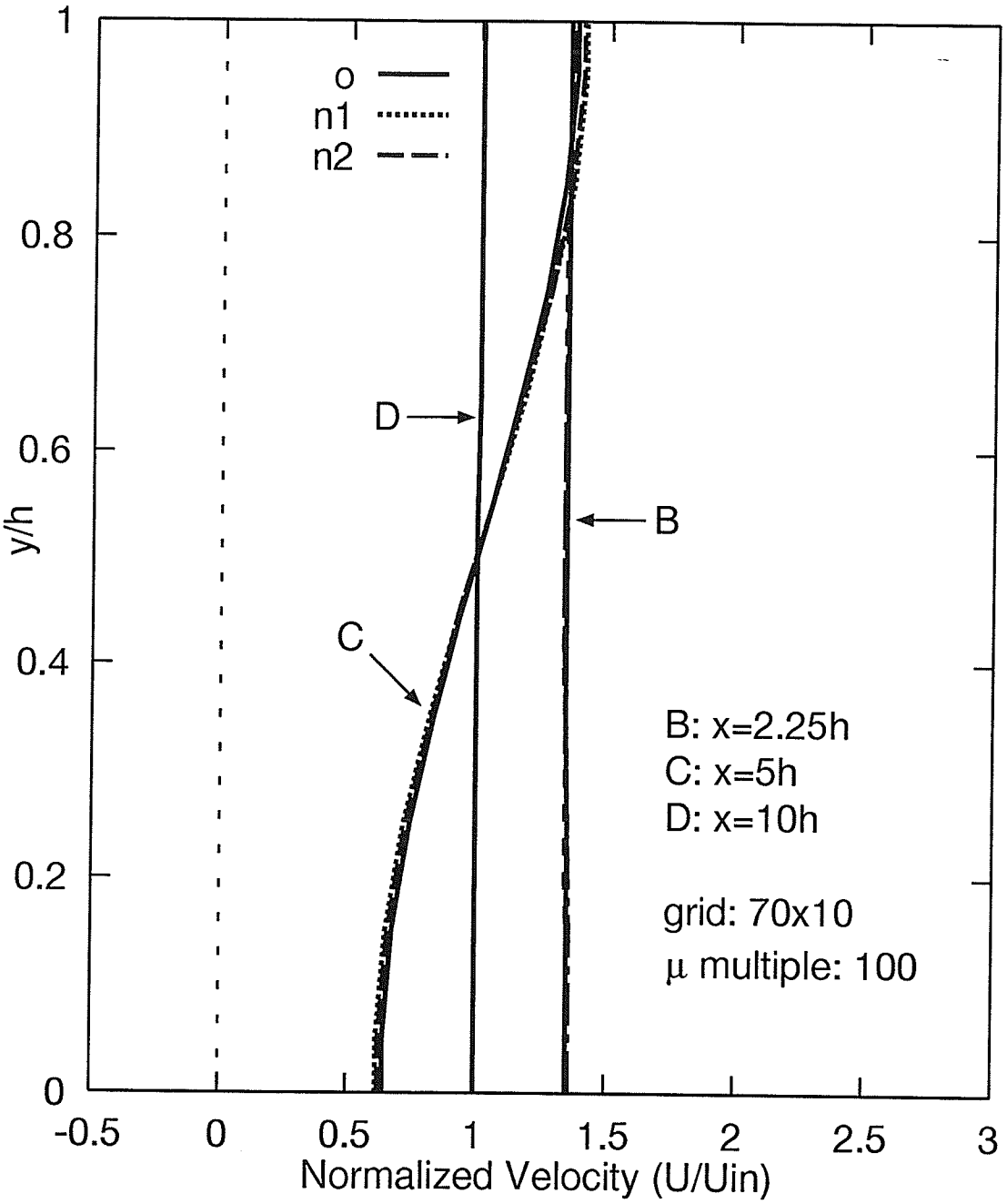

Figure 7.11: Slug Flow Normalized U Velocity Profiles: 70×10 Grid, $\mu * 100$.

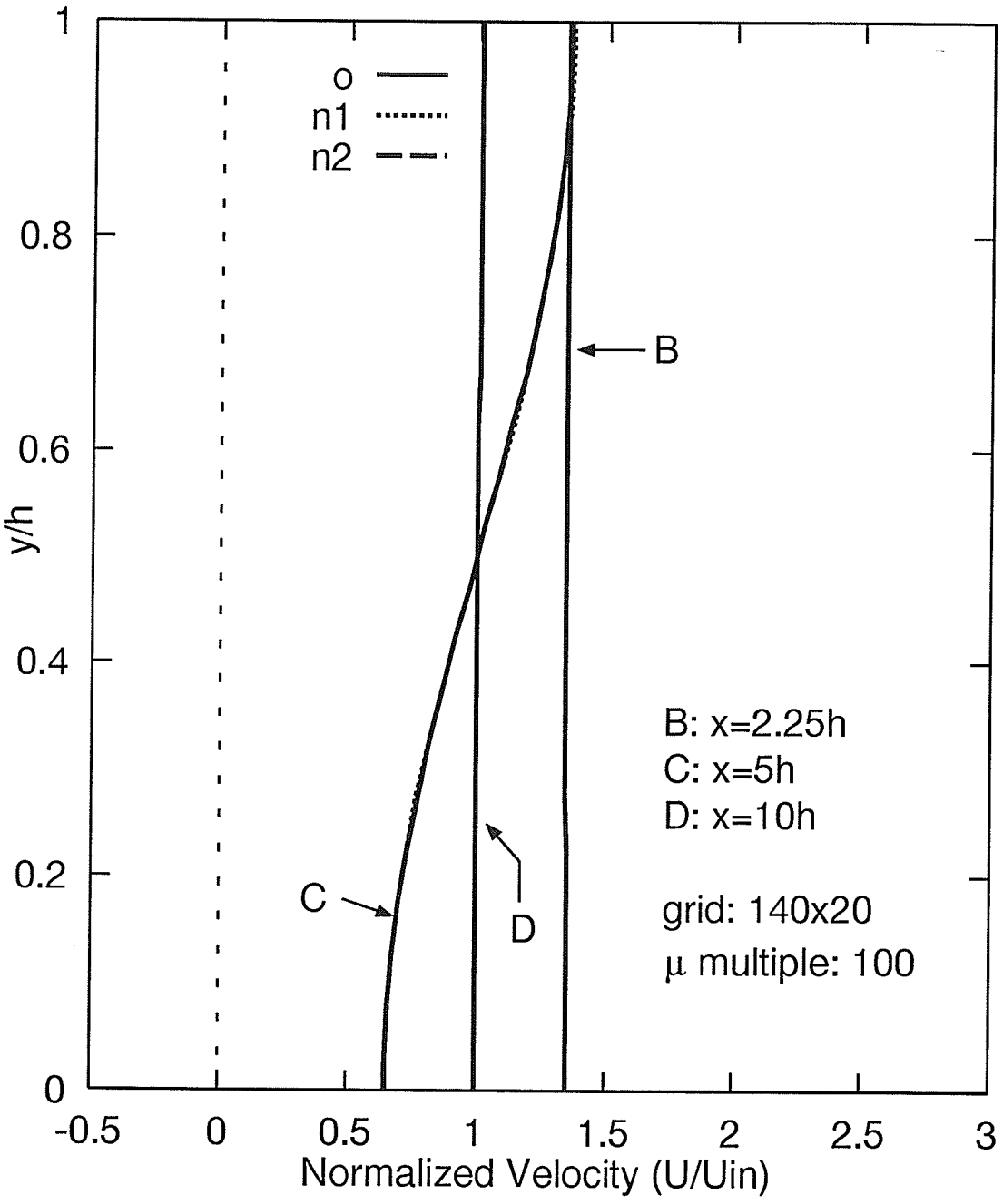

Figure 7.12: Slug Flow Normalized U Velocity Profiles: 140×20 Grid, $\mu * 100$.

for the orthogonal grid results and a 7.8% decrease in range from the coarser grid. The velocity profile at "D" cross-section has recovered the expected uniform profile.

Figure 7.13 shows the profiles for the 210×30 grid and the same viscosity multiple as Figure 7.11. The velocity profile at "C" on the orthogonal grid now ranges from 0.65 $[m/s]$ at the bottom to 1.35 $[m/s]$ at the top. This represents a 1.4% decrease in range from the lower grid resolution.

The second non-orthogonal grid, "n2", has a velocity ranging from 0.65 $[m/s]$ at the bottom to 1.35 $[m/s]$ at the top. This matches the range of velocities for the orthogonal grid results and a 1.4% decrease in range from the coarser grid. The velocity profile at "D" cross-section has recovered the expected uniform profile.

To summarize the results for the three grid resolutions and the three viscosity multiples, the ranges and percentage changes are presented in Tables 7.1 and 7.2. The column labeled "% change" indicates percentage change of the velocity range values from the previous coarser grid. The velocity ranges on the orthogonal grid, detailed in Table 7.1, change very little with increase of grid resolution for all three viscosity multiples. If one were to use grid independence criteria of change to 3%, then the 70×10 grid might be called grid independent for the results of the $\mu * 25$ test. The higher viscosity multiples show a greater amount of change, and therefore, may be called grid independent at the 140×20 resolution.

Grid	$\mu * 25$		$\mu * 50$		$\mu * 100$	
	Velocity Range, [m/s]	% Change	Velocity Range, [m/s]	% Change	Velocity Range, [m/s]	% Change
70×10	2.356	-	1.492	-	0.728	-
140×20	2.324	-1.4	1.451	-2.7	0.709	-2.7
210×30	2.315	-0.4	1.441	-0.7	0.703	-0.8

Table 7.1: Slug Flow Velocity Ranges at Profile "C" on the Orthogonal Grid, "o".

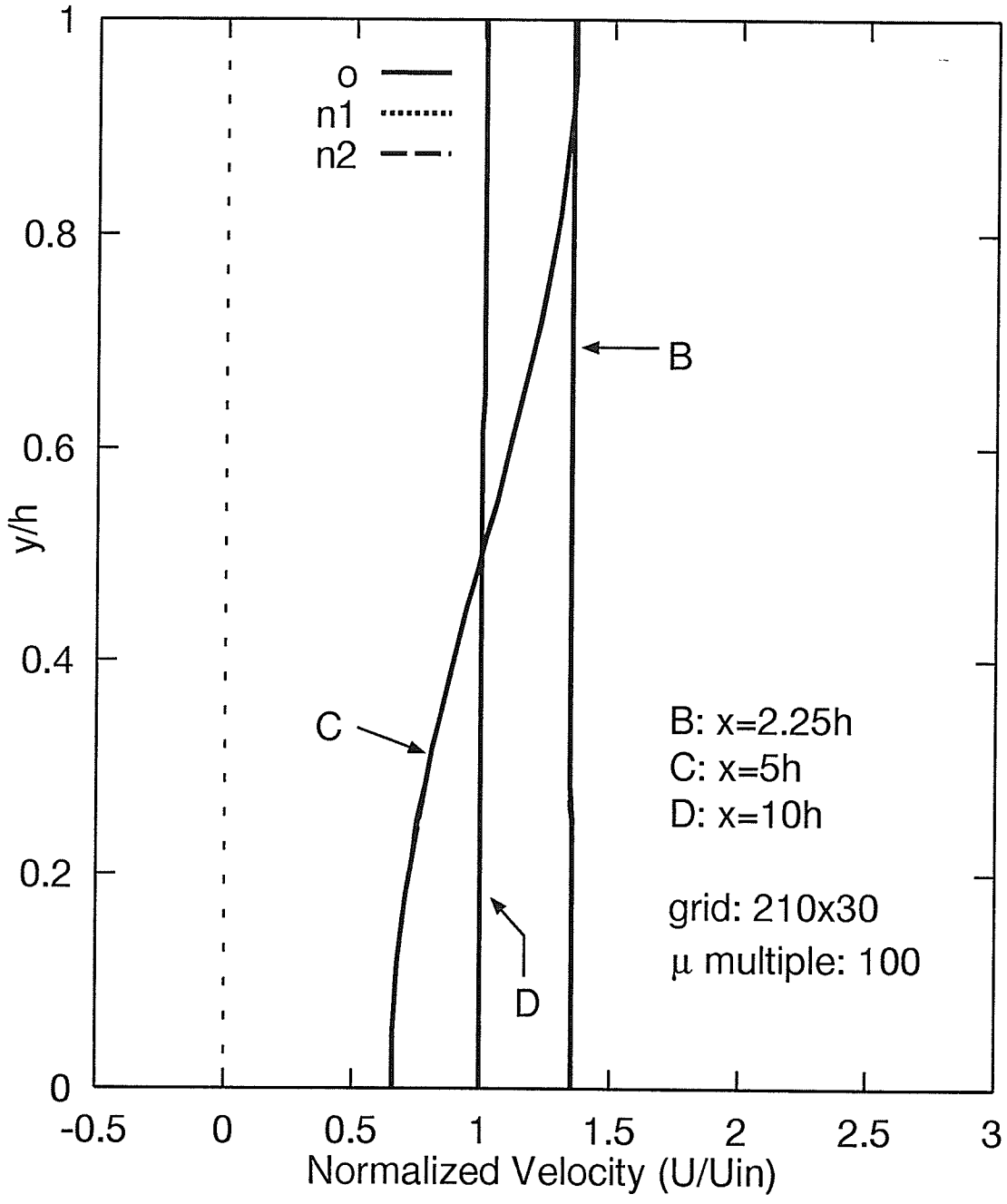

Figure 7.13: Slug Flow Normalized U Velocity Profiles: 210×30 Grid, $\mu * 100$.

The velocity ranges on the non-orthogonal grid, detailed in Table 7.2, change dramatically with increase of grid resolution for all three viscosity multiples. Even the finest non-orthogonal grid, 210×30, has changed above the chosen 3% criterion for the $\mu * 25$ case. The $\mu * 100$ case had the least change as the grid was refined and the 210×30 produces grid-independent results.

Grid	$\mu * 25$		$\mu * 50$		$\mu * 100$	
	Velocity Range, [m/s]	% Change	Velocity Range, [m/s]	% Change	Velocity Range, [m/s]	% Change
70×10	2.930	-	1.792	-	0.772	-
140×20	2.488	-15	1.500	-16	0.708	-8.3
210×30	2.382	-4.3	1.457	-2.9	0.701	-1.0

Table 7.2: Slug Flow Velocity Ranges at Profile "C" on the Non-Orthogonal Grid, "n2".

Therefore, while the orthogonal grid may produce grid independent results at 70×10 the non-orthogonal grid needs more refinement, beyond 210×30, to produce the same results at the low viscosity multiples. At higher effective viscosities the trend is the same, but the orthogonal grid results may become grid independent at 140×20 while the non-orthogonal grid results may be grid independent at 210×30. Because the results for the 210×30 non-orthogonal grid are closer to the results for the orthogonal grid than those for the coarse non-orthogonal grid, greater confidence may be placed in the orthogonal grid results for this tube bundle configuration.

These velocity profile comparisons indicate that the orthogonal grid produced grid independent results with much lower grid densities than the non-orthogonal grid for this particular flow. The viscosity level had some effect on the results, but did not change the conclusion. Increasing the viscosity multiple caused the orthogonal coarse grid results to be further away from the fine grid solution, while the non-orthogonal coarse grid results became closer to its fine grid solution with increase of viscosity multiple.

Non-Dimensional Pressure Drop

As an overall measure of a solution, a non-dimensional pressure drop (C_p^*) is defined as:

$$C_p^* = \frac{(\bar{p}_{in} - \bar{p}_{out})}{\left(\frac{\rho V_{in}^2}{2}\right)} \tag{7.1}$$

Where $\bar{p}$ is the average pressure at a domain boundary (either inlet or outlet). Tables 7.3, 7.4 and 7.5 list the non-dimensional pressure drop results for the orthogonal, non-orthogonal and composite non-orthogonal grids respectively. The percentages beside each value indicate the amount of change from the previous coarser grid.

	$\mu * 25$		$\mu * 50$		$\mu * 100$	
Grid	C_p^*	%	C_p^*	%	C_p^*	%
70×10	475.12	-	476.75	-	480.55	-
140×20	476.56	+0.30	478.21	+0.31	481.59	+0.22
210×30	476.82	+0.06	478.36	+0.03	481.60	+0.00

Table 7.3: Slug Flow Non-Dimensional Pressure Drop: Orthogonal Grid "o".

	$\mu * 25$		$\mu * 50$		$\mu * 100$	
Grid	C_p^*	%	C_p^*	%	C_p^*	%
70×10	458.75	-	461.42	-	467.22	-
140×20	471.20	+2.7	473.46	+2.6	477.63	+2.2
210×30	474.06	+0.6	475.94	+0.5	479.55	+0.4

Table 7.4: Slug Flow Non-Dimensional Pressure Drop: Non-Orthogonal Grid "n1".

These three tables of C_p^* values confirm that the orthogonal grid results could be considered grid independent at the 70×10 resolution, while the non-orthogonal grids, both "n1" and "n2", results would need at least a 210×30 grid to obtain changes less than 1% from the coarser grid.

	$\mu * 25$		$\mu * 50$		$\mu * 100$	
Grid	C_p^*	%	C_p^*	%	C_p^*	%
70×10	465.52	-	467.71	-	472.47	-
140×20	472.93	+1.6	474.93	+1.5	478.66	+1.3
210×30	474.81	+0.4	476.51	+0.3	479.91	+0.3

Table 7.5: Slug Flow Non-Dimensional Pressure Drop: Non-Orthogonal Grid "n2".

The Tube Bundle Edge Effects

Figures 7.14 through 7.16 show a detailed view of the tube bundle exit boundary on a 70×10 grid using the lowest viscosity multiple, $\mu * 25$. The velocity vectors cross the streamlines in both the non-orthogonal grids in Figures 7.14 and 7.15, but for the orthogonal grid results shown in Figure 7.16, the vectors are parallel to the streamlines, as expected.

Since the streamlines are based on face velocities, the conflict seen in the results on the non-orthogonal grids is actually between face and nodal velocities. There are sharp pressure changes at the trailing edge of the tube bundle, where the flow goes from porous region to the free-fluid region. The pressure changes cause the PWIM to give non-physical face velocities, inconsistent with nodal velocities. An example of non-physical face velocities might be the following: two nodal U velocities in adjacent control volumes equal 1 $[m/s]$ and the U face velocity between them is 1.1 $[m/s]$. Miller and Schmidt [23] also refer to this problem with the PWIM in areas of rapidly changing pressure gradients. This occurs to a greater extent when the grid lines lie exactly on the tube bundle boundary, the percentage of the control volume filled with tubes changes from 100% to 0% from one control volume to the next. On the other hand, the orthogonal grid aliasing of the tube bundle boundary has a 50% step because the physical boundary is defined across the control volume diagonal. This extra step turns out to be an advantage since the shock of the tube bundle edge effect is diminished, and the pressure can change more smoothly.

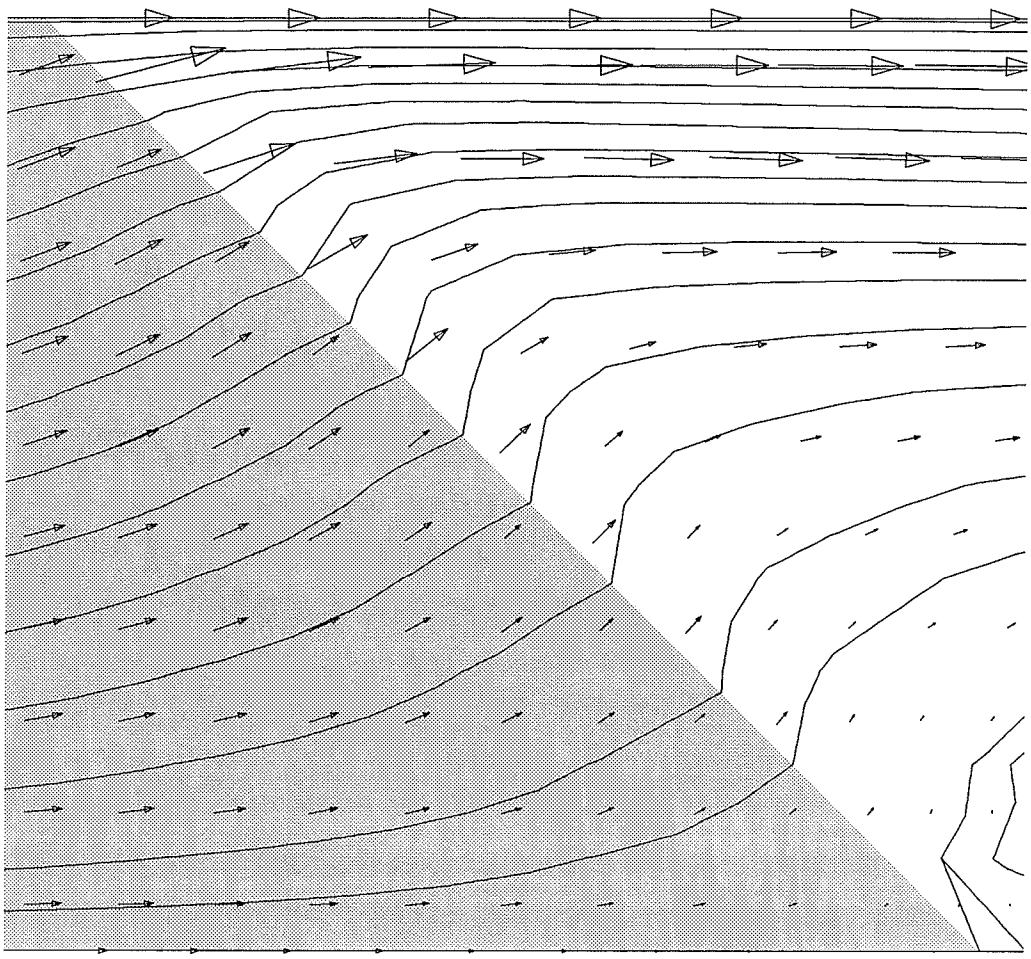

Figure 7.14: Slug Flow Velocity Vector and Streamline Detail on the Trailing Edge of the Tube Bundle, "n1" Grid.

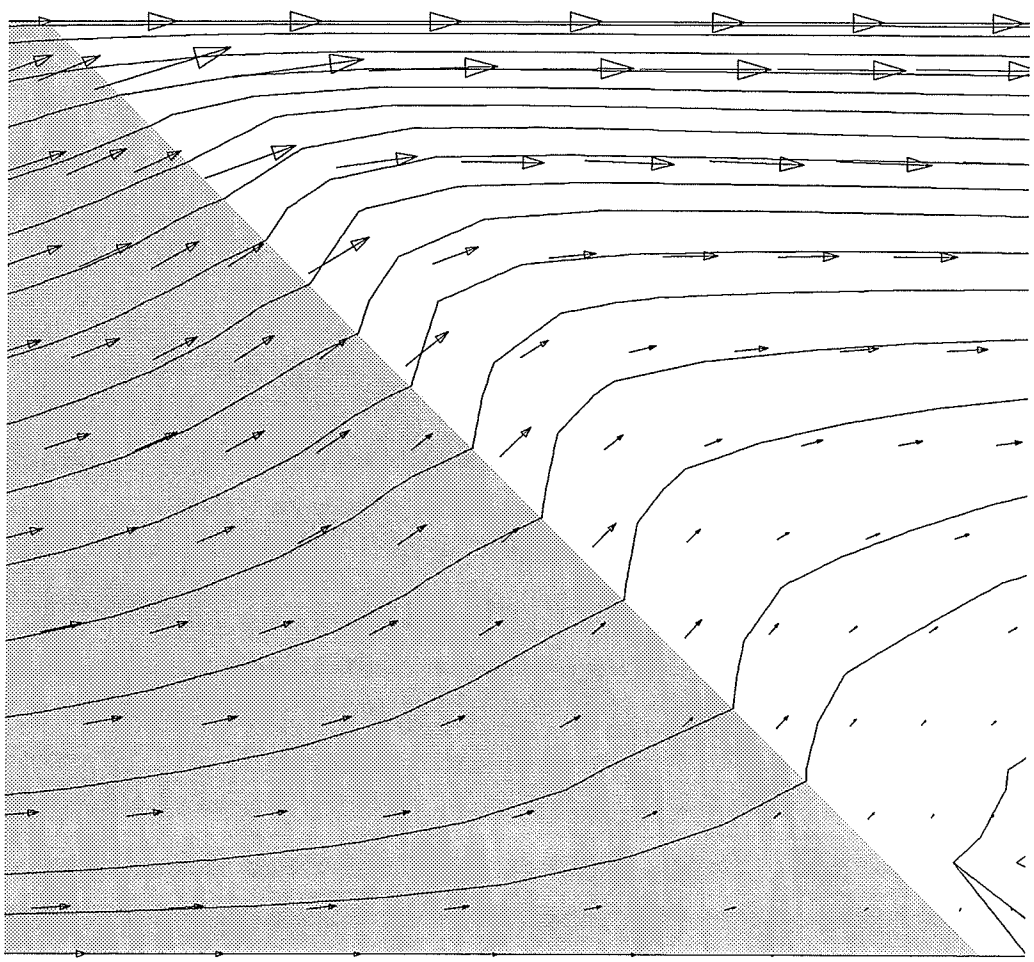

Figure 7.15: Slug Flow Velocity Vector and Streamline Detail on the Trailing Edge of the Tube Bundle, "n2" Grid.

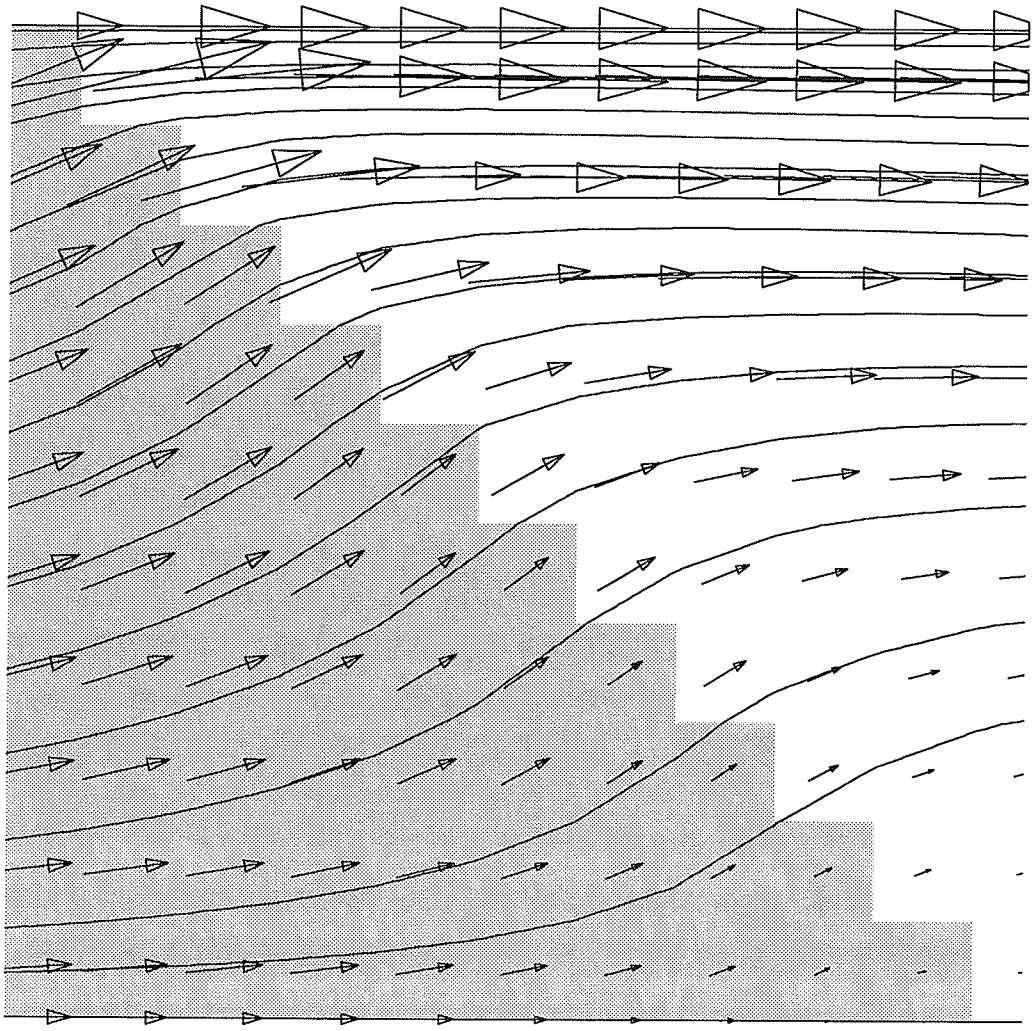

Figure 7.16: Slug Flow Velocity Vector and Streamline Detail on the Trailing Edge of the Tube Bundle, "o" Grid.

Pressure Drop through the Tube Bundle

Figure 7.17 shows the pressure drop along the horizontal centerline for the 70×10 set of grids for $\mu * 25$. At the elevation of $y = 0.5h$ the line enters the tube bundle at $x = 1.0h$ and exits at $x = 3.5h$. Considering how different the streamlines look for these three cases in Figure 7.2, the pressure levels look almost identical because the profile does not go through the recirculation zone. It is interesting to note that while the slope of the line is almost the same for all three grids, the overall pressure drop is slightly different. The orthogonal grid has a higher pressure drop than the non-orthogonal grids, with the composite grid, "n2", in the middle and the ordinary non-orthogonal grid, "n1", at the bottom. The edge effects are not as visible in these pressure profiles as in Section 6.3.2 because the tube bundle boundary is diagonal to the profile line. Also, the grid is quite coarse, therefore the peak pressures are not resolved.

The numerical value of pressure drop for the present results is less than 3% greater than the value given by the Butterworth correlation. This is a reasonable comparison even though the pressure profile is not perpendicular to the tube bundle boundaries and the flow is two-dimensional.

To help visualize the two-dimensional aspects of the pressure field, Figure 7.18 shows pressure contours for the first half of the domain for each of the three coarsest grids. Table 7.6 lists the labeled pressure values used in Figure 7.18 for comparison of the relative pressure levels.

Isobars are evenly spaced as follows: seven between "a", and "c", and seventeen between "d" and "f". In Figure 7.18(b) there are six isobars at increments of 1.0×10^{-4} $[N/m^2]$ above "g". In Figure 7.18(c) there are five isobars at increments of 1.0×10^{-4} $[N/m^2]$ above "h". In Figure 7.18(a) there are five isobars at increments of 1.0×10^{-4} $[N/m^2]$ above "i".

The isobars labeled "b" on the plot of the orthogonal grid results and "a" in the non-orthogonal grids' results indicate that the pressure falls below a certain level then rises again.

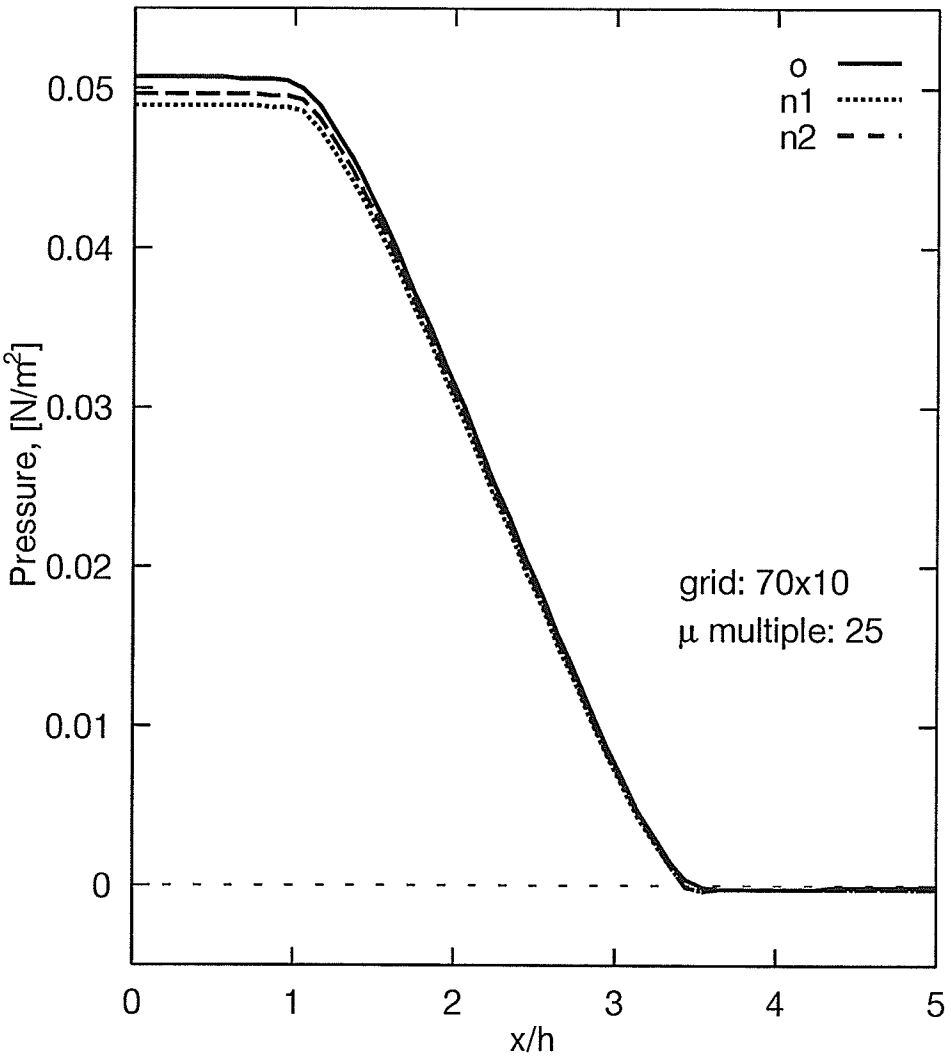

Figure 7.17: Slug Flow Pressure Drop along the Horizontal Centerline.

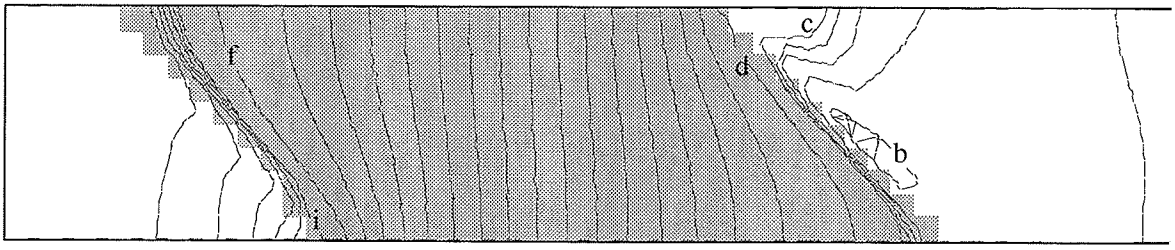

(a) Orthogonal Grid, o.

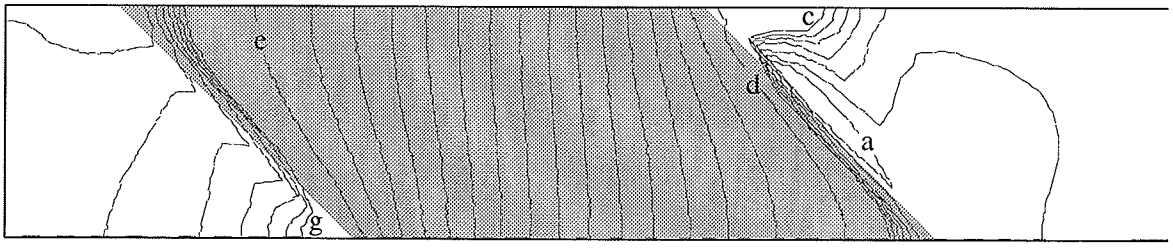

(b) Non-orthogonal Grid, n1.

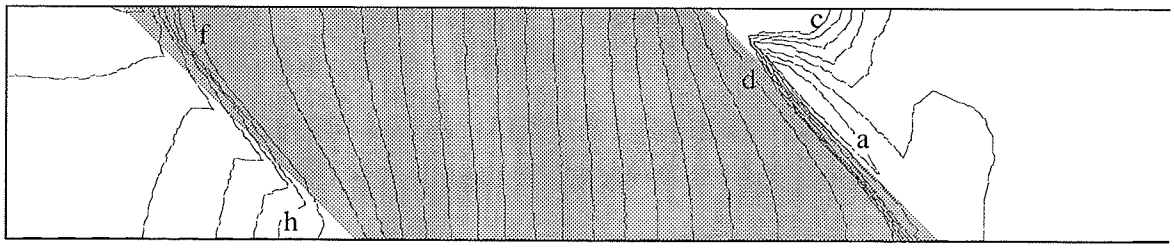

(c) Non-orthogonal Grid, n2.

Figure 7.18: Slug Flow Pressure Contours: 70×10 Grid, $\mu * 25$.

Label	Pressure $[N/m^2]$	Label	Pressure $[N/m^2]$
a	-3.0×10^{-4}	f	4.9×10^{-2}
b	-2.0×10^{-4}	g	4.84×10^{-2}
c	0	h	4.93×10^{-2}
d	1.0×10^{-3}	i	5.01×10^{-2}
e	4.6×10^{-2}		

Table 7.6: Slug Flow Pressure Labels for Figure 7.18.

The size of these pockets of low pressure is comparable with the size of control volumes in this area, as seen in Figure 7.1. The folding of the isobars around these low pressure areas indicate that the change of sign of the pressure gradient occurs within the space of one or two control volume widths. The effect is most clearly shown on the non-orthogonal grids in Figures 7.18(b) and 7.18(c). The orthogonal grid isobars are more loosely folded, therefore the pressure change is smoother than for the non-orthogonal grids' results. At the leading edge of the tube bundle there is a slight folding of the isobars, but not as much as at the trailing edge.

An Examination of Velocity Profiles at Section "B"

Figures 7.19 through 7.21 show a fine scale view of just the velocity profiles through the center of the tube bundle, at cross-section "B". The left part is a replot of curves found in previous graphs. The right part of each of the graphs is a close up view of the same curves. On a much finer scale, the curves no longer appear as straight lines. The first non-orthogonal, "n1", grid appears to give a jagged velocity curve that appears to show less mass flux than for either the "o" or "n2" grids, both of which have orthogonal sections around cross-section "B". Firstly, the jagged profile is a result of interpolations made to obtain a velocity value along the desired line. On a global scale this works fine but very small errors arise locally. Secondly, the appearance of improper global mass flow through the control volumes along

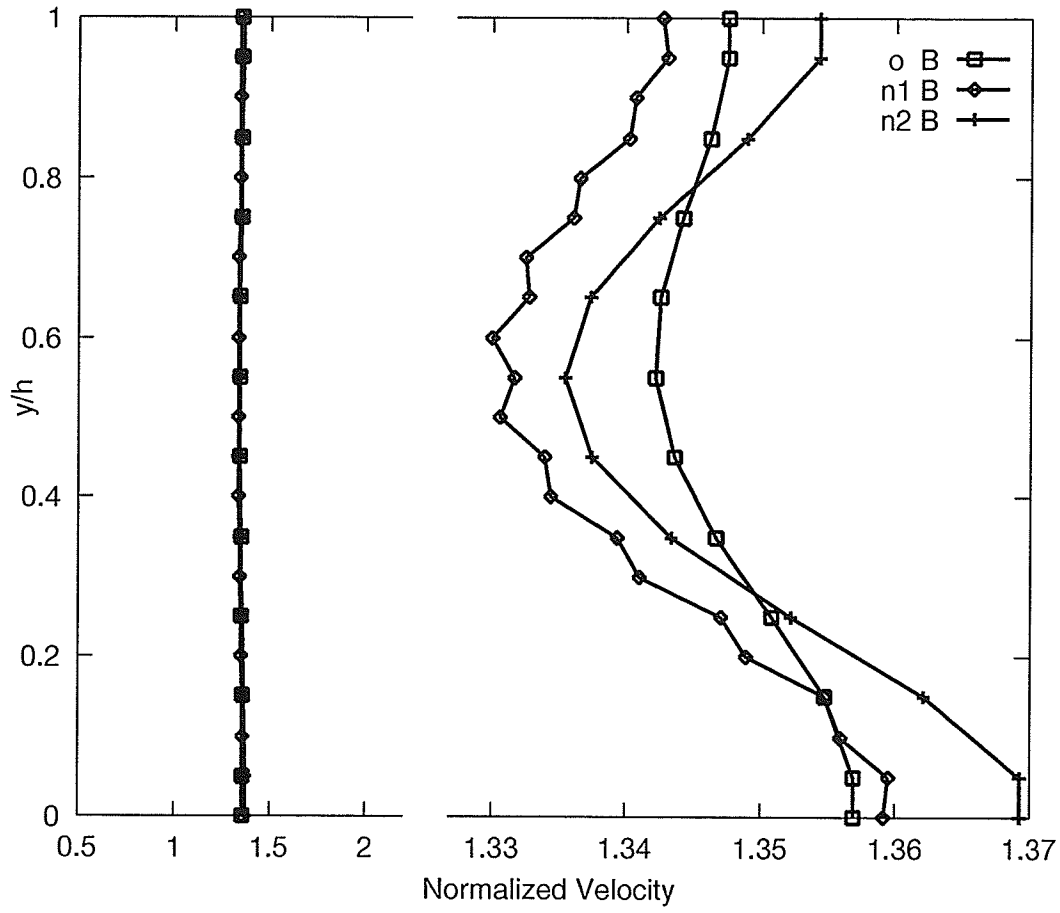

Figure 7.19: Slug flow Normalized U Velocity Profiles at marker "B": 70×10, $\mu * 25$.

this cross-section is a result of plotting only one component of velocity on a non-orthogonal grid. Even though the same amount of mass enters each test grid, the U velocity profile in the orthogonal grid solution shows a larger flow west to east than that of the non-orthogonal, "n1", grid. The "n2" grid, the one with the orthogonal section around this profile, seems to show the same mass but in different locations along the vertical line. This difference exists because this is a graph of the coarsest grid resolution and the flows have been proven to be quite different.

Figure 7.20 is a plot of the same values as in Figure 7.19, only with the highest viscosity multiple. There is a slight smoothing of the flow and some converging of the profiles but increasing viscosity alone does not eliminate the differences.

When the grid is refined to 210×30, the differences in velocity profiles become extremely small, even on the fine scale in Figure 7.21. Note that the velocity profile for the orthogonal grid has changed very little when compared to the same profile in Figure 7.19. However, both non-orthogonal grid velocity profiles have become much closer to the orthogonal grid results. This observation agrees with the previous discussion involving the velocity profiles at other locations in the flow.

A further explanation of the reason the non-orthogonal grid cannot give all the information in one velocity component is illustrated in Figure 7.22. An arbitrary control volume is shown that is not aligned with the Cartesian vertical dashed line along which a velocity profile is desired. In the non-orthogonal grid, the V face velocities are carrying some mass in the Cartesian x direction by virtue of carrying mass in and out of a control volume that straddles the proposed vertical line. Since only nodal velocities are considered, when plotting a velocity profile on a vertical line, only the U component of velocity can carry mass across the vertical plane. For example, consider the case when the west face U velocity, U_w, the nodal U velocity, U_P, and the east face U velocity, U_e, are all the same magnitude. The face velocity, U_e, carries the same mass as U_P and U_w because they act over the same area,

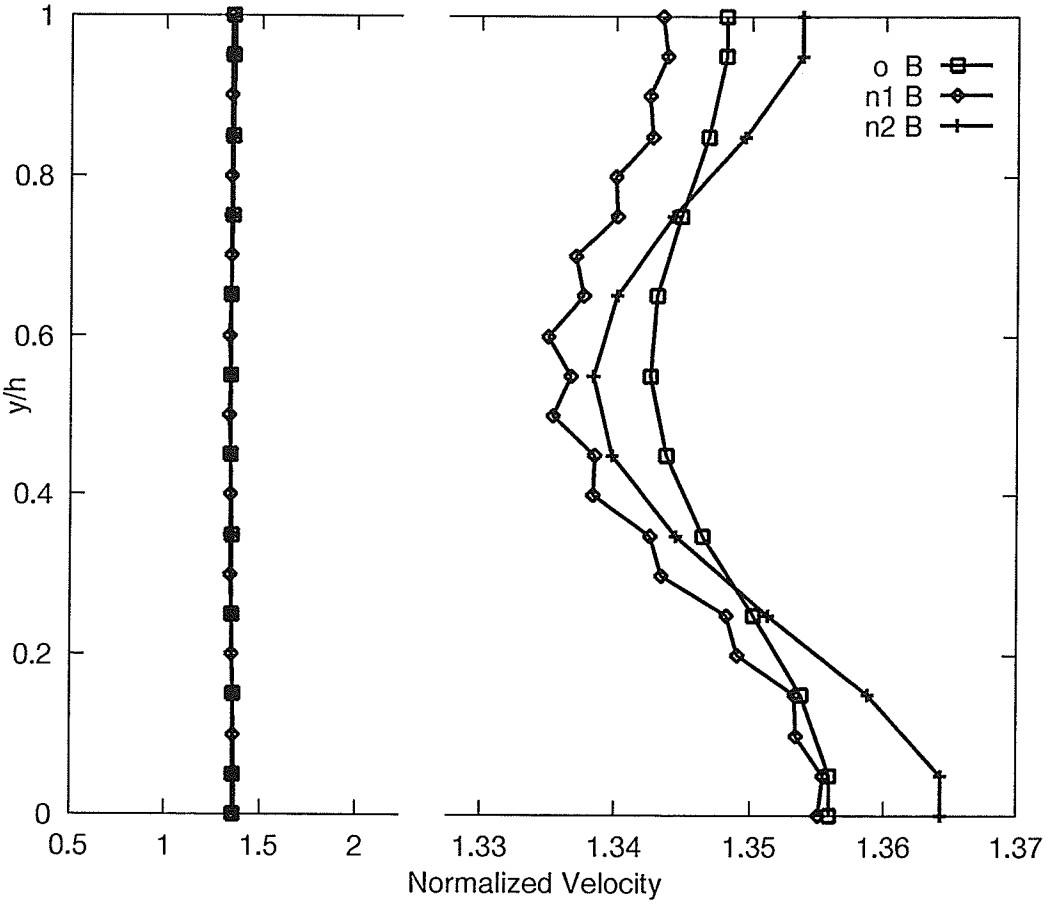

Figure 7.20: Slug flow Normalized U Velocity Profiles at marker "B": 70×10, $\mu * 100$.

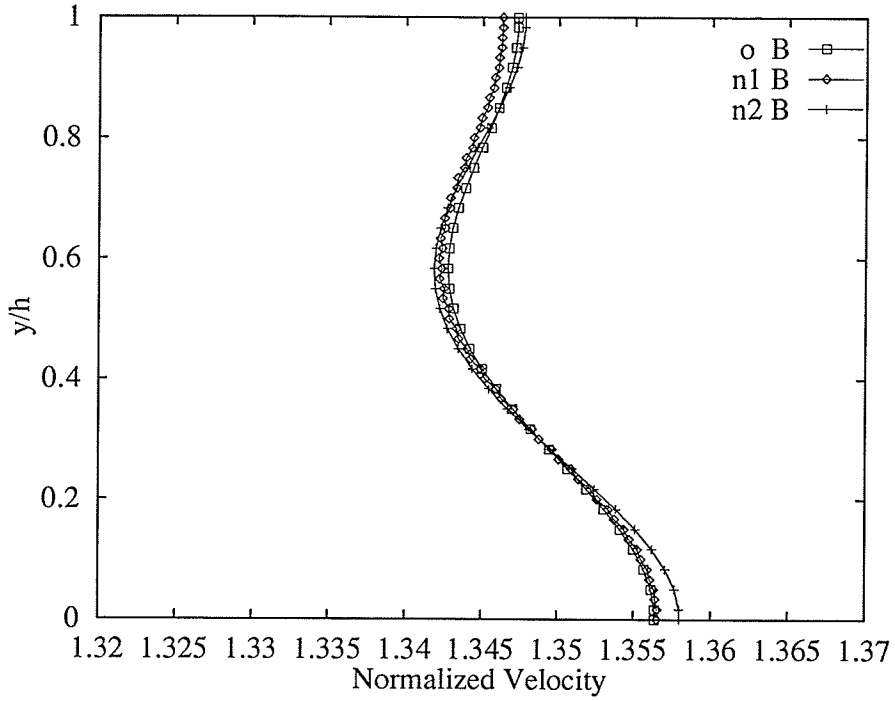

Figure 7.21: Slug flow Normalized U Velocity Profiles at marker "B": 210×30, $\mu * 25$.

"B". However, the south face V velocity, V_s, brings some mass into a control volume and the west face V velocity, V_w, takes some mass out of a control volume over the area "A". If V_s is greater than the V_w, there is mass brought into the control volume that must exit either the north or east face of the control volume and therefore cross the vertical plane without being counted in the U velocity component. Therefore the U velocity profile would not show all the mass that is flowing west to east.

In the orthogonal grid, the V velocities cannot carry any mass left to right because all the control volume boundaries are aligned with the Cartesian directions. The U nodal velocities are consistent with the U face velocities, and V face velocities only carry mass in or out the south and north faces. Therefore, on a vertical profile all the mass is accounted for by looking at only the nodal U velocity.

A way to alleviate this problem is to compare U velocity profiles in areas where the V face velocities are uniform or very small in relation to the U velocities. The finer the control

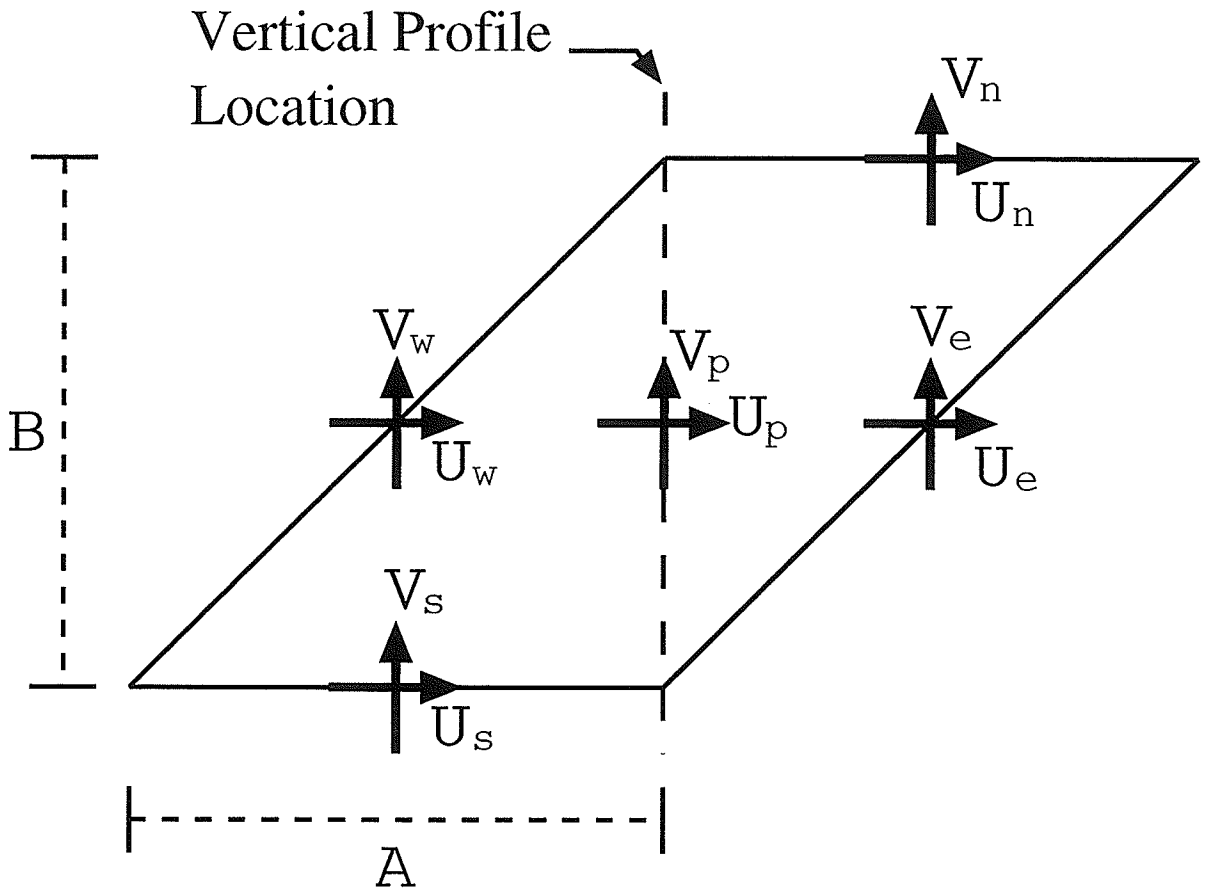

Figure 7.22: Non-Orthogonal Grid through which a Vertical Profile is Taken.

volume density the more likely the V face velocities will be similar and the better the U velocity profile will conserve mass. Another option is to compare U velocity profiles in areas where the grid is Cartesian, and this is the reason for the orthogonal section in the middle of the tube bundle for grid "n2".

7.2 The Rotated Square Tube Bundle Test Problem.

The process of developing a test problem that would exercise most of the capabilities of the present code was long and difficult. Many different grids and blockage configurations were attempted and revised because of problems of convergence, undesirable flow characteristics (recirculation zones at the exit, recirculation in tube bundle, too little flow in tube bundle, too much flow bypassing around the tube bundle, or too high pressure drops). The goal was to produce a simplified hypothetical heat exchanger model that could be used to perform a comparison of the use of orthogonal and non-orthogonal grids. In this comparison, the non-orthogonal grid matches the complex internal structure (tube bundle shape, sealing strips and baffles), while the orthogonal grid approximates them. This comparison was expected to illustrate the generality of the algorithm and to produce useful new information related to modeling complex heat exchanger flows.

The criteria that were applied in designing the test problem were:

- Use a diamond shape (a square rotated 45^o) to maximize the orthogonal grid aliasing. The peaks of the diamond were subsequently flattened to reduce convergence problems.
- Use a square shell and square sealing strips to make easy comparison between the orthogonal and non-orthogonal grids and to enable the external boundaries to be matched exactly with both styles of grids.
- Use sealing strips and blockages to direct flow only, not to block off large areas of the grid.

- Use a structured grid to enable the use of standard iterative solvers.
- Do not allow a short circuit in the flow (i.e. ensure a large percentage of the flow goes through the main part of the tube bundle).
- Do not use access lanes in the tube bundle, in order to keep it simple.
- Avoid flow separation from the wall at exit. A recirculation zone that crosses a fully-developed boundary cannot be permitted.

The problem definition that was finally derived, was called the Rotated Square Tube Bundle (RSTB) test problem, and is shown in Figure 7.23. The inlet region, at the top left, is 0.45 $[m]$ wide and the exit, at the top right, is 0.25 $[m]$ wide. The flow enters the inlet as a uniform profile, $V_{in} = -1.86\ [m/s]$, and leaves the exit fully-developed, $\frac{\partial V}{\partial y} = 0$ and $U = 0$. The fluid density is 0.995 $[kg/m^3]$ and the molecular viscosity is $2.082 \times 10^{-5}\ [N \cdot s/m^2]$. The Reynolds number based on inlet width is 40,000. All the rest of the walls and blockages are solid with zero slip boundary conditions. Wall functions and viscosity multiples were used to model turbulent flow. In the case of the non-orthogonal grid, because the wall functions were developed for only horizontal or vertical surfaces, the shear force on the slanted tip of the baffle was approximated by using wall functions on only the U velocity component. The light-shaded area is the tube bundle region, which has an area of 0.49 $[m^2]$. The dark-shaded areas are blockages, sealing strips and the baffle near the exit.

The comparison between orthogonal and non-orthogonal grids requires that there be as exact a correspondence between the two types of grids as possible. Therefore, the dimensions of the heat exchanger were chosen to match a Cartesian grid and the non-orthogonal grid was then made to match the interior details.

The exterior boundaries remain Cartesian so the orthogonal grid is easy to generate, as shown in Figure 7.24(a) for the 30×20 resolution. This grid is made of three panels. The first panel is a 20×20 uniform orthogonal grid that defines the sealing strip locations and the

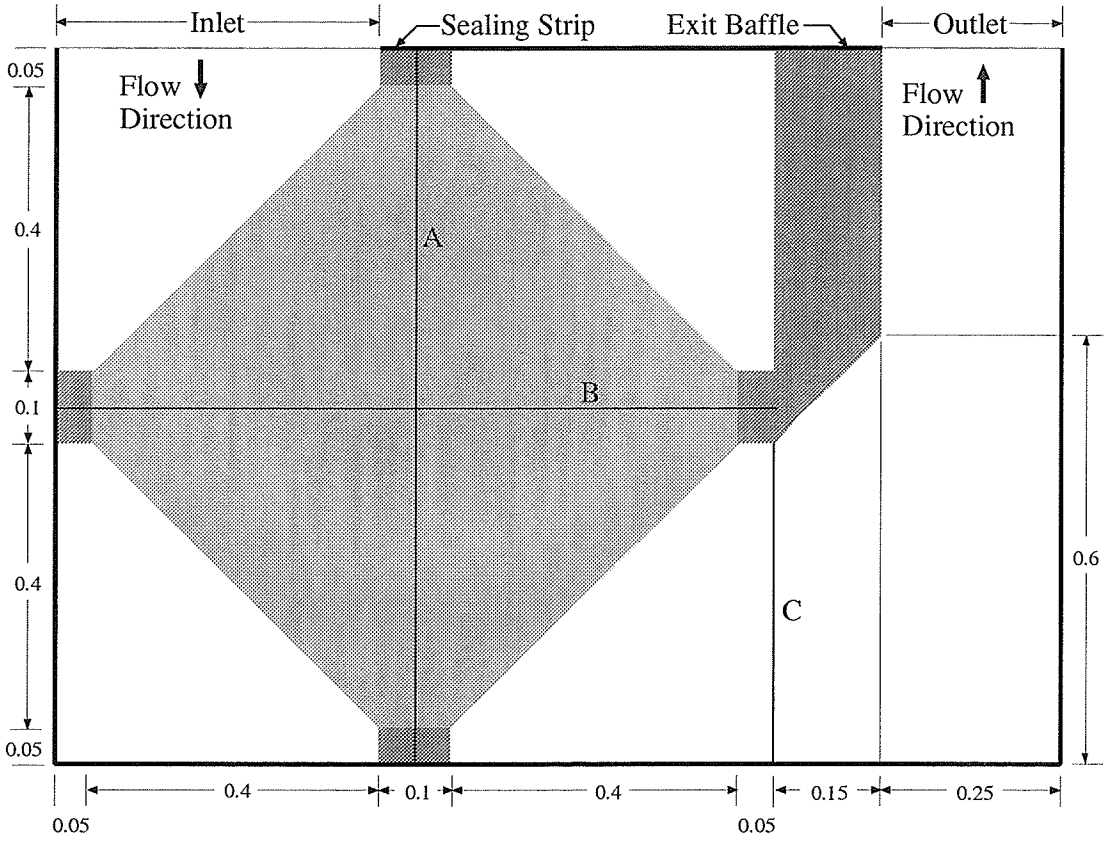

Figure 7.23: Rotated Square Tube Bundle (RSTB) Test Problem Definition.

tube bundle area. The tube bundle boundary was defined diagonally from corner to corner across each control volume so half the control volume contained free fluid and half contained tubes. The defined tube bundle boundary is approximated in a stepwise fashion (aliased) as is the bottom of the baffle that defines a channel for the exit region. Those control volumes that lie completely inside the defined tube bundle region have the porosity of $\varepsilon_t = 0.742$, but those that lie on the boundary have the porosity of $\varepsilon = 0.871$ (for a 50% tube-filled control volume). The result is a two-step process as the flow goes from a control volume of free fluid, to half tube-filled, to completely tube-filled.

The second panel of the orthogonal grid is a 3×20 grid with the same control volume spacing as the first panel and attached to the right side of the first panel. This second panel

defines the width of the exit baffle. The third panel is a 7×20 uniform grid with the same control volume spacing in the y direction but narrower control volumes in the x direction. This panel defines the width of the exit.

The 30×20 non-orthogonal grid is shown in Figure 7.24(b). This grid is made of 35 panels each having uniformly-spaced control volumes. The panel boundaries are not Cartesian and the grid is constrained to be structured so the control volumes must change in size as the panel width or height changes. Each panel is defined from the vertex locations that were fixed using the 30×20 orthogonal grid. The result is that the grid lines now match the defined tube bundle boundary exactly, so the flow goes from 100% free fluid to 100% porous region as it enters the tube bundle region. The grid lines also match the blockage boundaries exactly. The general guideline of a minimum of four control volumes between solid boundaries was used in choosing the number of control volumes in each panel.

There is no unique grid distribution, either orthogonal or non-orthogonal, that would match the given problem as defined. Grid refinement was achieved by placing a larger number of uniformly-spaced control volumes in each panel. The number of control volumes was increased by the same factor in each panel. The importance of uniform spacing of control volumes in each panel reduces as the grid refinement increases because more control volumes are placed relatively evenly throughout the domain. Furthermore, the areas that would benefit more from finer grid resolution are given more control volumes at the same rate as other areas of the flow.

From the experience of developing grids for problems that include tube bundles, certain areas have been found to need at least a minimum number of control volumes. One example is the edge of a tube bundle that is not aliased (there is a single step between free-fluid and porous regions). The edge causes localized pressure fluctuations that take four or five control volumes to decay. If other obstructions, edges, or changes occur in that region then convergence difficulties may occur. Increasing the viscosity dampens out these disturbances

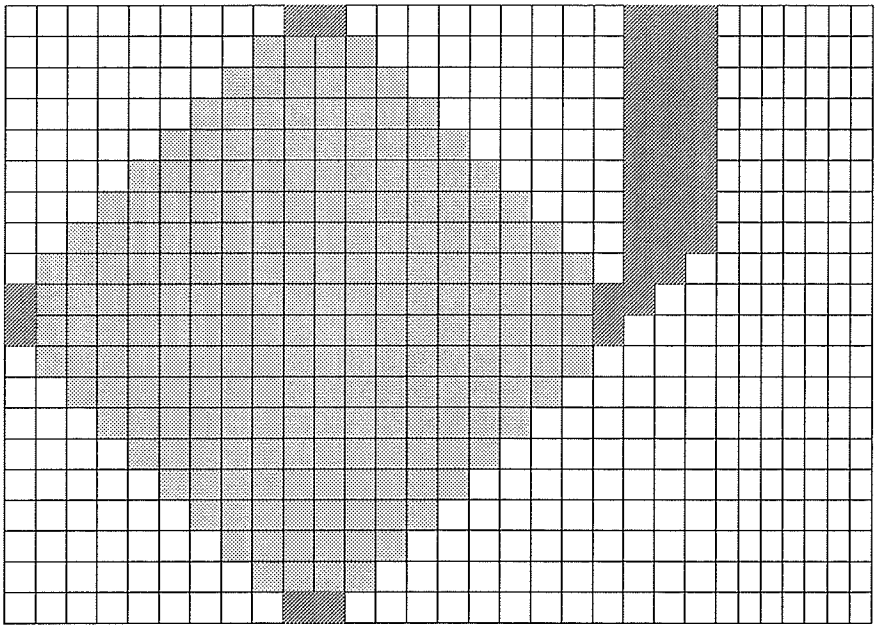

(a) Orthogonal Grid

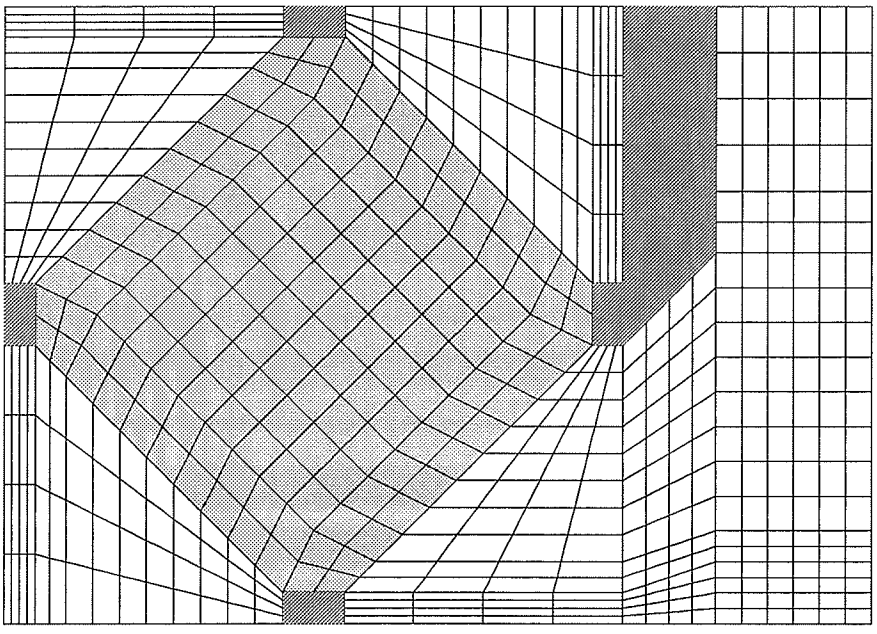

(b) Non-Orthogonal Grid

Figure 7.24: RSTB Test Problem 30×20 Grids.

faster. Increasing the control volume density at the tube bundle boundary makes the edge effect more localized and increases overall stability even if the converged solution is different from that for the orthogonal grid. This edge effect has been shown in Sections 6.3.2 and 7.1.1 and its effect in this problem is that the solution on the 30×20 non-orthogonal grid would not converge for the lowest viscosity multiple, but it would converge if the grid was refined to 45×30. The trailing edge of the tube bundle, the side closest to the line label "C" in Figure 7.23, is where the convergence difficulties are most evident because the grid is quite coarse and it has large aspect ratios in that region. Refining the grid puts more control volumes in this area and convergence progresses smoothly. The refinement is shown in the orthogonal and non-orthogonal 60×40 grids in Figure 7.25. Therefore, another guideline is that there be at least four control volumes between two edges of a tube bundle.

One must balance detailed results with reasonable computer run time. There is a point at which further refining the grid will not improve the results to a degree that is worth the longer run time. There are many possible choices of values to use for measuring grid independence. The non-dimensional pressure drop was used as a global measurement and peaks in velocity profiles were used as local measurements of the flow. The velocity peaks that were used were selected from velocity profiles along dashed lines labeled "A" (vertical centerline), "B" (horizontal centerline), and "C" (exit lane) in Figure 7.23. For this work, a particular solution is said to be grid independent if the change with refinement of a a chosen indicator falls below a given criterion. In order to determine the effect of grid refinement, the orthogonal and non-orthogonal solutions will be compared on four grid resolutions: 30×20, 60×40, 90×60, and 120×80. Beyond this amount of grid refinement the amount of CPU time required would became quite large, so a 150×100 case was not attempted. Three effective viscosity multiples: 25, 50 and 100, are used to examine the effect of the simple turbulence model and to test the trend toward grid independence over different turbulence levels. Only selected results are presented in this section, other results are contained in Appendix C.2.

The streamline plot of the results on the coarse grid, 60×40, and smallest viscosity

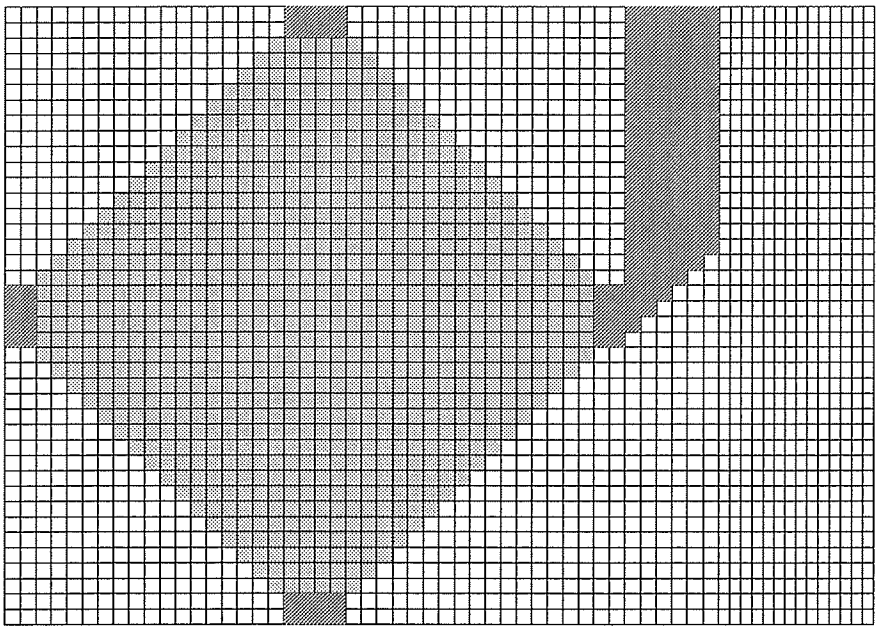

(a) Orthogonal Grid

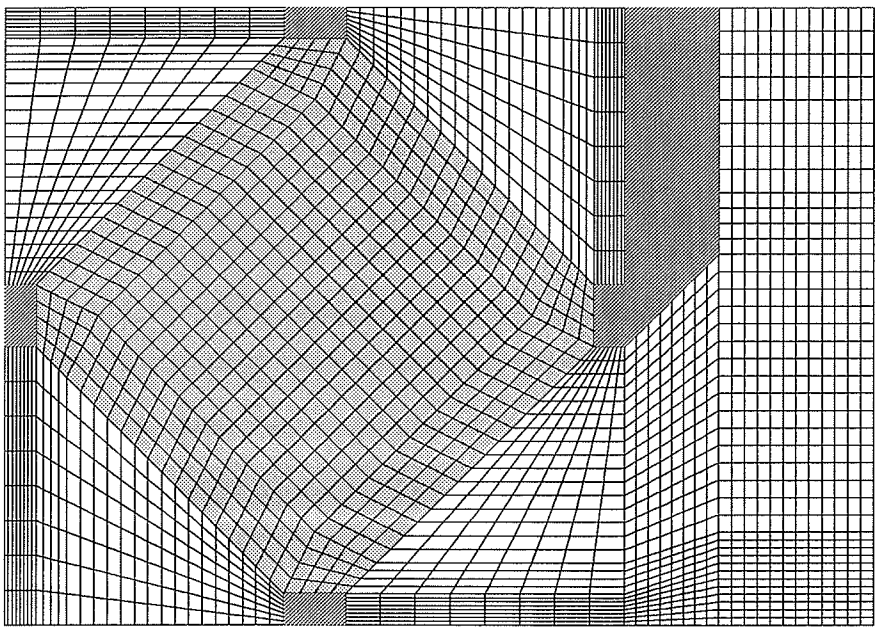

(b) Non-Orthogonal Grid

Figure 7.25: RSTB Test Problem 60×40 Grids.

multiple, $\mu * 25$, is shown in Figure 7.26. Each of the recirculation zones, on both the orthogonal and non-orthogonal grids, is associated with a blockage, sealing strip, or a 90^o change in flow direction. The one obvious difference between the two grid results is the recirculation zone in the upper right corner, just to the left of the baffle. The streamlines for the orthogonal grid indicate a much larger and stronger recirculation than those for the non-orthogonal grid. However, the streamlines for the non-orthogonal grid indicate a stronger recirculation in the lower left corner than in the orthogonal grid. The locations of these differences correspond to the areas where the non-orthogonal grid has greatest aspect ratios and the flow is slow. Where the flow is strong and aligned with the grid, the high aspect ratios do not seem to affect the results to a great extent. In certain locations the non-orthogonal grid is more refined than the orthogonal grid and in other locations it is more coarse. The difference in local refinement of these coarse grids used for the results shown in Figure 7.26 has a significant effect on the converged solution.

It is important to note that the recirculation zone at the lower end of the exit baffle is very small. In previous iterations on this test problem, when this baffle was narrower and had a square end, this recirculation zone was on the right side of the baffle and extended out the exit boundary. This long recirculation zone was caused by forcing the flow to bend around a very sharp peak at high velocities. In this test, the blockage is wide and has a smoother profile to allow the flow to bend gradually thus preventing a sharp change in flow direction close to the exit.

There are some streamline discontinuities seen in Figure 7.26(b). These discontinuities arise for the reasons described in Section 7.1.1, but are weaker in this case. There are fewer discontinuities in this case because in the areas where the velocity is high, the flow is already traveling perpendicular to the tube bundle boundary. Therefore, the nodal and face velocities agree well. Overall, there seems to be little problem with the tube bundle boundary at the 60×40 grid resolution and higher, whereas, the coarser 30×20 grid had much more difficulty in obtaining a converged solution.

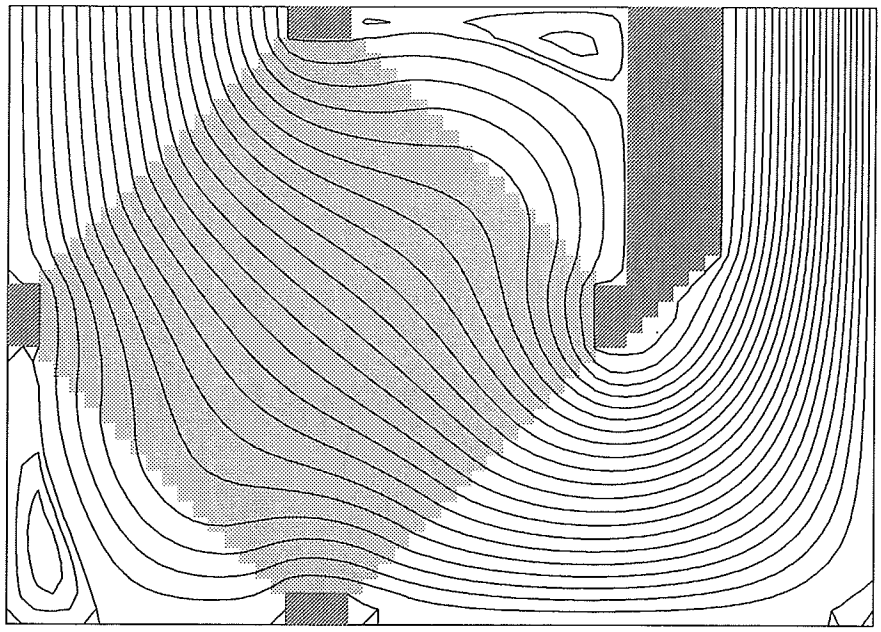

(a) Orthogonal Grid

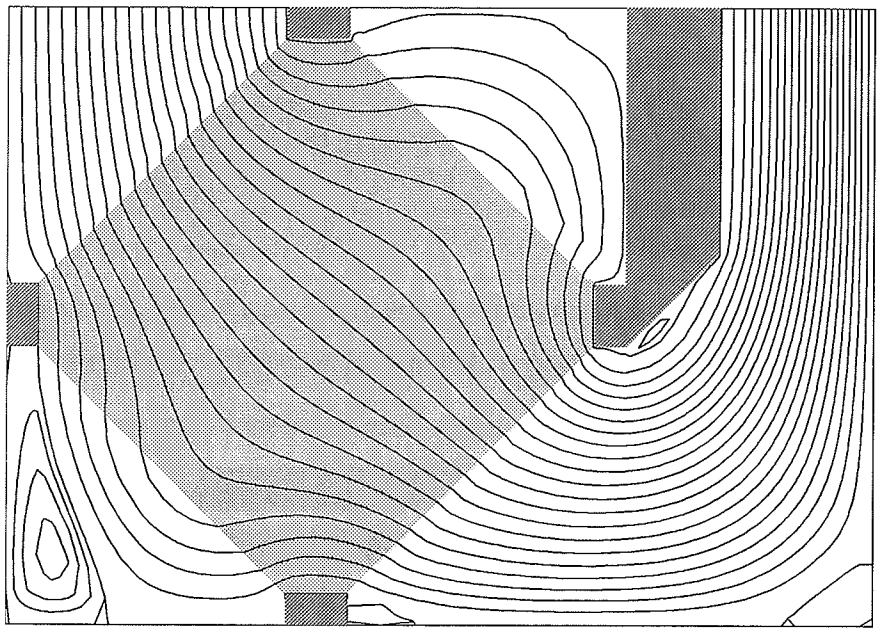

(b) Non-Orthogonal Grid

Figure 7.26: RSTB Test Problem Streamlines: 60×40 Grid, $\mu * 25$.

Figure 7.27 shows the streamline plots of the results on the finest grid, 120×80, and for the same viscosity multiple ($\mu * 25$) as Figure 7.26. The streamlines are smoother because of the finer grid. The streamlines for the orthogonal grid show that the solution predicts a larger recirculation zone in the upper right than that for the non-orthogonal grid. In this case there is a less dramatic difference between the streamline plots for the two grid types than for the coarser grids. The recirculation zone at the bottom of the exit baffle is slightly larger in the orthogonal grid streamline plot than for the non-orthogonal, while both fine grid results predict a larger recirculation than that for the coarser grids. The remainder of the recirculation zones are qualitatively the same for both grids, confirming the trend that as the grids are refined the results from each become more similar.

The streamline plot of the results for the highest viscosity multiple, $\mu * 100$, on the coarse grid, is shown in Figure 7.28. Some of the recirculation zones that were seen with the lower viscosity test do not exist for this viscosity multiple. The two recirculation zones in the lower left corner of the orthogonal grid are comparable in size to the recirculation zone in the non-orthogonal grid, which is quite narrow. The remainder of flow pattern is qualitatively the same on both types of grids.

Figure 7.29 shows the streamline plots of the results on the finest grid, 120×80, and for the same viscosity multiple ($\mu * 100$) as Figure 7.28. There is very little difference between these two results except that the orthogonal grid streamlines show a slightly stronger recirculation at the bottom of the exit baffle than for the non-orthogonal grid. The recirculation zones in the lower left corner have become two distinct zones rather than one large recirculation as seen on the coarser non-orthogonal grid.

The pressure field is interesting to study because it indirectly affects the streamlines. Because of the PWIM, the face velocities are based on interpolations between nodal velocities that are weighted by the pressure gradients. The face velocities, which must conserve mass, are used to calculate the stream function. The pressure reference is set to zero at the right

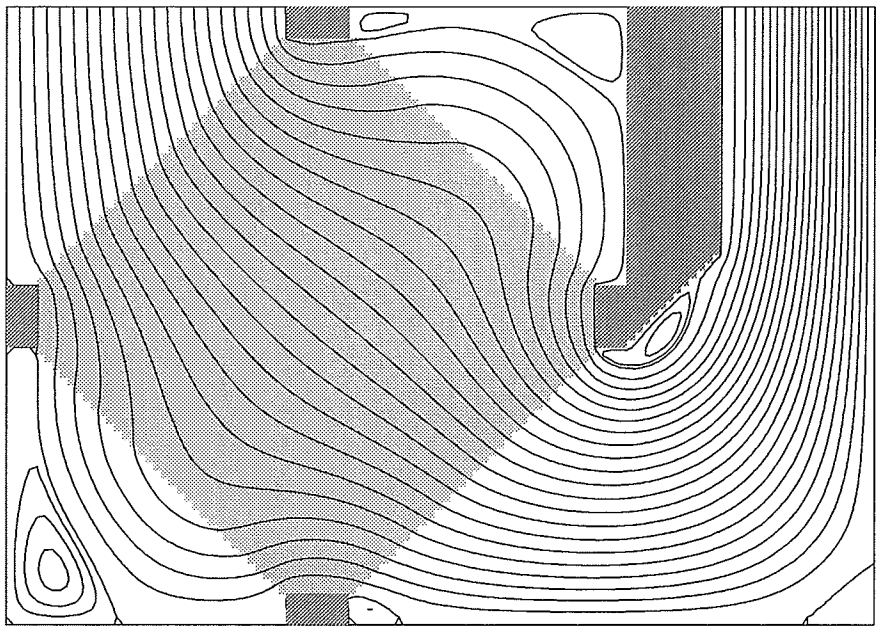

(a) Orthogonal Grid

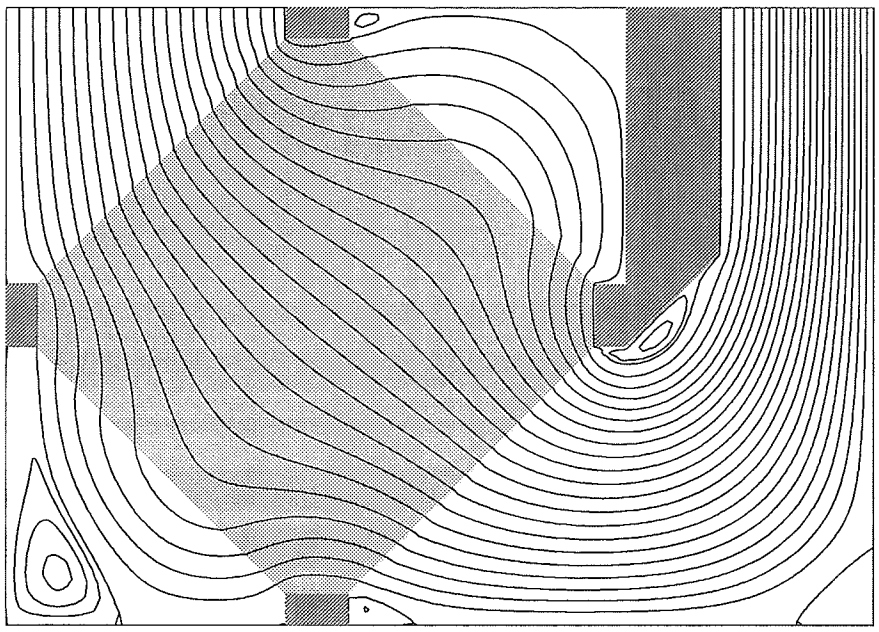

(b) Non-Orthogonal Grid

Figure 7.27: RSTB Test Problem Streamlines: 120×80 Grid, $\mu * 25$.

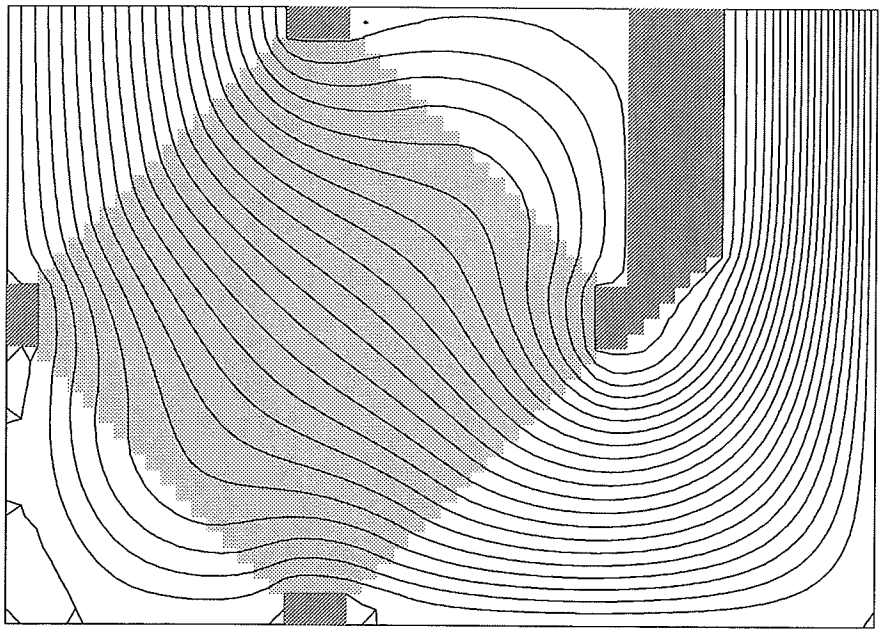

(a) Orthogonal Grid

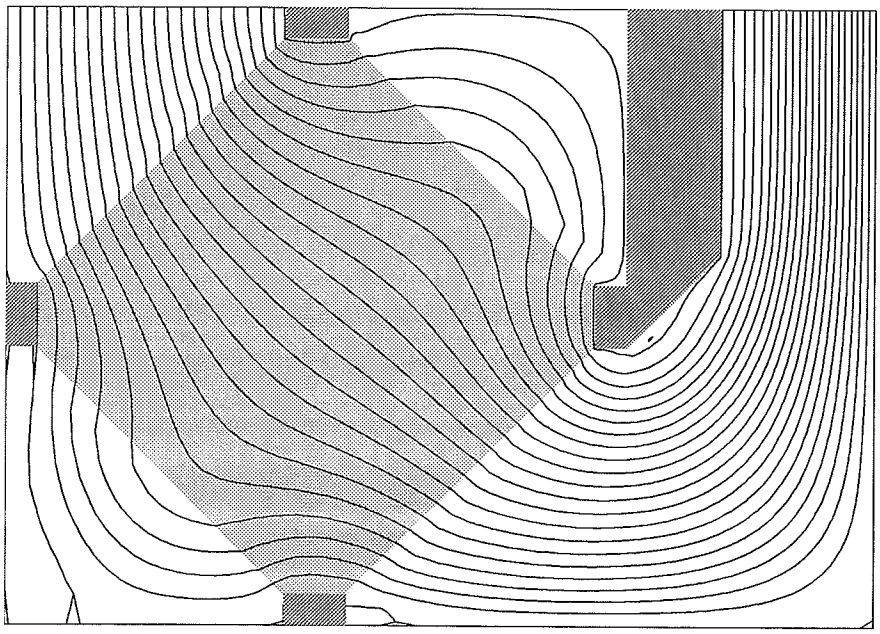

(b) Non-Orthogonal Grid

Figure 7.28: RSTB Test Problem Streamlines: 60×40 Grid, $\mu * 100$.

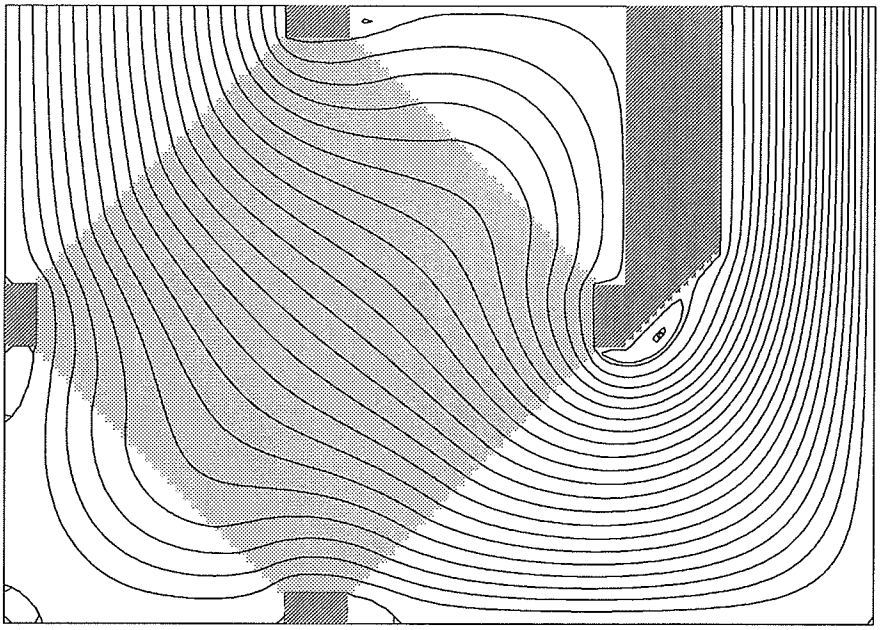

(a) Orthogonal Grid

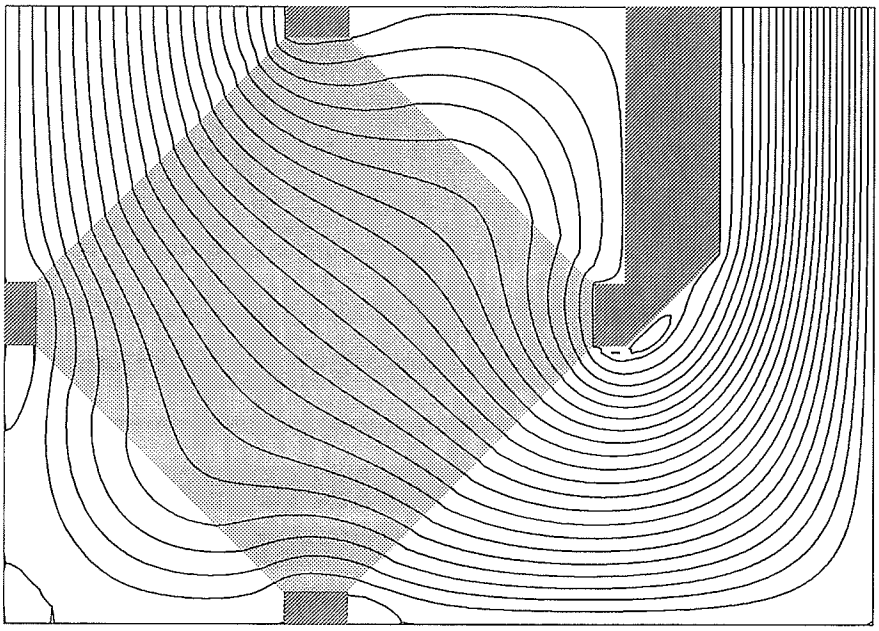

(b) Non-Orthogonal Grid

Figure 7.29: RSTB Test Problem Streamlines: 120×80 Grid, $\mu * 100$.

side of the exit, in the upper right control volume next to the top boundary. In the pressure contours discussed below, the pressure contours are set at the following levels: there are 26 levels evenly spaced at an interval of 1 $[N/m^2]$ between 0 and 25 $[N/m^2]$. There are also five negative pressure contours between -0.1 $[N/m^2]$ and -2 $[N/m^2]$ that are used to highlight the small areas where the pressure is below the reference value. Those areas are referred to as the "negative" pressure areas in the discussion below.

The pressure contours for the low viscosity multiple on the coarse grid are shown in Figure 7.30. The negative pressure areas are at the bottom and to the right of the exit baffle, which corresponds to a recirculation zone. The results on the orthogonal grid have all positive pressures at the exit boundary while the results for the non-orthogonal grid have half of its exit region in negative pressure. All around tube bundle boundary the results for the orthogonal grid show smoother isobars than the non-orthogonal grid. The non-orthogonal grid isobars have a sharp fold characteristic which causes non-physical face velocities.

The pressure contour plots for the low viscosity multiple on the finest grids are shown in Figure 7.31. In both these fine grids the pressure contours are more refined than the coarse grids of Figure 7.30. The areas of negative pressure are now almost identically defined by both the orthogonal and non-orthogonal grid solutions. With the 120×80 grid even the orthogonal grid isobars have sharp folds along the tube bundle boundary, but the non-orthogonal grid isobars are still larger and sharper.

The pressure contour plots for the high viscosity multiple on the coarse grid are shown in Figure 7.32. The negative pressure region in the outflow channel is almost the same for both orthogonal and non-orthogonal grids. Again, the isobar folds along the tube bundle boundaries are smoother in the orthogonal grid than the non-orthogonal grid.

The pressure contour plots on the fine grids for the highest viscosity multiple are shown in Figure 7.33. In those plots the negative pressure region in the outflow channel is almost the same for both orthogonal and non-orthogonal grids. The negative pressure region at

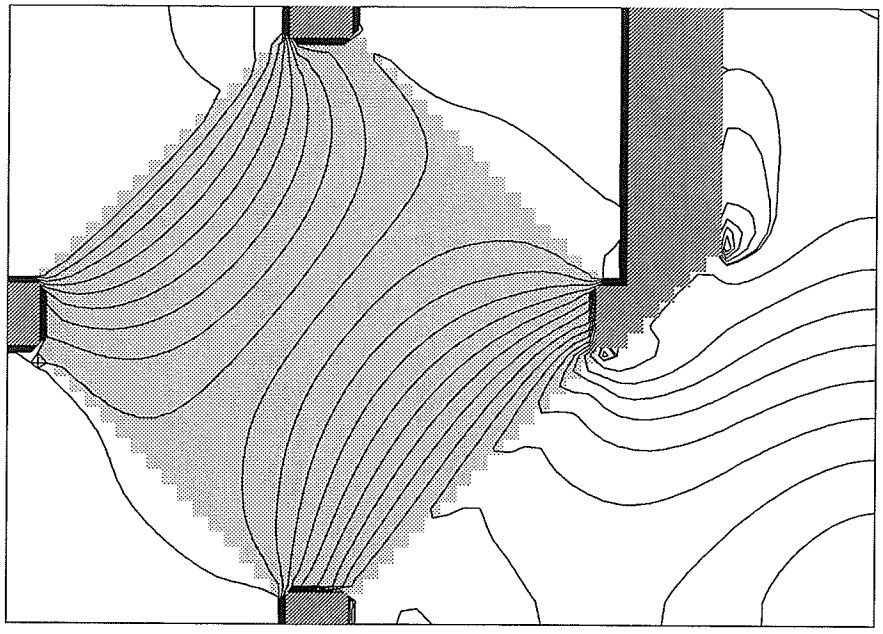

(a) Orthogonal Grid

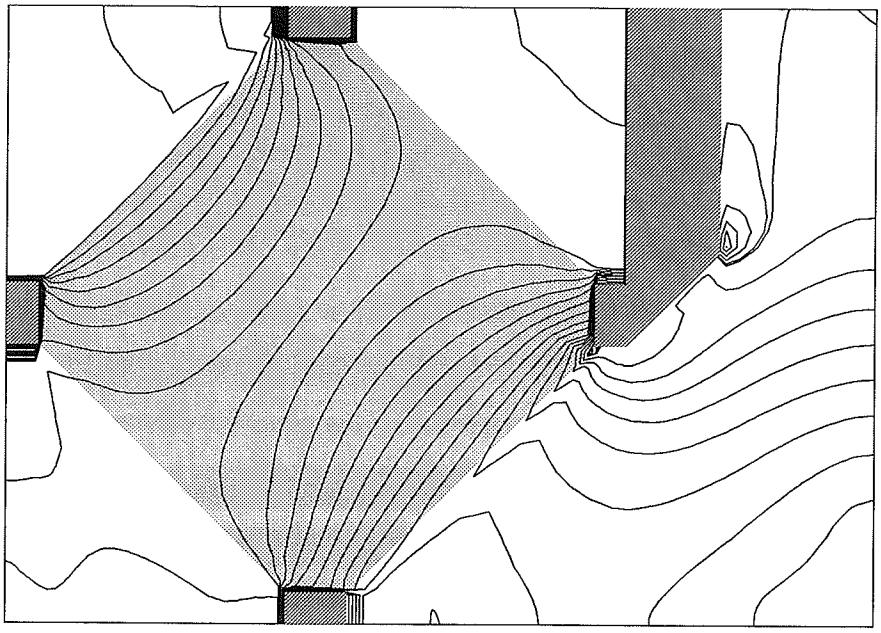

(b) Non-Orthogonal Grid

Figure 7.30: RSTB Test Problem Pressure Contours: 60×40 Grid, $\mu * 25$.

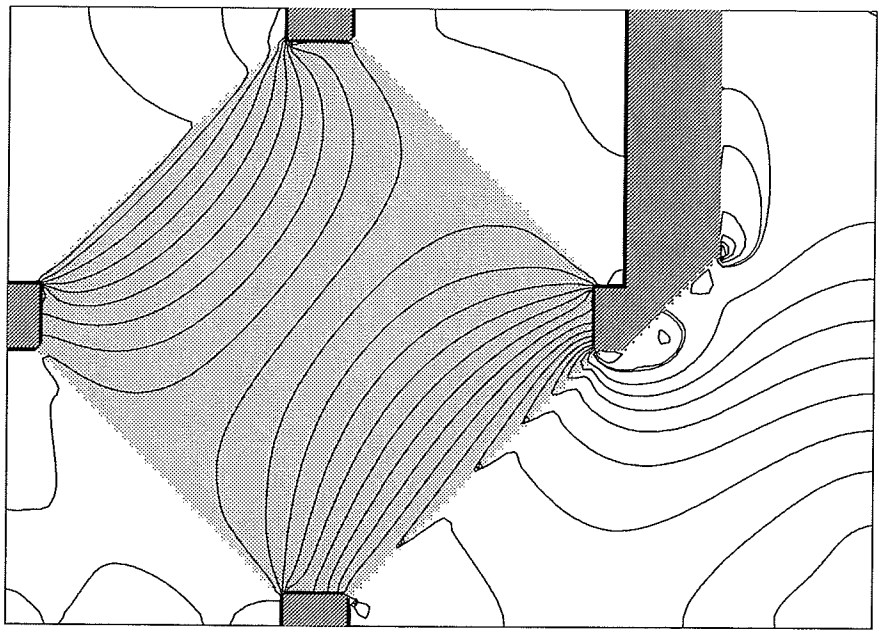

(a) Orthogonal Grid

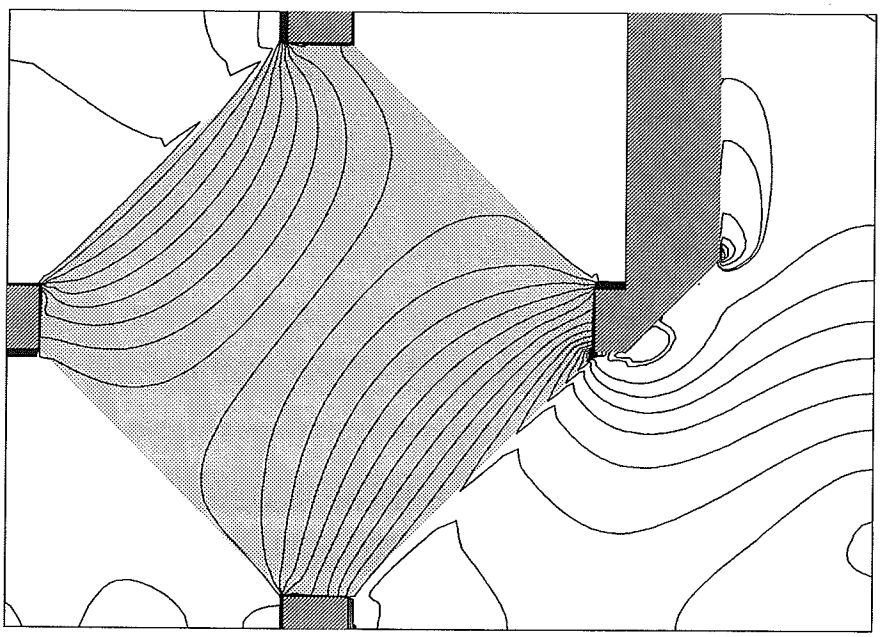

(b) Non-Orthogonal Grid

Figure 7.31: RSTB Test Problem Pressure Contours: 120×80 Grid, $\mu * 25$.

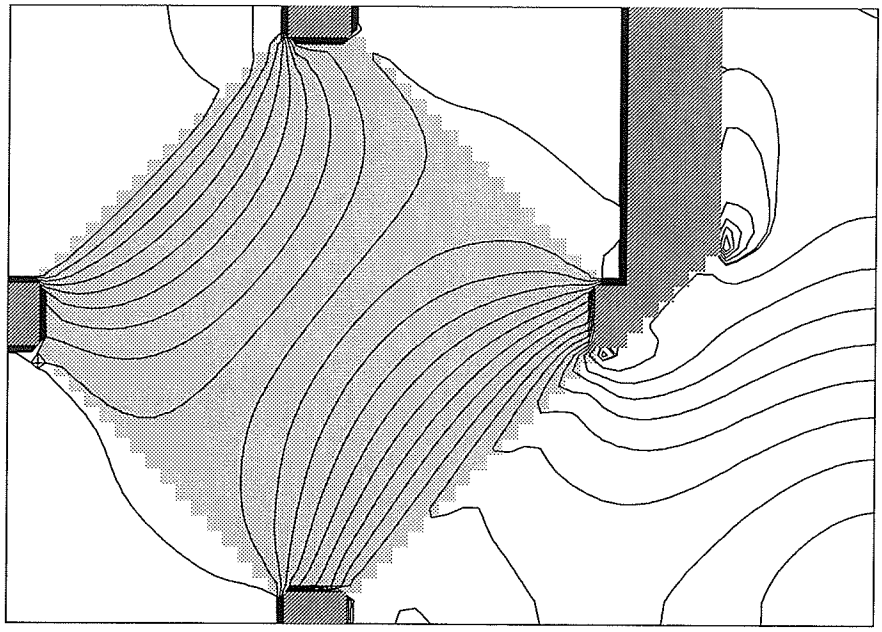

(a) Orthogonal Grid

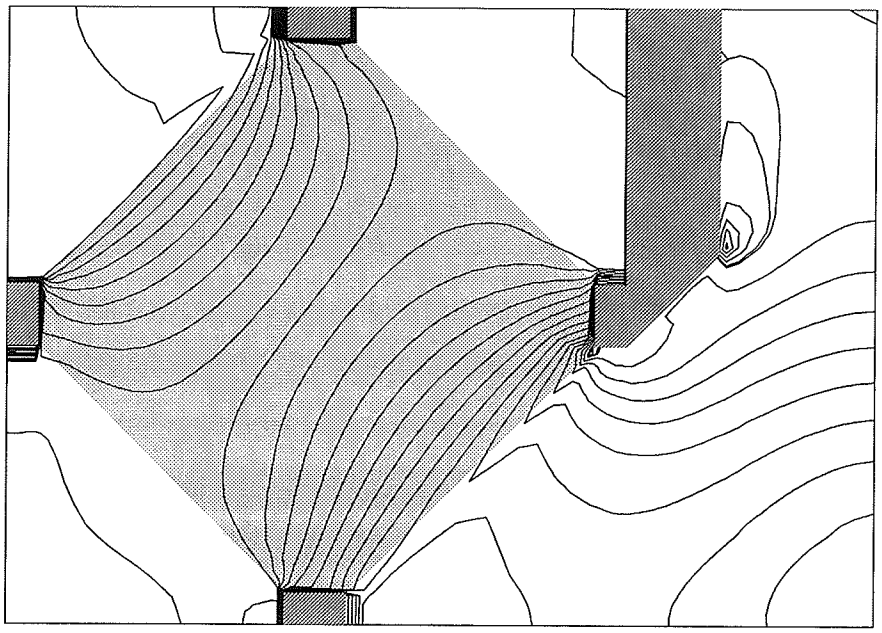

(b) Non-Orthogonal Grid

Figure 7.32: RSTB Test Problem Pressure Contours: 60×40 Grid, $\mu * 100$.

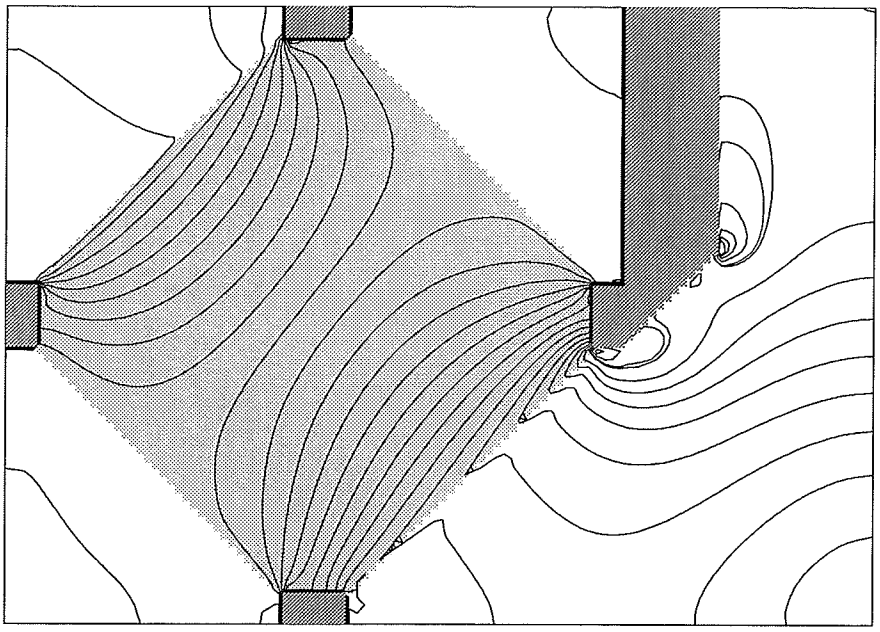

(a) Orthogonal Grid.

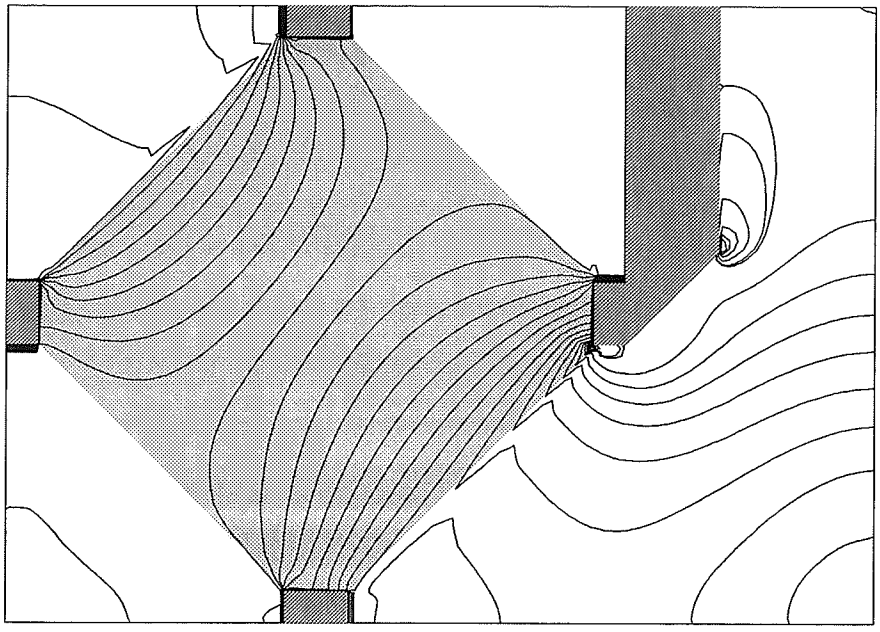

(b) Non-Orthogonal Grid.

Figure 7.33: RSTB Test Problem Pressure Contours: 120×80 Grid, $\mu * 100$.

the bottom of the blockage is larger in the orthogonal grid than the non-orthogonal grid. This corresponds to the stronger recirculation for the orthogonal grid. The grid refinement is responsible for the increase in sharpness of the isobar folds along the tube bundle boundaries. The sudden changes in pressure are a result of the step from tube-filled to free-fluid regions. The orthogonal grid isobars are smoother than those for the non-orthogonal grid even though the porous region edge effect remains.

7.2.1 Grid Independence

There are no suitable experiments that may be used to quantitatively validate the results of the flow calculations in this section. Therefore, one can only determine the point at which a particular model reaches the grid independence criterion. This work seeks to compare the two different grids on the basis of the amount of grid refinement necessary to produce results that reach a grid independence criterion.

The grid resolution is used as a general measurement of computational effort. The coarser grid and less complex method usually results in reasonable approximations with short solution time. The finer grid and more complex method takes more time but gives more detailed results. There is a balance where further refining the grid will not produce more accurate results that are worth the cost of longer run times. To determine at what resolution a particular kind of grid produces reasonably grid-independent results, a representative velocity and overall non-dimensional pressure drop are used.

Table 7.7 lists the values of non-dimensional pressure drop, defined in Equation (7.1), for each orthogonal grid resolution and each viscosity multiple. The same values for each non-orthogonal grid are listed in Table 7.8. The percentages represent the amount of change of each value from the previous coarser grid.

The tables of non-dimensional pressure drop show that the non-orthogonal grid overall solution changes very little with increase in grid resolution while the orthogonal grid solution

Grid	$\mu * 25$		$\mu * 50$		$\mu * 100$	
	C_p^*	%	C_p^*	%	C_p^*	%
30×20	15.04	-	15.03	-	15.00	-
60×40	14.56	-3.2	14.51	-3.5	14.45	-3.7
90×60	14.34	-1.5	14.29	-1.5	14.24	-1.5
120×80	14.19	-1.0	14.14	-1.0	14.10	-1.0

Table 7.7: RSTB Test Problem Non-Dimensional Pressure Drop: Orthogonal Grid.

Grid	$\mu * 25$		$\mu * 50$		$\mu * 100$	
	C_p^*	%	C_p^*	%	C_p^*	%
30×20	N/A	-	14.19	-	14.17	-
60×40	14.23	-	14.21	+0.1	14.17	0.0
90×60	14.15	-0.6	14.11	-0.7	14.08	-0.6
120×80	14.07	-0.6	14.03	-0.6	14.02	-0.4

Table 7.8: RSTB Test Problem Non-Dimensional Pressure Drop: Non-Orthogonal Grid.

has a larger change for the first doubling of grid resolution. Between the next three grid resolutions the change becomes smaller. The orthogonal grid shows relatively greater change than the non-orthogonal grid with increase in resolution because of the aliasing of the tube bundle and the blockage.

Aliasing of the baffle presents a jagged surface over which the fluid must flow. This jagged surface increases the pressure drop compared to a smoother surface modeled with the non-orthogonal grid. With increasing grid resolution, the orthogonal grid aliasing of the blockage becomes smoother and the pressure drop decreases, while flow on the non-orthogonal grid remains the same in that area.

A similar argument may be made regarding the tube bundle boundary aliasing. Even though the area of the tube bundle is the same for both grid types, the orthogonal grid will

apply a small porosity to a control volume that is only partially inside the defined edge of the tube bundle. This way the porous region appears larger than the actual tube bundle. As the grid is more refined, the aliasing approximation becomes more accurate. The porous region appears to shrink towards the actual tube bundle size as the resolution increases. However, the tube bundle definition remains constant with the non-orthogonal grid. This change in the numerical approximation of the tube bundle size is the second reason why the orthogonal grid has a larger change in non-dimensional pressure drop than the non-orthogonal grid.

When using the lowest grid resolutions and lowest effective viscosities, the flow solution becomes unstable on a non-orthogonal grid. For a 30×20 grid a converged solution was not obtained for $\mu*25$. The higher effective viscosity results show that the 30×20 non-orthogonal grid is too coarse to give an accurate solution because the C_p^* does not change monotonically, as seen in Table 7.8. The orthogonal grid solution is more robust at low grid resolutions because the abrupt pressure change at the tube bundle boundaries is smoothed out by a more gradual change of porosity.

If one were to set a grid independence criterion of 1% change in C_p^*, then the non-orthogonal grid reaches that criterion at much lower grid resolutions than the orthogonal grid. The non-orthogonal grid can be considered grid-independent for this criterion at 60×40 while the orthogonal grid meets this criterion at 120×80. The orthogonal 120×80 grid gives basically the same pressure drop results and takes about six times longer to solve than the non-orthogonal 60×40 grid.

As an aside, it is noted that the non-dimensional pressure drop remains practically unchanged as the effective viscosity increases. Two possible explanations for this behavior arise from the use of wall functions and tube drag.

First, the increased viscosity would normally increase the shear stress in the fluid next to solid objects. However, in the case of turbulent flow, wall functions were used that adjust the viscosity in the first control volume next to a wall to allow a turbulent velocity profile

to be modeled. This adjustment effectively reduces the amount of drag relative to keeping the same viscosity and using the high velocity gradient that is characteristic of a turbulent profile. This effect is approximately the same for flows with different effective viscosities.

Second, it is expected that the pressure drop in the tube bundle is dominated by the drag terms in the governing equations. Those drag terms are calculated using molecular viscosity which does not change. Furthermore, if the drag term dominates, then the diffusion terms sensitive to effective viscosity are expected to be small in magnitude by comparison. Only changes in free-fluid flow regions, where there is no tube drag, would cause a change in the pressure drop due to mean flow shear. Therefore, the changes in pressure drop are small because the overall flow patterns are relatively similar.

The local velocity profiles are another measure of grid independence because they show the differences in specific areas of the flow in a way that can be easily compared. For the purpose of finding grid-independent solutions for specific flow patterns one could look at the results for $\mu * 50$ on all four grid solutions. The other velocity profiles at viscosity multiples $\mu * 25$ and $\mu * 100$ are shown in Appendix C.2.

A cross-section at the vertical centerline (line "A" in Figure 7.23) is taken from the bottom boundary inside the bottom sealing strip, $y = 0$, to the top of the sealing strip on the top boundary, $y = 1.0$. The U component of velocity, crossing the vertical centerline, is plotted in Figure 7.34 for the orthogonal grid at different densities. The graph shows two peaks in the velocity near the sealing strips and a deep "trough" in the center. The peaks indicate faster flow in areas of least flow resistance from the bundle, the narrow section of tube bundle near each sealing strip. These high flow areas show greater changes for different grid resolutions. The peak velocity is used as an indication of the differences between the velocity solutions because the rest of the profile is very similar for each grid resolution. In some cases the peak velocity does not change monotonically because of the rapid changes in the velocities due to tube bundle edge effects. When two edges are separated by only two

or three control volumes, as occurs with a very coarse grid, the velocity between them may have wider variation than in the rest the field.

The upper peak in the 30×20 curve has much lower velocity than any of the finer resolutions, and as the grid becomes more refined the differences get smaller. The coarse grid does not happen to have a node at the highest flow location so the peak velocity is not always represented properly. The lower peak, by contrast, shows a smaller amount of change than the upper peak. Other than at the two peaks, the four curves appear very similar.

To quantify the change in the velocity profiles with grid resolution, the peak velocities and the percentage changes are listed in Table 7.9. The change of peak U velocity as the grid is refined is decreasing for the top peak but non-monotonic for the bottom peak. The bottom peaks are so close to each other that the change there is not significant.

	Lower Peak		Upper Peak	
Grid	Velocity	%	Velocity	%
30×20	1.046	-	0.852	-
60×40	1.040	-0.6	0.895	+5.0
90×60	1.040	0.0	0.908	+1.5
120×80	1.055	+1.4	0.921	+1.4

Table 7.9: RSTB Test Problem Line "A" U Velocity Peaks: Orthogonal Grid, $\mu * 50$.

The U velocity profile along the vertical centerline of the non-orthogonal grid is shown in Figure 7.35. The difference between this profile and the one in Figure 7.34 is that the lower peak velocities are more spread out for the different grid resolutions.

The values of the peak U velocity for Figure 7.35 are listed in Table 7.10. The change of peak U velocity as the grid is refined is decreasing steadily for the top peak. The bottom peak is increasing in size at a variable rate, similar to the orthogonal grid results.

The V component of velocity crossing the horizontal centerline is plotted in Figure 7.36

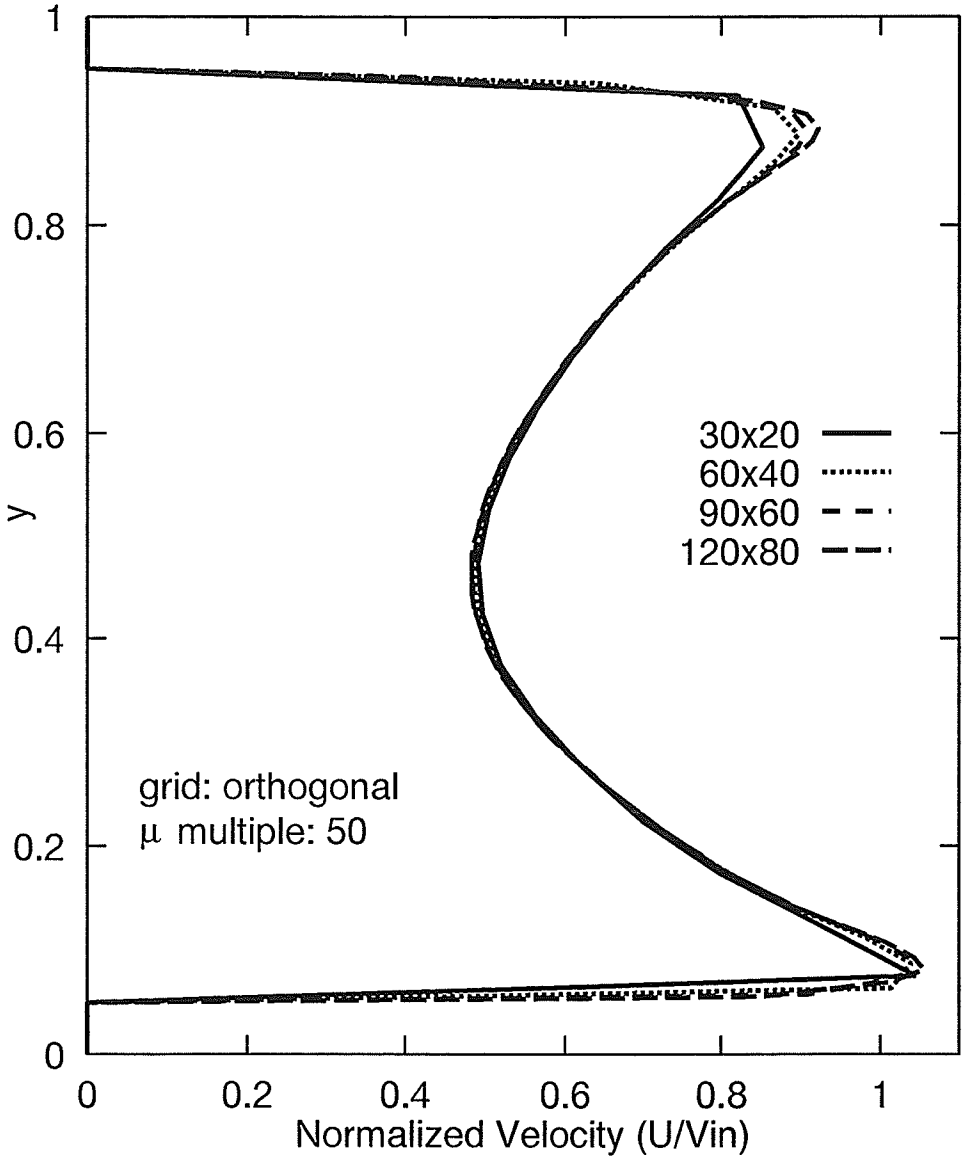

Figure 7.34: RSTB Test Problem U Velocity Profiles at "A": Orthogonal Grid, $\mu * 50$.

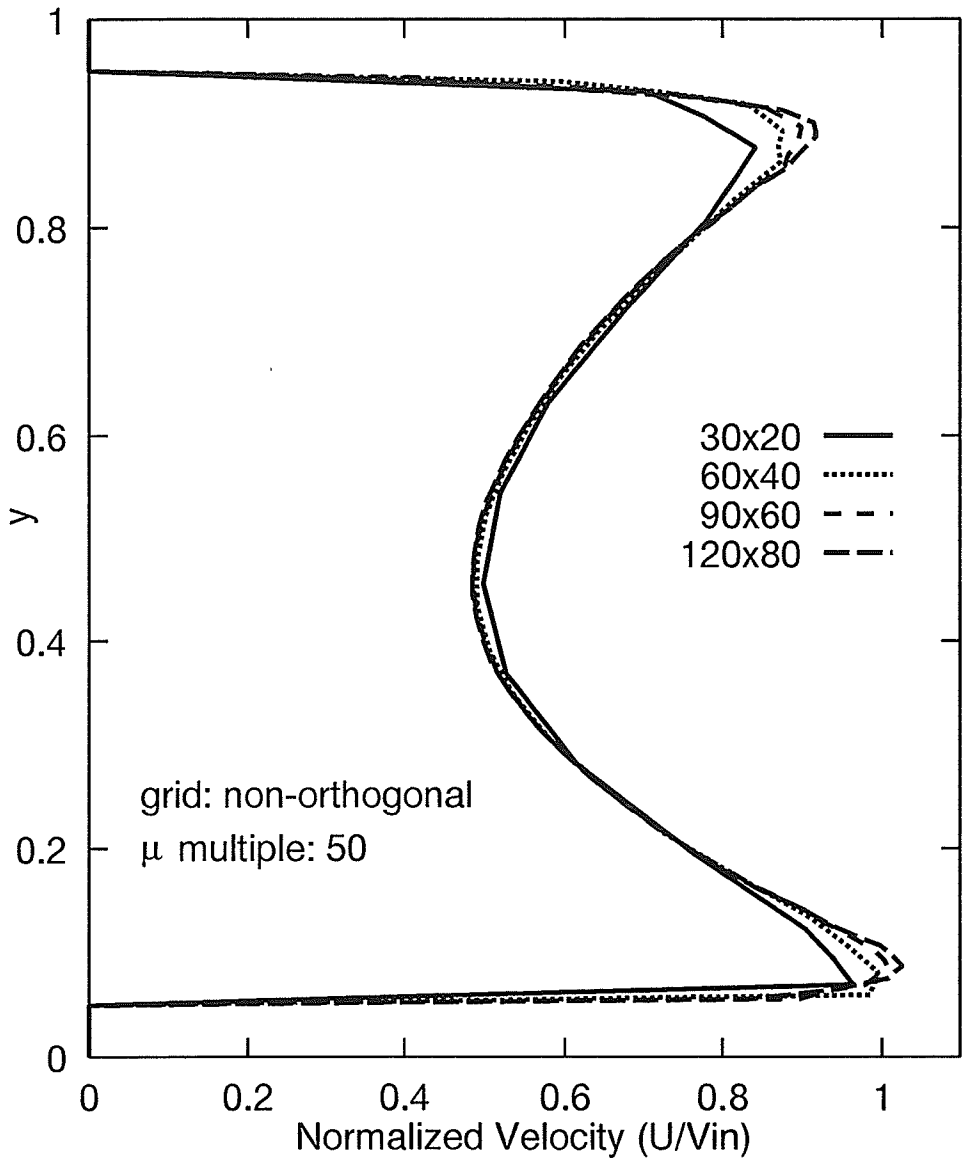

Figure 7.35: RSTB Test Problem U Velocity Profiles at "A": Non-Orthogonal Grid, $\mu * 50$.

	Lower Peak		Upper Peak	
Grid	Velocity	%	Velocity	%
30×20	0.963	-	0.843	-
60×40	0.995	+3.3	0.876	+3.9
90×60	1.009	+1.4	0.898	+2.5
120×80	1.026	+1.7	0.918	+2.2

Table 7.10: RSTB Test Problem Line "A" U Velocity Peaks: Non-Orthogonal Grid, $\mu * 50$.

for the orthogonal grid at different densities. The V velocity curves show negative velocity peaks near the sealing strips and a large "trough" in the center. There is little change in the magnitude of peak velocities between the grids, but a small change of the location of the peak in the x direction exists. The trough in between the two peaks shows little change with increase in grid resolution.

Again, to quantify the change in the velocity profiles with grid resolution the peak velocities and the percentage changes are listed in Table 7.11. Only small changes in the peak V velocities are seen.

	Left Peak		Right Peak	
Grid	Velocity	%	Velocity	%
30×20	-1.056	-	-1.190	-
60×40	-1.058	+0.2	-1.200	+0.8
90×60	-1.064	+0.6	-1.202	+0.2
120×80	-1.073	+0.8	-1.209	+0.6

Table 7.11: RSTB Test Problem Line "B" V Velocity Peaks: Orthogonal Grid, $\mu * 50$.

The V velocity profile along the horizontal centerline for the non-orthogonal grid is shown in Figure 7.37. There are significant changes visible in both magnitude and location of the peak velocities.

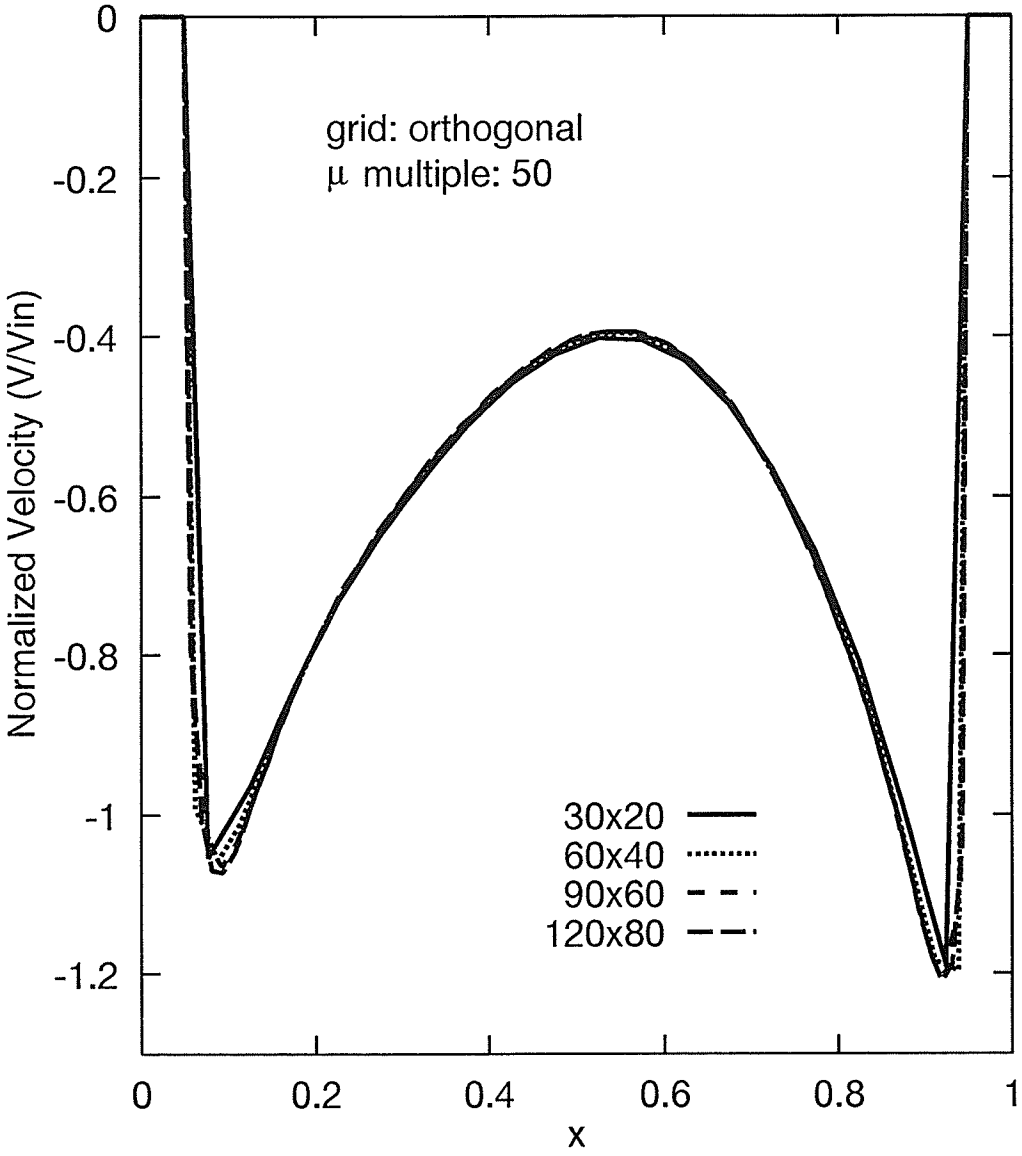

Figure 7.36: RSTB Test Problem V Velocity Profiles at "B": Orthogonal Grid, $\mu * 50$.

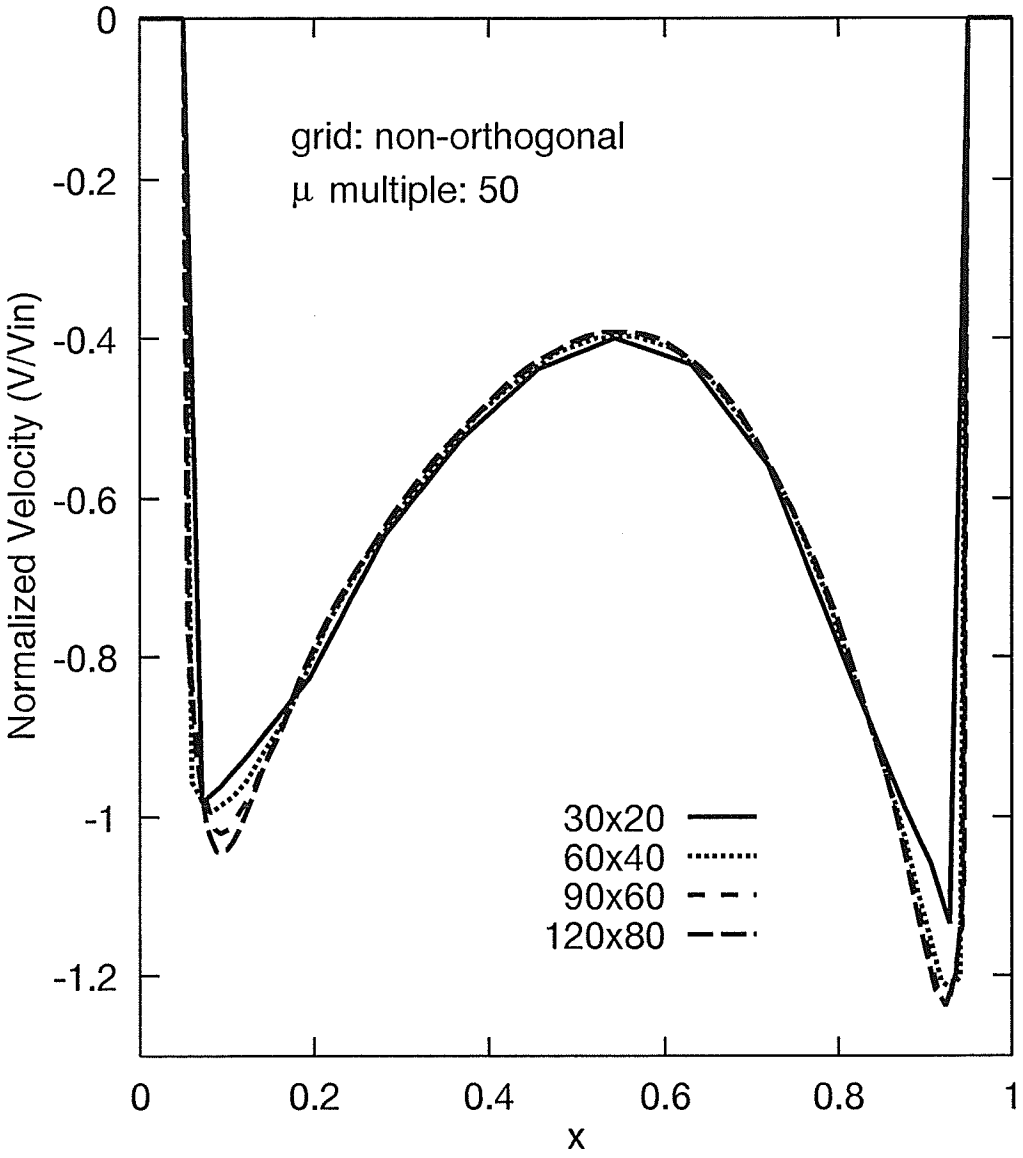

Figure 7.37: RSTB Test Problem V Velocity Profiles at "B": Non-Orthogonal Grid, $\mu * 50$.

The values of the peak V velocity, in Figure 7.37, are given in Table 7.12. The largest change in peak velocity magnitude is between the coarsest and second grid resolutions. This large change is to be expected given that the coarse non-orthogonal grid had difficulties reaching a converged solution.

	Left Peak		Right Peak	
Grid	Velocity	%	Velocity	%
30×20	-0.982	-	-1.134	-
60×40	-0.995	+1.3	-1.215	+7.1
90×60	-1.021	+2.6	-1.227	+1.0
120×80	-1.043	+2.2	-1.238	+0.9

Table 7.12: RSTB Test Problem Line "B" V Velocity Peaks: Non-Orthogonal Grid, $\mu * 50$.

The exit region is the region to the right of the tube bundle. A profile is taken along line "C" of Figure 7.23 to determine if the flows are different after leaving the tube bundle. The profile is plotted for the orthogonal grid and $\mu * 50$ in Figure 7.38. The velocity starts at the bottom wall at zero then increases rapidly to about the inlet velocity. The velocity then stays approximately equal to the inlet velocity for most of the traverse towards the baffle, whose bottom face is located at $y = 0.45$. The negative velocities near $y = 0.45$ indicate the recirculation zone. Since the recirculation zone has different sizes and intensities for the different grids and resolutions, the velocity peaks and magnitudes vary widely. The two coarsest grids do not have a recirculation zone so the peak is reduced and no negative velocities exist. The other two grid resolutions appear to have similar velocity profiles except for the difference in peak velocity magnitudes. There is a velocity peak near the baffle, at about $y = 0.37$, that is used as a representative velocity. This velocity peak is a better indicator of grid independence than the profiles inside the tube bundle, since this profile is not directly affected by the tube bundle edges.

The values of the upper peak U velocity, in Figure 7.38, are given in Table 7.13. The

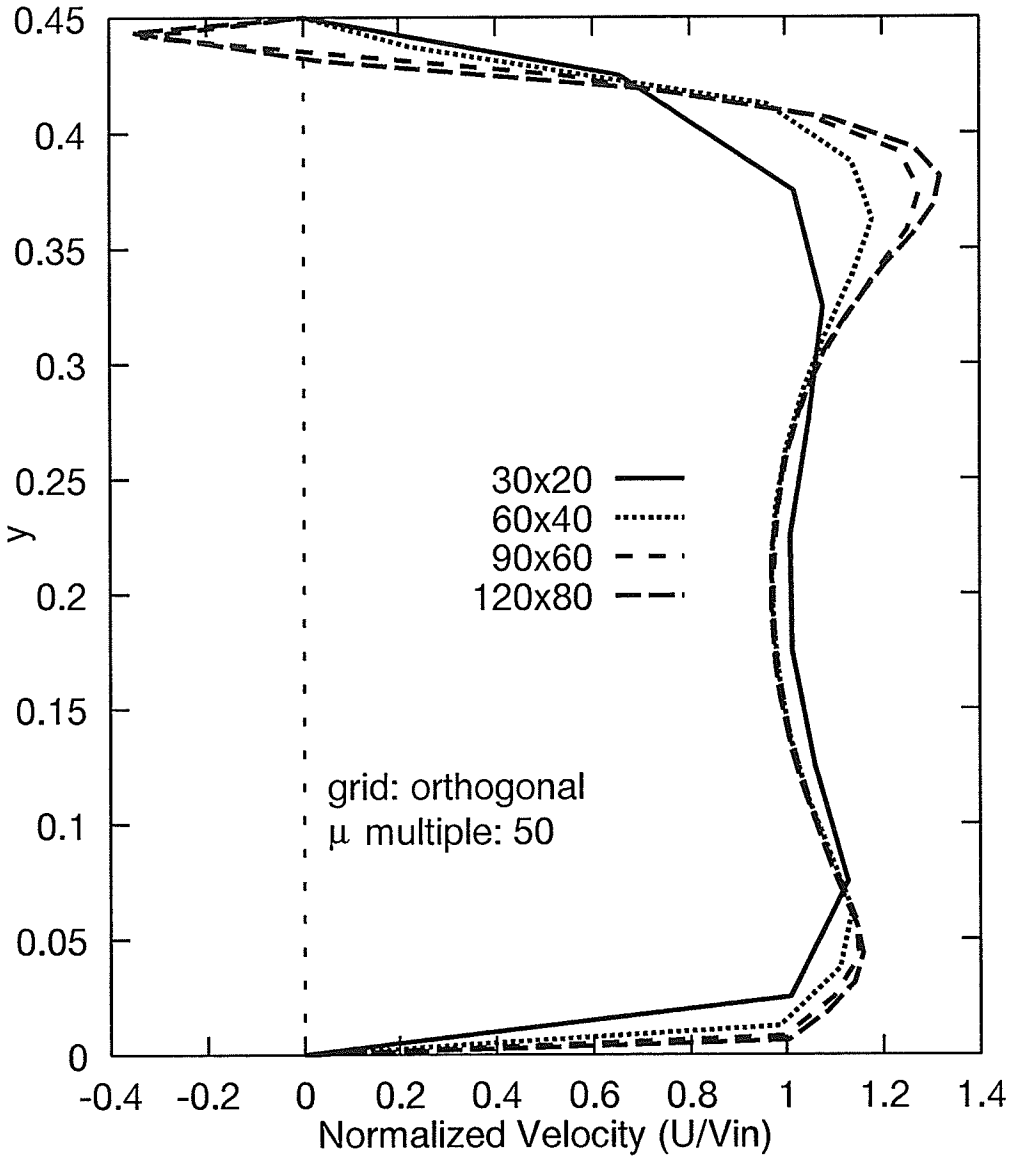

Figure 7.38: RSTB Test Problem U Velocity Profiles at "C": Orthogonal Grid, $\mu * 50$.

magnitude of the change of peak velocities along this line is much larger than inside the tube bundle along lines "A" and "B". The strong recirculation zone near the baffle and the absence of drag to dampen flow variation are possible reasons for the greater change in peak velocity with grid refinement.

	Upper Peak	
Grid	Velocity	%
30×20	1.075	-
60×40	1.177	+9.5
90×60	1.277	+8.5
120×80	1.319	+3.3

Table 7.13: RSTB Test Problem Line "C" U Velocity Peak: Orthogonal Grid, $\mu * 50$.

The U-velocity curve along line "C" for the non-orthogonal grid is shown in Figure 7.39. The coarsest two grids do not have a recirculation zone below the blockage and therefore no negative velocities. The velocity profile for coarsest grid resolution appears much different than the other three resolutions The overall profile of the other three grids presented are very similar except for the peak velocity magnitude.

The values of the upper peak velocity, at about $y = 0.37$ in Figure 7.39, are given in Table 7.14. The magnitude of the change of peak velocities is decreasing with grid refinement.

If one were to set the criterion for grid independence at a 5% change in a particular peak velocity, then both the orthogonal and non-orthogonal grid 120×80 solutions would meet the criterion when only the profile at line "C" is considered. Using the non-dimensional pressure drop to compare the grids indicates that the non-orthogonal grid can be considered grid-independent at 60×40 and the orthogonal grid at 120×80. The non-dimensional pressure drop is a more general test of overall solution while the change in peak velocities is a

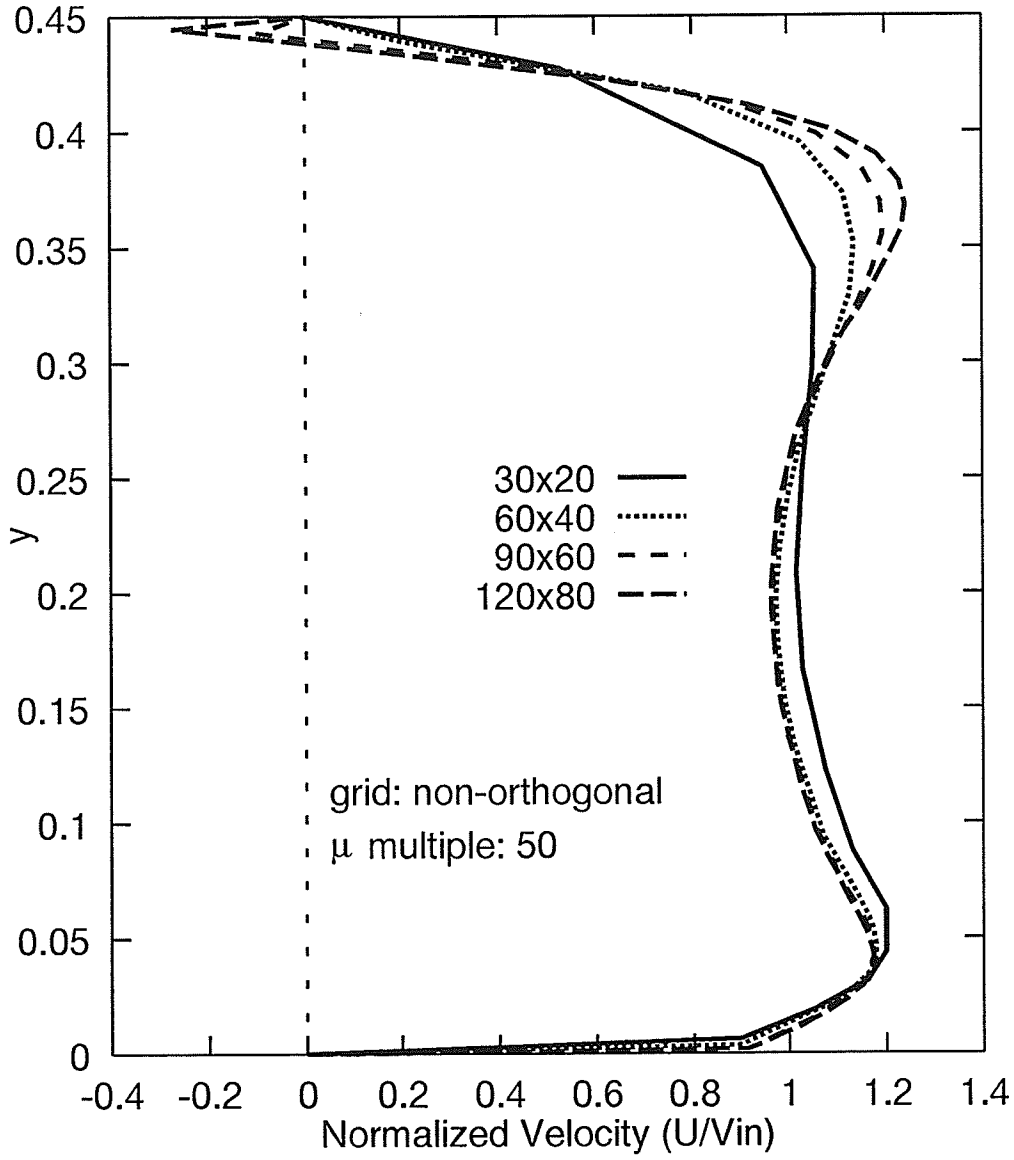

Figure 7.39: RSTB Test Problem U Velocity Profiles at "C": Non-Orthogonal Grid, $\mu * 50$.

Grid	Upper Peak Velocity	%
30×20	1.054	-
60×40	1.136	+7.8
90×60	1.195	+5.2
120×80	1.243	+4.0

Table 7.14: RSTB Test Problem Line "C" U Velocity Peak: Non-Orthogonal Grid, $\mu * 50$.

more sensitive indicator. Since the magnitude of the velocity peaks generally increased with increase in grid resolution, the orthogonal grid has a slight advantage when using the peak velocity test because its fine grid peak velocity magnitude is higher than the non-orthogonal result. Which grid method gives the most realistic results cannot be answered by this study due to a lack of experimental comparisons. The conclusions that can be reached here are that the non-orthogonal grid produces grid-independent overall measurements at lower grid refinement, (as indicated by the non-dimensional pressure drop comparison), and that when flow details are examined, the orthogonal grid shows smaller changes. These trends are for the $\mu * 50$ viscosity multiple case, other viscosity multiples are examined shortly.

7.2.2 Grid Comparisons

The direct comparison of the results for orthogonal and non-orthogonal grids is done using the finest grid resolution and $\mu * 50$ for each of the three profile locations.

The U velocity curve along line "A" for the orthogonal and non-orthogonal 120×80 grids is shown in Figure 7.40. The two profiles shown here are very close except at the lower peak. The trend, shown in Figures 7.34 and 7.35 and in Tables 7.9 and 7.10, is that, as the grid is refined, the peak velocities increase. For the orthogonal grid, the upper peak velocity is 0.3% larger than the non-orthogonal grid peak velocity. For the lower peak, the orthogonal

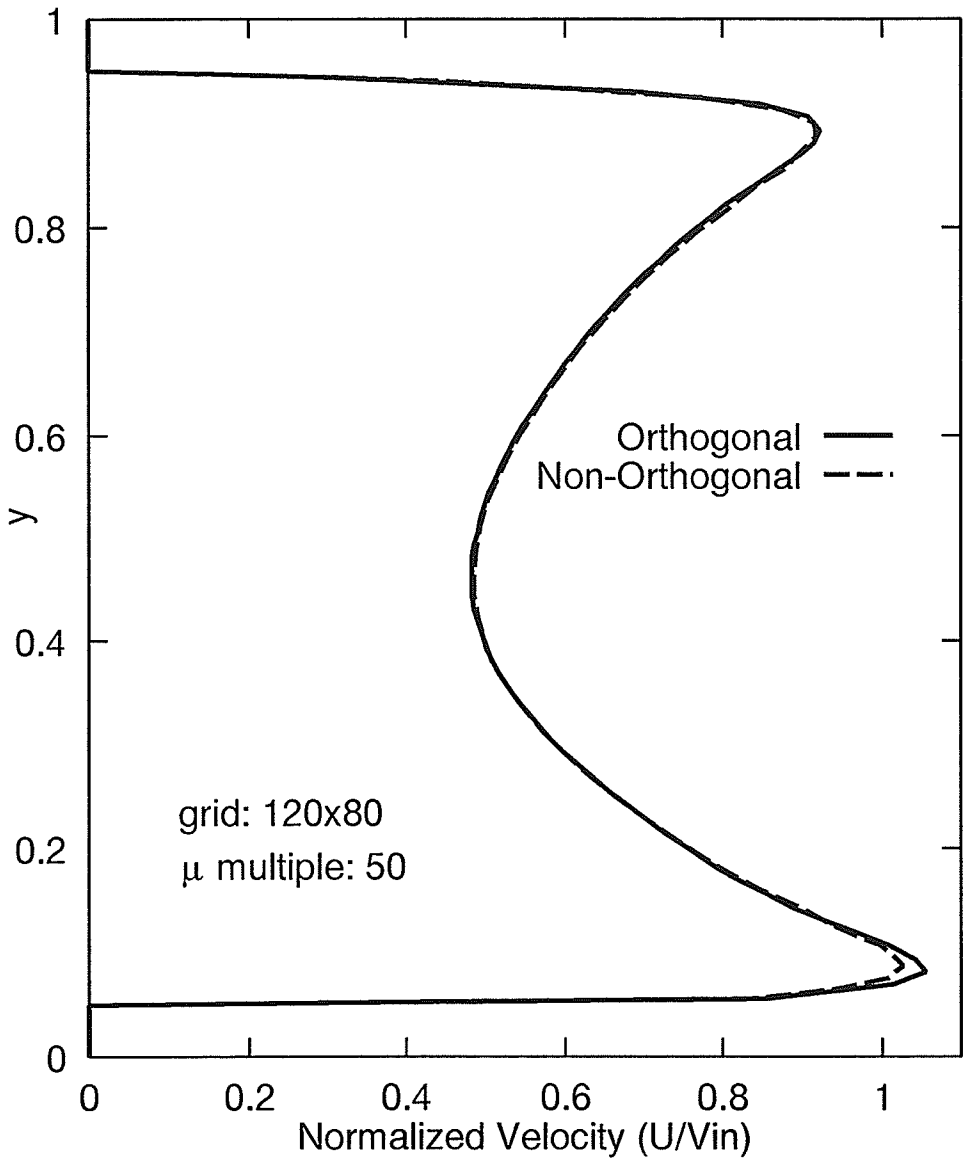

Figure 7.40: RSTB Test Problem U Velocity Profiles at "A": 120×80 Grid, $\mu * 50$.

grid velocity is 2.8% larger than the non-orthogonal grid peak velocity. Since the orthogonal grid velocity profile peaks are larger than the non-orthogonal peak velocities and the trend using both grids is toward increasing peak velocities with increasing grid refinement, the orthogonal grid appears to be closer to a grid-independent solution for this velocity profile.

The V-velocity curve along line "B" for both the orthogonal and non-orthogonal 120×80 grids is shown in Figure 7.41. Both the orthogonal and non-orthogonal grid velocity profiles are very close except for the peaks. The trend, shown in Figures 7.36 and 7.37 and in Tables 7.11 and 7.12, is that as the grid is refined the peak velocities increase. For the left peak velocity, the magnitude of the orthogonal grid result is 2.9% larger than that for the non-orthogonal grid. For the right peak, the non-orthogonal grid velocity magnitude is 2.4% larger than that for the orthogonal grid peak velocity.

The U-velocity curve along line "C" for both the orthogonal and non-orthogonal 120×80 grid is shown in Figure 7.42. The orthogonal and non-orthogonal grid profiles, shown here, are generally the same except for the velocity peak and the recirculation zone. The trend, shown in Figures 7.38 and 7.39 and in Tables 7.13 and 7.14 is that as the grids are refined the peak velocities increase dramatically. The orthogonal grid peak velocity is 6.1% larger than the non-orthogonal grid peak velocity. Since the orthogonal grid velocity profile peak is larger than the non-orthogonal peak velocity, the orthogonal grid appears be closer to grid independence in predicting this velocity profile. The orthogonal grid results shows a larger area of negative velocities than the non-orthogonal grid results and therefore a larger recirculation zone, which also fits with the trend as the grids are refined. A large difference remains between the two results even for the finest grids which indicates the need for further refinement of the grid if a tighter grid independence criterion is desired.

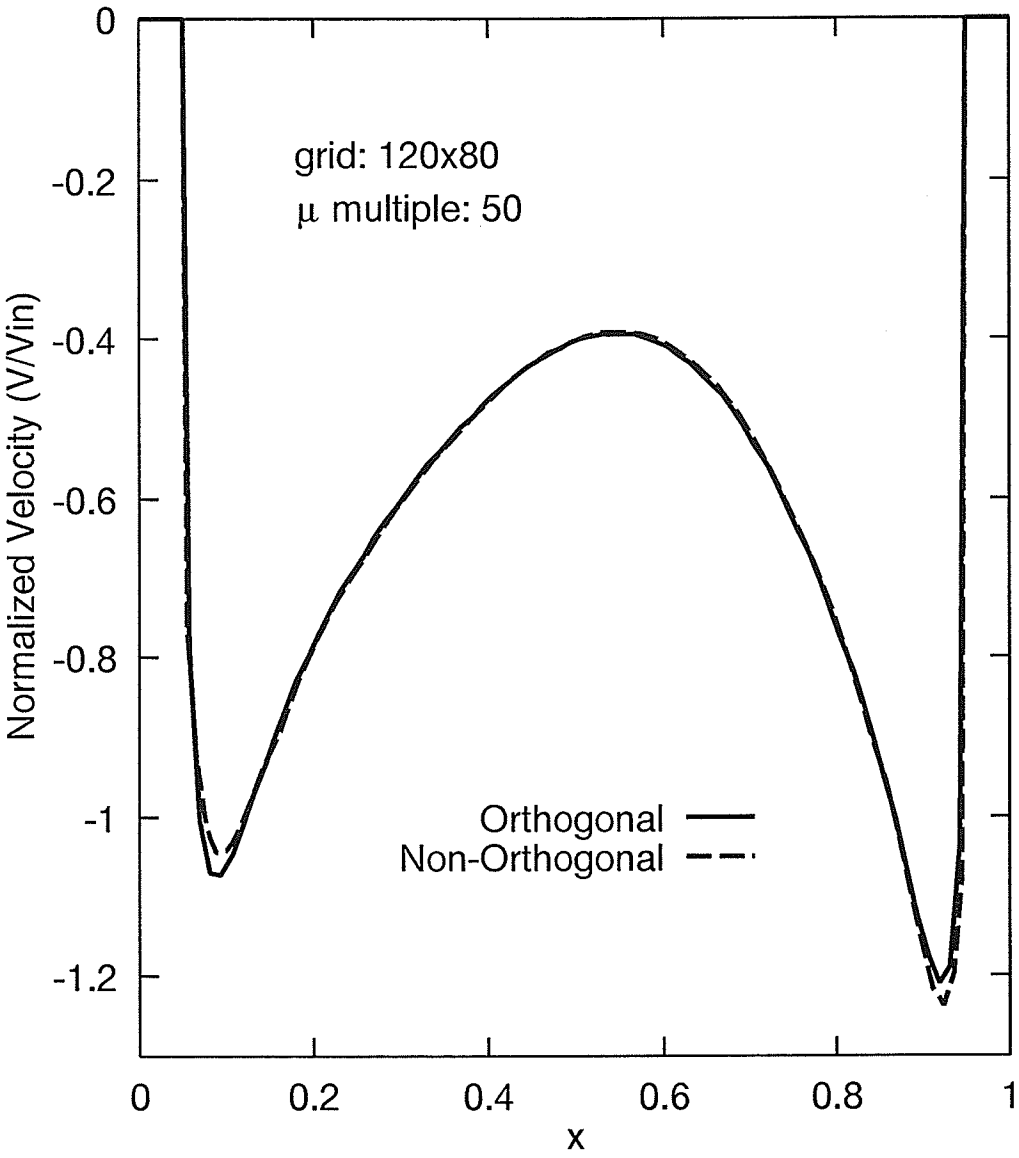

Figure 7.41: RSTB Test Problem V Velocity Profiles at "B": 120×80 Grid, $\mu * 50$.

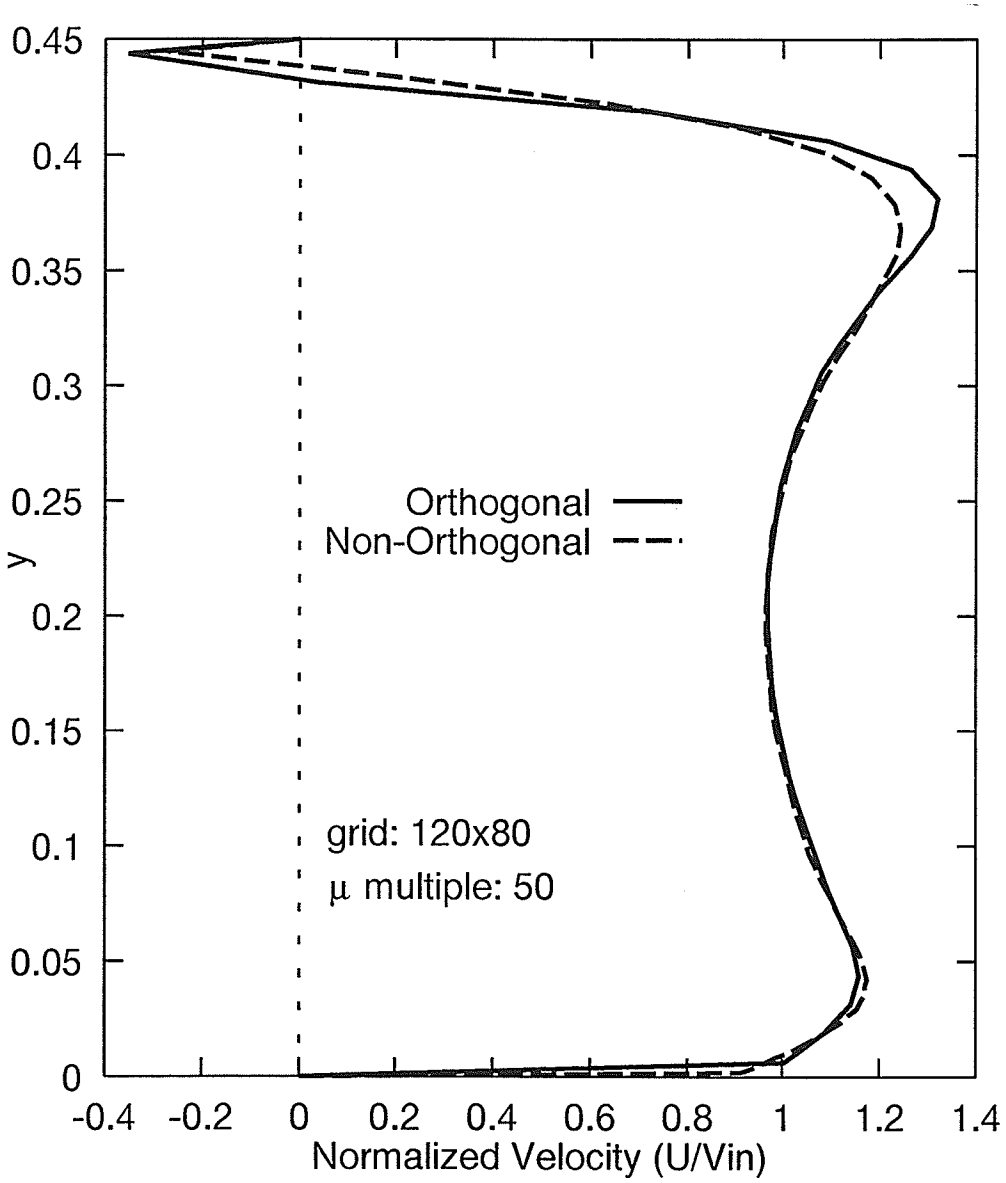

Figure 7.42: RSTB Test Problem U Velocity Profiles at "C": 120×80 Grid, $\mu * 50$.

7.2.3 Viscosity Effect

This section compares the differences in flow prediction when the effective viscosity is changed.

The U-velocity curves along line "A" for the 120×80 orthogonal grid for the three values of effective viscosity are shown in Figure 7.43. There is little effect on the U velocity on the vertical centerline in the orthogonal grid since all three viscosity multiples produced very similar velocity profiles.

The values of the peak velocity, for Figure 7.43, are given in Table 7.15. The percentages indicate the amount of change from the results for the previous lower viscosity multiple. The increase in viscosity served to smooth out the peak velocity slightly. The lower peak has the greatest effect at only 0.8% decrease in U velocity.

	Lower Peak		Upper Peak	
Grid	Velocity	%	Velocity	%
$\mu * 25$	1.059	-	0.921	-
$\mu * 50$	1.055	-0.4	0.921	0.0
$\mu * 100$	1.047	-0.8	0.918	-0.3

Table 7.15: RSTB Test Problem Line "A" U Velocity Peaks: Orthogonal 120×80 Grid.

The U-velocity curves along line "A" for the 120×80 non-orthogonal grid for the three viscosity multiples are shown in Figure 7.44. There is just a slight difference in the velocity peaks.

The values of the peak velocity, for Figure 7.44, are given in Table 7.16. Again, the lower peak has the greatest difference at only 0.7% decrease in U velocity with increase effective viscosity by a factor of 2.

The V-velocity curve along line "B" for the 120×80 orthogonal grid is shown in Figure 7.45. There is little difference in the three velocity profiles.

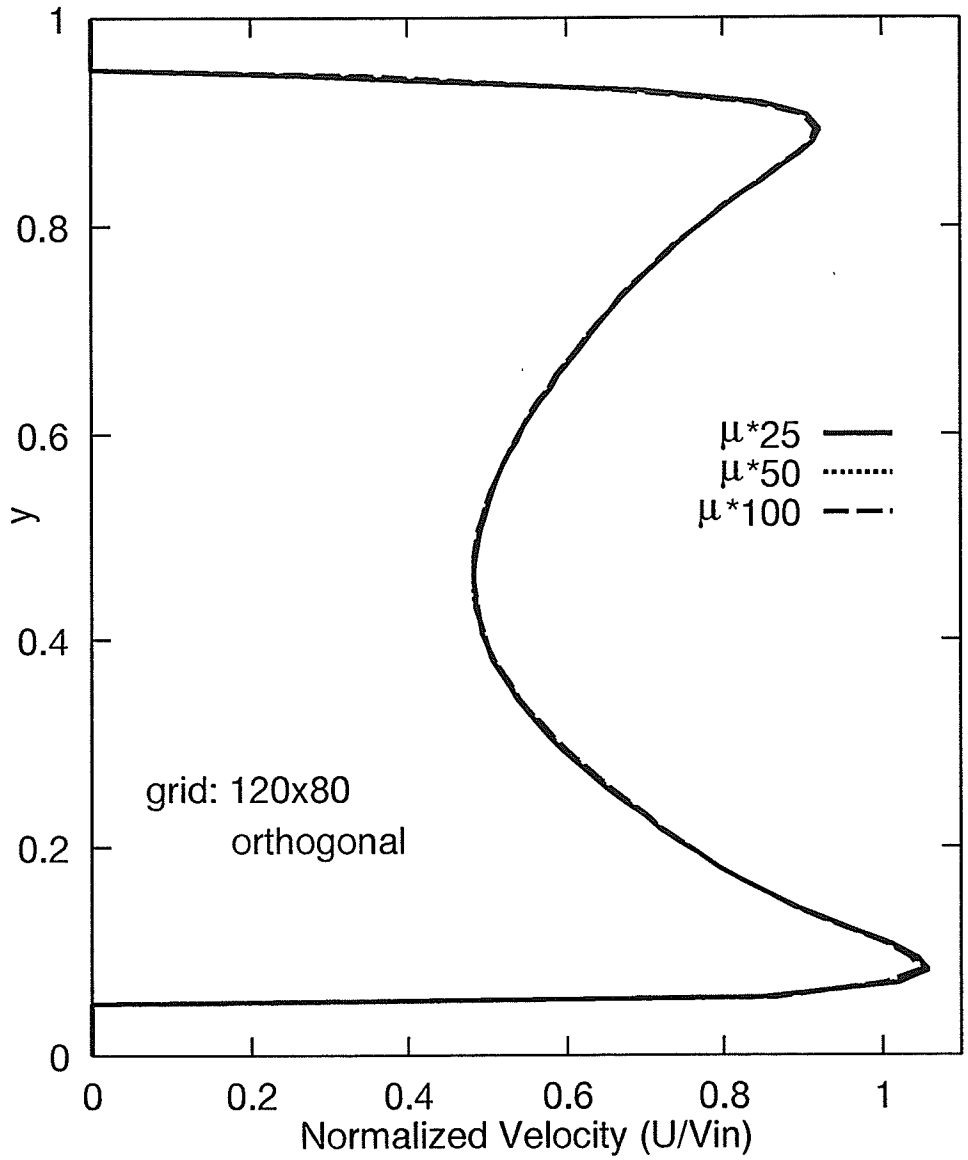

Figure 7.43: RSTB Test Problem U Velocity Profiles at "A": Orthogonal 120×80 Grid.

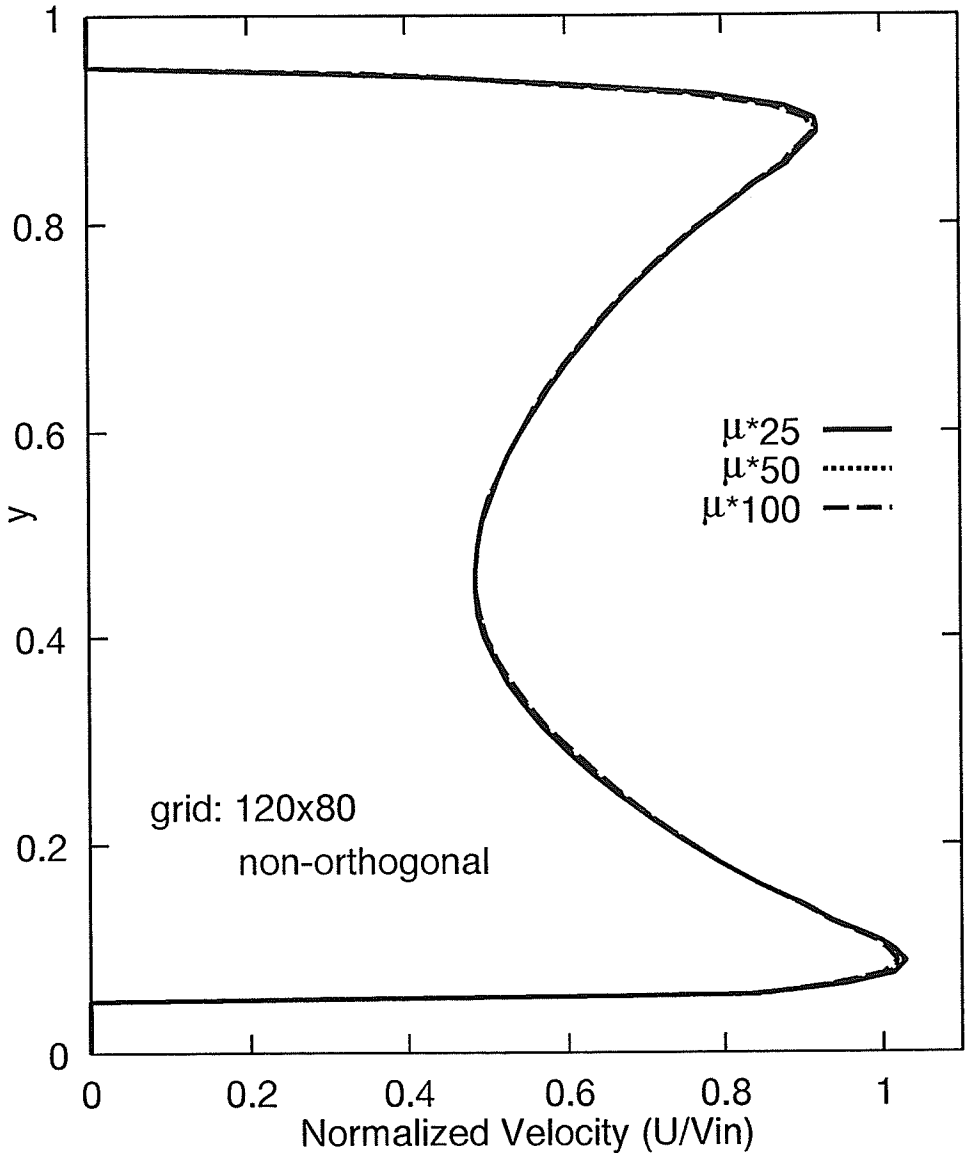

Figure 7.44: RSTB Test Problem U Velocity Profiles at "A": Non-Orthogonal 120×80 Grid.

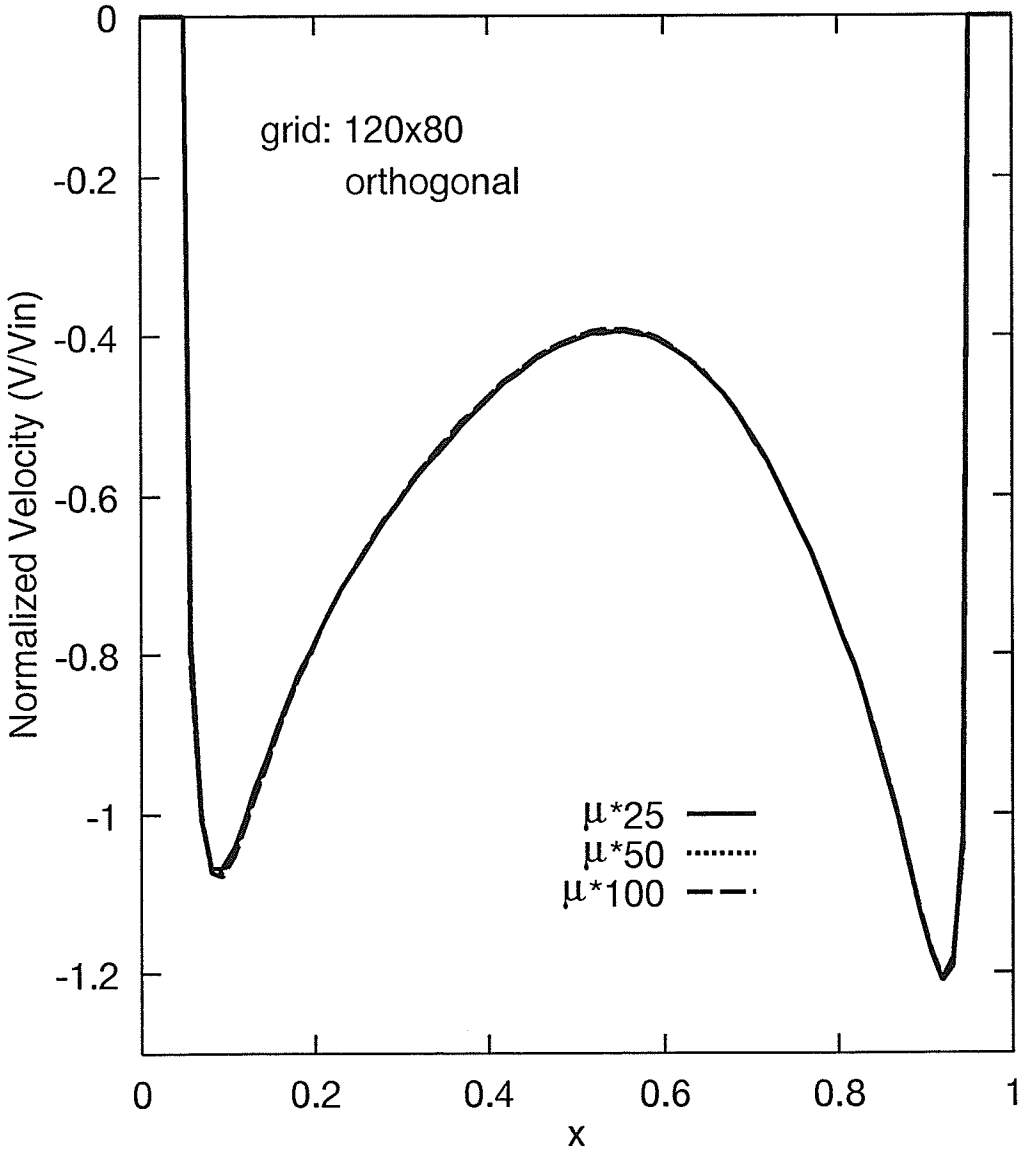

Figure 7.45: RSTB Test Problem V Velocity Profiles at "B": Orthogonal 120×80 Grid.

Grid	Lower Peak Velocity	%	Upper Peak Velocity	%
$\mu * 25$	1.029	-	0.920	-
$\mu * 50$	1.026	-0.3	0.918	-0.2
$\mu * 100$	1.019	-0.7	0.913	-0.5

Table 7.16: RSTB Test Problem Line "A" U Velocity Peaks: Non-Orthogonal 120×80 Grid.

The values of the peak velocity, for Figure 7.45, are given in Table 7.17. There is a slight increase in the left peak velocity with viscosity increase, but the amount is so small that the effect is not significant. As the viscosity increases, the flow is slightly greater near the wall which causes more flow to divert into the tube bundle around the left sealing strip when the effective viscosity is higher.

Grid	Left Peak Velocity	%	Right Peak Velocity	%
$\mu * 25$	-1.068	-	-1.211	-
$\mu * 50$	-1.073	+0.5	-1.209	-0.2
$\mu * 100$	-1.077	+0.4	-1.206	-0.2

Table 7.17: RSTB Test Problem Line "B" V Velocity Peaks: Orthogonal 120×80 Grid.

The V-velocity curve along line "B" for the 120×80 non-orthogonal grid is shown in Figure 7.46. There is only a slight difference in the peaks of three velocity profiles.

The values of the peak velocity, for Figure 7.46, are given in Table 7.18. As with the orthogonal grid velocities, the left peak velocity increases with higher effective viscosities.

Larger differences are expected in profile "C" than the "A" and "B" profiles because the previous plots of grid resolutions showed larger changes in the area along line "C". The U-velocity curve along line "C" for the 120×80 orthogonal grid is shown in Figure 7.47.

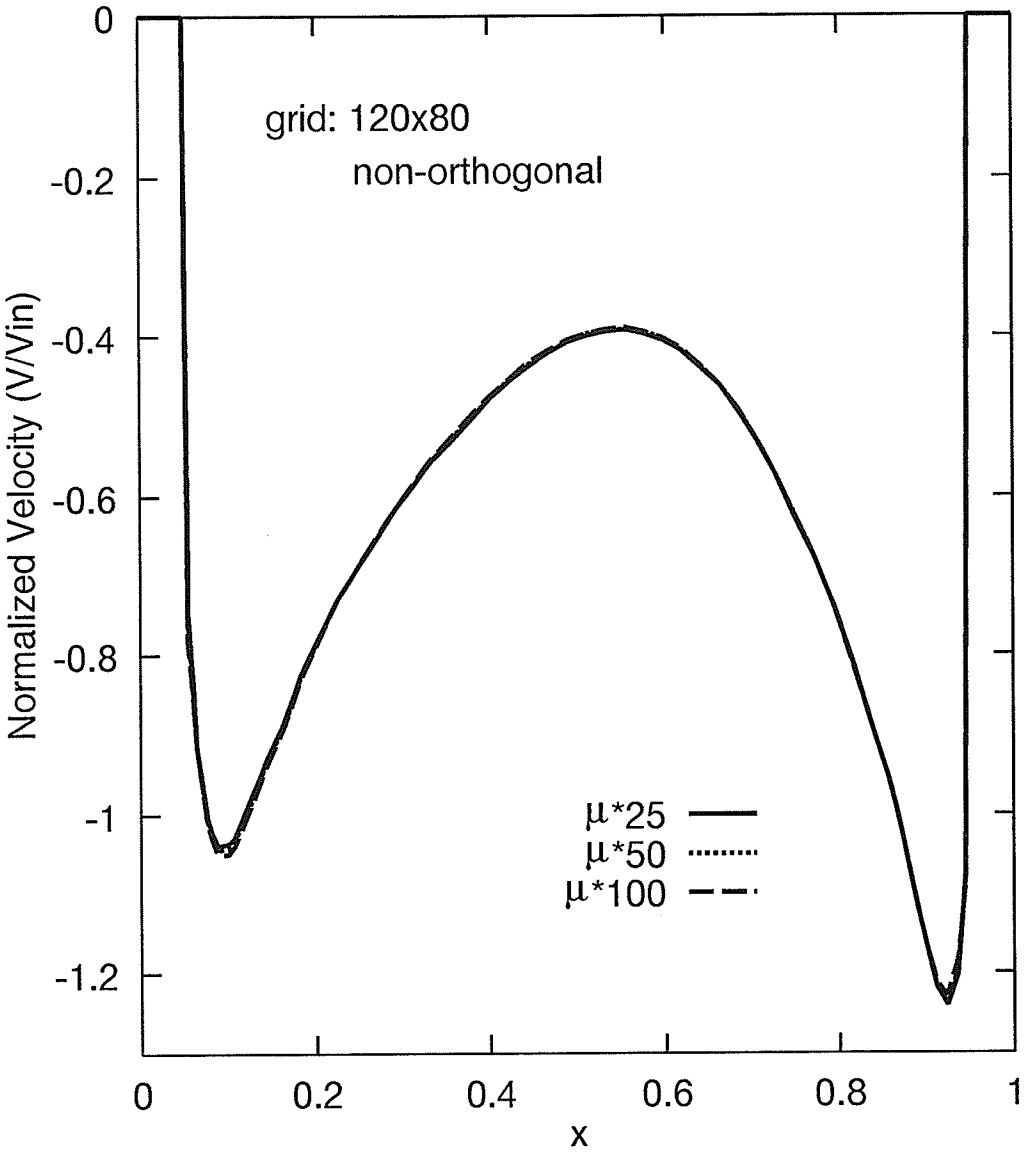

Figure 7.46: RSTB Test Problem V Velocity Profiles at "B": Non-Orthogonal 120×80 Grid, $\mu * 50$.

	Left Peak		Right Peak	
Grid	Velocity	%	Velocity	%
$\mu * 25$	-1.039	-	-1.242	-
$\mu * 50$	-1.043	+0.4	-1.238	-0.3
$\mu * 100$	-1.049	+0.6	-1.229	-0.7

Table 7.18: RSTB Test Problem Line "B" V Velocity Peaks: Non-Orthogonal 120×80 Grid.

The overall flow profile has small differences with two doublings of the effective viscosity. The recirculation zone width and the upper and lower peak velocity magnitudes are reduced with higher effective viscosities. There are also small differences visible on the graph near the bottom wall.

Near the bottom boundary, the wall function reduces the shear stress (relative to that for zero slip with the high effective viscosity) so that the velocity profile is similar to a turbulent profile. The wall function method, as used in the present work, only affects the velocity in the first control volume near the wall and is not sensitive to changes in effective viscosity. As a result, a large difference exists in the diffusion term between the first and second control volume This difference produces a discontinuity in the velocity profile. The greater the viscosity multiple, the sharper the discontinuity, and the flatter the peak near the bottom boundary. This result may be expected from such a simple turbulence model.

The values of the peak velocity, for Figure 7.47, are given in Table 7.19. The lower peak changes to a larger degree than the upper peak.

The U-velocity curve along line "C" for the 120×80 non-orthogonal grid is shown in Figure 7.48 The increase in the effective viscosity by factors of 2 has more effect on the non-orthogonal grid results than on the orthogonal grid results. The increase in viscosity multiple has a general smoothing effect which is most visible in the velocity peak near the bottom wall. Both the positive velocity peaks are reduced as the effective viscosity increases.

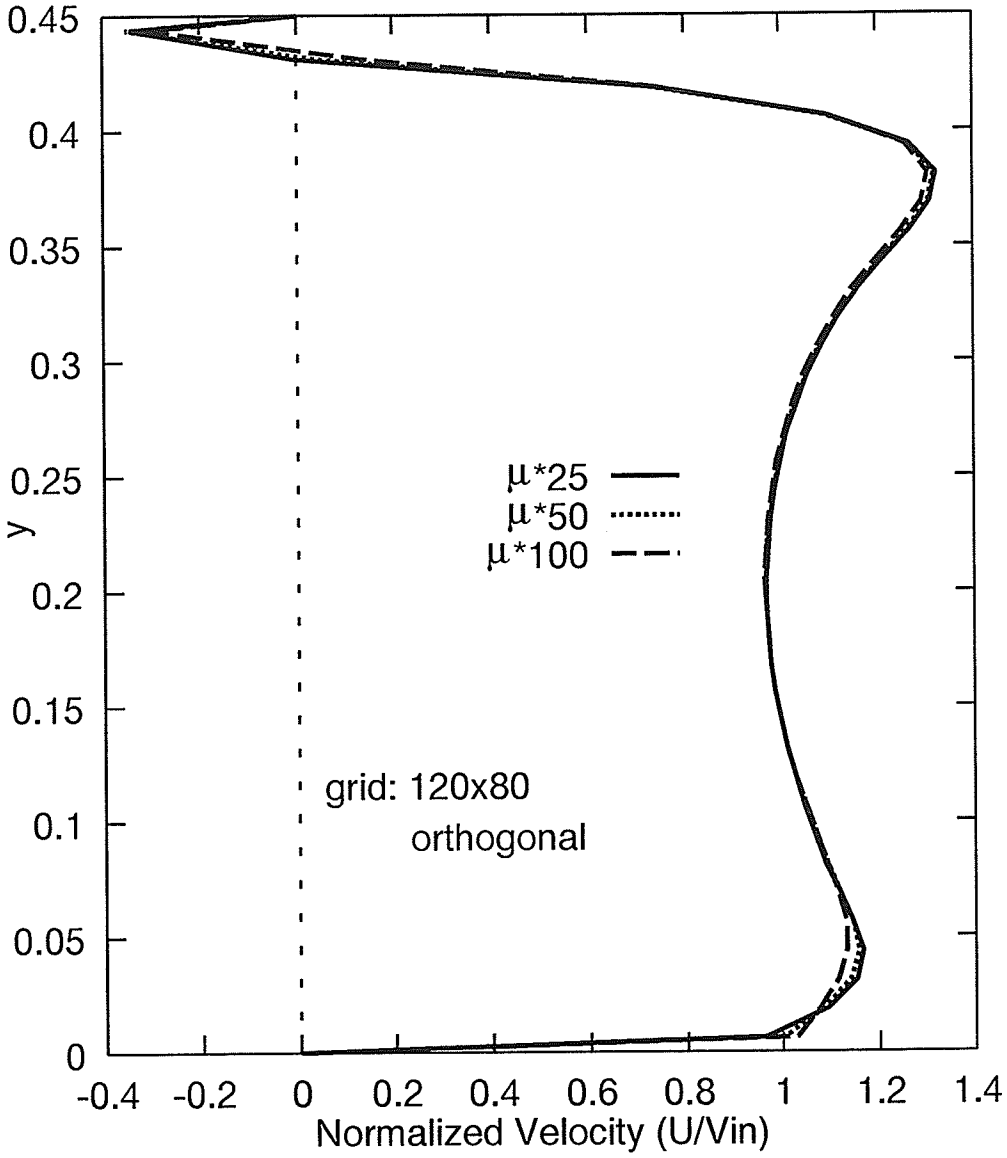

Figure 7.47: RSTB Test Problem U Velocity Profiles at "C": Orthogonal 120×80 Grid.

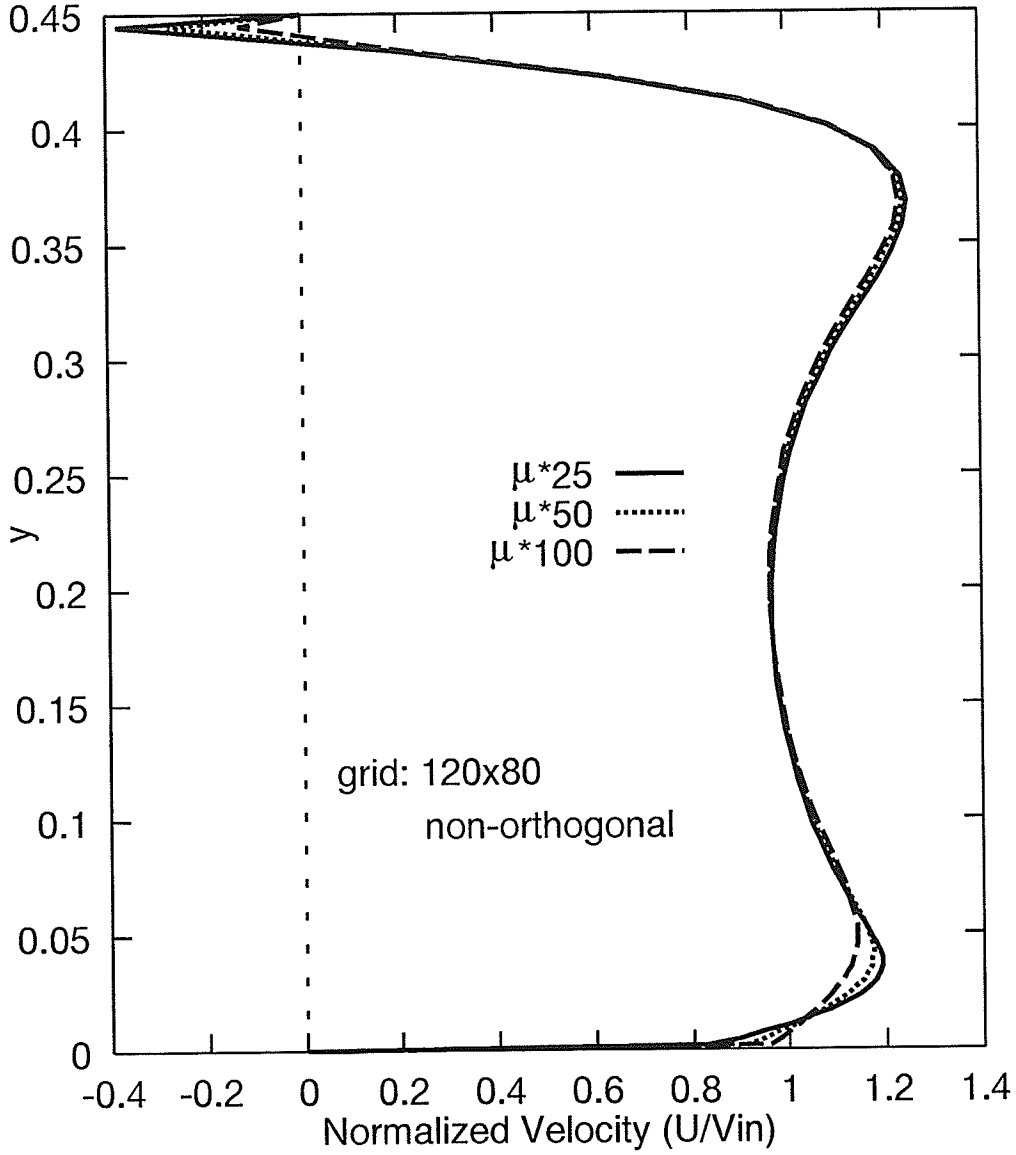

Figure 7.48: RSTB Test Problem U Velocity Profiles at "C": Non-Orthogonal 120×80 Grid.

Grid	Lower Peak Velocity	%	Upper Peak Velocity	%
$\mu * 25$	1.164	-	1.322	-
$\mu * 50$	1.156	-0.7	1.319	-0.2
$\mu * 100$	1.132	-2.1	1.308	-0.8

Table 7.19: RSTB Test Problem Line "C" U Velocity Peak: Orthogonal 120×80 Grid.

The non-orthogonal grid is much more refined than the orthogonal grid along the wall so the velocity profile is smoother. The discontinuity between the first and second node, caused by the use of wall functions, is not as evident.

The non-orthogonal grid is a bit more refined than the orthogonal grid around the bottom of the baffle as well. The sharp peak of negative velocities still exist in that region. Velocity peaks remain relatively the same shape but reduce in size dramatically. The dramatic decrease in size of the negative velocity peak indicates that the recirculation zone is getting smaller and weaker with higher effective viscosity.

The values of the positive peak velocity, for Figure 7.48, are given in Table 7.20. The change in the peak velocity values with increased viscosity multiple is slightly greater than with the orthogonal grid and the lower peak has a larger change than the upper peak.

Grid	Lower Peak Velocity	%	Upper Peak Velocity	%
$\mu * 25$	1.190	-	1.251	-
$\mu * 50$	1.171	-1.6	1.243	-0.6
$\mu * 100$	1.139	-2.7	1.235	-0.6

Table 7.20: RSTB Test Problem Line "C" U Velocity Peak: Non-Orthogonal 120×80 Grid.

It was concluded that changing the effective viscosity did not affect the flow in the tube bundle region greatly because the terms involving effective viscosity in the governing

equations were likely dominated by the tube drag terms. Also, in the free fluid regions only small changes with effective viscosity were noted because the turbulence model used was not sensitive to the details of the flow. The overall flow profile changed very little with doublings of the effective viscosity. The use of a fixed effective viscosity was considered adequate, however, and did not affect the trends produced by grid refinement and the comparison to the two types of grids. Other researchers have also used the fixed effective viscosity model and found similar results, see Section 1.2.1.

Chapter 8

Closure

8.1 Summary and Conclusions

A computer procedure has been developed to model the two-dimensional isothermal flow in a cross-section of a shell-and-tube heat exchanger with complex-shaped tube bundles, flow blockages, and a shell of any arbitrary shape. The tube bundle region is modeled using the porous media concept and isotropic drag correlations. The purpose of this work was to compare the results obtained using orthogonal and non-orthogonal grids with this simplified heat exchanger model.

The differential equations for momentum in the x and y directions, conservation of mass, and conservation of energy were discretized on a co-located non-orthogonal grid using a Finite Volume Method. The algebraic equations for U and V velocity, temperature, and pressure correction were solved with a nine-diagonal iterative solver. The pressure-velocity coupling was handled using the PWIM and SIMPLEC algorithms.

Blockages such as sealing strips and baffles were modeled as solids with zero slip velocity boundary conditions on their surfaces. The effective viscosity in the momentum equations was set to a fixed multiple of molecular viscosity as a simple model of turbulence. Wall

functions are used to provide the appropriate wall shear stress for a turbulent flow without the need for a dense packing of nodes along solid walls.

A grid generator was developed that creates two-dimensional grids that conform to the boundaries of complex shapes in a heat exchanger cross-section. A paneling method and transfinite interpolation were used to control the arrangement and the shape of control volumes and the exact location of internal and external boundaries.

A series of test problems were performed to validate the non-orthogonal method and the general numerical model. The test problems performed to validate the non-orthogonal approach were the tilted lid-driven cavity, and annulus natural convection. Each test confirmed that the present non-orthogonal grid results agreed well with published results. Further test problems were performed to compare the orthogonal and non-orthogonal approaches relative to each other and to known results. The square lid-driven cavity test and the flow between parallel plates showed that both approaches produced very similar results and at the same level of agreement with published and known results.

The tube bundle porosity approximation and the edge effects were introduced using a comparison of two orthogonal grids on a slug flow test. One had large control volumes and the other had fine control control volumes along the tube bundle boundary. This test demonstrated the pressure and velocity fluctuations as the fluid crossed the boundary between the tube-filled and tube-free regions.

The comparison of orthogonal and non-orthogonal approaches was advanced by including a slanted tube bundle region in a standard slug flow problem. The 45^o slant was used to cause the greatest amount of aliasing error on the orthogonal grid, while the non-orthogonal grid lines were skewed to match the 45^o slant. The slug flow solution is known but the slanted tube bundle diverts the flow to one side. The flow is still predominantly in one direction and a long tube-free region allowed the flow to return to the expected uniform profile. The results for the two approaches were compared at three different effective viscosities and at

three different grid resolutions. The purpose was to find which approach met the defined grid independence criterion with the coarsest grid and what, if any, effect the viscosity multiple had on the trend towards grid independence.

After the validation, the results of the two approaches, orthogonal and non-orthogonal grids, were compared on a simple slug flow that included a sample tube bundle tilted at 45^o to the main direction of flow. Finally, the two approaches were compared on a simplified heat exchanger which included the tube bundle tilted at 45^o, sealing strips, and a baffle. The results were compared in the form of streamlines, velocity profiles, and non-dimensional pressure drop in order to observe the trend toward grid independence as the grid resolution was increased.

The results of the slug flow test, showed that for a low viscosity multiple, $\mu * 25$ the orthogonal grid appears to give grid-independent results with a coarse grid, 70×10, while the non-orthogonal grid needs more refinement, up to at least 210×30, to produce the same results. At a higher viscosity multiple the orthogonal grid appeared to give independent results for a 140×20 grid while the non-orthogonal grid results are nearly grid independent for a 210×30 grid. The orthogonal grid approach seemed to perform more efficiently than the non-orthogonal grid in this test.

The final test problem was developed to explore the non-orthogonal method on a true two-dimensional flow in a simplified heat exchanger. To make the model somewhat realistic sealing strips and baffles were added, but the shell shape remained Cartesian for clear comparison with the orthogonal grid approach. The tube bundle was defined as a square rotated at 45^o. The general flow distributions were observed using streamlines and problem areas along the tube bundle boundary were indicated on plots of isobars. The results were then analyzed in terms of velocity profiles through the tube bundle and in the exit region. A comparison of the non-dimensional pressure drop was also used as an overall solution indicator. The trends observed are restricted to the Cartesian shell shape and the very simple

internal geometry because of the focus on the tube bundle aliasing effects.

The results for the rotated square tube bundle test showed that using the non-dimensional pressure drop to compare the results leads to the conclusion that the non-orthogonal grid can be considered grid independent for a 60×40 grid while the orthogonal grid needed a refinement to 120×80. The orthogonal grid results had a slightly smaller change in peak velocity as the grid was refined, however, because of more gradual pressure gradients at the tube bundle boundary. Both the orthogonal and non-orthogonal approaches reached the defined grid independence criterion for peak velocity at the same level of grid refinement with the orthogonal grid convergence behavior being more robust and predictable. The conclusion is that the non-orthogonal grid is more efficient in producing grid independent overall measurements, as indicated by the pressure drop test, but when flow details are required, using an orthogonal grid has a slight advantage.

The effects of the viscosity were isolated and the results showed that changing the effective viscosity does not affect the flow in the tube bundle region greatly. These small effects were attributed to the tube bundle drag dominating the flow in that region. Only small changes were noted in the free-fluid regions because the simple fixed effective viscosity is not sensitive to details of the flow and the wall functions are not sensitive to change in effective viscosity. In addition, the change in effective viscosity has only a small effect on grid independence results and does not alter previous conclusions.

8.2 Recommendations for Future Work

The tube bundle edge effects are a very complex area that warrants further study. The interaction of the PWIM and the pressure fluctuations at the interface between tube-free and tube-filled regions has a large effect on the stability of the solution method. More detailed examination of this phenomenon is needed. A modification of the PWIM to account

for pressure gradients that change rapidly over the space of one or two control volumes is required.

One way of analyzing the tube bundle edge effect is the modeling of flow around individual tubes. The present code has the capability of solving the small scale problem by defining a non-orthogonal grid around half of each tube in a row and using symmetry boundary conditions. A comparison could then be made between the large scale model (using a porous medium approximation to model the tube bundle) and this small scale model.

Further refinement of the grids in the simplified heat exchanger is needed to more clearly define an actual grid independent solution. Hortmann [13] used the Richardson extrapolation from a series of solutions that show a monotonic trend to get an estimate of values for the grid independent solution. Using this method along with the multi-grid solution techniques to establish a benchmark case would show the usefulness of the non-orthogonal grid approach to heat exchanger modeling.

The convergence difficulties that were encountered were overcome to some extent by using the nine-diagonal solver. Further work needs to be done to improve the diagonal dominance of the pressure-correction equation. An understanding of how some of the approximations applied in this work may contribute to convergence behavior problems is needed.

References

[1] Al-Sanea, S., Rhodes, N., Tatchell, D., and Wilkinson, T. A computer model for detailed calculation of the flow in power station condensers. In *Condensers: Theory and Practice* (London, 1983), D. Butterworth, Ed., Inst. Chem. Eng. Symp. Series No. 75, Inst. Chem. Eng., pp. 70–88.

[2] Brown, J., and Raithby, G. A numerical study of the turbulent flow through a tube bundle with a bypass lane and sealing strip. Master's thesis, Department of Mechanical Engineering, University of Waterloo, May 1984.

[3] Butterworth, D. The correlation of cross-flow pressure drop data by means of the permeability concept. Engineering sciences division, AERE harwell, United Kingdom Atomic Energy Authority Report AERE-R-9435, Oxfordshire, Apr. 1979.

[4] Caremoli, C. Numerical computation of steam flow in power plant condensers. In *Condensers: Theory and Practice* (London, 1983), D. Butterworth, Ed., Inst. Chem. Eng. Symp. Series No. 75, Inst. Chem. Eng., pp. 89–96.

[5] Carlucci, L., and Cheung, I. The effects of symmetric/asymmetric boundary conditions on the flow of an internally heated fluid. In *AIChE Symposium Series* (Chalk River, Ontario, July 1983), vol. 79 of *225*. Also Tech. rep., Atomic Energy of Canada Ltd. Repost AECL-8118.

[6] CARLUCCI, L., GALPIN, P., AND BROWN, J. Numerical predictions of shellside heat exchanger flows. In *A Reappraisal of Shellside Flow in Heat Exchangers* (Niagara Falls, NY., Aug. 1984), vol. 36 of *22nd Heat Transfer Conference and Exhibition*, ASME HTD, pp. 1–8.

[7] CARLUCCI, L., GALPIN, P., BROWN, J., AND FRISINA, V. Computation of two-dimensional isothermal flow in shell-and-tube heat exchangers. Tech. rep., Atomic Energy of Canada Ltd. Report AECL-8180, Chalk River, Ontario, July 1983.

[8] CARVER, M. Development and application of computer codes for multidimensional thermalhydraulic analyses of nuclear reactor components. In *Proceedings of the Canadian Nuclear Society/American Nuclear Society International Conference on Numerical Methods in Nuclear Engineering* (Montreal, Canada, Sept. 1983), C. Phillips, Ed., pp. 3–27.

[9] FRISINA, V., CARLUCCI, L., AND CAMPAGNA, A. SPOC - a computer program for simulation of power-plant condenser performance. In *Proceedings of the EPRI Condenser Technology Conference* (Boston, MA., Sept. 1990), vol. 2, pp. 93–106.

[10] FRISINA, V., CARLUCCI, L., CAMPAGNA, A., AND PETTIGREW, M. Heat exchanger analysis to resolve potential vibration problems. In *Maldistribution of Flow and Its Effect on Heat Exchanger Performance* (Pittsburgh, PA., Aug. 1987), vol. 75 of *24th National Heat Transfer Conference*, ASME HTD.

[11] GHIA, U., GHIA, K., AND SHIN, C. High-Re solutions for incompressible flow using the Navier-Stokes equations and a multigrid method. *Journal of Computational Physics 48* (1982), 387–411.

[12] GLAKPE, E., AND ASFAW, A. Prediction of two-dimensional natural convection in enclosures with inner bodies of arbitrary shapes. *Numerical Heat Transfer, Part A 20* (1991), 279–296.

[13] HORTMANN, M., PERIĆ, M., AND SCHEUERER, G. Finite volume multigrid prediction of laminar natural convection: Bench-mark solutions. *International Journal for Numerical Methods in Fluids 11* (1990), 189–207.

[14] INCROPERA, F., AND DEWITT, D. *Fundamentals of Heat and Mass Transfer*, 3rd ed. John Wiley and Sons, New York, 1990.

[15] JESSEE, J., AND FIVELAND, W. A cell-vertex algorithm for the incompressible navier-stokes equations on non-orthogonal grids. *Numerical Developments in CFD, ASME FED 215* (1995), 35–45.

[16] KAO, M., AND CHO, S. Three-dimensional numerical modelling of a recirculating PWR steam generator. In *A Reappraisal of Shellside Flow in Heat Exchangers* (Niagara Falls, NY., Aug. 1984), vol. 36 of *22nd Heat Transfer Conference and Exhibition*, ASME HTD, pp. 11–17.

[17] KARKI, K., AND PATANKAR, S. Calculation procedure for viscous incompressible flows in complex geometries. *Numerical Heat Transfer 14* (1988), 295–307.

[18] KNUPP, P., AND STEINBERG, S. *Fundamentals of Grid Generation.* CRC Press, Boca Raton, 1993.

[19] KOBAYASHI, M., AND PEREIRA, J. Calculation of incompressible laminar flows on a nonstaggered, nonorthogonal grid. *Numerical Heat Transfer, Part B 19* (1991), 243–262.

[20] LAUNDER, B., AND SPALDING, D. The numerical computation of turbulent flows. *Comp. Methods Appl. Mech. Eng. 3* (1974), 269–289.

[21] LONSDALE, R., AND TIERNEY, M. CFD predictions of the hydraulic performance of heat exchangers. Tech. Rep. HTFS RS 886, Harwell Laboratory, Didcot, Oxon, 0X11, ORA., 1992.

[22] MAJUMDAR, S. Role of underrelaxation in momentum interpolation for calculation of flow with nonstaggered grids. *Numerical Heat Transfer 13* (1988), 125–132.

[23] MILLER, T., AND SCHMIDT, F. Use of a pressure-weighted interpolation method for the solution of the incompressible Navier-Stokes equations on a nonstaggered grid system. *Numerical Heat Transfer 14* (1988), 213–233.

[24] ORMISTON, S., RAITHBY, G., AND CARLUCCI, L. Numerical modeling of power station steam condensers–part 1: Convergence behavior of a finite-volume model. *Numerical Heat Transfer, Part B 27* (1995), 81–102.

[25] ORMISTON, S., RAITHBY, G., AND CARLUCCI, L. Numerical modeling of power station steam condensers–part 2: Improvement of solution behavior. *Numerical Heat Transfer, Part B 27* (1995), 103–125.

[26] PATANKAR, S. *Numerical Heat Transfer and Fluid Flow.* Hemisphere, New York, 1980.

[27] PATANKAR, S., AND SPALDING, D. A calculation procedure for heat, mass and momentum transfer in three-dimensional parabolic flows. *International Journal of Heat Mass Transfer 15* (1972), 1787–1806.

[28] PATANKAR, S., AND SPALDING, D. A calculation procedure for the transient and steady-state behavior of shell-and-tube heat exchangers. In *Heat Exchangers: Design and Theory sourcebook*, N. Afgan and E. Schlünder, Eds. McGraw-Hill, New York, 1974, ch. 7, pp. 155–176.

[29] PEACEMAN, D., AND RACHFORD, H. The numerical solution of parabolic and elliptic differential equations. *J. Soc. Ind. Appl. Math. 3* (1955), 28–41.

[30] PERIĆ, M. *A Finite volume method for the Prediction of Three-Dimensional fluid flow in Complex Ducts.* PhD thesis, Imperial college of Science and Technology, University of London, 1985.

[31] PERIĆ, M. Efficient semi-implicit solving algorithm for nine-diagonal coefficient matrix. *Numerical Heat Transfer 11* (1987), 251–279.

[32] PERIĆ, M. Analysis of pressure-velocity coupling on nonorthogonal grids. *Numerical Heat Transfer, Part B 17* (1990), 63–82.

[33] PERIĆ, M., KESSLER, R., AND SCHEUERER, G. Comparison of finite-volume numerical methods with staggered and colocated grids. *Computers and Fluids 16*, 4 (1988), 389–403.

[34] RAITHBY, G. Personal communication. Department of Mechanical Engineering, University of Waterloo, 1991.

[35] RAITHBY, G., GALPIN, P. F., AND VAN DOORMAAL, J. Prediction of heat and fluid flow in complex geometries using general orthogonal coordinates. *Numerical Heat Transfer 9* (1986), 125–142.

[36] RAITHBY, G., AND SCHNEIDER, G. Numerical solution of problems in incompressible fluid flow: Treatment of the velocity-pressure coupling. *Numerical Heat Transfer 2*, 2 (1979), 417–440.

[37] RAITHBY, G., AND TORRANCE, K. Upstream-weighted differencing schemes and their application to elliptical problems involving fluid flow. *Conput. Fluids 2* (1974), 191–206.

[38] RHIE, C., AND CHOW, W. Numerical study of the turbulent flow past an airfoil with trailing edge separation. *AIAA Journal 21*, 11 (Nov. 1983), 1525–1532.

[39] RHODES, D., AND CARLUCCI, L. Predicted and measured velocity distributions. In *Proceedings of the Canadian Nuclear Society/American Nuclear Society International Conference on Numerical Methods in Nuclear Engineering* (Montreal, Canada, Sept. 1983), C. Phillips, Ed., pp. 934–948.

[40] SEOK, K. C., HO, Y. N., AND MANN, C. Use of the momentum interpolation method for numerical solution of incompressible flows in complex geometries: Choosing cell face velocities. *Numerical Heat Transfer, Part B 23* (1993), 21–41.

[41] STUBLEY, G. Personal communication. Department of Mechanical Engineering, University of Waterloo, 1991.

[42] THEODOSSIOU, V., SOUSA, A., AND CARLUCCI, L. Flow field predictions in a model heat exchanger. *Computational Mechanics 3* (1988), 419–428.

[43] VAN DOORMAAL, J., AND RAITHBY, C. Enhancements of the SIMPLE method for predicting incompressible fluid flows. *Numerical Heat Transfer 7* (1984), 147–163.

[44] VAN DOORMAAL, J., RAITHBY, C., AND STRONG, A. Prediction of natural convection in nonrectangular enclosures using orthogonal curvilinear coordinates. *Numerical Heat Transfer 4* (1981), 21–38.

[45] WHITE, F. M. *Viscous fluid Flow.* McGraw-Hill Book Company, New York, 1974.

[46] ZHANG, C. Numerical modeling using a quasi-three-dimensional procedure for large power plan condensers. *Journal of Heat Transfer 116* (Feb. 1994), 180–188.

[47] ZHANG, C., AND SOUSA, A. Comparison of different turbulence models for shell-side flow in a model heat exchanger. *International Journal of Heat and Technology 7* (1989), 99–110.

[48] ZHANG, C., AND SOUSA, A. A computational method for simulation of steam flow in condensers. In *Proc. First International conference on Advanced Computational Methods in Heat Transfer* (Portsmouth, UK., July 1990), Springer, Ed., vol. 3, Phase Change and Combustion Simulations.

[49] ZHANG, C., AND SOUSA, A. Numerical simulation of turbulent shear flow in an isothermal heat exchanger model. *Journal of Fluids Engineering 112* (1990), 48–55.

[50] ZHANG, C., SOUSA, A., AND VENART, J. Numerical simulation of different types of steam surface condensers. *Journal of Energy Resources Technology 113* (1991), 63–70.

Appendix A

Solution Procedure

The following is a detailed, step-by-step description of the procedure used in the computer code to perform the flow calculation.

STEP:1 Read in the input data, variables that control how the program behaves, fluid properties, and boundary conditions.

STEP:2 Read in the grid data (everything that defines the discretization of the domain).

STEP:3 Read in the material data, description of the tube bundle and blockage materials.

STEP:4 Read in the porosity data, description of the tube bundle configuration.

4–(i) Calculate porosity from tube pitch and diameter information.

4–(ii) Modify areas and volumes using porosity, which reduces the fluid volume in a control volume.

STEP:5 Read in the blockage data, location of blockages.

STEP:6 Initialize field variables, T, U, V, U_e, V_e, U_n, V_n, P.

STEP:7 Read the previous field variables if continuing from a previous simulation.

STEP:8 Echo all the input data.

STEP:9 Zero the face velocities on the surface and inside a blockage.

STEP:10 Calculate and store the unit vectors for the grid ($\hat{n}$, $\hat{s}$, and $\hat{t}$) using grid dimensions.

STEP:11 Set up the fictitious pressure coefficients for linear extrapolation on the boundary of the domain, using grid distances.

STEP:12 Set the pressure-correction convection coefficients (volume/distance). Zero the coefficients that cross a boundary.

STEP:13 Zero the convection coefficients around blockages in exactly the same way as on the domain boundary. Also zero the convection coefficient inside the blockage and raise a blockage flag.

STEP:14 Set the continuity coefficients (for example, $ACUE = (\rho * A_e) * \hat{n}_{xe}$). No need to modify the continuity coefficient in a blockage because face velocities are set to zero.

STEP:15 Calculate the mass flows at the faces of the control volumes. $ACUW$ and $ACVW$ are only used on the west boundary. $ACUS$ and $ACVS$ are only used on the south boundary.

STEP:16 For constant properties: (density, thermal conductivity, specific heat and viscosity) Calculate the mass in a control volume, the diffusive conductance coefficient and the effective viscosity.

STEP:17 Set the viscosity in a blockage (specified in the materials list for the blockage). This viscosity is specified to be large (roughly 1×10^{15} times the fluid viscosity) to ensure that the blockage face has a zero velocity.

STEP:18 Calculate the diffusion coefficients for U and V momentum using the harmonic mean. This will give the correct viscosity at a blockage. Just the same as at a boundary wall with a nonzero width.

STEP:19 Set up velocity monitoring location (pick nearest node or face velocity nearest the desired point).

STEP:20 **BEGIN MAIN LOOP**

Main:1 Set old variables from present values at previous step.

Main:2 Set domain corner U velocity based on the boundary conditions.
Using $(IB-1, JB-1)$ as an example:

- If both south and west boundaries are Dirichlet use the average.
- If one boundary condition is Dirichlet set the corner value equal to that boundary condition.
- If both are Neumann take the nearest nodal value, (In this case $\Phi(IB, JB)$).
- If boundary conditions do not match the above three cases, set $\Phi(IB-1, JB-1)$ = an average of the linear interpolation along the west side and a linear interpolation along the south side.

Main:3 Set northeast U velocities of each control volume. The boundaries use single linear interpolation between nodes because of the zero-width control volumes. Then interior control volumes use a simple average of the four nearest nodes.

Main:4 Set domain corner V velocity. Same as with U. This has the effect of using the velocity field of the previous step to set the corner values.

Main:5 Set northeast V velocities.

Main:6 Set all the northeast velocities to zero inside a blockage and on its perimeter.

Main:7 If using wall functions, calculate the wall shear stress using wall function method. This subroutine also zeroes the diffusion coefficient along walls and blockages.

Main:8 Set the face velocity boundary conditions using the nodal boundary conditions and store them in the fictitious continuity coefficients.

Main:9 Calculate the velocity profile weights, α and β. These are used in exponential upwind differencing and are found using a Peclet number.

Main:10 Set the U momentum source term from the wall function shear stress. The diffusion weighting should be equal to 1 because the diffusion coefficient was set to zero while calculating shear stress with wall functions.

Main:11 Set the U momentum tube drag source. Because of source term linearization, the drag goes completely into the present active nodal coefficient. A local Reynolds number is calculated based on tube diameter and a 'free stream' velocity for each control volume. Drag correlation, valid between $1 < RE_d < 1{\times}10^5$, sets the active portion of the source term.

Main:12 Set the boundary conditions for U momentum. Store in fictitious U momentum coefficients.

Main:13 Set the U momentum coefficients in either five- or nine-point form.

Main:14 Absorb the U velocity boundary conditions.

Main:15 Zero the U coefficients in the blockage and those referring to velocities in a blockage.

Main:16 Set the V momentum source term from the wall function shear stress.

Main:17 Set the V momentum tube drag source.

Main:18 Set the boundary conditions for V momentum.

Main:19 Set the V momentum coefficients in either five- or nine-point form.

Main:20 Absorb the V velocity boundary conditions.

Main:21 Zero the V coefficients in the blockage and those referring to velocities in a blockage.

Main:22 Set the pressure correction coefficients based on continuity and momentum coefficients.

Main:23 Zero the coefficients in the blockage and adjust blockage boundary coefficients.

Main:24 **Begin (P–$\vec{V}$) Loop**

- (P–$\vec{V}$):1 Set domain corner pressures. Take the average of two linear interpolations and the nearest nodal pressure.
- (P–$\vec{V}$):2 Set northeast pressures just like in the momentum equation.
- (P–$\vec{V}$):3 Calculate face pressures as linear interpolation of nodal pressures.
- (P–$\vec{V}$):4 Use linear extrapolation to set face pressures on a blockage.
- (P–$\vec{V}$):5 Set northeast pressures on a blockage by linear interpolation between face pressure on blockage face.
- (P–$\vec{V}$):6 Add pressure gradient force to U momentum source term.
- (P–$\vec{V}$):7 Add buoyancy force to U momentum source term.
- (P–$\vec{V}$):8 Add pressure gradient force to V momentum source term.
- (P–$\vec{V}$):9 Add buoyancy force to V momentum source term.
- (P–$\vec{V}$):10 Use either the LGS2D solver on the five-point, or PLR92D on the nine-point U momentum equation. This produces a guessed field of U velocities.
- (P–$\vec{V}$):11 Update fictitious control volumes to enforce the U velocity boundary conditions.
- (P–$\vec{V}$):12 Use either the LGS2D solver on the five-point, or PLR92D on the nine-point V momentum equation. This produces a guessed field of V velocities.
- (P–$\vec{V}$):13 Update fictitious control volumes to enforce the V velocity boundary conditions.

$\boxed{(P\text{–}\vec{V}):14}$ Use the PWIM algorithm to calculate the guessed face velocities.

$\boxed{(P\text{–}\vec{V}):15}$ Apply the face velocity boundary conditions.

$\boxed{(P\text{–}\vec{V}):16}$ Zero the face velocities in a blockage.

$\boxed{(P\text{–}\vec{V}):17}$ Calculate guessed mass flow rates from guessed velocities

$\boxed{(P\text{–}\vec{V}):18}$ Zero the pressure correction field.

$\boxed{(P\text{–}\vec{V}):19}$ Calculate the pressure correction source term from the guessed velocity-based mass flows.

$\boxed{(P\text{–}\vec{V}):20}$ Zero the pressure correction coefficients in a blockage and set the source term using the mass deficit.

$\boxed{(P\text{–}\vec{V}):21}$ If using the five-point solver with $\lambda = 1$ (improved five-point formulation) or the nine-point solver then (Pressure-Correction calculation):

- Pick a location to specify the pressure correction or allow it to float, depending on the type of problem.
- Use either the LGS2D solver on the five-point, or PLR92D on the nine-point pressure correction equation. This produces a field of pressure corrections.
- Update fictitious control volumes using the linear extrapolation set in the fictitious pressure-correction coefficients.

If $\lambda = 0$ (pressure correction source term update loop, standard five-point formulation) begin the inner $(P\text{–}\vec{V})$ loop.

- Lag corner pressure corrections in the source term.
- Pick a location to specify the pressure correction or allow it to float, depending on the type of problem.
- Zero pressure correction source term in a blockage.
- Use LGS2D one iteration

- Update fictitious control volumes using the linear extrapolation set in the fictitious pressure-correction coefficients.
- Repeat inner (P–$\vec{V}$) loop until a residual reduction criterion is met.

(P–$\vec{V}$):22 Calculate face pressure corrections using a linear interpolation of nodal pressure corrections.

(P–$\vec{V}$):23 Use linear extrapolation to set face pressure corrections on a blockage.

(P–$\vec{V}$):24 Write guessed fields out to an unformatted file for use in debugging.

(P–$\vec{V}$):25 Correct face velocities using nodal pressure corrections.

(P–$\vec{V}$):26 Correct nodal velocities using face pressure corrections.

(P–$\vec{V}$):27 Update fictitious control volumes to enforce U velocity boundary conditions.

(P–$\vec{V}$):28 Update fictitious control volumes to enforce V velocity boundary conditions.

(P–$\vec{V}$):29 Set domain corner U velocity.

(P–$\vec{V}$):30 Set domain corner V velocity.

(P–$\vec{V}$):31 Apply the face velocity boundary conditions

(P–$\vec{V}$):32 Correct the mass flow rate using corrected face velocities.

(P–$\vec{V}$):33 Calculate and check mass deficits.

(P–$\vec{V}$):34 Correct the pressure field with the nodal pressure corrections.

(P–$\vec{V}$):35 Shift the floating pressure level.

Main:25 **End of (P–$\vec{V}$) loop**

Main:26 Calculate the value of energy equation diffusion factor ($\Gamma = k/Cp$).

Main:27 Set the diffusion conductance ("D") coefficients for the temperature equation using the same method as for U and V momentum.

Main:28 Calculate profile weights α and β for upwinding of temperature.

Main:29 Zero the temperature source term.

Main:30 Set the domain corner temperatures using the boundary conditions and the same method as with velocities.

Main:31 Set the northeast temperatures the same way as velocities.

Main:32 Set both parts of the linearized temperature source term.

Main:33 Set the temperature boundary conditions and store them in the fictitious nodes.

Main:34 Set the algebraic temperature equation coefficients in either five- or nine-point form.

Main:35 Absorb the temperature boundary conditions.

Main:36 Use either the five-point (LGS2D) or nine-point (PLR92D) solver.

Main:37 Update fictitious control volumes to enforce temperature boundary conditions.

Main:38 Perform steady-state convergence checks.

38–(i) Evaluate convergence of U velocity.

38–(ii) Evaluate convergence of V velocity.

38–(iii) Evaluate convergence of Pressure.

38–(iv) Evaluate convergence of Temperature.

Main:39 Check convergence behavior by watching slope of a line fit through the thirty most recent check values and mass deficits at each step. No need to continue if they are all increasing (divergence is likely).

Main:40 Write fields out to an unformatted file for use in plotting and continuation.

Main:41 Check interactive file for what to do on a slope error or stop without meeting the convergence criteria.

Main:42 Check mass flux at boundaries and print them out.

Main:43 Write out monitored velocity and convergence data for this step to a separate file.

Main:44 In some problems, if the Reynolds number was specified, check and adjust the boundary conditions to get the correct value.

Main:45 Check the non-dimensional pressure drop from inlet to outlet.

STEP:21 **End of MAIN LOOP**

STEP:22 Start post processing.

22–(i) Calculate wall shear stress without wall functions.

22–(ii) Calculate shear stress on specified shear boundaries.

22–(iii) Calculate stream function

22–(iv) Calculate face pressures as linear interpolation of nodal pressures.

22–(v) Use linear extrapolation to set face pressures on a blockage.

22–(vi) Calculate domain corner temperatures from the boundary conditions.

22–(vii) Write fields out to an unformatted file for use in plotting and continuation.

22–(viii) Calculate non-dimensional temperature and distance to compare with benchmarks.

22–(ix) Check the non-dimensional pressure drop from inlet to outlet.

22–(x) Calculate Nusselt, Grashof, Rayleigh, and Prandtl numbers, and heat transfer.

STEP:23 **THE END**

Appendix B

Five-Point Algebraic Equations

B.1 General Discretized Equations

The generalized discretized equation that is presented here uses the U velocity as an example. The V velocity and temperature equations are analogous.

B.1.1 Standard Five-Point Equation

To solve Equation (4.30) using a five-point solver, it is necessary to collect terms into the five-point coefficients and produce a five-point algebraic equation. The equation becomes

$$A_P^u U_P = A_E^u U_E + A_W^u U_W + A_N^u U_N + A_S^u U_S + b^u = \sum A_{NB}^u U_{NB} + b^u \qquad \text{(B.1)}$$

which has the present nodal velocity on the left and the four neighboring nodal velocities on the right along with the source term. The coefficients of Equation (B.1) are

$$A_E^u = \frac{D_e \beta_e}{\hat{n}_e \cdot \hat{s}_e} - 0.5\, \dot{m}_e + |\alpha_e|\, |\dot{m}_e| \qquad \text{(B.2)}$$

$$A_W^u = \frac{D_w \beta_w}{\hat{n}_w \cdot \hat{s}_w} + 0.5\ \dot{m}_w + |\alpha_W|\,|\dot{m}_w| \tag{B.3}$$

$$A_N^u = \frac{D_n \beta_n}{\hat{n}_n \cdot \hat{t}_n} - 0.5\ \dot{m}_n + |\alpha_n|\,|\dot{m}_n| \tag{B.4}$$

$$A_S^u = \frac{D_s \beta_s}{\hat{n}_s \cdot \hat{t}_s} + 0.5\ \dot{m}_s + |\alpha_s|\,|\dot{m}_s| \tag{B.5}$$

and

$$\begin{aligned} b^u = {} & \frac{M_P^o}{\Delta t} U_P^o - \overline{\nabla_P} \left.\frac{\partial P}{\partial x}\right|_P + Q_P^u \\ & - D_e \beta_e \frac{(ds)_e}{(dt)_e} (U_{ne} - U_{se}) \frac{\hat{t}_e \cdot \hat{s}_e}{\hat{n}_e \cdot \hat{s}_e} + D_w \beta_w \frac{(ds)_w}{(dt)_w} (U_{nw} - U_{sw}) \frac{\hat{t}_w \cdot \hat{s}_w}{\hat{n}_w \cdot \hat{s}_w} \\ & - D_n \beta_n \frac{(dt)_n}{(ds)_n} (U_{ne} - U_{nw}) \frac{\hat{t}_n \cdot \hat{s}_n}{\hat{n}_n \cdot \hat{t}_n} + D_s \beta s \frac{(dt)_s}{(ds)_s} (U_{se} - U_{sw}) \frac{\hat{t}_s \cdot \hat{s}_s}{\hat{n}_s \cdot \hat{t}_s} \\ & = \frac{M_P^o}{\Delta t} U_P^o - \overline{\nabla_P} \left.\frac{\partial P}{\partial x}\right|_P + Q_P^u + \widetilde{b^u} \end{aligned} \tag{B.6}$$

The source term contains part of the transient term, pressure gradient term, Buoyancy term, linearized source term and cross-derivative terms. The pressure gradient in the x direction is approximated with a combination of pressure gradients in the $\hat{s}$ and $\hat{t}$ directions. The pressure gradient details are given in terms of the gradient of pressure corrections as discussed in Section 5.2.5. The velocities in the cross-derivatives are located at the corners of the control volume so they are approximated as the average of the four nearest nodal velocities from the previous time step. Therefore, all cross-derivatives contain lagged velocities.

Finally, the diagonal coefficient, A_P^u, is

$$\begin{aligned} A_P^u = {} & \frac{D_e \beta_e}{\hat{n}_e \cdot \hat{s}_e} + 0.5\ \dot{m}_e + |\alpha_e|\,|\dot{m}_e| + \frac{D_w \beta_w}{\hat{n}_w \cdot \hat{s}_w} - 0.5\ \dot{m}_w + |\alpha_W|\,|\dot{m}_w| \\ & + \frac{D_n \beta_n}{\hat{n}_n \cdot \hat{t}_n} + 0.5\ \dot{m}_n + |\alpha_n|\,|\dot{m}_n| + \frac{D_s \beta_s}{\hat{n}_s \cdot \hat{t}_s} - 0.5\ \dot{m}_s + |\alpha_s|\,|\dot{m}_s| + \frac{M_P}{\Delta t} - R_P^u \end{aligned} \tag{B.7}$$

Equation (4.44) can also be written as the sum of neighboring coefficients, mass flows and linearized source term as

$$A_P^u = \underbrace{A_E^u + A_W^u + A_N^u + A_S^u}_{A_P^{u^*}} + \underbrace{\dot{m}_e - \dot{m}_w + \dot{m}_n - \dot{m}_s + \frac{M_P}{\Delta t}}_{+\frac{M_P^o}{\Delta t}} - R_P^u \tag{B.8}$$

Defining $A_P^{u^*}$, from Equations (B.2) through (B.5) as:

$$A_P^{u^*} = \frac{D_e\beta_e}{\hat{n}_e \cdot \hat{s}_e} - 0.5\,\dot{m}_e + |\alpha_e|\,|\dot{m}_e| \quad + \frac{D_w\beta_w}{\hat{n}_w \cdot \hat{s}_w} + 0.5\,\dot{m}_w + |\alpha_W|\,|\dot{m}_w|$$
$$+ \frac{D_n\beta_n}{\hat{n}_n \cdot \hat{t}_n} - 0.5\,\dot{m}_n + |\alpha_n|\,|\dot{m}_n| \quad + \frac{D_s\beta_s}{\hat{n}_s \cdot \hat{t}_s} + 0.5\,\dot{m}_s + |\alpha_s|\,|\dot{m}_s| \tag{B.9}$$

and using continuity, Equation (4.9), to reduce Equation (B.8) to simpler form produces:

$$A_P^u = A_P^{u^*} - R_P^u + \frac{M_P^o}{\Delta t} \tag{B.10}$$

For the standard five-point formulation $A_P^{u^*}$ is synonymous with the sum of the four neighboring coefficients, $\sum_{e,w,s,n} A_{NB}^u$.

The discretized momentum equation has been separated into a standard five-point algebraic equation. This formulation works well for orthogonal (or nearly orthogonal) grids but when the grid is skewed the cross-derivative terms become more important and having those terms lagged causes convergence difficulties. Convergence improves if all cross-derivative terms are connected to the five "active" nodes. That is the basis for the improved five-point equation.

B.1.2 Improved Five-Point Equation

To improve the five-point solution technique there must be some approximation for U_{ne}, and other corner velocities, in the active coefficients (instead of lagging them completely). The simplest approximation is to have the corner velocity equal to the average of the surrounding

four nodal velocities. The northeast corner velocity, U_{ne}, for example, is approximated as suggested by Perić [32] as follows:

$$\widetilde{U_{ne}} = \frac{1}{4}\left(U_N + U_{NE} + U_P + U_E\right) \tag{B.11}$$

A new parameter, λ, is introduced to permit control of the use of the new approximation

$$U_{ne} = \lambda^u\, \widetilde{U_{ne}} + \left(1 - \lambda^u\right)\, U^o_{ne} \tag{B.12}$$

Substituting Equation (4.33) into Equation (B.12) produces:

$$U_{ne} = \frac{\lambda^u}{4}\left(U_N + U_{NE} + U_P + U_E\right) + \left(1 - \lambda^u\right) U^o_{ne} \tag{B.13}$$

Substituting Equation (B.13) (and its equivalents for all the other corner velocities) into Equation (B.6) produces a new expression for the source term:

$$\begin{aligned}
b^u = {} & \left(\frac{M^o_P}{\Delta t}\right) U^o_P - \overline{\nabla_P}\left.\frac{\partial P}{\partial x}\right|_P + Q^u_P \\
& - D_e\beta_e \frac{(ds)_e}{(dt)_e}\frac{\hat{t}_e\cdot\hat{s}_e}{\hat{n}_e\cdot\hat{s}_e}\left[\frac{\lambda^u}{4}\left(U_N + U_{NE} + U_P + U_E\right) + \left(1-\lambda^u\right)U^o_{ne}\right. \\
& \qquad \left. -\frac{\lambda^u}{4}\left(U_S + U_{SE} + U_P + U_E\right) + \left(1-\lambda^u\right)U^o_{se}\right] \\
& + D_w\beta_w \frac{(ds)_w}{(dt)_w}\frac{\hat{t}_w\cdot\hat{s}_w}{\hat{n}_w\cdot\hat{s}_w}\left[\frac{\lambda^u}{4}\left(U_N + U_{NW} + U_P + U_W\right) + \left(1-\lambda^u\right)U^o_{nw}\right. \\
& \qquad \left. -\frac{\lambda^u}{4}\left(U_S + U_{SW} + U_P + U_W\right) + \left(1-\lambda^u\right)U^o_{sw}\right] \\
& - D_n\beta_n \frac{(dt)_n}{(ds)_n}\frac{\hat{t}_n\cdot\hat{s}_n}{\hat{n}_n\cdot\hat{t}_n}\left[\frac{\lambda^u}{4}\left(U_N + U_{NE} + U_P + U_E\right) + \left(1-\lambda^u\right)U^o_{ne}\right. \\
& \qquad \left. -\frac{\lambda^u}{4}\left(U_N + U_{NW} + U_P + U_W\right) + \left(1-\lambda^u\right)U^o_{nw}\right] \\
& + D_s\beta_s \frac{(dt)_s}{(ds)_s}\frac{\hat{t}_s\cdot\hat{s}_s}{\hat{n}_s\cdot\hat{t}_s}\left[\frac{\lambda^u}{4}\left(U_S + U_{SE} + U_P + U_E\right) + \left(1-\lambda^u\right)U^o_{se}\right. \\
& \qquad \left. -\frac{\lambda^u}{4}\left(U_S + U_{SW} + U_P + U_W\right) + \left(1-\lambda^u\right)U^o_{sw}\right]
\end{aligned} \tag{B.14}$$

Using a $\lambda = 0$ is the same as lagging all corner velocities completely, the previous five-point set of coefficients. Using a $\lambda = 1$ includes some of the influences of the corner velocities in the active five-point coefficients. The case of $\lambda > 1$ would emphasize the cross derivative and the approximated corner velocity. With the five-point solver, the nodal corner velocities used in this source term are all from the previous time step.

Cancelling and collecting terms produces the following modification to the previous five-point algebraic equation:

$$
\begin{aligned}
b^u = \left(\frac{M_P^o}{\Delta t}\right) U_P^o - \overline{\forall_P} \left.\frac{\partial P}{\partial x}\right|_P + Q_P^u \\
- D_e\beta_e \frac{(ds)_e}{(dt)_e} \frac{\hat{t}_e \cdot \hat{s}_e}{\hat{n}_e \cdot \hat{s}_e} \left[\frac{\lambda^u}{4}\left(U_{NE} - U_{SE}\right) + \left(1-\lambda^u\right)\left(U_{ne}^o - U_{se}^o\right)\right] \\
+ D_w\beta_w \frac{(ds)_w}{(dt)_w} \frac{\hat{t}_w \cdot \hat{s}_w}{\hat{n}_w \cdot \hat{s}_w} \left[\frac{\lambda^u}{4}\left(U_{NW} - U_{SW}\right) + \left(1-\lambda^u\right)\left(U_{nw}^o - U_{sw}^o\right)\right] \\
- D_n\beta_n \frac{(dt)_n}{(ds)_n} \frac{\hat{t}_n \cdot \hat{s}_n}{\hat{n}_n \cdot \hat{t}_n} \left[\frac{\lambda^u}{4}\left(U_{NE} - U_{NW}\right) + \left(1-\lambda^u\right)\left(U_{ne}^o - U_{nw}^o\right)\right] \\
+ D_s\beta_s \frac{(dt)_s}{(ds)_s} \frac{\hat{t}_s \cdot \hat{s}_s}{\hat{n}_s \cdot \hat{t}_s} \left[\frac{\lambda^u}{4}\left(U_{SE} - U_{SW}\right) + \left(1-\lambda^u\right)\left(U_{se}^o - U_{sw}^o\right)\right]
\end{aligned}
\tag{B.15}
$$

The east neighbor coefficient, from Equation (B.2), gains two cross derivative terms as follows:

$$
A_E^u = \frac{D_e\beta_e}{\hat{n}_e \cdot \hat{s}_e} - 0.5\,\dot{m}_e + |\alpha_e|\,|\dot{m}_e| - \frac{\lambda^u}{4} D_n\beta_n \frac{(dt)_n}{(ds)_n} \frac{\hat{t}_n \cdot \hat{s}_n}{\hat{n}_n \cdot \hat{t}_n} + \frac{\lambda^u}{4} D_s\beta_s \frac{(dt)_s}{(ds)_s} \frac{\hat{t}_s \cdot \hat{s}_s}{\hat{n}_s \cdot \hat{t}_s}
\tag{B.16}
$$

The west neighbor coefficient, from Equation (B.3), gains two cross derivative terms as follows:

$$
A_W^u = \frac{D_w\beta_w}{\hat{n}_w \cdot \hat{s}_w} + 0.5\,\dot{m}_w + |\alpha_W|\,|\dot{m}_w| + \frac{\lambda^u}{4} D_n\beta_n \frac{(dt)_n}{(ds)_n} \frac{\hat{t}_n \cdot \hat{s}_n}{\hat{n}_n \cdot \hat{t}_n} - \frac{\lambda^u}{4} D_s\beta_s \frac{(dt)_s}{(ds)_s} \frac{\hat{t}_s \cdot \hat{s}_s}{\hat{n}_s \cdot \hat{t}_s}
\tag{B.17}
$$

The north neighbor coefficient, from Equation (B.4), gains two cross derivative terms as follows:

$$A_N^u = \frac{D_n\beta_n}{\hat{n}_n \cdot \hat{t}_n} - 0.5\ \dot{m}_n + |\alpha_n|\,|\dot{m}_n| - \frac{\lambda^u}{4} D_e\beta_e \frac{(ds)_e}{(dt)_e} \frac{\hat{t}_e \cdot \hat{s}_e}{\hat{n}_e \cdot \hat{s}_e} + \frac{\lambda^u}{4} D_w\beta_w \frac{(ds)_w}{(dt)_w} \frac{\hat{t}_w \cdot \hat{s}_w}{\hat{n}_w \cdot \hat{s}_w} \tag{B.18}$$

The south neighbor coefficient, from Equation (B.5), gains two cross derivative terms as follows:

$$A_S^u = \frac{D_s\beta_s}{\hat{n}_s \cdot \hat{t}_s} + 0.5\ \dot{m}_s + |\alpha_s|\,|\dot{m}_s| + \frac{\lambda^u}{4} D_e\beta_e \frac{(ds)_e}{(dt)_e} \frac{\hat{t}_e \cdot \hat{s}_e}{\hat{n}_e \cdot \hat{s}_e} - \frac{\lambda^u}{4} D_w\beta_w \frac{(ds)_w}{(dt)_w} \frac{\hat{t}_w \cdot \hat{s}_w}{\hat{n}_w \cdot \hat{s}_w} \tag{B.19}$$

The center nodal coefficient, A_P^u, does not change from Equation (4.46) where $A_P^{u^*}$ is no longer equal to the sum of neighbors because of the additional terms in the the neighboring coefficients.

This new formulation may be used with a five-point solver to improve convergence. If, however, the grid is highly skewed and flow conditions are such that convergence difficulties still remain, a nine-point formulation (and nine-diagonal solver) is required.

B.2 Five-Point P′ Equation

B.2.1 Standard Five-Point Formulation

To solve Equation (5.50) using a five-point solver, the northeast, northwest, southeast and southwest P' approximations would be put in the source term. The five-point algebraic equation is:

$$A_P^{p'} P'_P = A_E^{p'} P'_E + A_W^{p'} P'_W + A_N^{p'} P'_N + A_S^{p'} P'_S + b^{p'} = \sum A_{NB}^{p'} P'_{NB} + b^{p'} \tag{B.20}$$

where the four neighboring coefficients are the same as defined in Equations (5.52) through (5.55). The simplest five-point source term, with the four diagonal coefficients lumped in, would be as follows:

$$\begin{aligned} b^{p'} = &-\dot{m}_e + \dot{m}_w - \dot{m}_n + \dot{m}_s + b_P^c \\ &+ \frac{1}{4}\left(-A_{u_e}^c C_{Ve} Uh + A_{v_e}^c C_{Ve} Vh + A_{u_n}^c C_{Un} Uh - A_{v_n}^c C_{Un} Vh\right) P'^o_{NE} \\ &+ \frac{1}{4}\left(-A_{u_w}^c C_{Vw} Uh + A_{v_w}^c C_{Vw} Vh - A_{u_n}^c C_{Un} Uh + A_{v_n}^c C_{Un} Vh\right) P'^o_{NW} \\ &+ \frac{1}{4}\left(A_{u_e}^c C_{Ve} Uh - A_{v_e}^c C_{Ve} Vh + A_{u_s}^c C_{Us} Uh - A_{v_s}^c C_{Us} Vh\right) P'^o_{SE} \\ &+ \frac{1}{4}\left(A_{u_w}^c C_{Vw} Uh - A_{v_w}^c C_{Vw} Vh - A_{u_s}^c C_{Us} Uh + A_{v_s}^c C_{Us} Vh\right) P'^o_{SW} \end{aligned} \quad \text{(B.21)}$$

This source term has to be updated after each solver iteration as the P'_{NE}, P'_{NW}, P'_{SE}, and P'_{SW} has to come from the from the previous P' equation iteration not the previous time step.

B.2.2 Improved Five-Point Formulation

Just as with velocity there can be some improvements to the five-point solution method to avoid needing a nine-point solver. In order to assimilate the diagonal terms, Perić used the following definition of a parameter, α, which gives the diagonal node in terms of regular five-point nodes:

$$P'_{NW} = \alpha\left(P'_N + P'_W - P'_P\right) \quad \text{(B.22)}$$

This can be used, only for P', for all four diagonal nodes. Using Equation (B.22) and the same means of controlling this feature λ (as in Equation (B.12)) Equation (5.50) becomes:

$$\Delta m = -\left[G_e^c + G_w^c + G_n^c + G_s^c\right] \quad \text{(B.23)}$$

where

$$
\begin{aligned}
G_e^c = A_{u_e}^c \Big\{ & C_{Ue} U h \ (P'_E - P'_P) \\
& - C_{Ve} U h \ \frac{1}{4} \Big(\Big(P'_N + \lambda^{P'} \alpha \left(P'_N + P'_E - P'_P \right) + \left(1 - \lambda^{P'} \right) P'^{o}_{NE} \Big) \\
& - \Big(P'_S + \lambda^{P'} \alpha \left(P'_S + P'_E - P'_P \right) + \left(1 - \lambda^{P'} \right) P'^{o}_{SE} \Big) \Big) \Big\} \\
& + A_{v_e}^c \Big\{ C_{Ve} V h \ \frac{1}{4} \Big(\Big(P'_N + \lambda^{P'} \alpha \left(P'_N + P'_E - P'_P \right) + \left(1 - \lambda^{P'} \right) P'^{o}_{NE} \Big) \\
& - \Big(P'_S + \lambda^{P'} \alpha \left(P'_S + P'_E - P'_P \right) + \left(1 - \lambda^{P'} \right) P'^{o}_{SE} \Big) \Big) - C_{Ue} V h \ (P'_E - P'_P) \Big\}
\end{aligned} \tag{B.24}
$$

$$
\begin{aligned}
G_w^c = A_{u_w}^c \Big\{ & C_{Uw} U h \ (P'_P - P'_W) \\
& - C_{Vw} U h \ \frac{1}{4} \Big(\Big(P'_N + \lambda^{P'} \alpha \left(P'_N + P'_W - P'_P \right) + \left(1 - \lambda^{P'} \right) P'^{o}_{NW} \Big) \\
& - \Big(P'_S + \lambda^{P'} \alpha \left(P'_S + P'_W - P'_P \right) + \left(1 - \lambda^{P'} \right) P'^{o}_{SW} \Big) \Big) \Big\} \\
& + A_{v_w}^c \Big\{ C_{Vw} V h \ \frac{1}{4} \Big(\Big(P'_N + \lambda^{P'} \alpha \left(P'_N + P'_W - P'_P \right) + \left(1 - \lambda^{P'} \right) P'^{o}_{NW} \Big) \\
& - \Big(P'_S + \lambda^{P'} \alpha \left(P'_S + P'_W - P'_P \right) + \left(1 - \lambda^{P'} \right) P'^{o}_{SW} \Big) \Big) - C_{Uw} V h \ (P'_P - P'_W) \Big\}
\end{aligned} \tag{B.25}
$$

$$
\begin{aligned}
G_n^c = A_{u_n}^c \Big\{ & C_{Un} U h \ \frac{1}{4} \Big(\Big(P'_E + \lambda^{P'} \alpha \left(P'_N + P'_E - P'_P \right) + \left(1 - \lambda^{P'} \right) P'^{o}_{NE} \Big) \\
& - \Big(P'_W + \lambda^{P'} \alpha \left(P'_N + P'_W - P'_P \right) + \left(1 - \lambda^{P'} \right) P'^{o}_{NW} \Big) \Big) - C_{Vn} U h \ (P'_N - P'_P) \Big\} \\
& + A_{v_n}^c \Big\{ C_{Vn} V h \ (P'_N - P'_P) \\
& - C_{Un} V h \ \frac{1}{4} \Big(\Big(P'_E + \lambda^{P'} \alpha \left(P'_N + P'_E - P'_P \right) + \left(1 - \lambda^{P'} \right) P'^{o}_{NE} \Big) \\
& - \Big(P'_W + \lambda^{P'} \alpha \left(P'_N + P'_W - P'_P \right) + \left(1 - \lambda^{P'} \right) P'^{o}_{NW} \Big) \Big) \Big\}
\end{aligned} \tag{B.26}
$$

$$
\begin{aligned}
G_s^c = A_{u_s}^c \Big\{ & C_{Us} U h \ \frac{1}{4} \Big(\Big(P'_E + \lambda^{P'} \alpha \left(P'_S + P'_E - P'_P \right) + \left(1 - \lambda^{P'} \right) P'^{o}_{SE} \Big) \\
& - \Big(P'_W + \lambda^{P'} \alpha \left(P'_S + P'_W - P'_P \right) + \left(1 - \lambda^{P'} \right) P'^{o}_{SW} \Big) \Big) - C_{Vs} U h \ (P'_P - P'_S) \Big\} \\
& + A_{v_s}^c \Big\{ C_{Vs} V h \ (P'_P - P'_S) - C_{Us} V h \ \frac{1}{4} \Big(\Big(P'_E + \lambda^{P'} \alpha \left(P'_S + P'_E - P'_P \right) + \left(1 - \lambda^{P'} \right) P'^{o}_{SE} \Big) \\
& - \Big(P'_W + \lambda^{P'} \alpha \left(P'_S + P'_W - P'_P \right) + \left(1 - \lambda^{P'} \right) P'^{o}_{SW} \Big) \Big) \Big\}
\end{aligned} \tag{B.27}
$$

Cancelling and collecting terms produces:

$$\begin{aligned}
\Delta m = -\Bigg[& A^c_{u_e}\Bigg\{C_{Ue}Uh\ (P'_E - P'_P) \\
& -C_{Ve}Uh\ \left[\left(\frac{1+\lambda^{P'}\alpha}{4}\right)(P'_N - P'_S) + \left(\frac{1-\lambda^{P'}}{4}\right)\left(P'^o_{NE} - P'^o_{SE}\right)\right]\Bigg\} \\
& + A^c_{v_e}\Bigg\{C_{Ve}Vh\ \left[\left(\frac{1+\lambda^{P'}\alpha}{4}\right)(P'_N - P'_S) + \left(\frac{1-\lambda^{P'}}{4}\right)\left(P'^o_{NE} - P'^o_{SE}\right)\right] \\
& - C_{Ue}Vh\ (P'_E - P'_P)\Bigg\} + A^c_{u_w}\Bigg\{C_{Uw}Uh\ (P'_P - P'_W) \\
& -C_{Vw}Uh\ \left[\left(\frac{1+\lambda^{P'}\alpha}{4}\right)(P'_N - P'_S) + \left(\frac{1-\lambda^{P'}}{4}\right)\left(P'^o_{NW} - P'^o_{SW}\right)\right]\Bigg\} \\
& + A^c_{v_w}\Bigg\{C_{Vw}Vh\ \left[\left(\frac{1+\lambda^{P'}\alpha}{4}\right)(P'_N - P'_S) + \left(\frac{1-\lambda^{P'}}{4}\right)\left(P'^o_{NW} - P'^o_{SW}\right)\right] \\
& - C_{Uw}Vh\ (P'_P - P'_W)\Bigg\} \\
& + A^c_{u_n}\Bigg\{C_{Un}Uh\ \left[\left(\frac{1+\lambda^{P'}\alpha}{4}\right)(P'_E - P'_W) + \left(\frac{1-\lambda^{P'}}{4}\right)\left(P'^o_{NE} - P'^o_{NW}\right)\right] \\
& - C_{Vn}Uh\ (P'_N - P'_P)\Bigg\} + A^c_{v_n}\Bigg\{C_{Vn}Vh\ (P'_N - P'_P) \\
& -C_{Un}Vh\ \left[\left(\frac{1+\lambda^{P'}\alpha}{4}\right)(P'_E - P'_W) + \left(\frac{1-\lambda^{P'}}{4}\right)\left(P'^o_{NE} - P'^o_{NW}\right)\right]\Bigg\} \\
& + A^c_{u_s}\Bigg\{C_{Us}Uh\ \left[\left(\frac{1+\lambda^{P'}\alpha}{4}\right)(P'_E - P'_W) + \left(\frac{1-\lambda^{P'}}{4}\right)\left(P'^o_{SE} - P'^o_{SW}\right)\right] \\
& - C_{Vs}Uh\ (P'_P - P'_S)\Bigg\} + A^c_{v_s}\Bigg\{C_{Vs}Vh\ (P'_P - P'_S) \\
& -C_{Us}Vh\ \left[\left(\frac{1+\lambda^{P'}\alpha}{4}\right)(P'_E - P'_W) + \left(\frac{1-\lambda^{P'}}{4}\right)\left(P'^o_{SE} - P'^o_{SW}\right)\right]\Bigg\}\Bigg] \qquad \text{(B.28)}
\end{aligned}$$

In this case the coefficients for the P' algebraic equation become

$$\begin{aligned}
A^{p'}_W = & -A^c_{u_w}C_{Uw}Uh + A^c_{v_w}C_{Uw}Vh \\
& + \left(\frac{1+\lambda^{P'}\alpha}{4}\right)\left(-A^c_{u_n}C_{Un}Uh + A^c_{v_n}C_{Un}Vh - A^c_{u_s}C_{Us}Uh + A^c_{v_s}C_{Us}Vh\right) \qquad \text{(B.29)}
\end{aligned}$$

$$A_E^{p'} = A_{u_e}^c C_{Ue} Uh - A_{v_e}^c C_{Ue} Vh + \left(\frac{1+\lambda^{P'}\alpha}{4}\right)\left(A_{u_n}^c C_{Un} Uh - A_{v_n}^c C_{Un} Vh + A_{u_s}^c C_{Us} Uh - A_{v_s}^c C_{Us} Vh\right) \quad \text{(B.30)}$$

$$A_N^{p'} = -A_{u_n}^c C_{Vn} Uh + A_{v_n}^c C_{Vn} Vh + \left(\frac{1+\lambda^{P'}\alpha}{4}\right)\left(-A_{u_e}^c C_{Ve} Uh + A_{v_e}^c C_{Ve} Vh - A_{u_w}^c C_{Vw} Uh + A_{v_w}^c C_{Vw} Vh\right) \quad \text{(B.31)}$$

$$A_S^{p'} = A_{u_s}^c C_{Vs} Uh - A_{v_s}^c C_{Vs} Vh + \left(\frac{1+\lambda^{P'}\alpha}{4}\right)\left(A_{u_e}^c C_{Ve} Uh - A_{v_e}^c C_{Ve} Vh + A_{u_w}^c C_{Vw} Uh - A_{v_w}^c C_{Vw} Vh\right) \quad \text{(B.32)}$$

The pressure correction source term is just like Equation (B.21) if $\lambda^{P'} = 1$ as follows:

$$\begin{aligned} b^{p'} = {} & -\dot{m}_e + \dot{m}_w - \dot{m}_n + \dot{m}_s + b_P^c \\ & + \frac{1-\lambda^{P'}}{4}\left(-A_{u_e}^c C_{Ve} Uh + A_{v_e}^c C_{Ve} Vh + A_{u_n}^c C_{Un} Uh - A_{v_n}^c C_{Un} Vh\right) P'^o_{NE} \\ & + \frac{1-\lambda^{P'}}{4}\left(-A_{u_w}^c C_{Vw} Uh + A_{v_w}^c C_{Vw} Vh - A_{u_n}^c C_{Un} Uh + A_{v_n}^c C_{Un} Vh\right) P'^o_{NW} \\ & + \frac{1-\lambda^{P'}}{4}\left(A_{u_e}^c C_{Ve} Uh - A_{v_e}^c C_{Ve} Vh + A_{u_s}^c C_{Us} Uh - A_{v_s}^c C_{Us} Vh\right) P'^o_{SE} \\ & + \frac{1-\lambda^{P'}}{4}\left(A_{u_w}^c C_{Vw} Uh - A_{v_w}^c C_{Vw} Vh - A_{u_s}^c C_{Us} Uh + A_{v_s}^c C_{Us} Vh\right) P'^o_{SW} \end{aligned} \quad \text{(B.33)}$$

In each of the five-point coefficients and the source term (Equation (B.29) to (B.33)) when $\lambda = 0$ the standard five-point equations result, but if $\lambda = 1$ the improvements come into effect. Note that the $A_P^{p'}$ is the same as in Equation (5.60).

B.3 Five-Point P′ Boundary Conditions

B.3.1 Standard Five-Point Formulation

The boundary condition formulation of the algebraic P' equation using the five-point solver is presented here. The easiest change from the nine-point method, detailed in Section 5.2.6,

would be to lump the northeast and southeast correction terms into the source term as follows:

$$\begin{aligned} b^{p'} = & -\dot{m}_e + \dot{m}_w - \dot{m}_n + \dot{m}_s + b_P^c \\ & + \frac{1}{4}\left(-\left(A_{u_e}^c\right)^{\oplus} C_{Ve} U h + \left(A_{v_e}^c\right)^{\oplus} C_{Ve} V h + A_{u_n}^c C_{Un} U h - A_{v_n}^c C_{Un} V h \right) P'^{o}_{NE} \\ & + \frac{1}{4}\left(\left(A_{u_e}^c\right)^{\oplus} C_{Ve} U h - \left(A_{v_e}^c\right)^{\oplus} C_{Ve} V h + A_{u_s}^c C_{Us} U h - A_{v_s}^c C_{Us} V h \right) P'^{o}_{SE} \end{aligned} \quad \text{(B.34)}$$

The diagonal northeast and southeast pressure corrections would be updated from the previous solver iteration.

B.3.2 Improved Five-Point Formulation

Using Perić's approximation, Equation (B.22), for the corner pressure correction nodes, and λ as before Equation (5.70) becomes:

$$-\left[G_{e_{bc}}^c + G_{n_{bc}}^c + G_{s_{bc}}^c\right] = \Delta m \quad \text{(B.35)}$$

Where

$$\begin{aligned} G_{e_{bc}}^c = & \left(A_{u_e}^c\right)^{\oplus} \Big\{ C_{Ue} U h \, \left(P'_E - P'_P\right) \\ & - C_{Ve} U h \, \frac{1}{4}\Big(\left(P'_N + \lambda^{P'} \alpha \left(P'_N + P'_E - P'_P\right) + \left(1 - \lambda^{P'}\right) P'^{o}_{NE}\right) \\ & - \left(P'_S + \lambda^{P'} \alpha \left(P'_S + P'_E - P'_P\right) + \left(1 - \lambda^{P'}\right) P'^{o}_{SE}\right)\Big) \Big\} \\ & + \left(A_{v_e}^c\right)^{\oplus} \Big\{ C_{Ve} V h \, \frac{1}{4}\Big(\left(P'_N + \lambda^{P'} \alpha \left(P'_N + P'_E - P'_P\right) + \left(1 - \lambda^{P'}\right) P'^{o}_{NE}\right) \\ & - \left(P'_S + \lambda^{P'} \alpha \left(P'_S + P'_E - P'_P\right) + \left(1 - \lambda^{P'}\right) P'^{o}_{SE}\right)\Big) - C_{Ue} V h \, \left(P'_E - P'_P\right) \Big\} \end{aligned} \quad \text{(B.36)}$$

$$
\begin{aligned}
G^c_{n_{bc}} = A^c_{u_n} \Big\{ & C_{Un} U h \ \Big(\frac{1}{4} \left(P'_N + P'_P + P'_E + \lambda^{P'} \alpha \left(P'_N + P'_E - P'_P \right) + \left(1 - \lambda^{P'} \right) P'^{o}_{NE} \right) \\
& - f_n \left(A^{p'}_{P(IB-1,j)} P'_P + A^{p'}_{E(IB-1,j)} P'_E \right) - (1.0 - f_n) \left(A^{p'}_{P(IB-1,j+1)} P'_N \right. \\
& \left. + A^{p'}_{E(IB-1,j+1)} \left(\lambda^{P'} \alpha \left(P'_N + P'_E - P'_P \right) + \left(1 - \lambda^{P'} \right) P'^{o}_{NE} \right) \right) - C_{Vn} U h \ \left(P'_N - P'_P \right) \Big\} \\
& + A^c_{v_n} \Big\{ C_{Vn} V h \ \left(P'_N - P'_P \right) \\
& - C_{Un} V h \ \Big(\frac{1}{4} \left(P'_N + P'_P + P'_E + \lambda^{P'} \alpha \left(P'_N + P'_E - P'_P \right) + \left(1 - \lambda^{P'} \right) P'^{o}_{NE} \right) \\
& - f_n \left(A^{p'}_{P(IB-1,j)} P'_P + A^{p'}_{E(IB-1,j)} P'_E \right) - (1.0 - f_n) \left(A^{p'}_{P(IB-1,j+1)} P'_N \right. \\
& \left. \left. + A^{p'}_{E(IB-1,j+1)} \left(\lambda^{P'} \alpha \left(P'_N + P'_E - P'_P \right) + \left(1 - \lambda^{P'} \right) P'^{o}_{NE} \right) \right) \right\}
\end{aligned} \tag{B.37}
$$

$$
\begin{aligned}
G^c_{s_{bc}} = A^c_{u_s} \Big\{ & C_{Us} U h \ \Big(\frac{1}{4} \left(P'_S + P'_P + P'_E + \lambda^{P'} \alpha \left(P'_S + P'_E - P'_P \right) + \left(1 - \lambda^{P'} \right) P'^{o}_{SE} \right) \\
& - f_s \left(A^{p'}_{P(IB-1,j-1)} P'_S + A^{p'}_{E(IB-1,j-1)} \left(\lambda^{P'} \alpha \left(P'_S + P'_E - P'_P \right) + \left(1 - \lambda^{P'} \right) P'^{o}_{SE} \right) \right) \\
& + (1.0 - f_s) \left(A^{p'}_{P(IB-1,j)} P'_P + A^{p'}_{E(IB-1,j)} P'_E \right) \Big) - C_{Vs} U h \ \left(P'_P - P'_S \right) \Big\} \\
& + A^c_{v_s} \Big\{ C_{Vs} V h \ \left(P'_P - P'_S \right) \\
& - C_{Us} V h \ \Big(\frac{1}{4} \left(P'_S + P'_P + P'_E + \lambda^{P'} \alpha \left(P'_S + P'_E - P'_P \right) + \left(1 - \lambda^{P'} \right) P'^{o}_{SE} \right) \\
& - f_s \left(A^{p'}_{P(IB-1,j-1)} P'_S + A^{p'}_{E(IB-1,j-1)} \left(\lambda^{P'} \alpha \left(P'_S + P'_E - P'_P \right) + \left(1 - \lambda^{P'} \right) P'^{o}_{SE} \right) \right) \\
& \left. + (1.0 - f_s) \left(A^{p'}_{P(IB-1,j)} P'_P + A^{p'}_{E(IB-1,j)} P'_E \right) \right) \Big\}
\end{aligned} \tag{B.38}
$$

Collecting terms of Equation (B.35) into the form of the five-point algebraic equation produces the following coefficients:

$$
\begin{aligned}
A^{p'}_S = & A^c_{u_s} \left(C_{Vs} U h + C_{Us} U h \left(\left(\frac{1 + \lambda^{P'} \alpha}{4} \right) - f_s \left(A^{p'}_{P(IB-1,j-1)} + A^{p'}_{E(IB-1,j-1)} \lambda^{P'} \alpha \right) \right) \right) \\
& - A^c_{v_s} \left(C_{Vs} V h + C_{Us} V h \left(\left(\frac{1 + \lambda^{P'} \alpha}{4} \right) - f_s \left(A^{p'}_{P(IB-1,j-1)} + A^{p'}_{E(IB-1,j-1)} \lambda^{P'} \alpha \right) \right) \right) \\
& + \left(\frac{1 + \lambda^{P'} \alpha}{4} \right) \left(\left(A^c_{u_e} \right)^{\oplus} C_{Ve} U h - \left(A^c_{v_e} \right)^{\oplus} C_{Ve} V h \right)
\end{aligned} \tag{B.39}
$$

$$
\begin{aligned}
&A_N^{p'} = \\
&- A_{u_n}^c \left(C_{Vn}Uh - C_{Un}Uh \left(\left(\frac{1+\lambda^{P'}\alpha}{4} \right) - (1.0 - f_n) \left(A_{P(IB-1,j+1)}^{p'} + A_{E(IB-1,j+1)}^{p'} \lambda^{P'}\alpha \right) \right) \right) \\
&+ A_{v_n}^c \left(C_{Vn}Vh - C_{Un}Vh \left(\left(\frac{1-\lambda^{P'}\alpha}{4} \right) - (1.0 + f_n) \left(A_{P(IB-1,j+1)}^{p'} + A_{E(IB-1,j+1)}^{p'} \lambda^{P'}\alpha \right) \right) \right) \\
&\qquad + \left(\frac{1+\lambda^{P'}\alpha}{4} \right) \left(- \left(A_{u_e}^c \right)^{\oplus} C_{Ve}Uh + \left(A_{v_e}^c \right)^{\oplus} C_{Ve}Vh \right) \qquad \text{(B.40)}
\end{aligned}
$$

$$
\begin{aligned}
&A_E^{p'} = \left(A_{u_e}^c \right)^{\oplus} C_{Ue}Uh - \left(A_{u_e}^c \right)^{\oplus} C_{Ue}Vh \\
&+ \left(\left(\frac{1+\lambda^{P'}\alpha}{4} \right) - f_n A_{E(IB-1,j)}^{p'} - (1.0 - f_n) A_{E(IB-1,j+1)}^{p'} \lambda^{P'}\alpha \right) \left(A_{u_n}^c C_{Un}Uh - A_{v_n}^c C_{Un}Vh \right) \\
&+ \left(\left(\frac{1+\lambda^{P'}\alpha}{4} \right) - f_s A_{E(IB-1,j-1)}^{p'} \lambda^{P'}\alpha - (1.0 - f_s) A_{E(IB-1,j)}^{p'} \right) \left(A_{u_s}^c C_{Us}Uh - A_{v_s}^c C_{Us}Vh \right)
\end{aligned} \qquad \text{(B.41)}
$$

$$
\begin{aligned}
&A_P^{p'} = \left(A_{u_e}^c \right)^{\oplus} C_{Ue}Uh - \left(A_{v_e}^c \right)^{\oplus} C_{Ue}Vh \\
&+ A_{u_s}^c \left(C_{Vs}Uh - C_{Us}Uh \left(\left(\frac{1-\lambda^{P'}\alpha}{4} \right) - (1.0 - f_s) A_{P(IB-1,j)}^{p'} + f_s A_{E(IB-1,j-1)}^{p'} \lambda^{P'}\alpha \right) \right) \\
&- A_{v_s}^c \left(C_{Vs}Vh - C_{Us}Vh \left(\left(\frac{1-\lambda^{P'}\alpha}{4} \right) - (1.0 - f_s) A_{P(IB-1,j)}^{p'} + f_s A_{E(IB-1,j-1)}^{p'} \lambda^{P'}\alpha \right) \right) \\
&- A_{u_n}^c \left(C_{Vn}Uh + C_{Un}Uh \left(\left(\frac{1-\lambda^{P'}\alpha}{4} \right) - f_n A_{P(IB-1,j)}^{p'} + (1.0 - f_n) A_{E(IB-1,j+1)}^{p'} \lambda^{P'}\alpha \right) \right) \\
&+ A_{v_n}^c \left(C_{Vn}Vh + C_{Un}Vh \left(\left(\frac{1-\lambda^{P'}\alpha}{4} \right) - f_n A_{P(IB-1,j)}^{p'} + (1.0 - f_n) A_{E(IB-1,j+1)}^{p'} \lambda^{P'}\alpha \right) \right)
\end{aligned} \qquad \text{(B.42)}
$$

$$
\begin{aligned}
&b^{p'} = -\dot{m}_e + \dot{m}_w - \dot{m}_n + \dot{m}_s + b_P^c \\
&\qquad + \left(\frac{1-\lambda^{P'}}{4} \right) \left\{ - \left(A_{u_e}^c \right)^{\oplus} C_{Ve}Uh + \left(A_{v_e}^c \right)^{\oplus} C_{Ve}Vh \right. \\
&\quad \left. + \left(A_{u_n}^c C_{Un}Uh - A_{v_n}^c C_{Un}Vh \right) \left(1 - 4 (1.0 - f_n) A_{E(IB-1,j+1)}^{p'} \right) \right\} P'^o_{NE} \\
&\qquad + \left(\frac{1-\lambda^{P'}}{4} \right) \left\{ \left(A_{u_e}^c \right)^{\oplus} C_{Ve}Uh - \left(A_{v_e}^c \right)^{\oplus} C_{Ve}Vh \right. \\
&\quad \left. + \left(A_{u_s}^c C_{Us}Uh - A_{v_s}^c C_{Us}Vh \right) \left(1 - 4 f_s A_{E(IB-1,j-1)}^{p'} \right) \right\} P'^o_{SE}
\end{aligned} \qquad \text{(B.43)}
$$

The coefficients, given in Equations (B.39) to (B.43), were used in easier computations that employed a five-point solver.

Appendix C

Further Results for the Tube Bundle Flow Tests

This appendix gives the details of the $\mu * 50$ results for the slug flow through a tilted tube bundle omitted from Section 7.1.1 and the details of the simulated heat exchanger with a rotated square tube bundle that were omitted from Section 7.2

C.1 The Slug flow with a Tilted Tube Bundle

The material found in this section is the remainder of the plots of the results for the slug flow through a tilted tube bundle. A comparison of the orthogonal and non-orthogonal streamlines is shown for each grid level at the $\mu * 50$ viscosity multiple that was not included in Section 7.1.1.

Figure C.1 shows the Streamlines on the 70×10 Grid. Figure C.2 shows the Streamlines on the 140×20 Grid. Figure C.3 shows the Streamlines on the 210×30 Grid. Figure C.4 shows the U velocity profiles for the 70×10 grid. Figure C.5 shows the U velocity profiles for the 140×20 grid. Figure C.6 shows the U velocity profiles for the 210×30 grid.

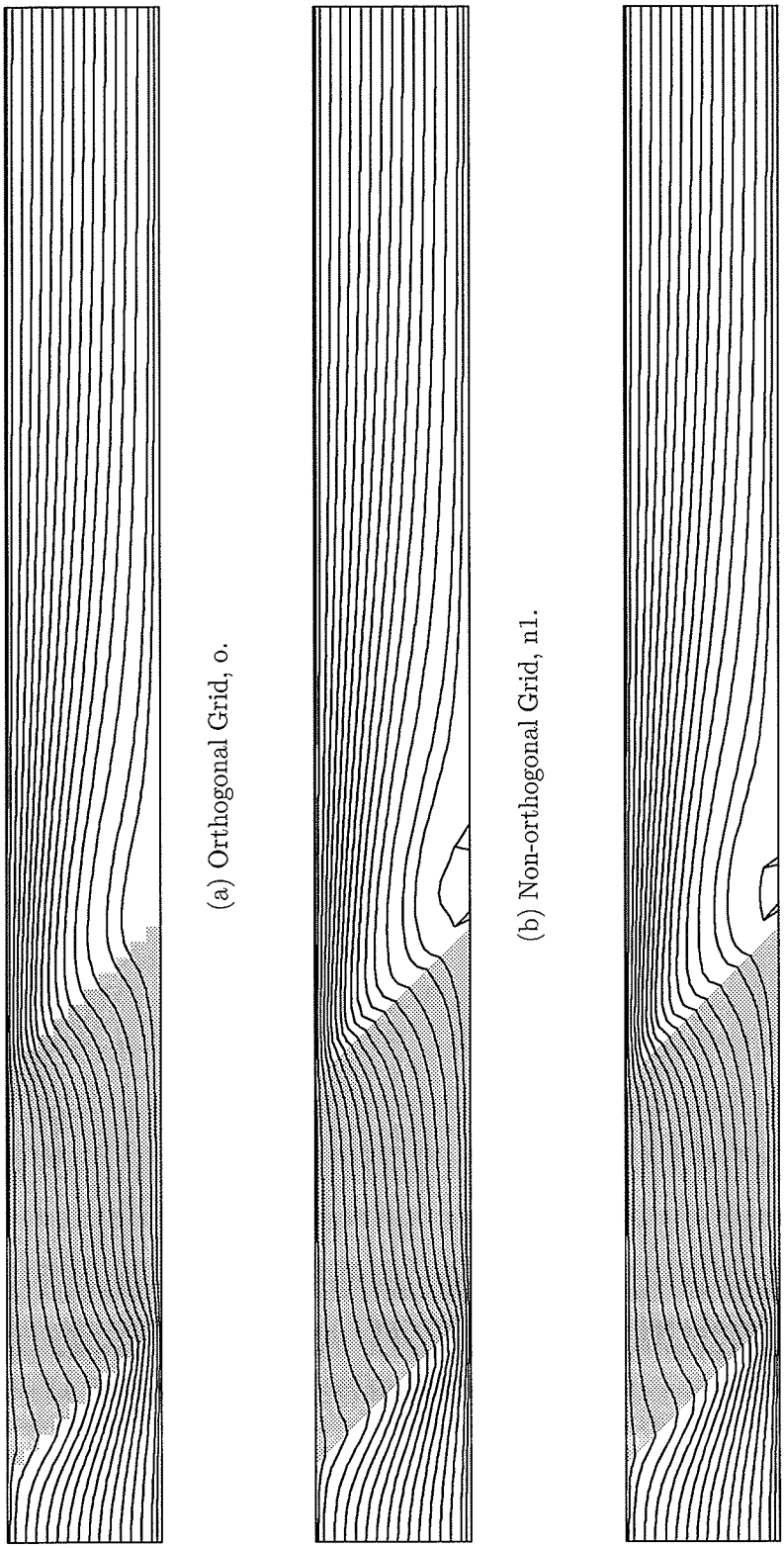

(a) Orthogonal Grid, o.

(b) Non-orthogonal Grid, n1.

(c) Non-orthogonal Grid, n2.

Figure C.1: Slug Flow Streamlines: 70×10 Grid, $\mu * 50$.

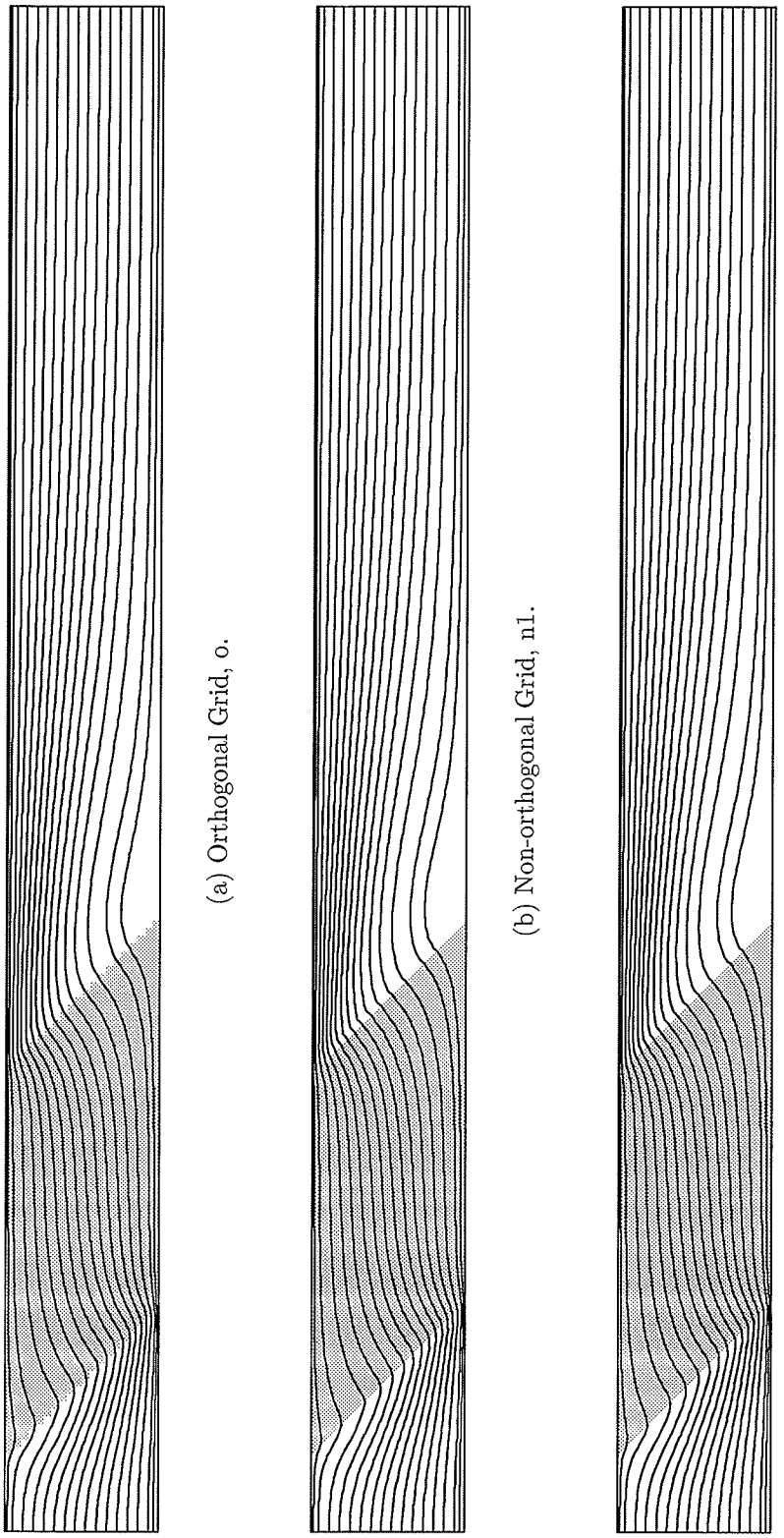

(a) Orthogonal Grid, o.

(b) Non-orthogonal Grid, n1.

(c) Non-orthogonal Grid, n2.

Figure C.2: Slug Flow Streamlines: 140×20 Grid, $\mu * 50$.

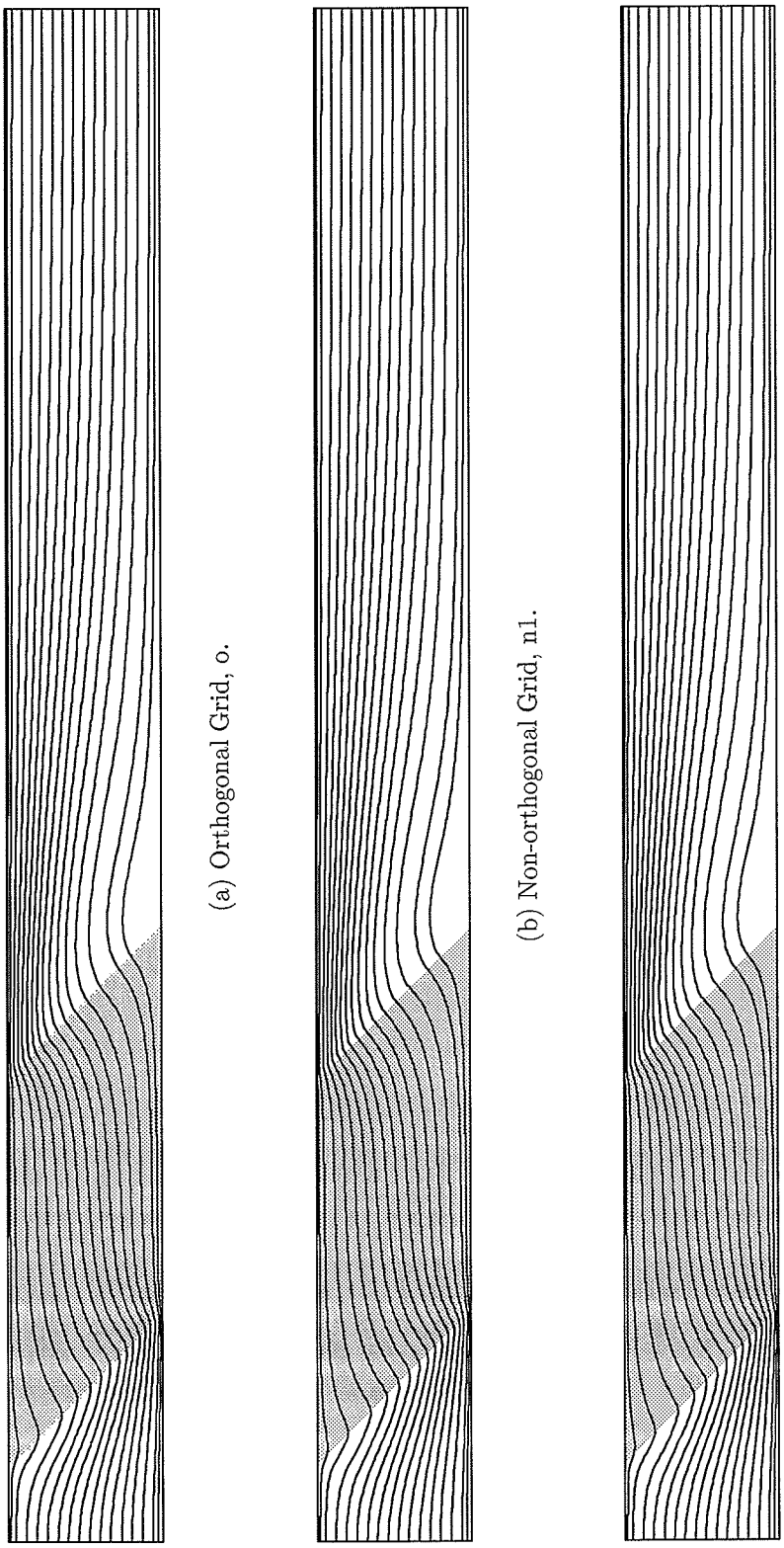

(a) Orthogonal Grid, o.

(b) Non-orthogonal Grid, n1.

(c) Non-orthogonal Grid, n2.

Figure C.3: Slug Flow Streamlines: 210×30 Grid, $\mu * 50$.

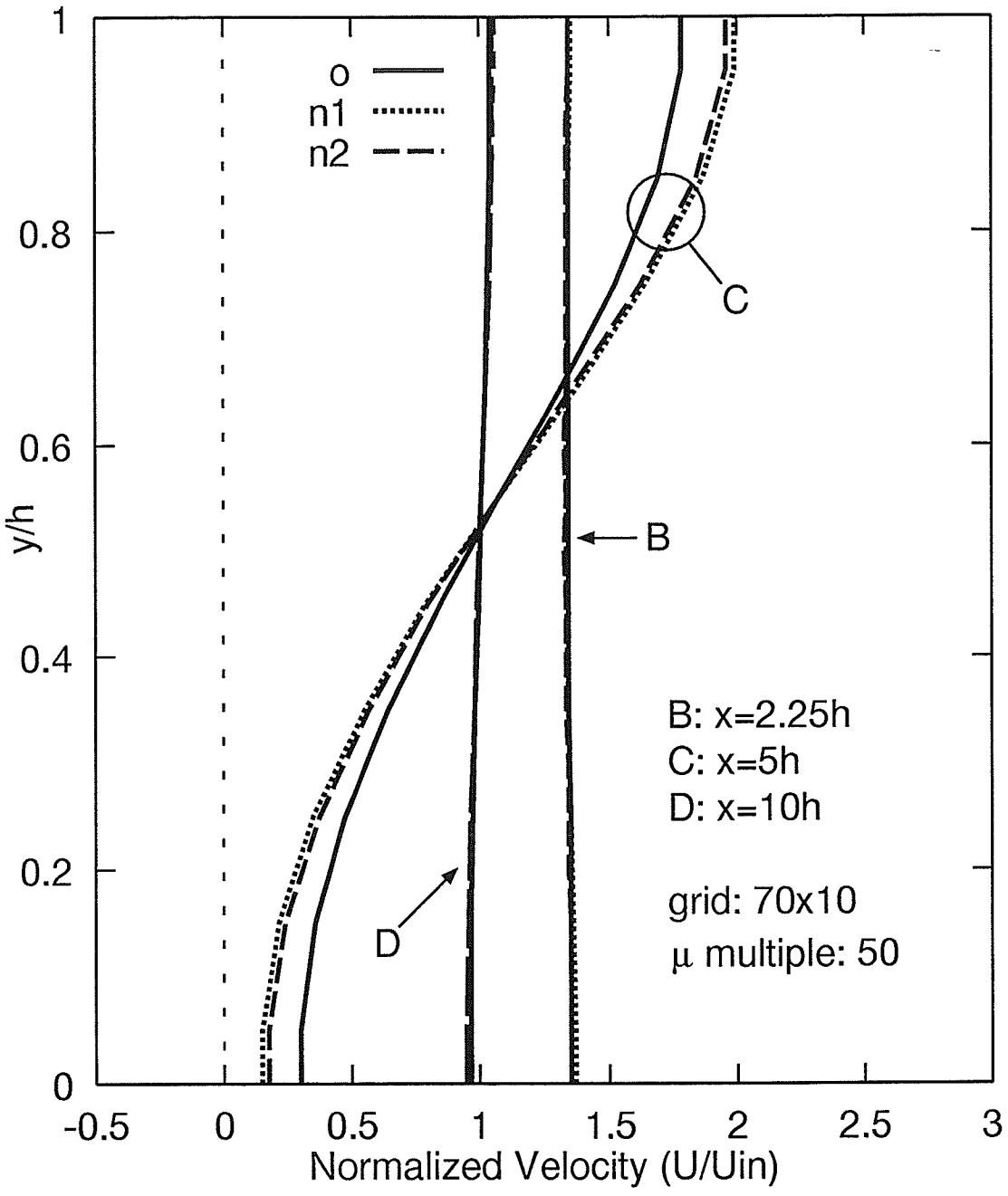

Figure C.4: Slug Flow Normalized U Velocity Profiles: 70×10 Grid, $\mu * 50$.

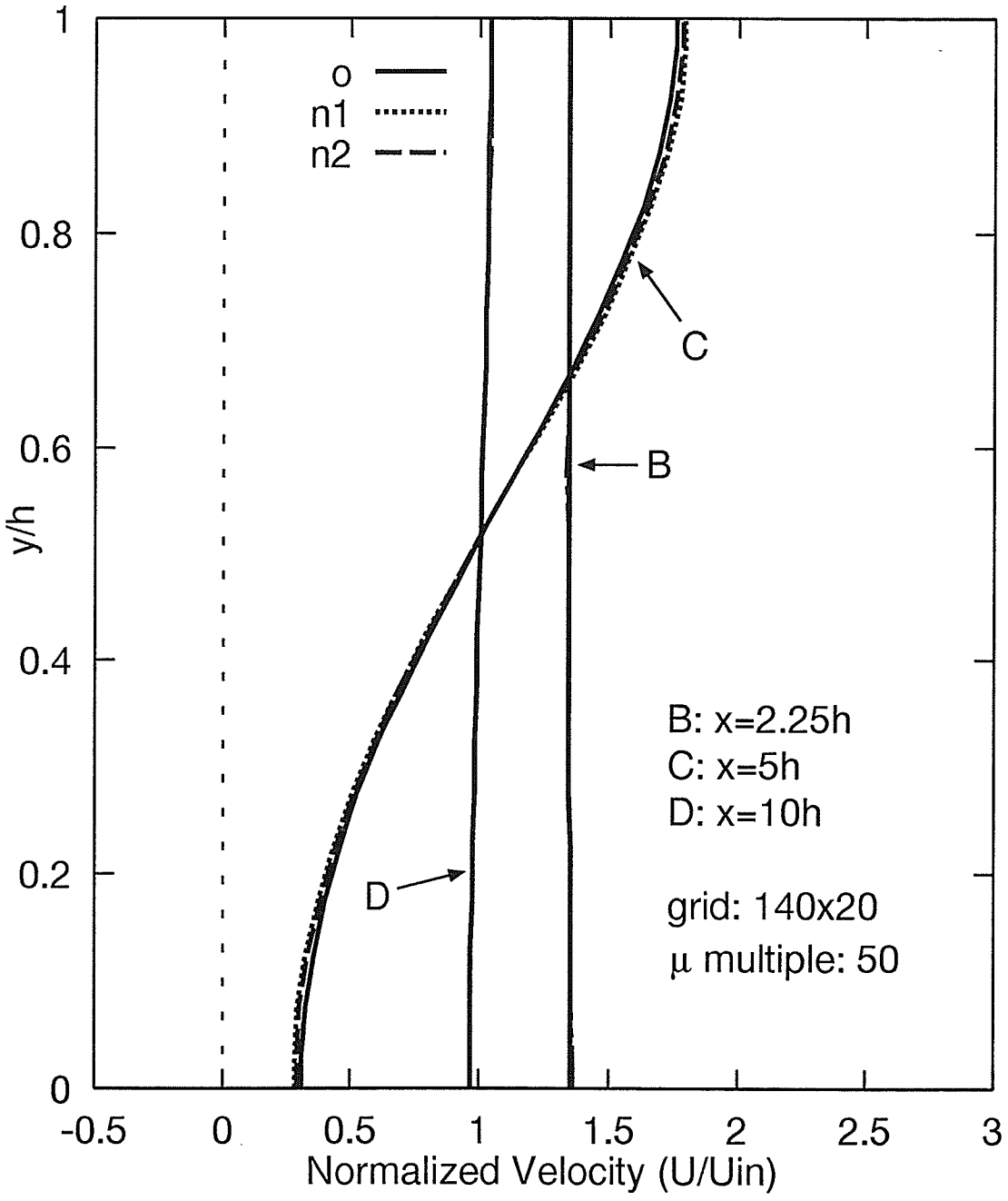

Figure C.5: Slug Flow Normalized U Velocity Profiles: 140×20 Grid, $\mu * 50$.

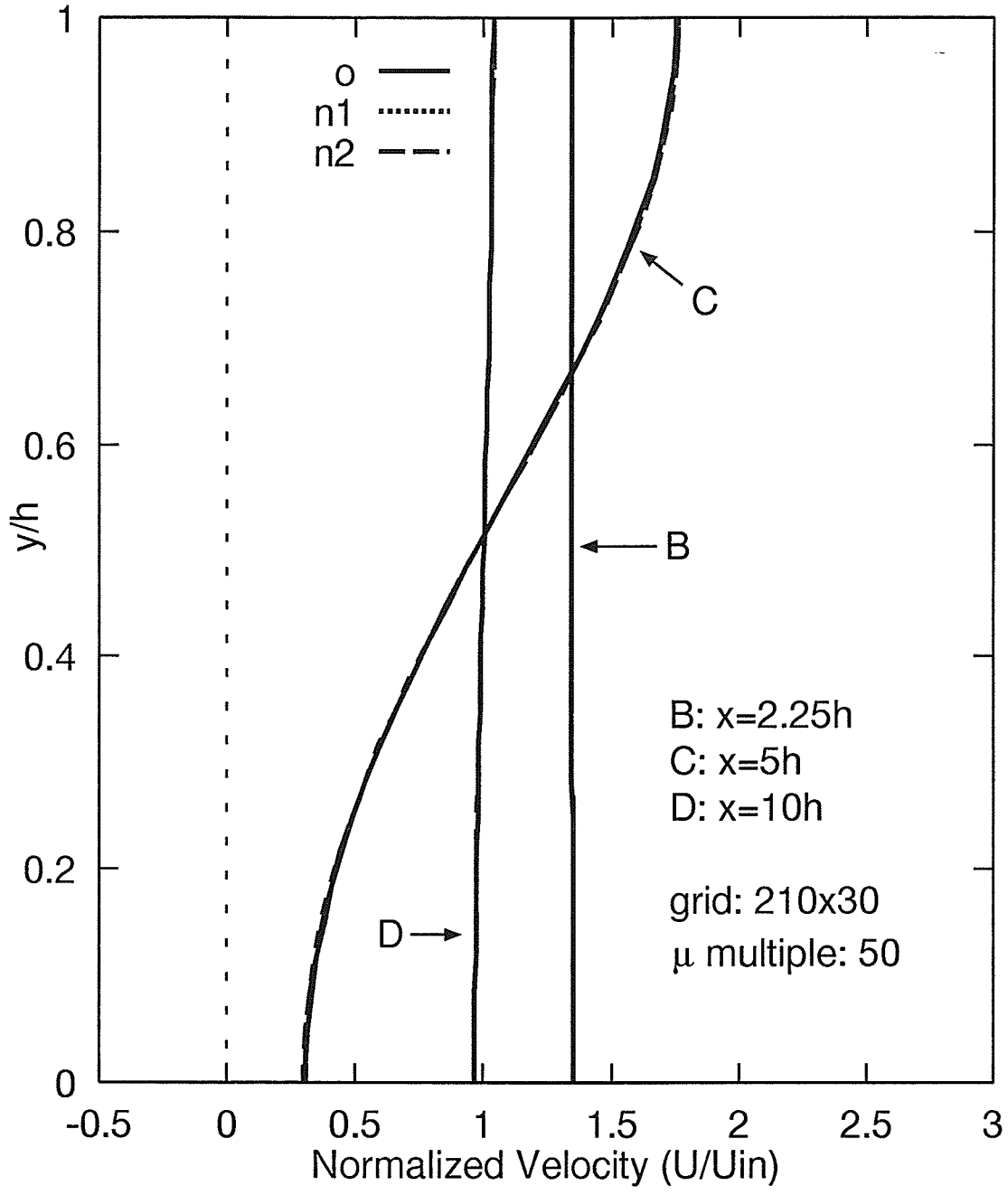

Figure C.6: Slug Flow Normalized U Velocity Profiles: 210×30 Grid, $\mu * 50$.

C.2 The Rotated Square Tube Bundle Test Problem

C.2.1 Streamlines

The material found in this section is the remainder of the streamline plots detailing the flow through the sample heat exchanger. A comparison of the orthogonal and non-orthogonal streamlines is shown for each grid level and viscosity multiple that was not included in Section 7.2.

Figure C.7 shows the streamlines for the coarsest orthogonal grid, 30×20, at the lowest viscosity multiple, $\mu * 25$. The solution for the coarsest non-orthogonal grid is not available to compare with this orthogonal result because it would not converge. Figure C.8 and C.9 show the streamlines for the coarsest orthogonal and non-orthogonal grids respectively at the middle viscosity multiple, $\mu * 50$. Figure C.10 and C.11 show the streamlines for the coarsest orthogonal and non-orthogonal grids respectively at the highest viscosity multiple, $\mu * 100$. Figure C.12 and C.13 show the streamlines for the 60×40 orthogonal and non-orthogonal grids respectively at the middle viscosity multiple, $\mu * 50$. Figure C.14 and C.15 show the streamlines for the 90×60 orthogonal and non-orthogonal grids respectively at the lowest viscosity multiple, $\mu * 25$. Figure C.16 and C.17 show the streamlines for the 90×60 orthogonal and non-orthogonal grids respectively at the middle viscosity multiple, $\mu * 50$. Figure C.18 and C.19 show the streamlines for the 90×60 orthogonal and non-orthogonal grids respectively at the highest viscosity multiple, $\mu * 100$. Figure C.20 and C.21 show the streamlines for the 120×80 orthogonal and non-orthogonal grids respectively at the middle viscosity multiple, $\mu * 50$.

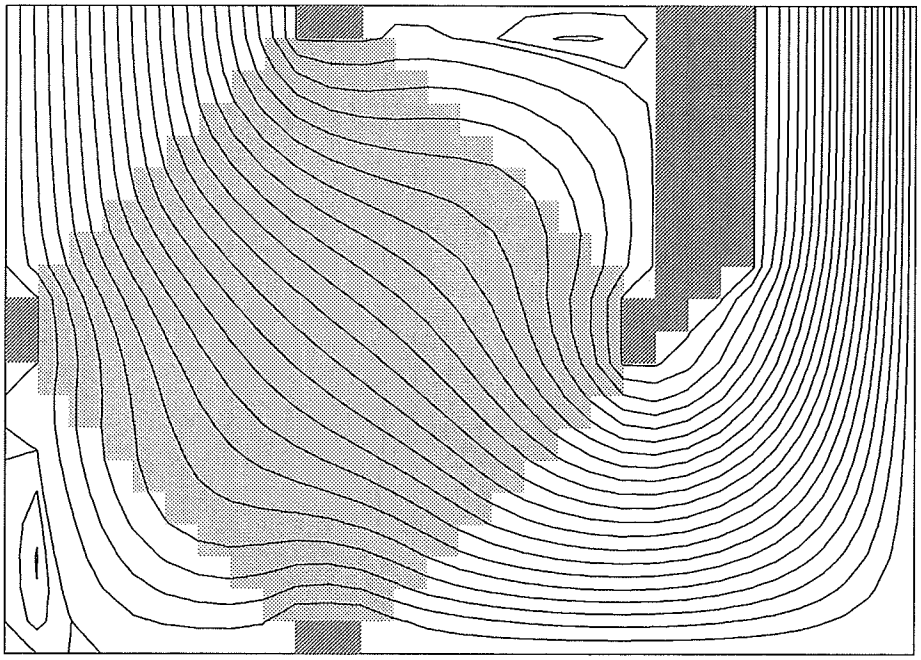

Figure C.7: RSTB Test Problem Streamlines: Orthogonal 30×20 Grid, $\mu * 25$.

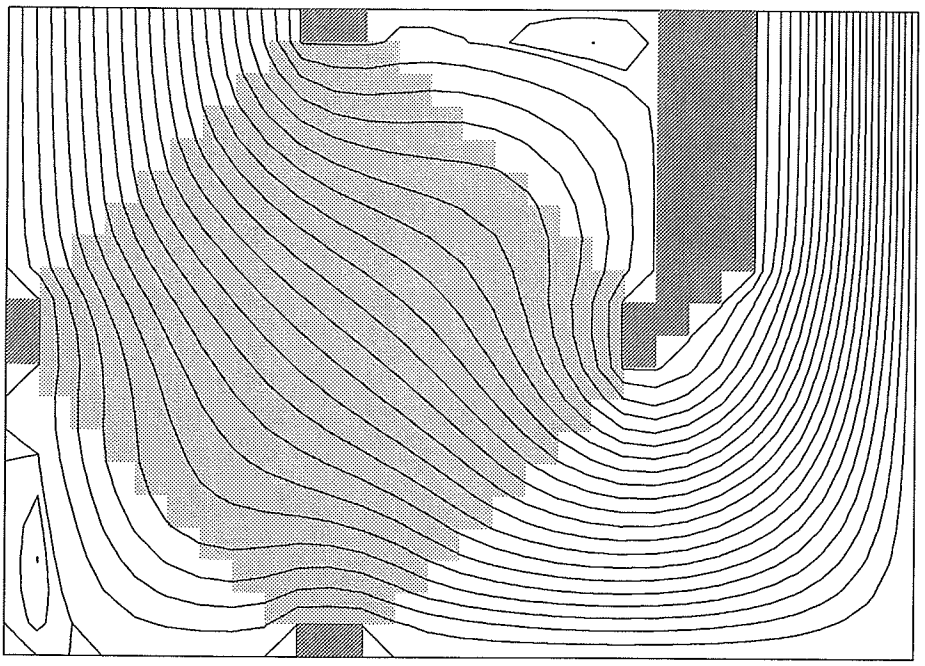

Figure C.8: RSTB Test Problem Streamlines: Orthogonal 30×20 Grid, $\mu * 50$.

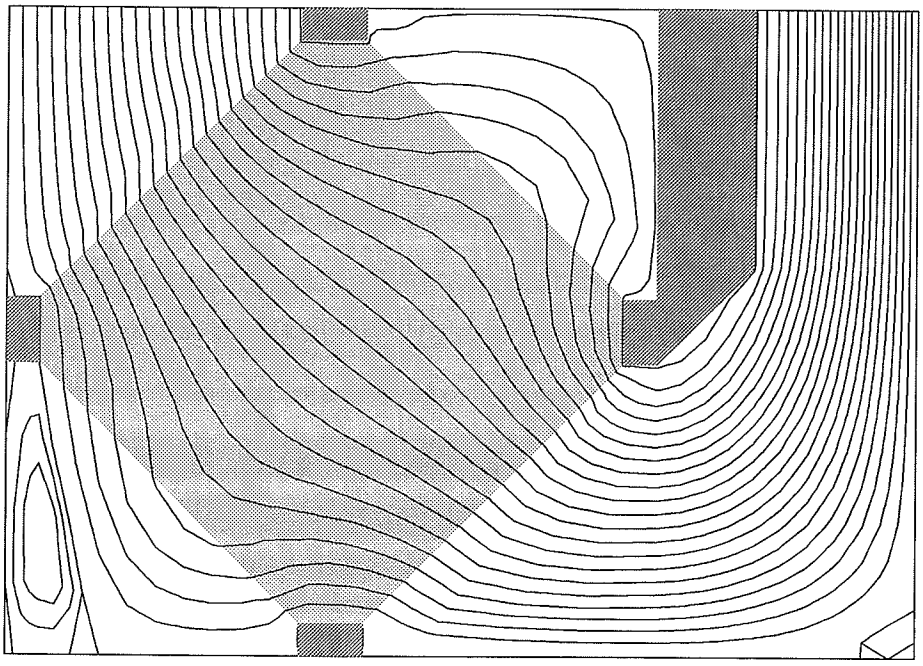

Figure C.9: RSTB Test Problem Streamlines: Non-Orthogonal 30×20 Grid, $\mu * 50$.

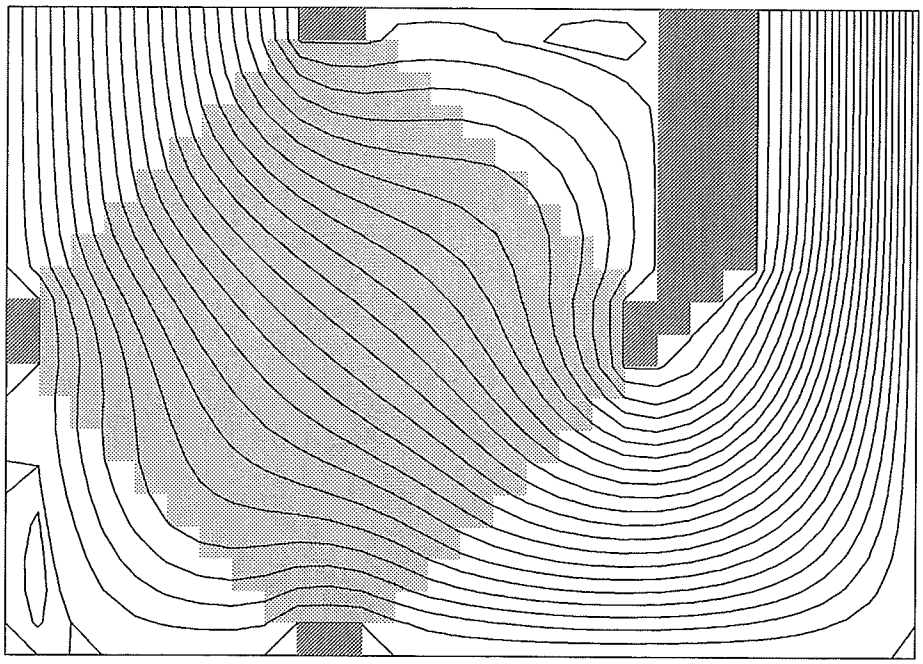

Figure C.10: RSTB Test Problem Streamlines: Orthogonal 30×20 Grid, $\mu * 100$.

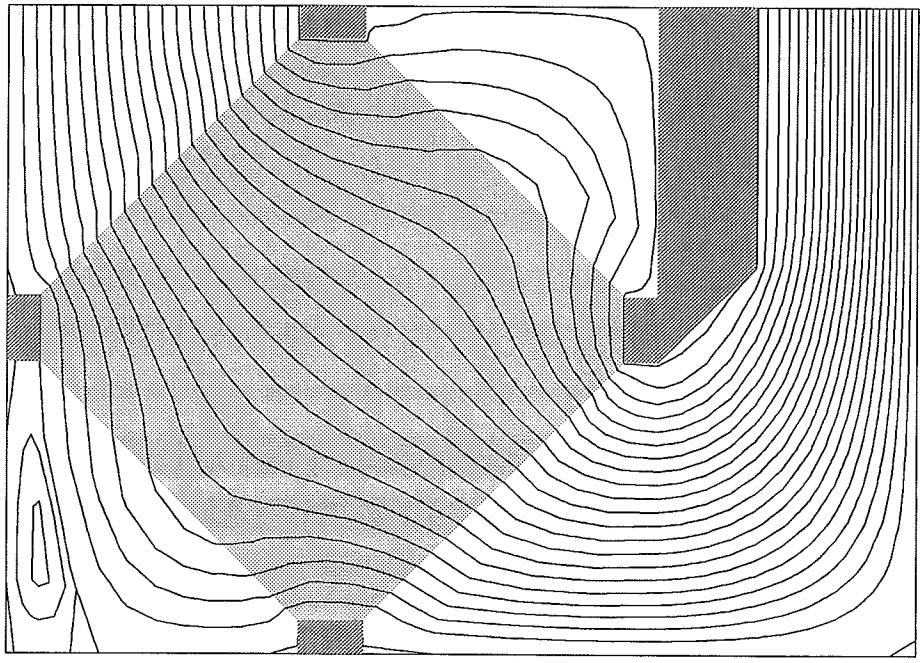

Figure C.11: RSTB Test Problem Streamlines: Non-Orthogonal 30×20 Grid, $\mu * 100$.

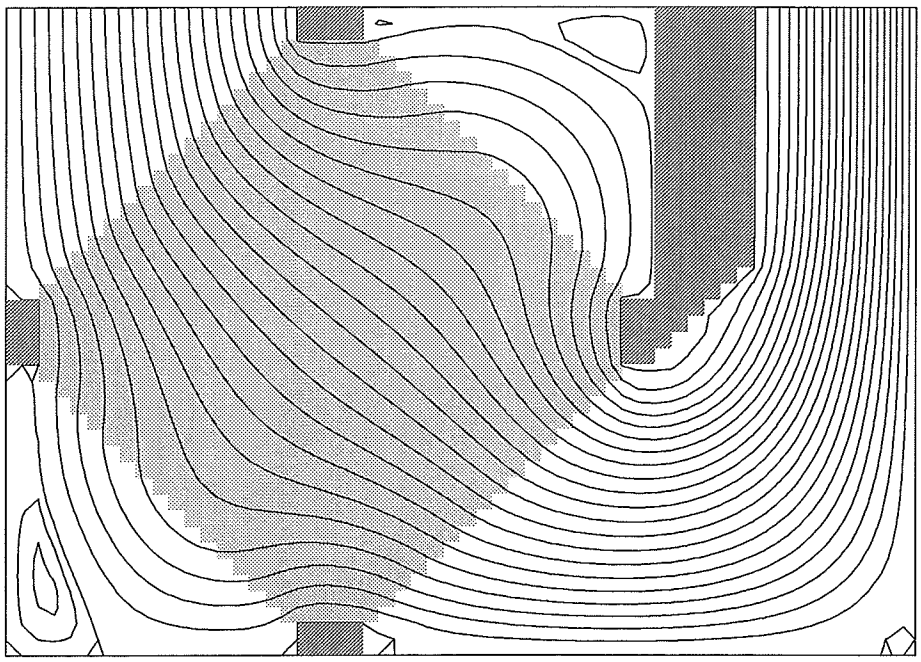

Figure C.12: RSTB Test Problem Streamlines: Orthogonal 60×40 Grid, $\mu * 50$.

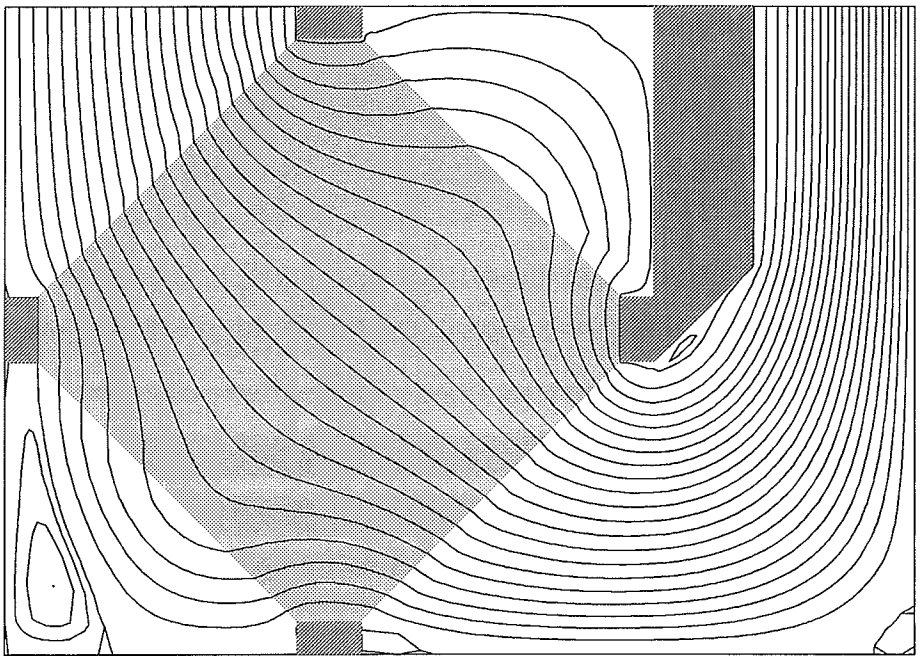

Figure C.13: RSTB Test Problem Streamlines: Non-Orthogonal 60×40 Grid, $\mu * 50$.

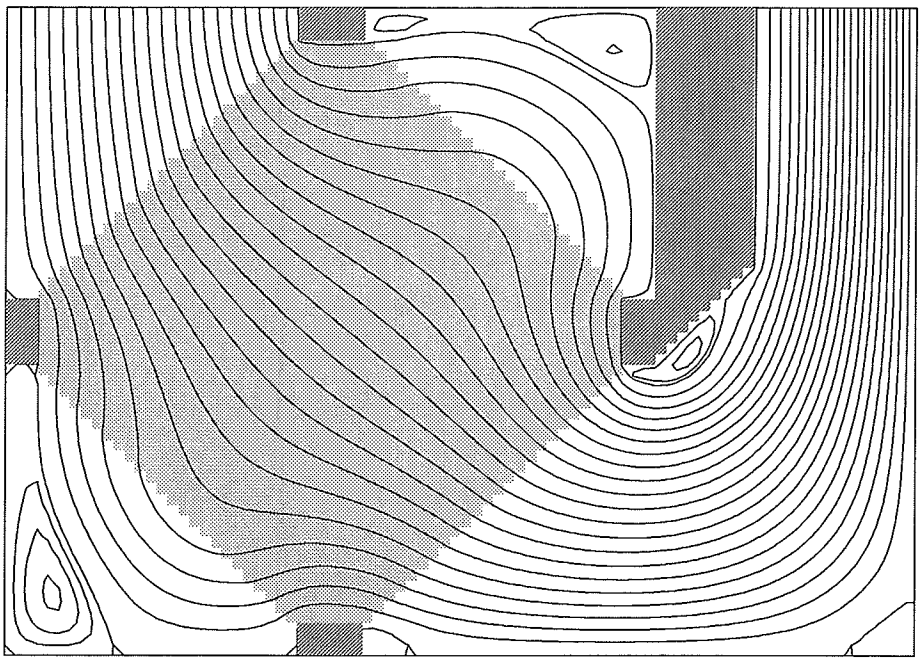

Figure C.14: RSTB Test Problem Streamlines: Orthogonal 90×60 Grid, $\mu * 25$.

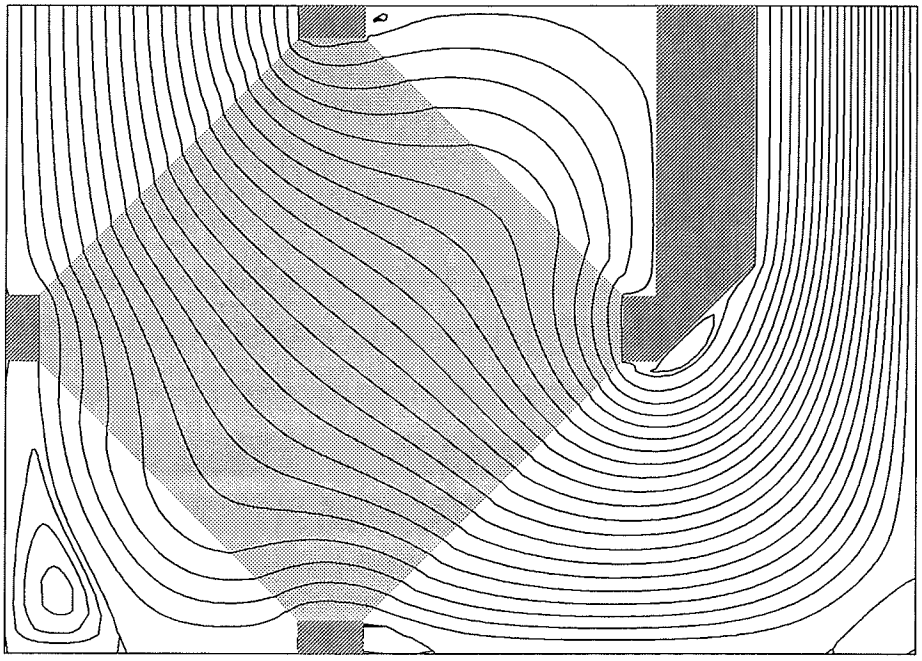

Figure C.15: RSTB Test Problem Streamlines: Non-Orthogonal 90×60 Grid, $\mu * 25$.

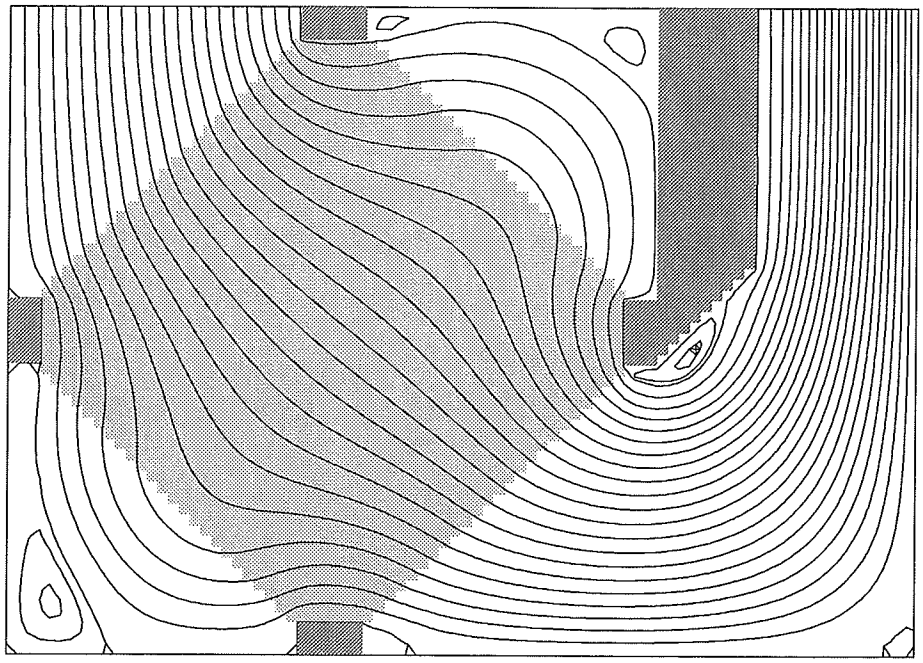

Figure C.16: RSTB Test Problem Streamlines: Orthogonal 90×60 Grid, $\mu * 50$.

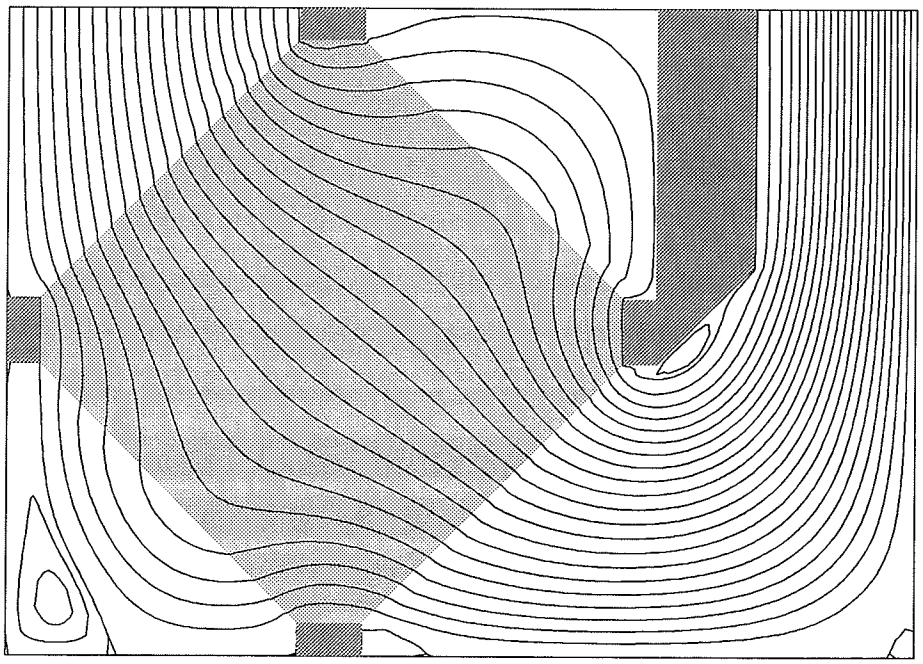

Figure C.17: RSTB Test Problem Streamlines: Non-Orthogonal 90×60 Grid, $\mu * 50$.

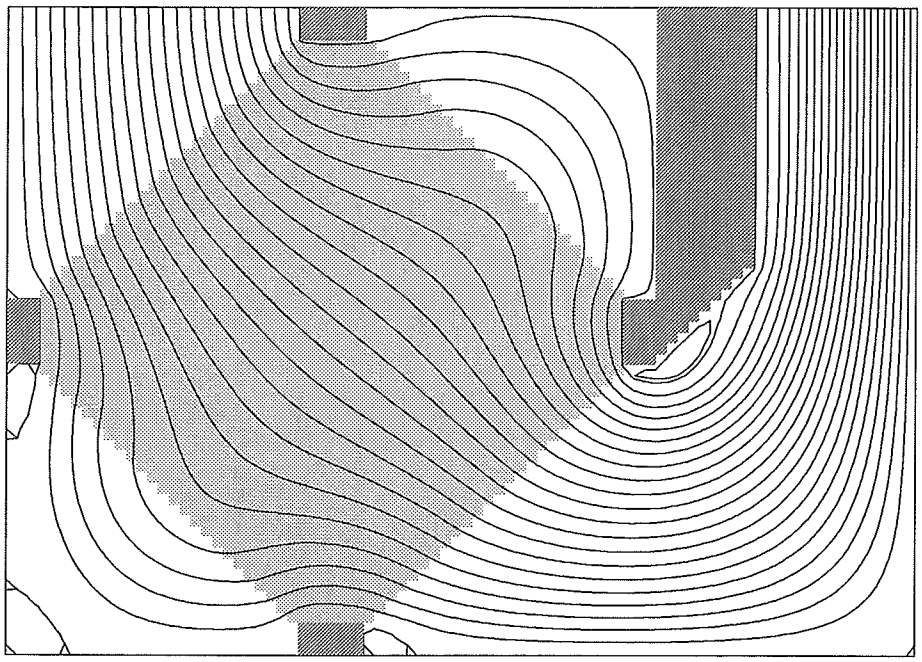

Figure C.18: RSTB Test Problem Streamlines: Orthogonal 90×60 Grid, $\mu * 100$.

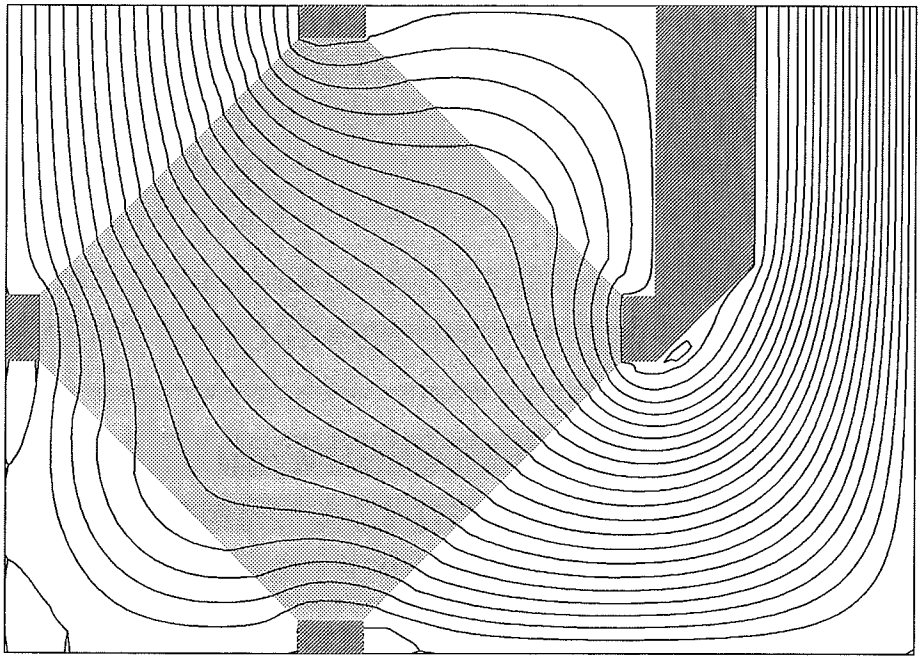

Figure C.19: RSTB Test Problem Streamlines: Non-Orthogonal 90×60 Grid, $\mu * 100$.

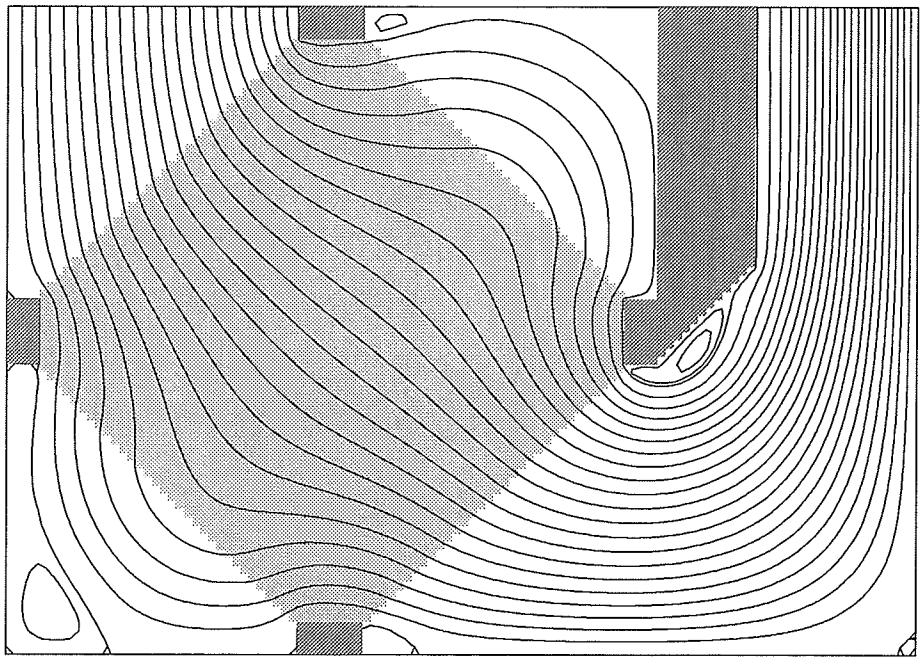

Figure C.20: RSTB Test Problem Streamlines: Orthogonal 120×80 Grid, $\mu * 50$.

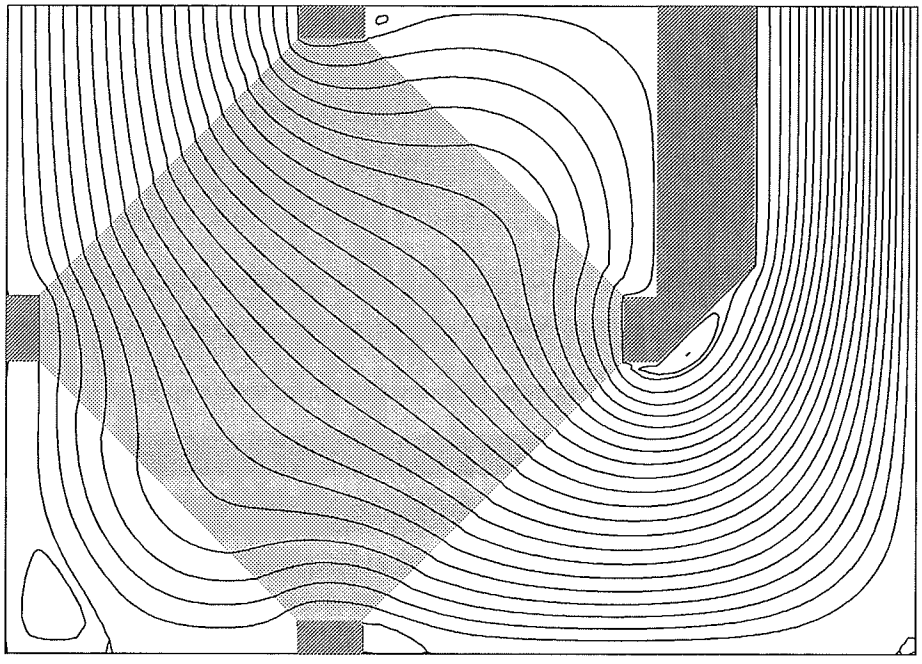

Figure C.21: RSTB Test Problem Streamlines: Non-Orthogonal 120×80 Grid, $\mu * 50$.

C.2.2 Velocity Profiles

The material found in this section is the remainder of the velocity profiles detailing the flow through the sample heat exchanger. A comparison of the orthogonal and non-orthogonal velocity profiles is shown for each grid level and viscosity multiple that was not included in Section 7.2.

Figure C.22 and C.23 show the velocity profile along the vertical centerline for orthogonal and non-orthogonal grids respectively at the lowest viscosity multiple, $\mu * 25$. Figure C.24 and C.25 show the velocity profile along the vertical centerline for orthogonal and non-orthogonal grids respectively at the highest viscosity multiple, $\mu * 100$. Figure C.26 and C.27 show a direct comparison of the orthogonal and non-orthogonal grids in terms of the velocity profile along the vertical centerline at the lowest and highest viscosity multiple respectively. Figure C.28 and C.29 show the velocity profile along the horizontal centerline for orthogonal and non-orthogonal grids respectively at the lowest viscosity multiple, $\mu * 25$. Figure C.30 and C.31 show the velocity profile along the horizontal centerline for orthogonal and non-orthogonal grids respectively at the highest viscosity multiple, $\mu * 100$. Figure C.32 and C.33 show a direct comparison of the orthogonal and non-orthogonal grids in terms of the velocity profile along the horizontal centerline at the lowest and highest viscosity multiple respectively. Figure C.34 and C.35 show the velocity profile along the horizontal centerline for orthogonal and non-orthogonal grids respectively at the lowest viscosity multiple, $\mu * 25$. Figure C.36 and C.37 show the velocity profile along line "C" in the exit region for orthogonal and non-orthogonal grids respectively at the highest viscosity multiple, $\mu * 100$. Figure C.38 and C.39 show a direct comparison of the orthogonal and non-orthogonal grids in terms of the velocity profile along line "C" in the exit region at the lowest and highest viscosity multiple respectively.

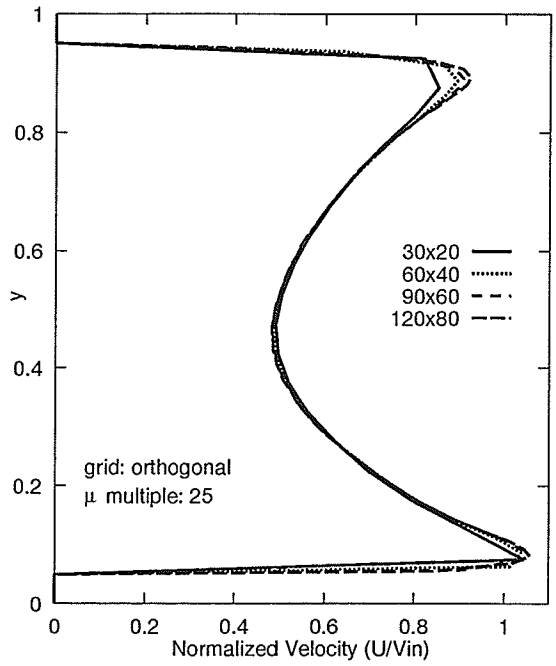

Figure C.22: RSTB Test Problem U Velocity Profiles at "A": Orthogonal Grid, $\mu * 25$.

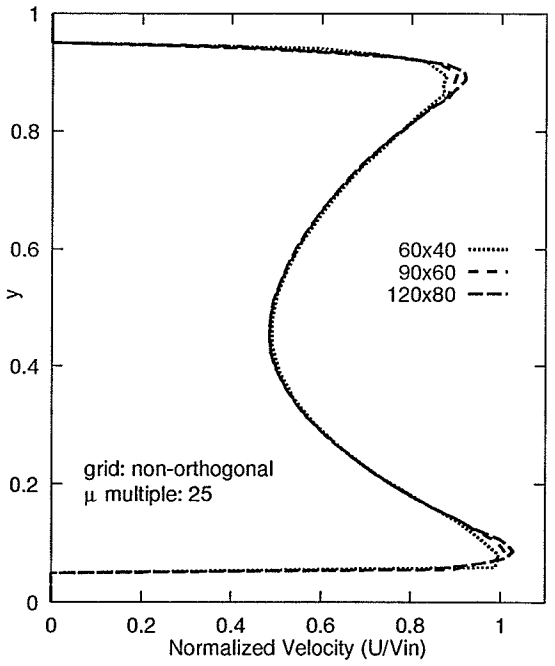

Figure C.23: RSTB Test Problem U Velocity Profiles at "A": Non-Orthogonal Grid, $\mu * 25$.

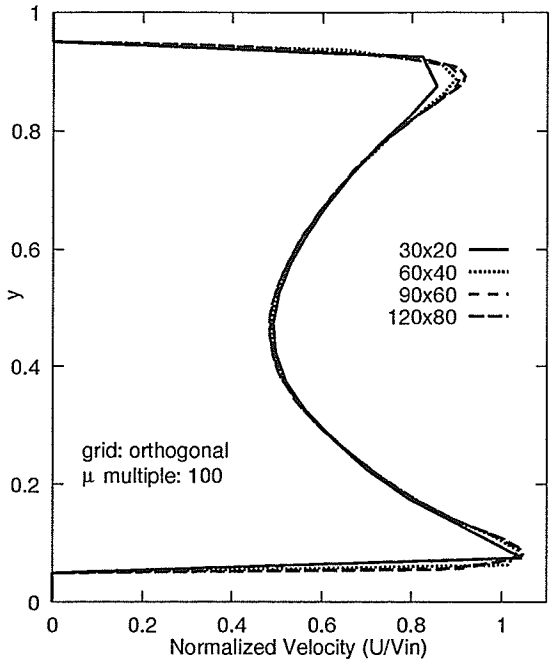

Figure C.24: RSTB Test Problem U Velocity Profiles at "A": Orthogonal Grid, $\mu * 100$.

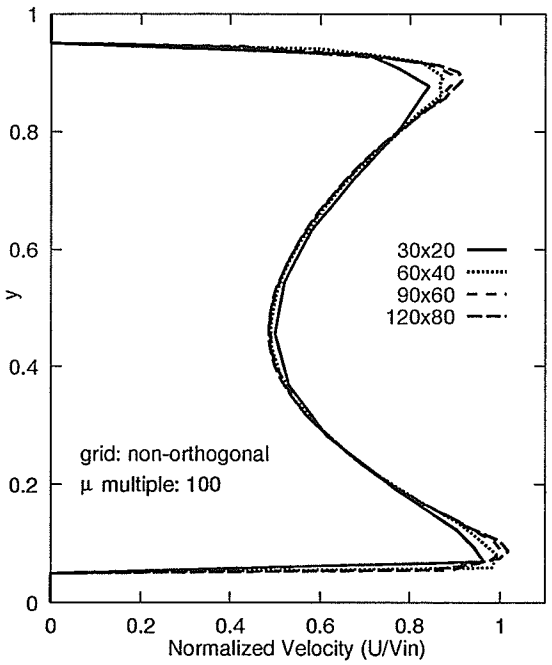

Figure C.25: RSTB Test Problem U Velocity Profiles at "A": Non-Orthogonal Grid, $\mu * 100$.

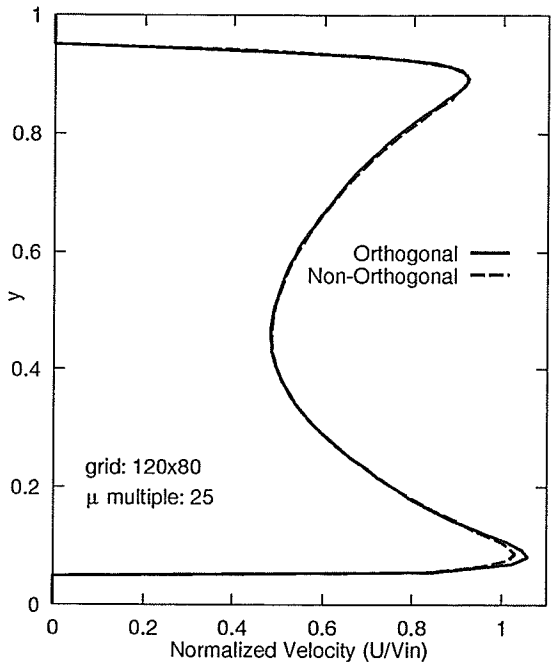

Figure C.26: RSTB Test Problem U Velocity Profiles at "A": 120×80 Grid, $\mu * 25$.

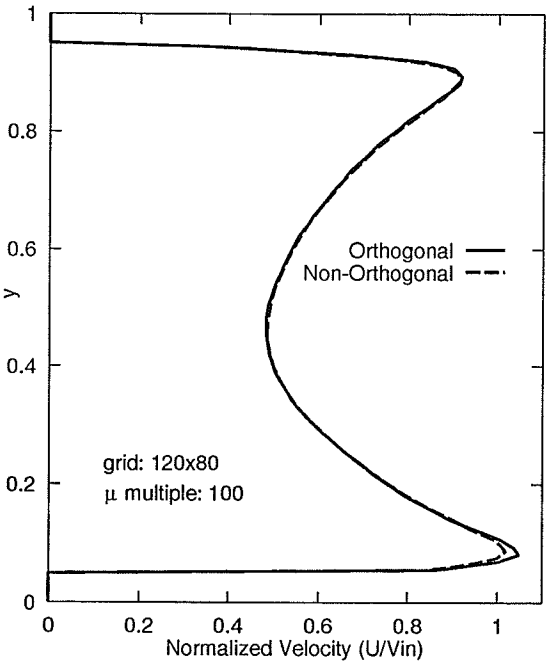

Figure C.27: RSTB Test Problem U Velocity Profiles at "A": 120×80 Grid, $\mu * 100$.

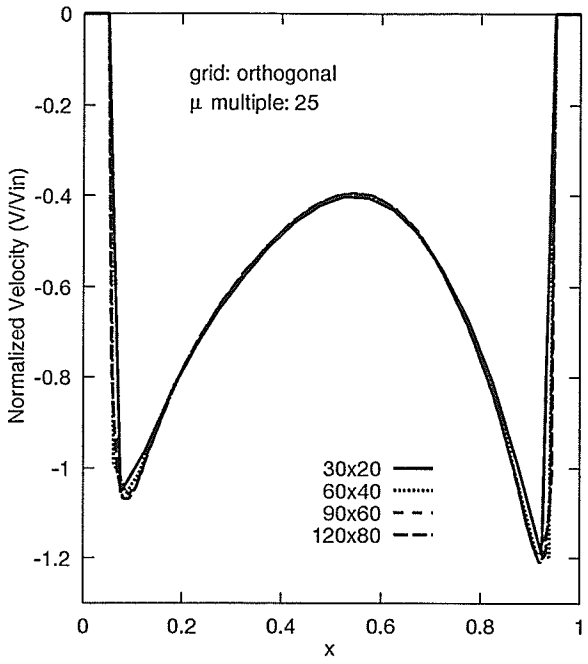

Figure C.28: RSTB Test Problem V Velocity Profiles at "B": Orthogonal Grid, $\mu * 25$.

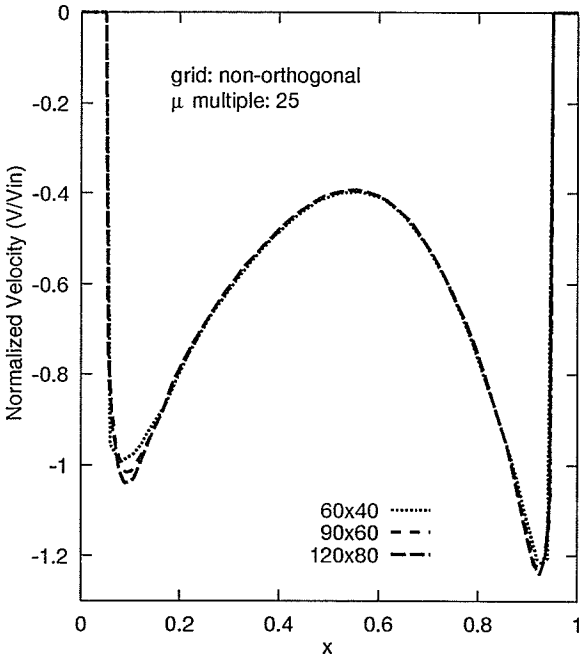

Figure C.29: RSTB Test Problem V Velocity Profiles at "B": Non-Orthogonal Grid, $\mu * 25$.

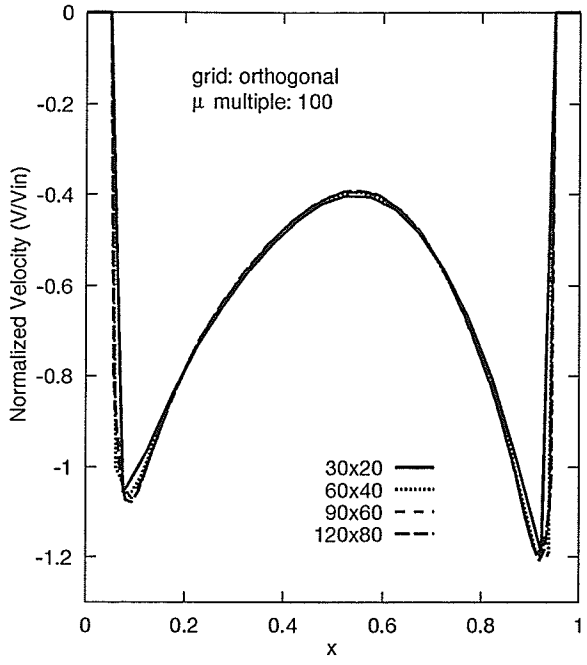

Figure C.30: RSTB Test Problem V Velocity Profiles at "B": Orthogonal Grid, $\mu * 100$.

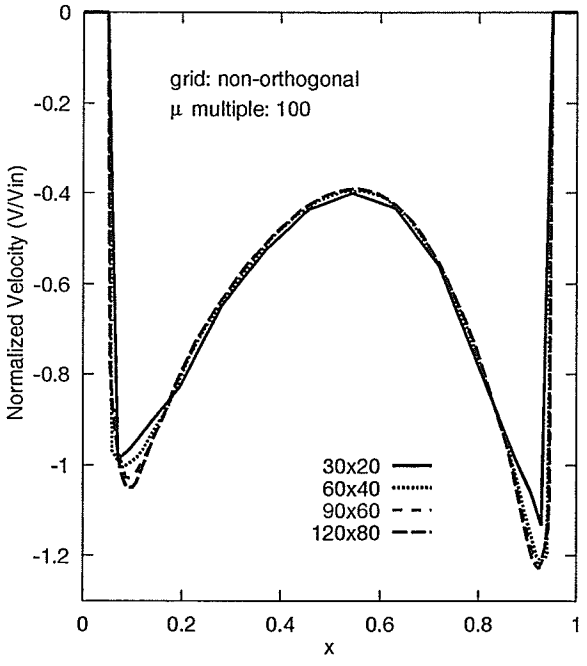

Figure C.31: RSTB Test Problem V Velocity Profiles at "B": Non-Orthogonal Grid, $\mu * 100$.

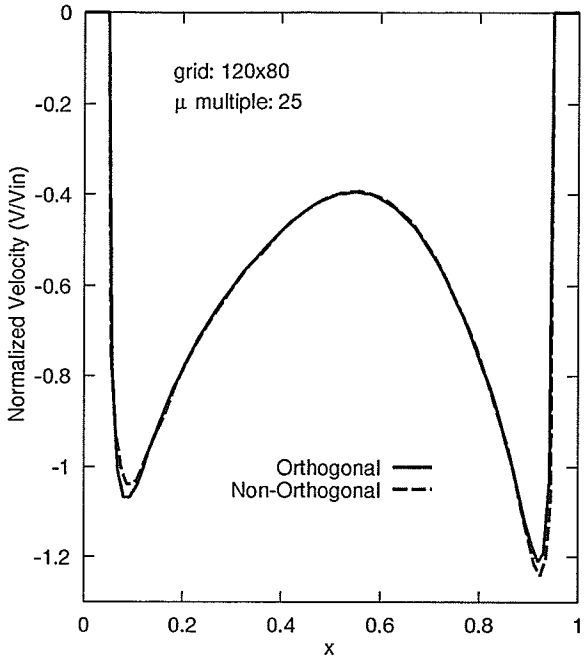

Figure C.32: RSTB Test Problem V Velocity Profiles at "B": 120×80 Grid, $\mu * 25$.

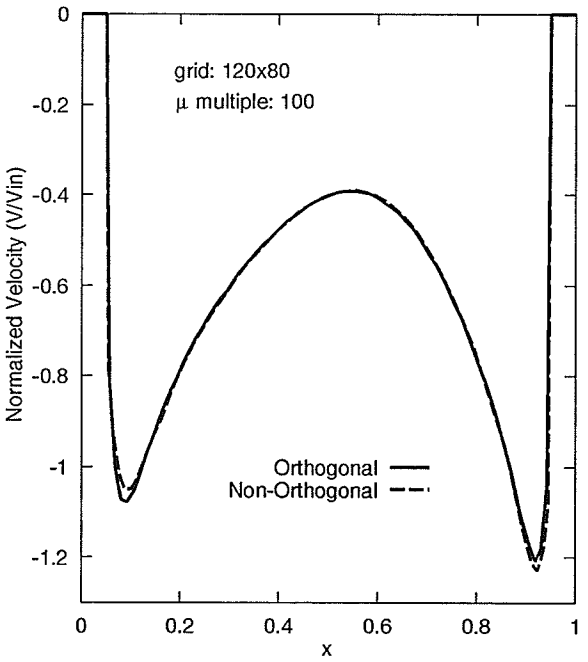

Figure C.33: RSTB Test Problem V Velocity Profiles at "B": 120×80 Grid, $\mu * 100$.

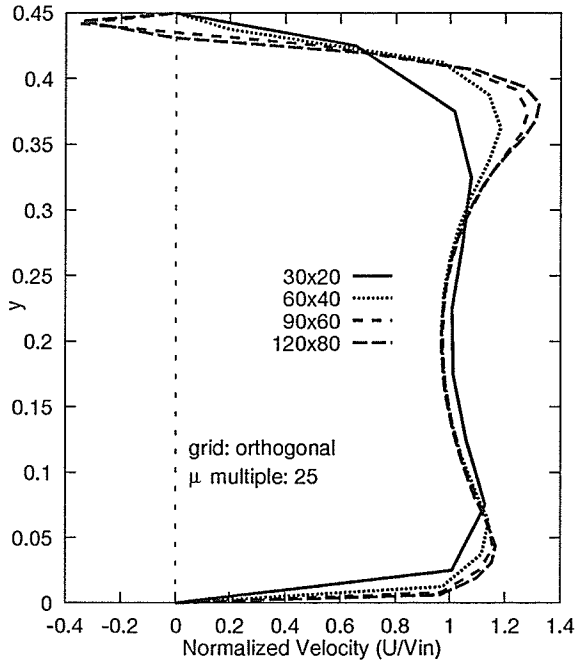

Figure C.34: RSTB Test Problem U Velocity Profiles at "C": Orthogonal Grid, $\mu * 25$.

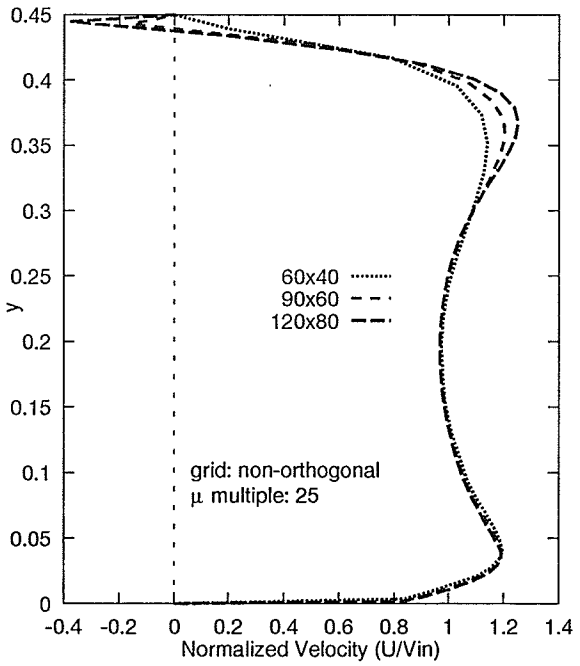

Figure C.35: RSTB Test Problem U Velocity Profiles at "C": Non-Orthogonal Grid, $\mu * 25$.

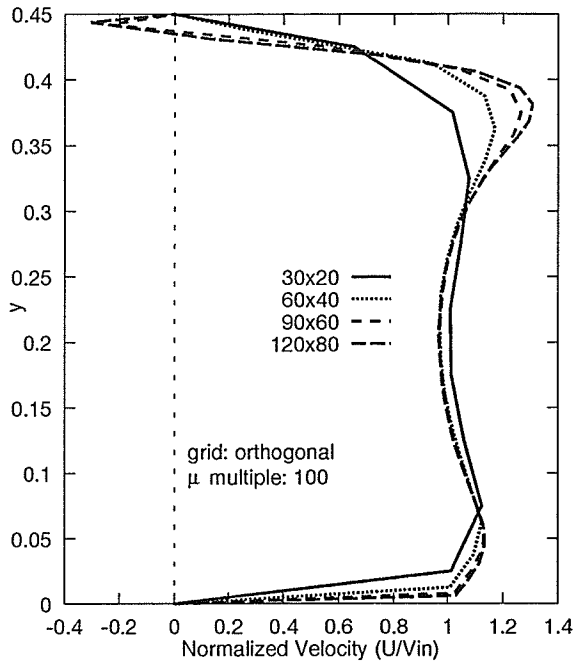

Figure C.36: RSTB Test Problem U Velocity Profiles at "C": Orthogonal Grid, $\mu * 100$.

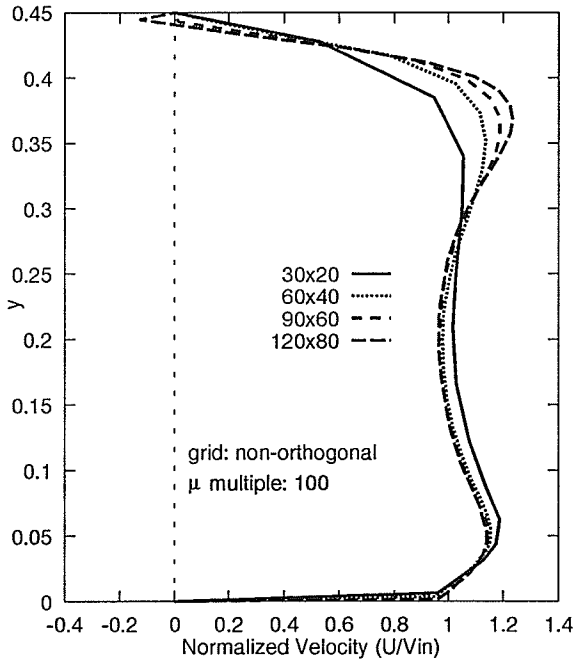

Figure C.37: RSTB Test Problem U Velocity Profiles at "C": Non-Orthogonal Grid, $\mu * 100$.

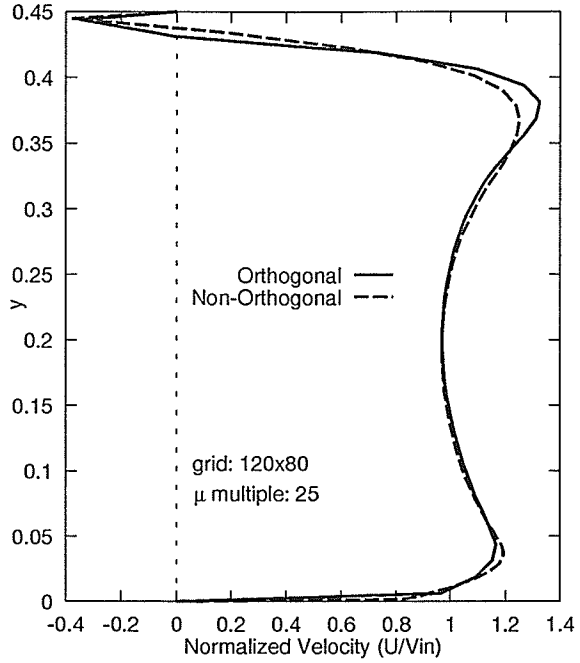

Figure C.38: RSTB Test Problem U Velocity Profiles at "C": 120×80 Grid, $\mu * 25$.

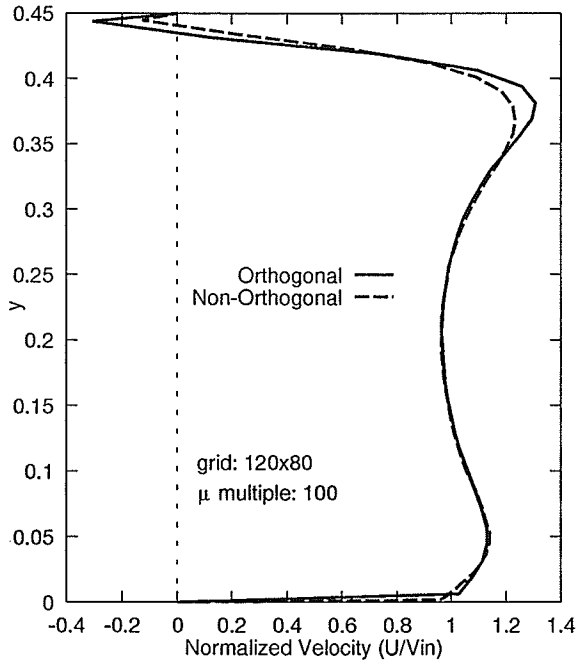

Figure C.39: RSTB Test Problem U Velocity Profiles at "C": 120×80 Grid, $\mu * 100$.